(NASA-CR-149585) THE MORPHOLOGY AND ORIGIN OF HADLEY RILLE, THE MOON Final Report (Boston Univ.) 281 p HC A13/MF A01 CSCL 03B

N77-17984

Unclas

G3/91 14927

THE MORPHOLOGY AND ORIGIN OF HADLEY RILLE, THE MOON

A final report on the work
carried out under NASA con-
tract no. ngr. 22-004-027.

THOMAS BREWER
Principal Investigator
Department of Geology, Boston University
Department of Regional Studies, Boston State College

August, 1976

Work Carried out at Boston University
Mohammed A. Gheith, Principal Administrator

ABSTRACT

This study is an investigation of the morphology of Hadley Rille and its relationship to surrounding structures.

Hadley Rille is wholly contained within mare basalts and appears to have been deflected by pre-mare material. The rille is cut by post-mare craters but cuts no post-mare crater. Irregular depressions at either end of the rille appear volcanic in origin. Thus, rille formation appears contemporaneous with mare filling. Rille wall outcrop probably represents a series of lava flows. Some debris accumulations in the rille are zoned resembling slides on quarry slopes. Others, without zonation, have an unclear mode of emplacement. Two boulder categories are present - light colored, rounded, partly buried boulders and dark colored, angular, exposed boulders. The former may be pre-mare talus into which the rille has been incised. Boulders in the rille are filleted above and undercut below. Thermal creep from intergranular adjustments during cyclic solar exposure may produce this effect.

Twenty-eight transverse profiles of the rille indicate that the southern section of the rille has a V-shaped profile with mildly concave limbs and no natural levees. U-shaped or asymmetric profiles have resulted from post-rille alteration. Asymmetry suggesting slip-off slopes is present on small radius corners. The mare surface slope is not consistently toward or away from the rille. The high side of the mare is not consistently on one side. Although not profiled, the

indistinct northern section of the rille appears U-shaped or flat bottomed. Volume calculations from profiles adjacent to mountains suggest a lunar slope erosion rate less than 35 meters/billion years.

Structures surrounding the rille are examined to determine their effect. Lineament strike directions are compared to computer simulated directions radial and circumferential to adjacent basins from structure locations. Structures in the Imbrium Basin appear related to the Serenitatis or Vaporum events. One such structure is the depression at the south end of the rille. A statistical comparison of structure and rille-segment azimuth frequency distributions indicates that structures and rille-segments are related in the north but unrelated in the south. A fracture density map indicates exceptionally high densities in significant locations.

The length and width of Hadley Rille place it with the largest 20% of sinuous rilles. Its channel volume of 20 km^3. corresponds to a block 40 km. x 50 km. x 10 meters. The absence of a depositional form is therefore significant. The power spectrum and meander wavelength are similar to values characteristic of terrestrial rivers.

Non-parametric statistical tests show that rille width decreases northward; that width and depth are directly correlated; that width shows abrupt increases followed by gradual tapering to the north; that limited segments show a width-azimuth relationship; and that increasing curvature of the rille may correlate with increasing rille width 2 km. northward.

Hadley Rille is directly related to the emplacement of mare basalts in Palus Putredinis. Existing hypotheses of sinuous rille origin are in discord with the cooling behavior of deep lava flows and the strength of materials. It is proposed that Hadley Rille is a channel which returned lava to the southern vent from which it initially extruded and that the channel persisted through many episodes of volcanism. This view is supported by available topographic information and is in accord with the observations of this study.

ACKNOWLEDGEMENTS

In the course of this study, several people and organizations have provided considerable support. The author particularly wishes to mention and thank the following: Prof. Mohamed A. Gheith of Boston University was instrumental in proposing this study and his continuing review throughout the work has been extremely perceptive. Prof. Dabney W. Caldwell of Boston University made many useful suggestions both before and during the writing phase of the work. Dr. Farouk El-Baz of the Smithsonian Institute opened many doors and provided the author with a rapid introduction to lunar research at the outset of the study. The personnel of the U.S.G.S. Experimental Cartographic Laboratory, McClean Va. were extremely cooperative in helping the author to use the facility's Kern PG-2 cartographic plotter on several occasions. Similar cooperation was extended by the personnel of the Lockheed Electronics Corp., MSC, Huston Texas, who educated the author in the use of the Bendix AS11A-1 analytical plotter at their laboratory. Data reduction was carried out at the Boston University Computer Center and at the Boston State College Computer Center. The personnel of both centers have provided much cheerful advice. Mr. Richard Gelpke drafted the majority of the line drawings and his skill is self-evident. This work was carried out during the author's graduate study at Boston University in connection with NASA grant no. ngr 22-004-027

TABLE OF CONTENTS

LIST OF TABLES

LIST OF FIGURES

CHAPTER I

INTRODUCTION

Preliminary Discussion:

Lunar rilles are long, narrow furrows on the lunar surface. Based on their appearance, they can be classed into groups which in reality tend to grade into one another. One distinct group has been called the sinuous lunar rilles. These have a serpentine aspect in map view which is a pattern similar to terrestrial stream channels. Their presence in the lunar environment has consequently been a matter of speculation since their discovery. Hadley Rille (fig. 1-1) is perhaps the freshest appearing sinuous lunar rille. Its proximity to the Apollo-15 landing site has made it the most photographed rille at all scales. This report is a study in detail of the geomorphology of this spectacular form and a discussion of the question of its origin.

Early observation of lunar rilles. The presence of valley-like features on the moon has been known for about 200 years. The first observation of lunar rilles was reported by Schroeter (1787) who identified a total of 11 rilles in the period 1787-1801. Subsequent early discoveries included Lohrman's observations of 75 rilles between 1832 and 1841. Schmidt, who himself discovered 243 rilles between 1842 and 1865, catalogued a total of 425 rilles. He was evidently the first to record Hadley Rille. By 1900, over 1000 lunar rilles had been described.

These discoverers did not note the sinuous nature of any of the

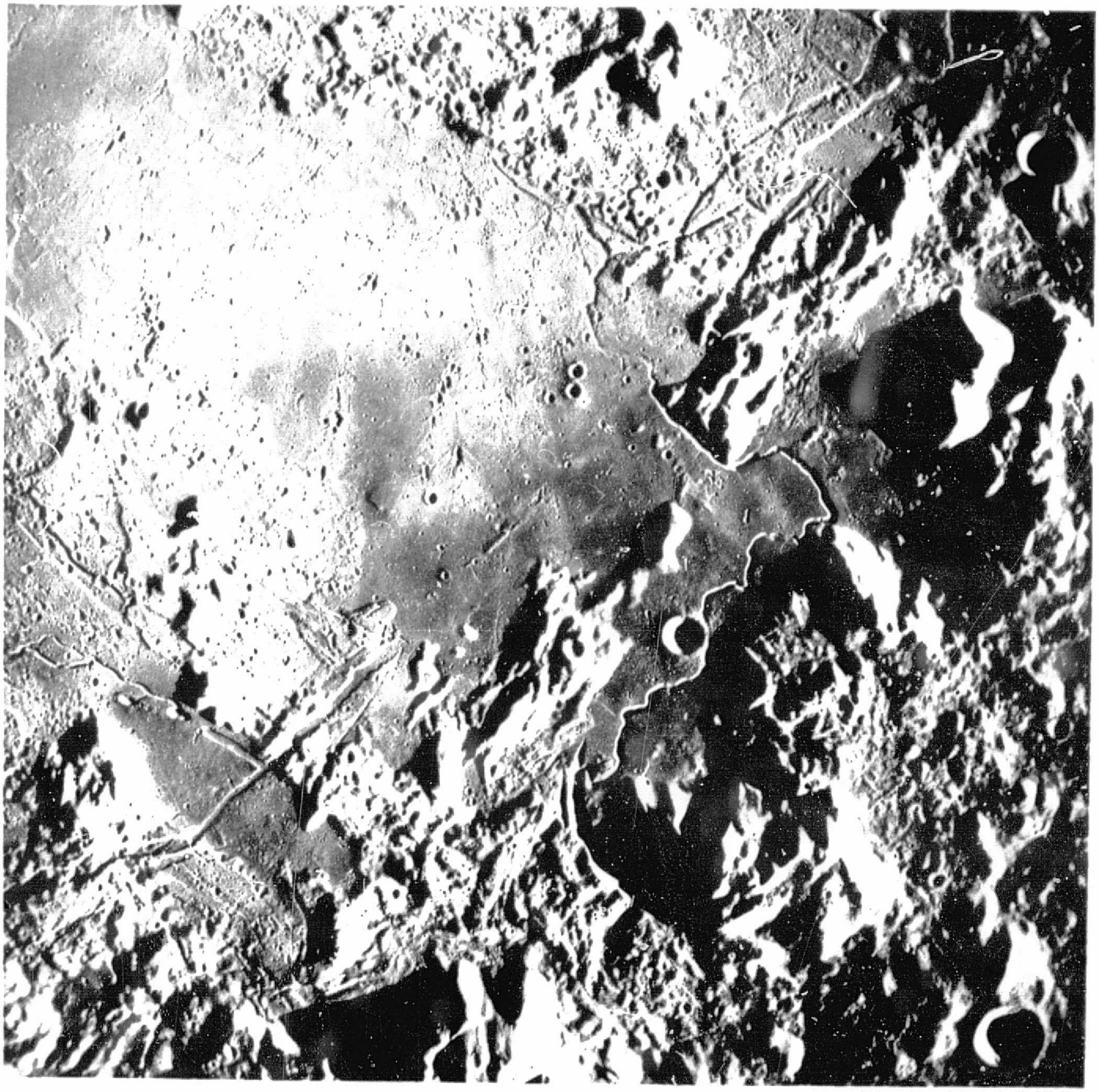

Fig. 1-1. Apollo-15 metric photograph 15-415: Hadley Rille early in the lunar day

rilles, however. Most furrows on the lunar surface, particularly those large enough for telescopic observation, are straight or gently curving. The photographs of lunar models prepared by Nasmyth and Carpenter (1874) show a slight sinuous aspect to the rilles on the Aristarchus Plateau. These authors believed the rilles to be structural in origin and did not mention the sinuous appearance. In 1893, Pickering made detailed observation of the Palus Putredinis region which resulted in an accurate sketch (fig. 1-2) of Hadley Rille. This is considerably more detailed than some sketches which have followed (for example, Goodacre, 1931). Pickering subsequently observed a number of sinuous rilles and was able to make important generalizations about their morphology and occurance. Due to limitations emposed by diffraction and air turbulance, Pickering's observations represent about the highest resolution visible from earth.

Figure 1-2 Sketch reproduced from Pickering (1903). This is the first accurate sketch of Hadley Rille. Only the southern half is portrayed. The remainder is not clearly visible from earth.

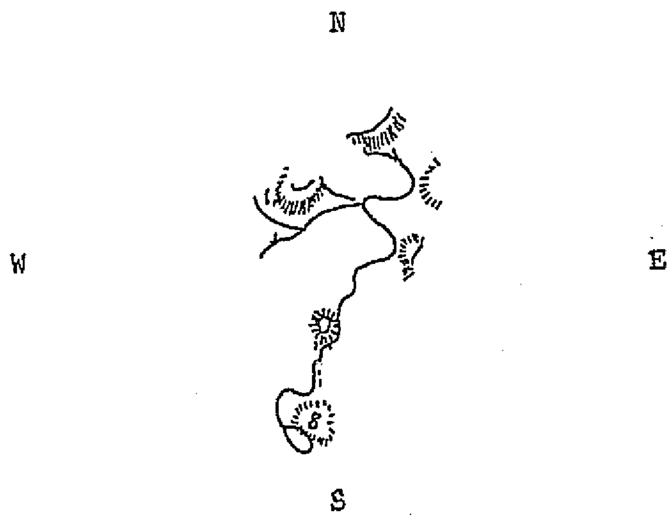

<u>Definition of Sinuous Lunar Rilles:</u>

Although space flight has enormously imporved the quality of data concerning lunar rilles, Pickering's initial characterization still serves as an adequate general description. He ascribes the following characteristics:

1. The sinuous rilles are wider at one end than the other.

2. The wide end originates in a pear-shaped depression.

3. The forms are composed of joined, short radius curves which impart to them the appearance of river channels.

4. One end appears higher than the other and the wide end (unlike rivers) appears to be the high end.

Hadley Rille departs from this characterization in that the depression at the wide end is arcuate, and that it is on a very nearly level surface.

Greeley (1971) has summarized the characteristics of the sinuous rilles as we know them from Lunar Orbiter photography as follows:

1. They appear to originate in irregularly shaped craters or depressions.

2. They generally trend down slope.

3. They have discontinuous channels and cut-off branches.

4. They are fairly uniform in width or occasionally taper toward the terminus.

5. They are restricted to mare surfaces and appear to be controlled by highland or pre-mare topography.

6. They form topographic highs along the rille axis.

Hadley Rille seems to conform to these criteria except for number 6. One must also question the use of "origin" and "terminus" to describe the ends of the rille.

Other authors have suggested definition on a quantitative basis. El-Baz, F. (1968) suggests that there are four major classes of rilles-linear, arcuate, sinuous and complex-and that they can be subclassified even further. He suggests that the subclasses can be distinguished by determining the sinuosity index, the percentage of curved portions of a rille compared to its total length.

Oberbeck, V. R. et al. (1971) have suggested that harmonic analysis, specifically, the coefficients of a Fourier sine series, might suffice to distinguish different classes of rilles.

The Problem of Sinuous Lunar Rilles:

The discovery of the sinuous rilles presented Pickering with the yet unanswered problem of how these large river-like features could form in an environment with little or no atmosphere. Until 1965, the resolution of observations was such that few astronomers were motivated to investigate the issue as relatively few of these forms could be recognized[1], and their sinuous nature is barely perceptable on telescopic photographs[2]. The general trend of thought seems to have been that the

[1]The state of knowledge just prior to Lunar Orbiter flights is summarized in Cameron, W.S. (1964) An interpretation of Schroeter's Valley and other Lunar Sinuous Rilles: J.G.R., Vol.69, p. 2423.

[2]A good telescopephoto of this region is found in Alter, D. (1967) Pictorial Guide to the Moon, Crowell, New York, p. 98. On p. 142 of this volume, a telescopic enlargement of the Alpine Valley illustrates the in visibility of its central rille which is so obvious on L.O. photos.

sinuous rilles are varieties of linear rilles and are structural in origin.

With the advent of Space flight, the realization hase come about that the sinuous rilles are both numerous and strikingly serpentine. A few investigators have made general observations on the geomorphology of the rilles (se ch. 2 of this report). A large number of writers have authored hypotheses concerning the origin of the rilles which are discussed in detail (see ch. 7 of this report). It is sufficient to note here that the hypotheses fall into categories classed according to mode of genesis as follows:

1. Tectonic movement
2. Ash flow following a volcanic eruption
3. Fluid flow
   a. Water
   b. Water and ice
   c. Water under ice
   d. Lava on the surface
   e. Lava in lava tubes followed by roof collapse
4. Fluidization of regolith over a gas fissure

The most pertinent work concerning the morphology of the Hadley Rille and its surroundings is found in the post-mission Apollo-15 preliminary science report and in the pre-mission planning for the flight. Prior to this report, there has evidently been no detailed geomorphic study of a specific lunar rille and its relation to its surroundings, and the problem of the origin of these forms remains unresolved.

The Purpose of this Study:

The selection of Palus Putredinis for the Apollo-15 landing site has provided a first hand observation of Hadley Rille. Excellent ground-based stereo coverage of several kilometers of the rille is available. In addition, this mission was the first to fly with metric mapping and panoramic cameras. The metric mapping camera has provided an undistorted view of the rille and surroundings as well as topographic control. The panoramic camera has produced oblique photographs of the surface with a resolution of two meters and less.

The purpose of this study is to:

1. Conduct a close qualitative examination of satellite and ground-based lunar photographs of Hadley Rille and its surroundings.

2. Make a precise and detailed quantitative examination of the rille and associated forms.

3. Establish statistical, algebraic and graphical relationships between measured parameters.

4. Discuss the genesis of the rille in terms of the relationships and observations and establish a most probable mode of origin for this sinuous rille.

CHAPTER II

PRIOR WORK IN THE APENNINE-HADLEY REGION

Location of the Study Area:

The location of Hadley Rille is detailed on the four maps, figures 2-1 to 2-4, which also serve to name various features of the region. These maps will serve as a useful reference for the lunar names used in this and subsequent chapters.

Due to the inverting nature of astronomical telescopes, there has been some confusion concerning the definition of lunar compass points. The most recent trend and the one which will be followed here is as follows: The north lunar pole is at the apparent top of the lunar disk as seen by an observer (unaided eye) standing in the earth's northern hemisphere. The east limb is then to the right and the west limb to the left. Zero degrees longitude bisects the visible side and otherwise, the coordinate system is identical to earth's.

Lunar Stratigraphic Nomenclature:

In the last 15 years, considerable effort on the part of a number of photogeologists has been devoted to developing a scheme of lunar stratigraphy. One apparent advantage on the moon is that impact events are essentially instantaneous and form widespread deposits, thus providing key beds. Significantly, the first attempt at establishing a lunar stratigraphy (Shoemaker and Hackman, 1962) was tied to impact events.

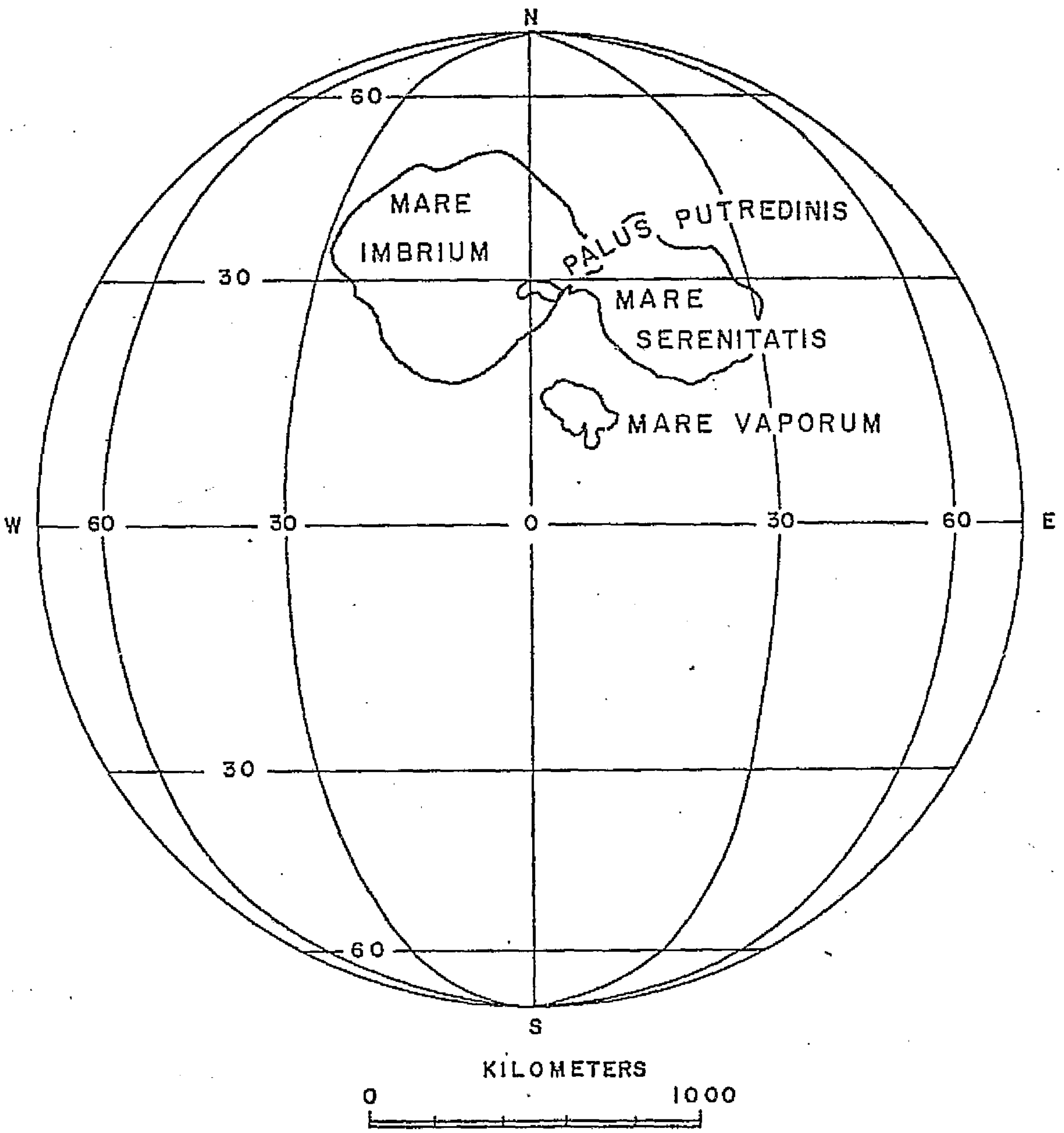

Fig. 2-1. Location of study area. Map indicating position on the moon.

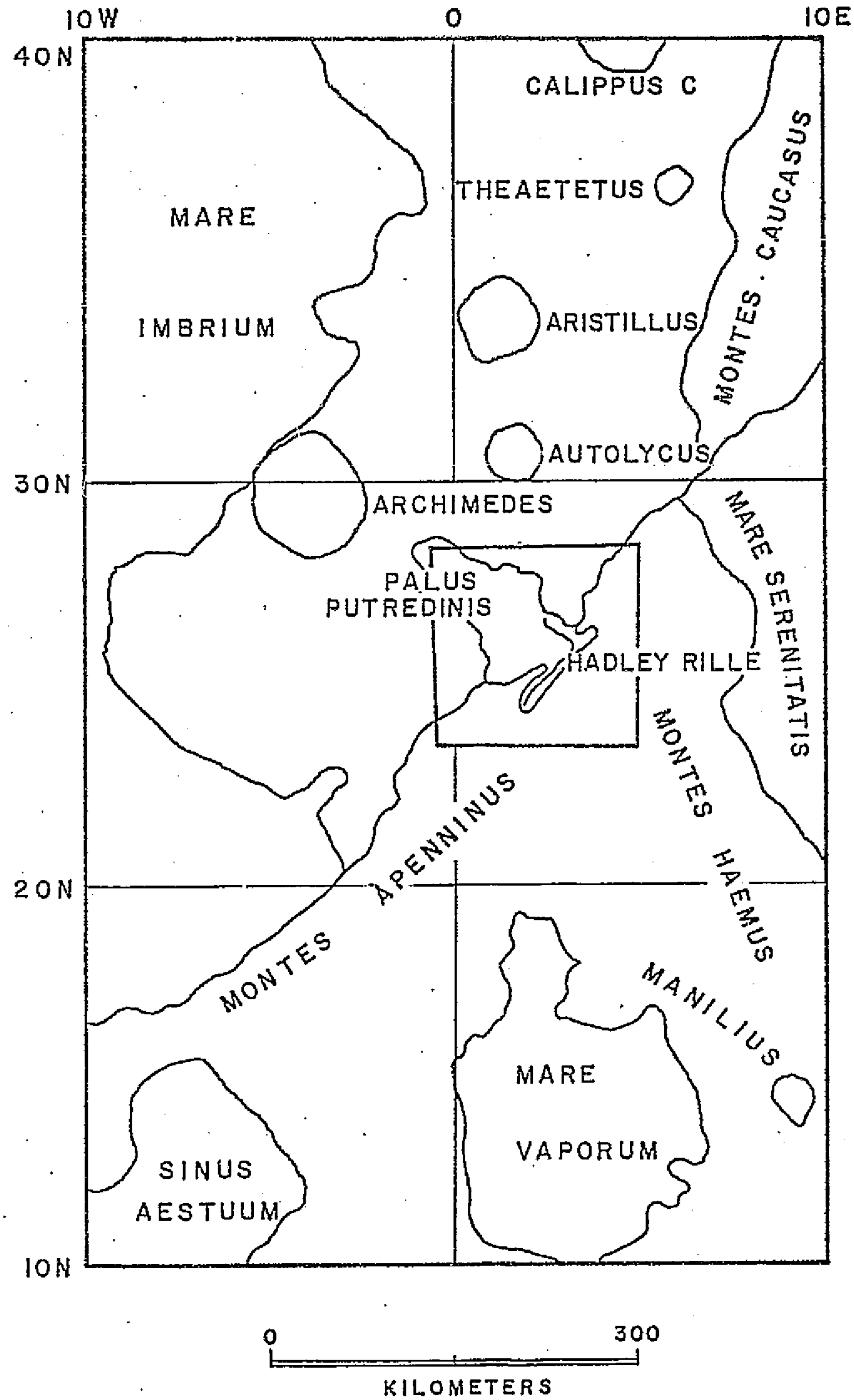

Fig. 2-2. Location of study area. Map indicating large features in the region.

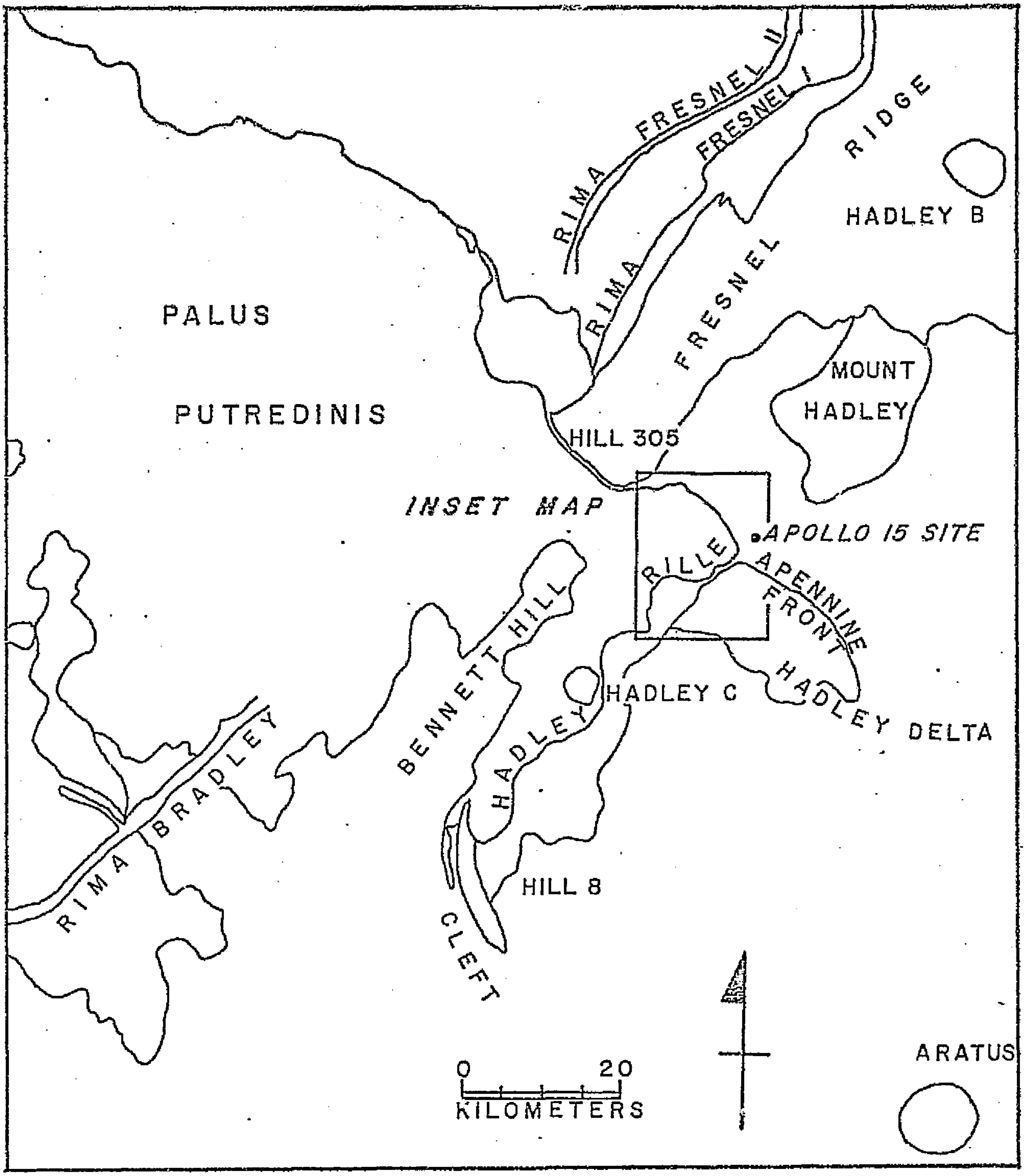

Fig. 2-3. Features surrounding Hadley Rille. Overlay to photograph 15-415 (fig. 1-1)

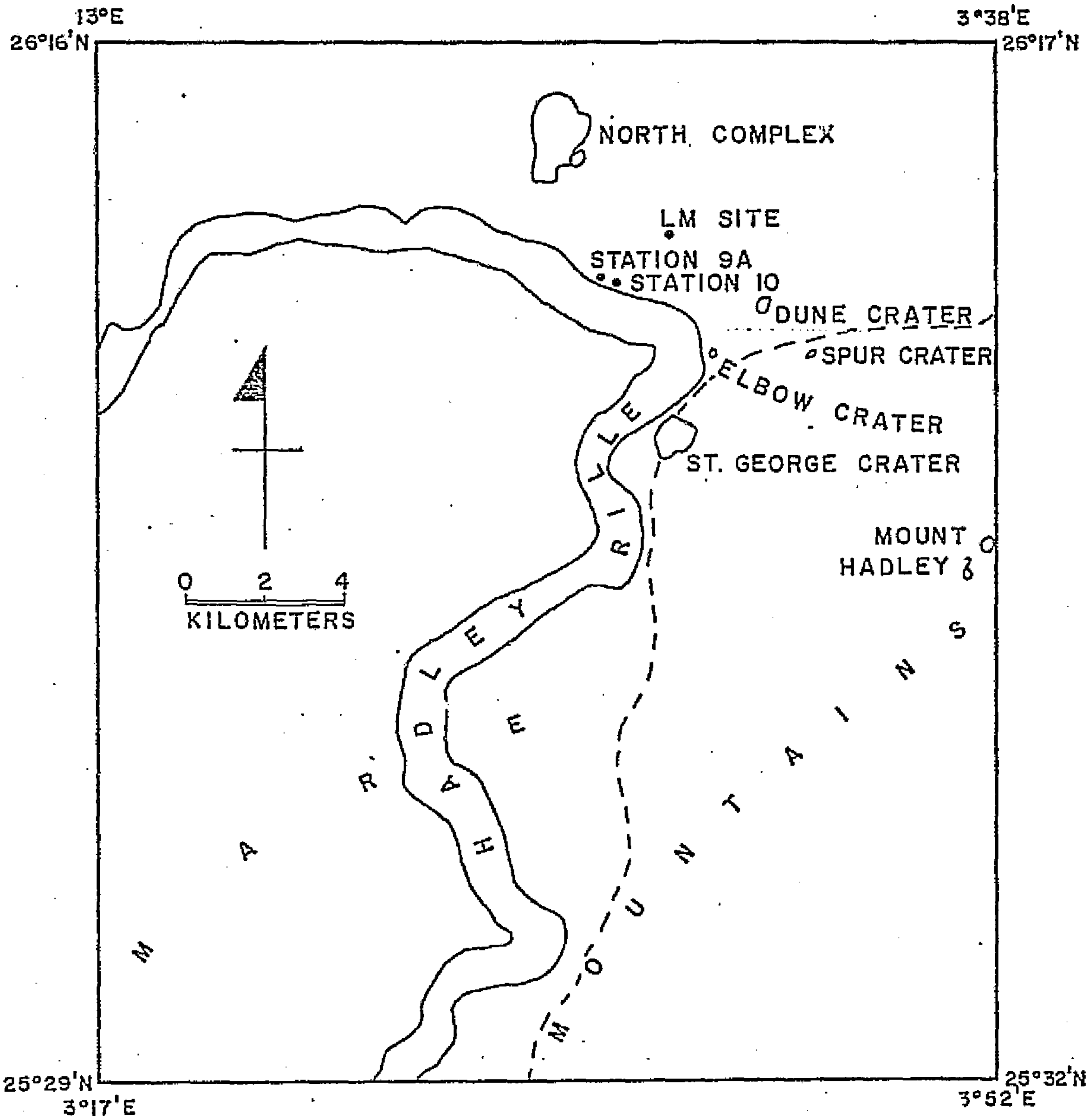

Fig. 2-4. Vicinity of the Apollo-15 landing site.

Difficulties in moon-wide correlation arise when units are sufficiently distant from type areas that no cross-cutting or superposed relationships are inferable with units in the type areas, a problem frequently recognized on earth. In this situation in lunar stratigraphy, secondary criteria such as morphology of superimposed craters (Soderbloom and Lebofsky, 1972) crater density or general surface appearance are used for correllation. In the current application of stratigraphic reasoning to lunar problems, the secondary criteria seem to have become primary and time stratigraphic designations based on surface appearance have been assigned in many studies. This is obviously an uncertain procedure, and many rock stratigraphic units displayed on lunar geologic maps have been assigned dual time stratigraphic designations reflecting the uncertainty (for example, Wilhelms and McCauley, 1971). Table 2-1 is a summary of pertinent lunar stratigraphic units and some of the criteria used to assign them.

Fortunately, the Imbrium event as represented by its assumed ejecta blanket, the Fra Mauro Formation, represents a fundamental time plane in lunar stratigraphy. This places Palus Putredinis, the rille location, in a very favorable geographic location for stratigraphic interpretation and its history can be related to the lunar stratigraphic sequence with some confidence.

Pre-Space Flight Geological Studies of the Palus Putredinis Region:

This region has been favored by most observers, probably because it lends itself to favorable undistorted telescopic viewing, and because of the complexity and variety of forms visible in a small sketchable area.

Table 2-1. Abridged scheme of lunar stratigraphic nomenclature

Rock stratigraphic unit	General characteristics and specific units[1].	Time unit	Estimated age YBP[2]
Copernican system	Deposits of Copernicus (primary definition) and other fresh appearing rayed craters.	Copernican period	
Eratosthenian system	Deposits of Eratosthenes (primary definition) and similar slightly subdued craters with rays no longer visible or very faint at high sun.	Eratosthenian period	3.2×10^9
Imbrian system	Upper member informally defined as the mare surface between Eratosthenes and Archemedes. Implication seems to be that this represents the contact between mare fill surface and Eratosthenian ejecta.	Imbrian period	
	Dark mare materials in the Imbrium Basin and Oceanus Procellarum.		
	Deposits of Archemedes and other mare-flooded craters superposed on circum-Imbrium deposits and structures.		
	Circum-Imbrium deposits and structures Basil member defined as the Fra Mauro Fm.		3.9×10^9
Pre-Imbrian system (informal)	Deposits of Julius Caesar and other similar degraded craters covered by Imbrium Basin ejecta or cut by its structures.	Pre-Imbrian time (not a formal period)	4.6×10^9

[1]Primarily from Wilhelms, D. E. and McCauley, J. F. (1971) Geologic map of the near side of the moon-rationalle, methods and format, p. 4, published to accompany U.S.G.S. Map No. I-703.

[2]Mutch, T. A. (1972) Geology of the Moon, Princeton University Press, Princeton, New Jersey.

Most 19th and 20th century books on lunar studies have maps, sketches or at least physiographic descriptions of the features in this region. At least two studies, Spurr (1944) and Shaler (1903) are caried out from a geological view point. Both of these authors believed that most lunar features are volcanic in origin and interpreted Palus Putredinis in this way. It is interesting that although extremely detailed physiographic maps of the moon were produced prior to space flight, little effort was devoted to interpreting geology on a regional basis. Most authors have described classes of lunar features and have illustrated their classifications with specific examples.

Post-Space Flight Geological Studies of the Palus Putredinis Region:

Because of the selection of the Apollo-15 landing site adjacent to Hadley Rille, considerable interest developed in interpreting the regional structure and stratigraphy. What follows are brief notes on the most significant studies of the regional geology. The regional setting itself is the subject of the next section.

Hackmann (1960) differentiates the mare material from the pre-mare material and illustrates the large scale structural elements on a 1;3,800,000 map.

Hackmann (1966) subdivides the area into several formations and establishes a stratigraphic sequence. This differentiates Imbrium material, post-Imbrium event basin filling material in two stages and several crater forming episodes on a 1:1,000,000 map.

Carr and El-Baz considerably redefine the boundaries given on Hackmann's 1966 map and add several stratigraphic units to account for erosional processes and secondary cratering. Some rock units on this 1:250,000 scale map receive a significantly different interpretation than on Hackmann's 1966 map. For example, Hackmann mapped a large exposure of Apennine Bench Formation south of Hadley Rille which was interpreted as early mare filling basalt. This was reinterpreted by Carr and El-Baz as a post-Imbrium event slump deposit. These changes may reflect the improved resolution of Lunar Orbiter photography.

Howard (1971) has mapped the region surrounding the Apollo-15 landing site to provide a detailed 1:50,000 scale map which is substantially in agreement with and was published simultaneously with the Carr and El-Baz map. There is considerably more detail concerning small craters, and the precise location of some of the boundaries of small units on the mare surface is modified.

Swann _et al_. (1971) have discussed the Apollo-15 landing site in their detailed post-Apollo-15 preliminary report. The authors make pertinent observations and interpretations from the ground-based photographs and discuss sample locations and observations station by station.

Swann _et al_. (1972) in an abriged version of the preceding paper have included a map of the landing site area at a scale of 1:32,000. This map which was drawn with the additional insight provided by Apollo-15 confirms the interpretation of Howard (1971).

Gast _et al_. (1972) have presented thin sections of the major rock types found during Apollo-15 and have classed the rocks according to mineralogy and texture. The genesis of the most prominent rocks is also discussed.

Regional Setting:

Hadley Rille is located in the Palus Putredinis (figs. 2-1, 2, 3, 4) an embayment of mare material just within the southeastern edge of the Imbrium Basin. The apennine Mountains form an arc which is the southeast edge of Mare Imbrium and are regarded as fault-bounded, rectilinear, upthrust blocks resulting from the basin-forming impact (Carr and El-Baz, 1971). The rille is adjacent to and apparently in places deflected by the prominent escarpement at the edge of the mountain block. The lunar coordinates of a point close to the center of the rille are: North 26°00', East 3°30'.

The Imbrium Basin (fig. 2-1) is generally regarded as a large impact feature formed toward the end of the moon's early history. It is thus an old lunar form, but it and its ejecta blanket cross-cut several older features (Wilhelms and McCauley, 1972). Adjacent to, and cross-cut by the Imbrium Basin are two other older basins - Serenetatis on the east and Vaporum on the southeast. The geologic complexity of the Hadley region is due in part to its Imbrium Basin marginal position. From a broad view, the bedrock geology and structure must have been affected by the Serenitatis and Vaporum events as well.

Structure. There are numerous linear or arcuate structural elements in this region which are for the most part circumferential or radial to the Imbrium Basin (Howard and Head, 1972). These lineaments are also aligned in the same directions as the well known Lunar Grid (Elston et al., 1971). It appears that the three nearby basin forming events and the overall lunar structural pattern have joined to produce the structures so well displayed at this site. Some structures, even structures within the Imbrium Basin, seem to be related to the formation of the Serenetatis Basin in pre-Imbrium time (see ch. 5 of this report). All the tectonism which produced the faults represented by some of these structures did not occur immediately after the Imbrium event. Some faults cut the low-lying Apennine Bench Formation which seems to be an early mare filling basalt (Carr and El-Baz, 1971).

Palus Putredinis, illustrated on figure 2-2, is bounded by faults to the northeast and southeast, bounded by hummocky hills of questionable origin (mapped by Carr and El-Baz (1971) as post-Imbrium slump deposits) to the southwest, by the rim deposits of the crater Archemedes to the northwest, and by ejecta from the craters Aristillus and Autolycus to the north. It seems to be topographically isolated from the adjacent floor of Mare Imbrium which implies that the basalts which fill it are of local origin. It is possible however, that at the time of mare filling that Rima Fresnell to the north was a local channel or that one existed under the present ejecta blanket of Autolycus.

Major craters. Large craters which have scattered ejecta throughout this region are Archemedes, Aristillus and Autolycus (fig. 2-2). Ejecta from the latter two have formed secondary impact features on the surface of Palus Putredinis indicating their recent age. Thr former, which is flooded with late mare basalt, has secondary structures remaining on the Apennine Bench Formation indicating an impact after the early stages of mare filling (Carr and El-Baz, 1971).

ck samples. Samples frcm Apollo-15 come from two distinct geological environments - the mare plains and the base of the mountain Hadley Delta (Swann et al., 1972). The rocks from the mare plains are predominantly basalt and those from the mountain are breccias and metaigneous rocks. These rocks have been further subdivided into groups which are simply reptrsented in the diagram (fig. 2-5), drawn for this report but based on the conclusions in the papers by Gast et al. (1972) and Swann et al. (1972). These two articles also discuss the genesis of the various rock types and come to the following conclusions:

1. The mare basalt samples are evidently related to the underlying mare filling material. The type 2 basalt was sampled directly from apparent outcrop at the rille lip, and was also found as a boulder in Dune Crater at the other extremity of the sampled area (fig. 2-4). The type 1 basalt was found as boulders throughout the mare area and is thought to consitiute the uppermost rock unit underlying most of the regolith at the site. The types 3 and 4 basalts were found at the rille lip (station 9a, fig. 2-4) and their origin is not clear. In the context of this investigation, it appears possible that these have been ejected by relatively recent impacts from early formed rock units exposed toward the bottom of the stratigraphic section in the rille.

2. Most of tne non-basalt samples are regarded as being related to the Imbrium impact either as impact-related breccias or as deep seated rocks brought up by the event.

3. Those breccias which contain mare basalts are though to have originated with local impacts on the mare.

4. The non-mare basalts which were found in rake samples at Spur

Figure 2-5. Classification of the suite of rocks from the Apollo-15 mission.

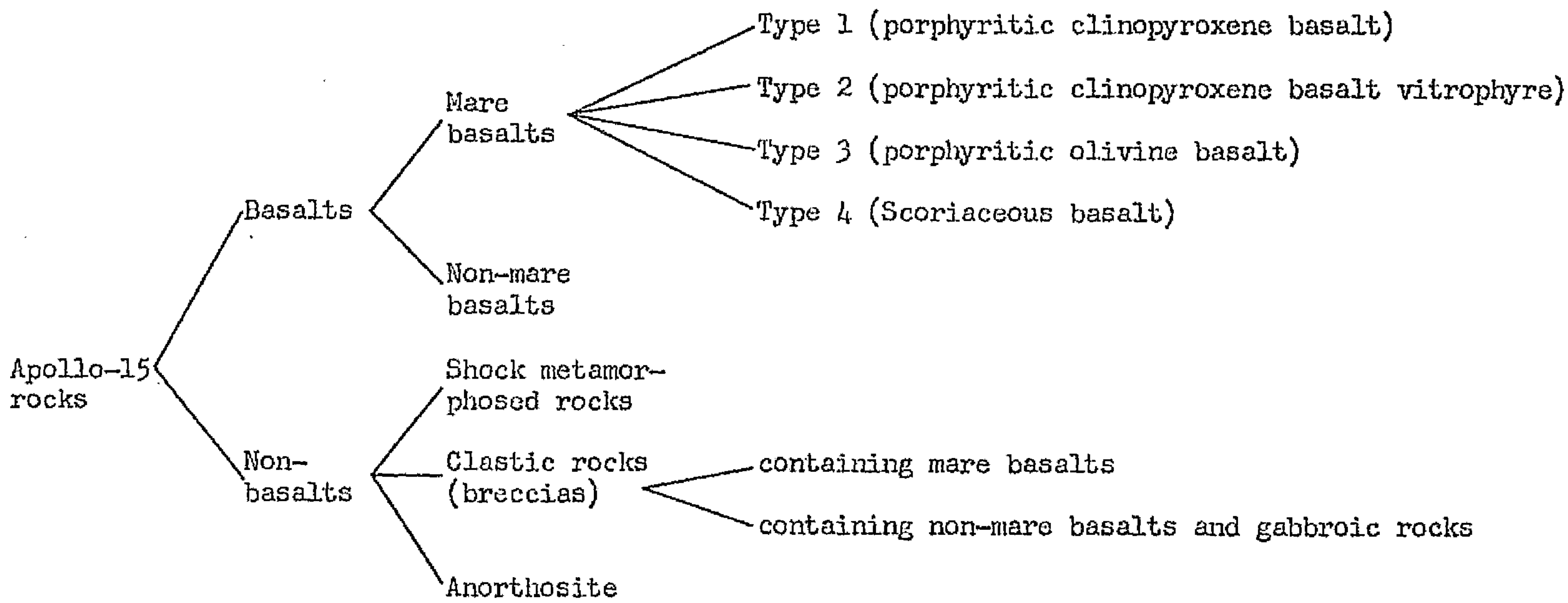

Crater (fig. 2-4) and in breccias from the Appennine Front, may have been transported from distant pre-mare te-rains after impacts.

Radiometric ages. In addition to the extensive petrologic work which has been reported on lunar rocks, radiometric ages have been reported for many samples. In particular, Husain (1972) has published a compilation of ^{40}Ar-^{39}Ar ages on five samples of mare basalt and eleven Apollo-14 samples from the Fra Mauro Formation. I have examined these values statistically to ascertain the elapsed time between the Imbrium event and the mare filling.

The five mare basalt values range from 3.15 to 3.32 x 10^9 YBP and have an average value of 3.26 x 10^9 years. The standard deviation is 0.064 x 10^9 indicating a 90% probability that another value from the same population would fall in the range 3.26 $\pm$ 0.11 x 10^9 years. The standard error is 0.03 x 10^9 years which after calculating the t-statistic indicates that the average value has a 90% probability of being within $\pm$ 0.06 x 10^9 years of the 'true' value of this population.

The Fra Mauro Formation samples show dates ranging from 3.50 to 3.92 x 10^9 YBP. The average value is 3.78 x 10^9 years with a standard deviation of 0.11 x 10^9 years indicating that another value from the same population would have a 90% probability of falling in the range 3.78 $\pm$0.18 x 10^9 years. The standard error is 0.054 x 10^9 years indicating that the average value has a 90% probability of being within $\pm$ 0.10 x 10^9 years of the 'true' value.

By subtracting these two averages and calculating the pooled 90% confidence limit for the difference, the time difference between the

Imbrium event and the mare filling can be estimated. This value is $0.52 \pm 0.10 \times 10^9$ years. Thus, at the 90% confidence level, 400 to 600 million years elapsed between the Imbrium event and mare filling. It should be noted that the confidence limits for these averages are about the same magnitude as the estimated experimental errors reported by the various investigators summarized by Husain. Therefore, this statistical treatment seems reasonable.

Geologic History of the Region:

The geologic history of the Hadley region has been discussed to some extent by most of the authors noted in the preceding section. A general statement is found in Carr and El-Baz (1971). The diversity of cross-cutting and overlapping relationships at the Imbrium Basin edge makes a detailed relative chronology of events possible. The discussion which follows and the chart (fig. 2-6) are based on interpretations in the previously discussed papers and my own observations of the Hadley region.

Events can be classed into three major time intervals in the order of decreasing age as follows:

1. Events preceding and including the Imbrium Basin forming event.
2. Events which occured between the time of the basin formation and the end of mare filling.
3. Events which occurred after mare filling.

These basic intervals are chosen because the breaks are represented by widespread rock units. The basin forming event is represented by the Imbrium Basin and its ejecta blanket. The mare filling is represented by the mare basalt surface. The regional history is discerned by ob-

Fig. 2-6. Chart indicating relative sequence of events around Hadley Rille (craters and features illustrated on maps, Figs. 2-1 to 2-4).

Assumed event (youngest at top)	Lunar time period PI	I	E	C	Evidence
Small primary craters				( )	Ejecta and boulder trails in rille
Aristillus event				( )	Craters and ejecta
Autolycus event				( )	Craters and ejecta
Hadley C impact			(	?	Crater and ejecta
Second generation of rille deposits			(	?	Exposed boulders in rille
Faulting			?	?	Lineaments near Hill 305
Rille deposits		(		?	Buried Boulders
Rille Formation		(	)		Hadley Rille
Adjustment of lava surface			? ?		Formation of mare volcanic morphology
Second sequence of mare filling		(	)		Mare surface basalts emplaced
Archemedes event		()			Rim deposits and structures on Apennine Bench Fm.
Faulting		?)			Rima Bradley, Rima Fresnell and associated structures
Early Mare filling		( )			Apennine Bench Fm.
Slumping into Imbrium Basin		()			Slump deposits
Imbrium Impact	(	)			Fra Mauro Fm., Apennine Mts., Imbrium Bn.
Serenetatis Impact	( )				Serenetatis Basin and rim
Vaporum Impact	( )				Vaporum Basin
Accretion of Moon	(?				Rock fragments in some breccias

( ) – indicates that the event took place within the indicated interval but not necessarily throughout the interval.

? – indicates that the limit is questionable.

serving how smaller features are related to these major features and to each other. Figure 2-6 is a chart which summarizes the major events and their inferred chronology. Most of the events have been mentioned in the preceding sections. The remainder are discussed in chapter 4 of this report:

Previous Work Concerning the Morphology of Lunar Rilles:

Several authors have written papers which include significant observations concerning the appearance of lunar rilles and how the rilles relate to their surroundings. The following fall into this category:

Pickering's (1903) initial and important characterization of the general properties of lunar sinuous rilles has already been discussed in chapter 1.

Murray (1971) has noted that some sinuous rilles are linear for part of their length and that in some cases, the land surface is higher on one side of the straight section than on the other. He also noted that rilles tend to be topographically controlled and to avoid topographic highs. He reports that sinuous rilles tend to be associated with established volcanic features. This paper also includes a map of the location of rilles and it is pointed out that 85% of the rilles lie in the maria.

Oberbeck et al. (1969) note the similarity between the sinuous rilles and a cratered sinuous ridge north of the Harbinger Mountains.

McCall (1970) points out that many sinuous rilles have apparent obstructions in them to lateral flow of fluids. He notes that some rilles have craters associated with them spaced along the length of the rille.

Strom (1968) makes careful observations of the cross-cutting relationship of the inner rille in Schroeter's Valley.

Schumm (1969) notes that several of the rilles in the vicinity of the crater Aristarchus seem to cut through topographic highs.

Hapke and Greenspan (1970) feel that an abnormally high number of craters occur in the bottoms of some sinuous rilles.

Cruikshank and Wood (1972) note that some rilles have distinctly flat bottoms while others have V-shaped profiles.

Greeley (1971) gives the geomorphic characteristics of several rilles in the Marius Hills region of the moon.

Other authors have investigated the rilles using numerical measures to group and compare them. These papers include the following:

Schubert et al. (1970) have performed a set of quantitative measurements on about 130 sinuous rilles and have reported histograms of length, width width/length ratio, meander wave length, and meander wave length/width ratio. They have also plotted the location of these rilles on a map of the nearside disk and have therby illustrated that there is a strong tendency for rilles to occur at the edge of the circular mare basins within mare material. The histograms presented in Schubert's report have been recast as cumulative frequency diagrams in chapter 6 of this report and the position of Hadley Rille is indicated on each.

Oberbeck, et al. (1971) have published a catalog of lunar rilles with varying sinuosity. This is intended as a working regerence for other investigators. They also develop the equations for writing a Fourier sine series to represent the rilles and apply the method to a specific example. The use of a Fourier series to characterize rilles was also proposed in 1969 by this author in the original porposal for this report. Such an aralysis has been carried out for Hadley Rille and forms a section of chapter 6 to follow.

<u>Previous Geomorphic Investigations of Hadley Rille:</u>

Pickering (1903) described Hadley Rille as the second largest sinuous rille visible on the moon (schroeter's Valley is larger). He was able to observe 50 miles of the rille's channel from the earth (end to end distance) and calculated that it had a sinuous length of 65 miles. (Lunar Orbiter imagery has shown the rille to be considerably longer and has also indicated a number of rilles which are even longer than Hadley Rille but less distinct.) Pickering also noted that the general course is slightly east of north (modern convention) and that the rille is about 2000 feet (600 meters) wide at the southern extremity narrowing to about 500 to 1000 feet (150 to 300 meters) in places. He noted that the southern end coincides with a crater on the south flank of Hill 8 in the Hadley range of the Apennine Mountains (fig. 2-2)

Cameron (1964) also noted the crater at the south end of the rille and compared it the terrestrial volcanic features.

Greeley (1971) described the rille as being 135 km. long, 1.2 km. wide, and 370 meters deep. He noted that the northern section is considerably different than the southern part. This difference is discussed in chapter 4 of this report. Greeley also reports that the rille is situated on a topographic high (an observation not confirmed here), notes the lack of tributaries, and discusses the obstruction in the channel near the Apollo-15 landing site.

Howard et al. (1972) have written a post Apollo-15 report on the geology and morphology of Hadley Rille with particularly emphasis on the landing site area. Using Apollo-15 photographs and maps prepared from them, they have reported that:

1. The southern half of the rille does not appear to be structurally controlled, wheras segments of the northern half do.

2. Around the landing site, the mare surface on the northwest side of the rille is higher than the surface on the southeast side.

3. The width and depth of the rille are in direct proportion.

4. The rille wall exhibits a distinct sequence of talus, outcrop and regolith with approptiate ledges and benches.

5. The materials within the rille can be attributed to mass wasting from the outcrop along the edge.

Wu et al. (1972) have published a map of the Apollo-15 landing site based on Apollo-15 metric and panoramic photographs. Their report also includes eight topographic profiles of the rille at the landing site produced on a Bendix AS-11 Analytical Plotter, using panoramic photographs. About thirty such profiles covering most of the southern part of the rille have been prepared for this report (see ch. 4).

CHAPTER III

EQUIPMENT AND METHODS

This chapter describes the photographs and physical equipment used for data aquisition and the methods used for data reduction and analysis.

Lunar Photography:

The two programs which have had exceptional significance in this study are the Lunar Orbiter program and the Apollo-15 mission.

Lunar Orbiter photography. A general description of the Lunar Orbiter camera system can be found in the volume by Bowker and Hughes (1971) or the volume by Kosofsky and El-Baz (1970). Briefly, the Lunar Orbiter spacecraft was equipped to expose and process film during flight. The resulting photographs were transmitted to earth by an optical scanning and transmission system. This approach allows much better resolution than a television camera permits. The photographic camera was equipped with short and long focal length lenses which allowed the transmission of medium and high resolution photographs during each flight. These pictures have good to excellent resolution (to one meter), but the metric fidelity is probably correct to only a few percent. Therefore, they are primarily useful for observation rather than measurement.

Apollo-15 photography. A general description of the Apollo camera systems is found in the report by Dietrich and Clanton (1972). The photographs which have been most relevant are the Apollo-15 metric, panoramic and ground-based Hasselblad photographs. The metric and panoramic photographs are individually described in the report by Lockheed Electronics

(1972). A report by Batson et al. (1971) describes the individual ground-based photographs. A technical summary of all the Apollo-15 photography is found in a report by Cameron and Niksch (1972).

A brief description of the three relevant camera systems follows:

1. The metric camera is primarily designed to take medium resolution photographs (to about ten meters depending on sun angle) with very high metric fidelity (or low point to point distortion). The camera has a 76 mm focal length which at the flight altitude of 100 km. yielded photos with a scale of about 1:1,300,000. These are usually supplied at an enlargement of about 1.66x yielding a scale of 1:800,000. Most of the metric photographs were taken with a vertical camera axis, although some oblique exposures were made.

2. The panoramic camera is designed to take high resolution (to one meter from orbit) photographs with low metric fidelity. In operation, the camera exposes the film serially as the optical system sweeps from horizon to horizon. The film simultaneously moves in a direction contrary to the lens motion. During the Apollo-15 mission, the optic axis was oriented oblique to the surface, and was shifted between a fore and aft orientation for successive exposures. This sequence provided stereo coverage because the exposure intervals were timed to have the aft exposure cover the same area as a preceding fore exposure. These can be successfully viewed in a conventional stereo viewer if only a small section is observed at a time.

Table 3-1. Specific photographs used in this study.

1. General monoscope observation of the Palus Putredinis region with some stereoscopic overlap.

Small scale- Lunar Orbiter IV, $102H_3$, $109H_3$

Intermediate scale - Lunar Orbiter V, 104M to 106M

2. Stereo, vertical, intermediate scale photos of the rille.

Low sun - Apollo-15 Metric, 411 to 419
Intermediate sun - Apollo-15 Metric, 583 to 590
Intermediate sun - Apollo-15 Metric, 990-995 (no shadow from adjacent mountains in this series)
High sun - Apollo-15 Metric 2304-2306 (coverage of south half only)

3. Stereo, oblique, intermediate scale, high resolution coverage of the rille (listed as stereo pairs).

Low sun - Apollo-15 Pan (9374 and 9379, 9376 and 9381)
Intermediate sun - Apollo-15 Pan (9795 and 9800, 9797 and 9802, 9801 and 9806, 9803 and 9808)

4. High metric fidelity coverage with appropriate shadowing for use on the Mann comparator.

Apollo-15 Metric, 416

5. Used to construct stereo models on the AS-11A plotter.

Metric model - Apollo-15 Metric, 992 and 994
Pan model - Apollo-15 Pan, 9795 and 9800

6. Ground-based photographs which can be used to construct panoramas of the rille (60 mm. Hasselblad).

Apollo-15, 11166, 11168, 11170, 11172, 11174, 11176, 11178, 11180, 11182, 11184 (taken from station 10)
Apollo-15, 11111, 11112, 11121, 11123, 11125, 11127 (station 9a)

7. Ground-based photographs which illustrate specific rille features near the landing site (500 mm. Hasselblad).

Apollo-15, 12023 and 12104, 12058 and 12125, 12056 and 12156

8. Used to construct a photomosaic for structural interpretation.

Apollo-15 Metric, 991-995

9. Large scale vertical monoscipic coverage of the Apollo-15 landing site.

Apollo-15 Rectified Pan, 9377 (4x enlargement)

3. The ground-based Hasselblad photographs were taken with hand-held cameras by astronauts during surface traverses. The cameras have focal lengths of 60 mm. and 500 mm. which provide normal and telephoto coverage. Many stereo pairs exist because objects were intentionally photographed from two or more traverse stations.

Table 3-1 specifically lists the numbers of photographs which were used for different purposes in this study.

Equipment and Procedures:

Large format stereo viewer. Several unusual problems associated with lunar photography make stereoviewing with a conventional stereoscope difficult.

1. Many of the photos are large (up to 70 cm diagonal dimension). These are too big to manipulate under a conventional mirror stereoscope.

2. The field of view of conventional stereoscopes is too small to see whole forms on photographs this size.

3. The ground-based Hasselblad photographs were taken from arbitrary positions that produced stereo coverage but with photographs of different scales. This makes stereo fusion in a conventional viewer difficult because each eye sees a different size image.

4. Many of the photographs are provided with a glossy surface. Rear lighting of these photographs is desireable for optimum and continuous viewing.

5. For purposes of analysis, it was desired to take azimuthal and length measurements of features while viewing photographs in stereo. This requires several inches of working space under the stereoscope.

6. A conventional mirror stereoscope is throughly uncomfortable

Fig. 3-1. Large Format Stereo Viewer

Fig. 3-2. Bridgeport Milling Machine. An Apollo photograph is in place on the milling table for coordinate measurement. (Courtesy of John C. Losch, Clockmaker, Holliston, Mass.)

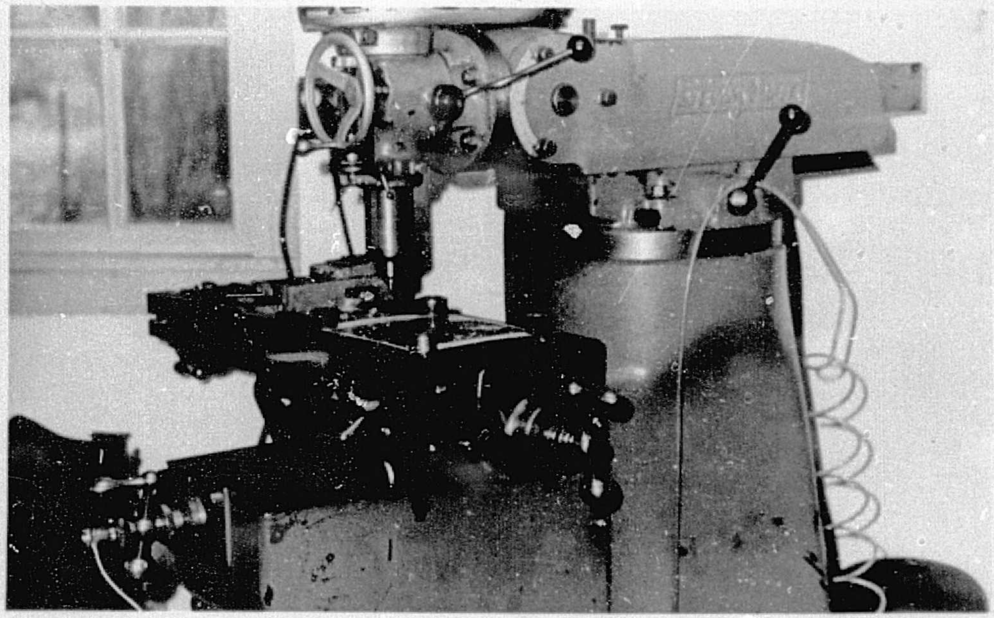

when used for continuous viewing.

In order to cope with these constraints a special stereo viewer was designed and built for this study (fig. 3-1). This instrument which has proven very useful has the following attributes:

1. It can sit on either an illuminated drawing table for rear lit viewing, or on a conventional 5' drawing table.

2. It has simple adjustments for eyebase, neck inclination, distance between photographs, and relative scale of photographs.

3. Extra large objective mirrors 17.1 x 12.4 cm. give a large field.

4. There is sufficient room beneath the mirrors to manipulate a drafting machine for accurate angular and distance measurements.

Cost of the optical parts (first surface mirrors were used) was about $20.00 (Edmund Scientific Co., Great Barrington, N.J., 1970). The remaining parts were salvage.

Measurement of length. The most accurate and detailed length measurements were made using the Mann 1200-3 comparator described below. For purposes requiring less precision, conventional drafting scales were at times used. Two instruments which provided relatively high precision at moderate cost are:

1. A Sears & Roebuck co. metric vernier caliper (Sears no. 40161) with a range of 13.5 cm. and vernier scale divisions to $\pm$ 0.05 mm.

2. An Edmund Scientific Co. optical comparator (Edmund no. 30325 with reticle no. 30584). This is a flat field large diameter 10x hand lens which is arranged to view a reticle which contains several angular,

linear and circular scales. One linear scale is 2. cm long and can be read to ± 0.05 mm.

The primary constraint on the use of these instruments is that although they provide precise information of specific features, they do not provide good information about the location of different features relative to each other. Size and relative location can be determined together if the x-y coordinates of points outlining features can be read on an arbitrary grid. An inaccurate, although simple way to accomplish this is to overlay a sheet of graph paper over the field being studied (for example-a photograph) and read x-y coordinates from the graph paper. A more accurate approach which was used for some preliminary analysis of profiles is carried out by placing the field to be surveyed on the table of a vertical milling machine (Bridgeport model no. 9BRM). The precision lead screws which normally drive the milling table can be turned to position different points of interest under a stylus held in the stationary jaws of the milling head chuck. After each location is positioned, its x and y coordinates are read from the lead screw dials. If the milling table is in good condition, this will provide coordinate data to an accuracy better than ± 0.025 mm. over a field 23 cm. by 50 cm. This potentially useful technique was not developed to is ultimate extent because the Mann 1200-3 comparator became available (fig. 3-2).

<u>The Mann 1200-3 Stellar Comparator</u>. The Mann 1200-3 stellar comparator (GCA/David W. Mann Co., Burlington, Mass.) was purchased by the Lockheed Corporation at the Manned Spacecraft Center, Houston, Texas to measure

the relative positions of stars on astral photographs. These measurements are needed to determine camera orientation in the Apollo mapping camera system. Conceptually, the mechanism is similar to the milling table described above with the following additions

1. The field is placed on a rear illuminated glass platform so that light is transmitted through the field.

2. The viewer looks through an optical system and locates coordinate positions under cross hairs.

3. Coordinate positions are electronically displayed and measurement numbers are electronically assigned.

4. The output can be directly punched on cards for subsequent data processing

5. The precision of the system is to within $\pm$ 0.001 mm. which corresponds to a ground distance of 10 meters at the scale used.

This system allowed the rapid compilation of several important data sets described in chapters 5 and 6.

Topographic measurements. Several methods were tried in an effort to obtain accurate topographic information about the rille and its surroundings. Preliminary information was extracted from NASA Lunar Topographic Photo Map Rima Hadley sheets A and B published by the U. S. Army Topographic Command. This map was printed as part of the pre-mission planning for Apollo-15 and is based on Lunar Orbiter photography. The vertical accuracy is $\pm$ 250 meters at the 90% probability level. This is adequate to describe the mountains bordering Palus Putredinis, but reveals little about Hadley Rille.

Initially, it was hoped that topographic information could be derived from stereo pairs of Apollo-15 metric photographs using conventional cartographic plotting equipment. An attempt was made to use the Kern PG-2 cartographic plotter at the U.S.G.S. experimental cartographic laboratory in McClean Va. There were severe difficulties with this machine in accomodating it to the lunar radius and in leveling the metric photos. A more basic problem appears to be that the rille can only be expanded to a scale width of a few millimeters with these photos in this machine. This fact combined with unfavorable sun angles produces inadequate resolution within the rillefor adequate elevation readings. Thus, to determine accurate topographic information, it was necessary to use Apollo-15 panoramic photographs. As detailed below, these can only be analyzed with an analytical plotter.

The AS-11A Analytical Plotter. The fundamental photogrammetric problem is to relate an object's position on a photograph to its true position on the ground, and thence to its proper position on a map. If the position and orientation of the cameras is simple and well controlled, cartographic data can be extracted very simply with primitive equipment. Thus, stereo pairs of vertical axis frame camera photographs taken from equal altitudes can be analyzed using only a good scale (Advertising Displays, Inc., 1970). Unfortunately, flight altitudes vary and camera axes generally deviate from vertical. If either the camera orientations with respect to the planetary radius is known, or if the exact three-dimensional ground coordinates of several common points in the overlap area of the two photographs are known, then it is possible to determine a set of unique three dimensional map coordinates for all the common points on the two photographs. An analysis of the stereo geometry results in a matrix equation (Tewinkel, 1966) with the form:

$$\begin{bmatrix} x \\ y \\ z \end{bmatrix} = M \begin{bmatrix} X \\ Y \\ Z \end{bmatrix} \qquad (3\text{-}1)$$

which relates the photo coordinates of points x,y,z (= -Focal length) to ground coordinates (X,Y,Z). M is a 3x3 matrix involving the cosines of angles between axes in the two coordinate systems. When multiplied, (3-1) becomes the equations of colinearity which represent the relationship between photos and the ground.

Historically, these equations have been resolved mechanically by setting up the photographs in projectors with orientations similar to the camera orientations with which the photographs were exposed. This results in a stereo-projected image called a stereo model which is an analog of the real ground surface. This can actually be contoured to produce a map. The geometry of these machines is straight forward in the case of double projection direct viewing plotters, and more complex in mechanical machines with optical trains such as the previously mentioned Kern PG-2 (Schermerhorn, 1966). It is conventional to regard machines in the latter class as mechanical analog computers which solve the colinearity equations to maintain the correct stereo model as different parts of it are scanned by the machine operator. The analog elements in the machine are rod lengths and cam profiles which maintain the correct relative geometry of the photographs, stereo model and drawing pen which sketches contour lines on the map. These machines are designed to solve the geometry of frame camera photographs which are those in which the entire film surface is exposed simultaneously and the photo geometry is symmetric about the optic axis. Apollo metric photographs are this type. The panoramic photographs which are exposed serially as the oblique camera axis sweeps from horizon to horizon have a much more complex geometry (Doyle, 1972).

The difference between mechanical plotters and the AS-11A analytical plotter is that the mechanical machines solve the equations of colinearity by adjusting angles and lengths within the machine, wheras the analytical plotter solves the equations by continuous computation in a digital computer. When the operator scans different portions of the stereo model, the photographs are adjusted by positioning servos to maintain the correct orientation. In other words, as the operator moves the index mark of the viewer from one point to the next across the stereoscopic model, the computer continuously computes new positioning parameters for the photo plate holders to give a geometrically correct stereomodel at the position being viewed. This means that the same set of calculations must be repeated very quickly to keep up with the operator's movement of the index. In the AS-11A, the repetition rate for some equations is 200 times per second (Bendix Corp., 1968).

When the AS-11A is operated, several mutually related things happen:

1. The operator moves the viewing field across the stereomodel which he observes through the viewer. As he does so, the model geometry is adjusted into a correct orientation by real time computation of the colinearity equations. This solution depends upon what part of the model the operator is viewing.

2. Interwoven with these calculations are other calculations which determine cartographic coordinate information. These depend upon the continually updated model geometry and the viewer index position on the model. The cartographic information is used to drive an electro-mechanical plotter to directly produce topographic maps <u>or</u> profiles at any desired scale.

The electronic rather than mechanical connections between different parts of this system give much more flexibility than previously possible. For example, the system can accomodate any pair of photographs for which colinearity equations can be programmed. Any analytically describable aberration such as lens distortion, uneven motion of the panoramic camera system, film shrinkage, or non-linear motion of mechanical elements of the machine can be programmed as corrections to the colinearity equations. Furthermore, if redundant ground control information is available, a least squares technique can be used to provide the best possible model parameters during the initial orientation procedures. Thus, the photogrammetric use of high resolution panoramic photographs with their low inherent metric fidelity is made possible.

The system operation for the purpose of producing profiles such as are illustrated in chapter 4 of this report can be divided into three steps:

1. Metric photographs are oriented in the system using known ground control information. For this study, five ground control points were used for absolute orientation of the model. A minimum of three points is required, so the use of redundant information permitted a least-squares fit. The ground control information was derived from Apollo-15

stellar photography and laser altimetry and was provided by Lockheed Electronics Corp.

2. Panoramic photographs are oriented in the machine by relating known positions on the panoramic photographs to the same points on the metric photographs. In this process, the colinearity equations for the panoramic photographs are established but with constants derived from the metric photographs.

3. The machine is switched to an operational mode and contour or profile information can be plotted at will. This is accomplished as in most photogrammetric equipment by moving an optical index across the stereomodel so that the index appears to touch the land surface.

Selection of photographs for photogrammetric analysis. The following criteria were considered in selecting photographs for use with the AS11-A analytical plotter:

1. The metric photos used for the metric control must be well documented. The laser altimeter ceased to operate during the 33rd revolution (Roberson and Kaula, 1972) which dictated the use of metric photos taken earlier in the flight.

2. The visual process used in positioning the index in the stereo comparator requires that the photos have a well-defined ground surface for comparison. A low sun angle gives the best contrast. Fortunately, the low sun exposure of the Apennine-Hadley region occured early in the flight.

3. The sun must be high enough to prevent shadows from obscuring features of interest.

4. Time limitations dictated that only one panoramic model could be set up. It was therefore necessary to select a pair of pan photos which covered as much of the rille as possible. Because of its relatively fresh appearance, the southern section of the rille was given preference. The photos chosen for the study (table 3-1) appear to best meet these constraints.

Mathematical Methods:

Fourier series: Any function which is defined throughout an interval of width 2L, is bounded within the interval, and has a finite number of discontinuities, and maxima and minima within the interval can be approximated by a series of the form (Skolnikoff and Redheffer, 1958):

$$f(x) = a_o/2 + \sum_{n=1} (a_n \cos(n\ \ x/L) + b_n \sin(n\ \ x/L))$$

where f(x) is the approximate value of the function, x is the independent variable, a_n, b_n are coefficients which must be determined, and L is one half the interval being approximated. Such an approximation is called the Fourier series corresponding to the function.

The Fourier series is being used in this study to approximate the function represented by a specific set of data. From a practical point of view, any data set (assumed to meet the above conditions) can be approximated by one of several forms of the Fourier series. The differences between the forms governs the behavior of periodic extensions of the series outside the approximated interval (Gaskell 1958). An appropriate form for use here appears to be the Fourier cosine series which is given by:

$$f(x) = a_o/2 + {}_{n\,=\,1}\, a_n \cos(n \quad x/L)$$

This series is suitable because it can represent non-zero values of the function at the point x = 0. Data for the Fourier series was acquired using the Mann comparator, and it is not convenient to initiate the data set at x and y equal to zero with this instrument. The coefficients of the cosine series are given by the equation:

$$a_n = 2/k \ {}_{i=1}^{k-1}\ f_i \cos(n \quad x_i/L)$$

where the values f_i are the data values at the x_i locations and k is the number of data points.

Spencer's formula. This formula is one of a family of curve smoothing formulas which have been developed for extracting significant trends in the data from random fluctuations. The formula calculates a moving average over an interval which includes ten data points on either side of the central point, but a moving average in which points close to the central point are given more weight than points which are distant. The equation for the smoothed y-value (y'_k) for a point x_k when values of data (y_1, y_2,.....y_k,..y_n) exist for equally spaced x-values (x_1 to x_n) is given by the equation (Harbaugh and Merriam, 1968)

$$y'_k = 1/350\ (60y_k + 57(y_{k+1} + y_{k-1}) + 47(y_{k+2} + y_{k-2}) + 33(y_{k+3} + y_{k-3})$$

$$+ 18(y_{k+4} + y_{k-4}) + 6(y_{k+5} + y_{k-5}) - 2(y_{k+6} + y_{k-6}) - 5(y_{k+7} + y_{k-7})$$

$$-5(y_{k+8} + y_{k-8}) - 3(y_{k+9} + y_{k-9}) - (y_{k+10} + y_{k-10})$$

When a list of data is smoothed using this formula, the first ten and last ten x-values cannot have smoothed y-values calculated for them. This follows because the form of the equation for the first smoothed value (y'_0 or y'_k at $k = 0$) requires ten y-values (unsmoothed data values y_{-1}, y_{-2} .....,y_{-10}) which correspond to x_{-1} to x_{-10}. y_{-10} is the first y value in the data set. However, if circular data is smoothed, a smoothed y-value can be calculated for all x-values if ten values are duplicated from each end of the data set and attached to the opposite end. For example, if a histogram of strike data is being smoothed, the first ten class intervals can be attached after the last class interval because strike data is repetitive with a 180° period. This allows the calculation of smoothed frequency values for intervals up to and including the last class interval. Similarly, by attaching the last ten values to the first end of the histogram, the first and succeeding frequencies can be smoothed.

Miscellaneous mathematical methods. Vector algebra is used in appendix 1 to solve a problem in spherical trigometry. A good discussion of vectors is found in the book by Thomas (1953). It appears that vector techniques could be much more extensively used in solving structural geology problems.

Several statistical tests are used in chapters 5 and 6. It seems impossible to divorce the test from the statistics being compared, so the tests are discussed and referenced in those chapters. A number of short special purpose programs were written for numerical processing of data in this study. These are listed in table 3-2 and unique programs are included in appendix 4.

Table 3-2. Programs developed for this study.

Name of program	Used in chapter	Description
*FORIER	6	Computes the Fourier coefficients for a full Fourier series and optionally, a cosine series. Also computes the power spectrum, value of the series approximation at each x-value and the residual value ($y_{data} - y_{Fourier\ approx.}$).
*SELECT	5	Compares numerically coded information with a user-supplied binary array to sort the coded data into groups.
*SPENCR	5,6	Computes smoothed values according to Spencer's formula. The smoothed curve is plotted graphically by the line printer. If the data is circular, the program fills in ten spaces at each end of the data set.
*RILLE	5,6	Computes, using the pythagorean theorem and the trapazoidial rule, various rille parameters from Mann comparator data. Computed values include width and length of channel for rille locations and segments and average values for the rille. Also prints and punches frequency distributions of relevant factors.
FREQ	5	Groups data into distributions of frequency, percent frequency, cumulative frequency and percent cumulative frequency. Prints result and optionally punches result.
DIF	5	Computes difference of two percent cumulative frequency distributions for the Smirnov test.
*BASIN	5	Computes the azimuth from any location to basin central locations and compares the computed direction with observed structure directions at the first location.

* - These five programs have been incorporated as appendix 4.

CHAPTER IV

DETAILED DESCRIPTION OF HADLEY RILLE

This chapter is a detailed discussion of Hadley Rille and the large and small scale features observed in and adjacent to it. The chapter is arranged so that features visible on small scale photographs are described first followed by descriptions of those seen at larger scales. Appropriate Apollo-15 photo references have been given in each section.

Description of Hadley Rille From Small Scale Photographs:

This section summarizes the features which can be seen monoscopically on small scale photographs of the Palus Putredinis region. Some appropriate photographs illustrating these features are Apollo-15 metric 414 (fig. 4-1) or 914, or Lunar Orbiter V, 105M and 106M.

Viewed as a whole, the rille is seen to cut through the mare surface in a series of curves which are smoothly sinuous in places yet orthogonally joined in others. The south end of the rille connects to an arcuate depression which is incised into both mare and pre-mare material. The north end of the rille adjoins a triangular depression one edge of which coincides with the contact between mare material and older rocks. Between these points the rille is continuous, although a constriction occurs east of Hill 305 (fig. 2-3) and the rille becomes indistinct in the plain northwest of the hill.

<u>The southern section</u>. The southern part of the rille has a considerably different appearance than the northern part, and thus, it is convenient to separate the rille into two sections for description. The southern section is that part southeast of Hill 305; the northern section is the portion adjacent to and northwest of the hill. For purposes of numerical treatment, point 84 on figure 6-2 is the dividing point.

The southern section of the rille is a deeply incised, clearly sinuous furrow which stands out in high optical relief. The walls of the rille in this section show a remarkable parallelism. Any small fluctuation in the direction of one wall is matched by a corresponding deviation on the opposite side. In profile view, the usual cross-section is a symmetric V-shape, although variations are present. Where appropriately illuminated, outcrop is observed along most of the southern section except perhaps the first two or three kilometers adjacent to the cleft-like depression. Pan photographs indicate that outcrop is found from the lip of the rille down, and that at several locations, it occupies the upper one-third of the rille wall. There appears to be a correllation between obvious outcrop and boulders on the rille bottom indicating that the outcrop is the source of the boulders. There are some locations, however, where boulders have obviously been ejected into the rille from nearby craters. There are no locations where outcrop is unequivocally exposed in the bottom of the rille. There appears to be a relative absence of small craters in the rille compared to the adjacent mare surface. The variable lighting of the rille wall makes a formal crater count of questionable value, but a spot check of the mare surface and favorably illuminated parts of the rille wall using the Edmunds 10X comparator (ch. 3) indicates considerably fewer craters in the rille. Several craters intersect the rille and have resulted in prominent ejecta deposits in it. The converse situation, subdued craters which are cut by the rille, would indicate some elapsed time between mare filling and rille formation. No such craters have been observed. The lowland occupied by this segment of the rille has a northeast trend which is circumferential to the Imbrium Basin. However, this direction is not selectively adopted by individual segments of the rille.

The small mare surface features surrounding the southern section can be interpreted and ranked in order of visual importance as follows:

1. Small, cup-shaped symmetrical craters with raised rims probably due to primary impacts and secondary impacts after Crater Hadley C.

2. Irregular depressions with little or no raised rims that probably are volcanic collapse features of different types.

3. Irregular, low hills of probable pre-mare material which have been left as islands after mare filling.

The reflectivity of the adjacent mare surface is more uniform than in other parts of Palus Putredinis, although two or three places are noticably brighter than the remainder.

The northern section. There are important qualitative and quantitative differences between the northern and southern sections. The general trend of the northern section is radial to the Imbrium Basin rather than circumferential. It will be shown quantitatively in subsequent chapters that the northern section of the channel is on the average straighter and that a closer relationship exists between the azimuth of individual rille segments and the regional structure. The channel width and depth are smaller and the profile is U-shaped or even flat-bottomed at the northern extreme. The previously noted indistinct section of the channel can only be well observed in low sun photography. In contrast to the southern section, the northern section shows little or no outcrop and the cratered surface within the rille looks identical to the cratered mare surroundings. As in the south, this section of the rille is not observed to cross-cut any other structures of the mare surface, but one of the plumose structures from the cratering events to the north does appear to cut the rille.

The surface surrounding the northern section has more relief features than that to the south. These can be ranked in order of visual importance and interpreted as follows:

1. Secondary plumose structures associated with cratering events to the north.

2. Small, cup-shaped craters with raised lips which are of probable primary or secondary impact origin.

3. Irregular depressions with small or no raised rims which may be either volcanic collapse features or imperfectly developed plumose structures.

4. Lineaments which probably represent post-mare filling tectonism.

5. Hills which probably represent islands of pre-mare material which were isolated during mare filling.

The reflectivity of this surface is highly variable from point to point. Much of the bright material correlates with the surface disturbance of the plumose structures, so much so that a bright halo probably serves to differentiate an irregular secondary crater from a volcanic depression.

Detailed Observations Within the Rille from Command Module Photography:

This section is concerned with specific features in the rille which can be observed on metric and panoramic photography. Appropriate photo references are the stereo pairs Apollo-15 metric 414-416 (fig. 4-1, 4-2) and pan photographs 9795-9800 (fig. 4-3, 4-4) and 9797-9802. Stereo

Fig. 4-3. Apollo-15-9795 Pan photograph (lower), Fig. 4-4. Apollo-15-9800 Pan photograph (upper). These copies do not retain the extraordinary resolution of the originals.

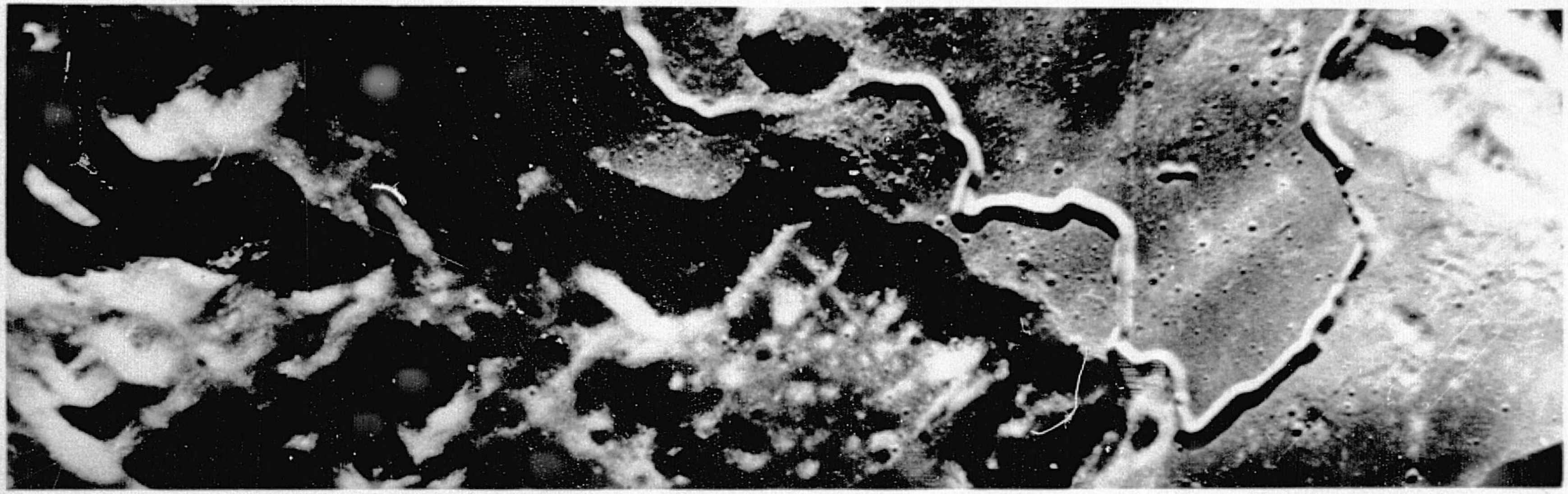

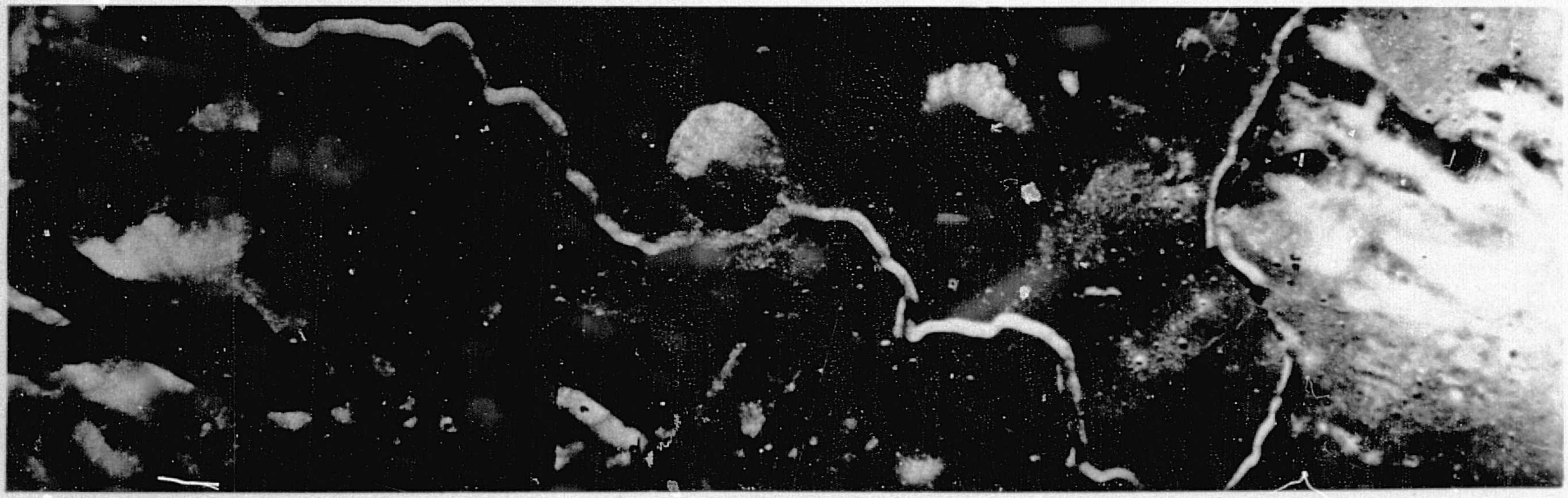

observation or the use of 10X magnification is necessary for many of the observations. The order of observation described here is as though an observer started at the southern extremity of the rille and progressed along the channel to the northern end. For convenience in description, features on the observer's left are referred to as being on the mare side of the rille since most of the Imbrium Basin lies on that side. Features to his right are designated as being to the mountain side because of the presence of the Apennine Front.

Many of the described features have been profiled using the AS-11A analytical plotter (ch. 3). Readers who have used this machine with panoramic photographs will question how profile lines directly across the rille can be established on the distorted panoramic model. This was accomplished by the following method:

1. The location of the panoramic stereo model was located on a metric photograph of the rille.

2. The desired profile lines were laid out on the metric photograph. In most cases, the profile lines were perpendicular to the rille direction at the point of intersection between the profile line and the rille.

3. Photo-identifiable objects (for the most part—craters) were located at each end of the profile lines.

4. These objects were then located on the panoramic model in the machine. The machine index was then traversed back and forth across the rille and adjustments were made to the profile direction. This was repeated until by trial and error, a profile line was established between the two photo-identifiable points. Then, the actual profile was plotted.

The profiles are reproduced in figures 4-6 to 4-17. Each profile is numbered and carries identifying letters which are keyed to a location map (fig. 4-5). Above each profile is a horizontal line for reference. The position of this line is the profile line indicated on the location map, and the ends of the line on both the profile drawings and the location map fall at the two photo-identifiable objects used to locate the profile direction. In two cases, profiles 6a and 30a, it was not possible to find photo-identifiable objects on the profile lines. Their locations and orientations are therefore less controlled than the other profiles which is the reason they were assigned special profile numbers.

In some places, there is difficulty in observing detail in the rille walls because of unfavorable illumination. All detail is lost in shadow or under direct illumination, whereas an oblique or grazing sun angle is most favorable. An examination of most of the available imagery and photographs of the region has shown that about one third of the rille wall is visually inaccessible. The remaining two thirds

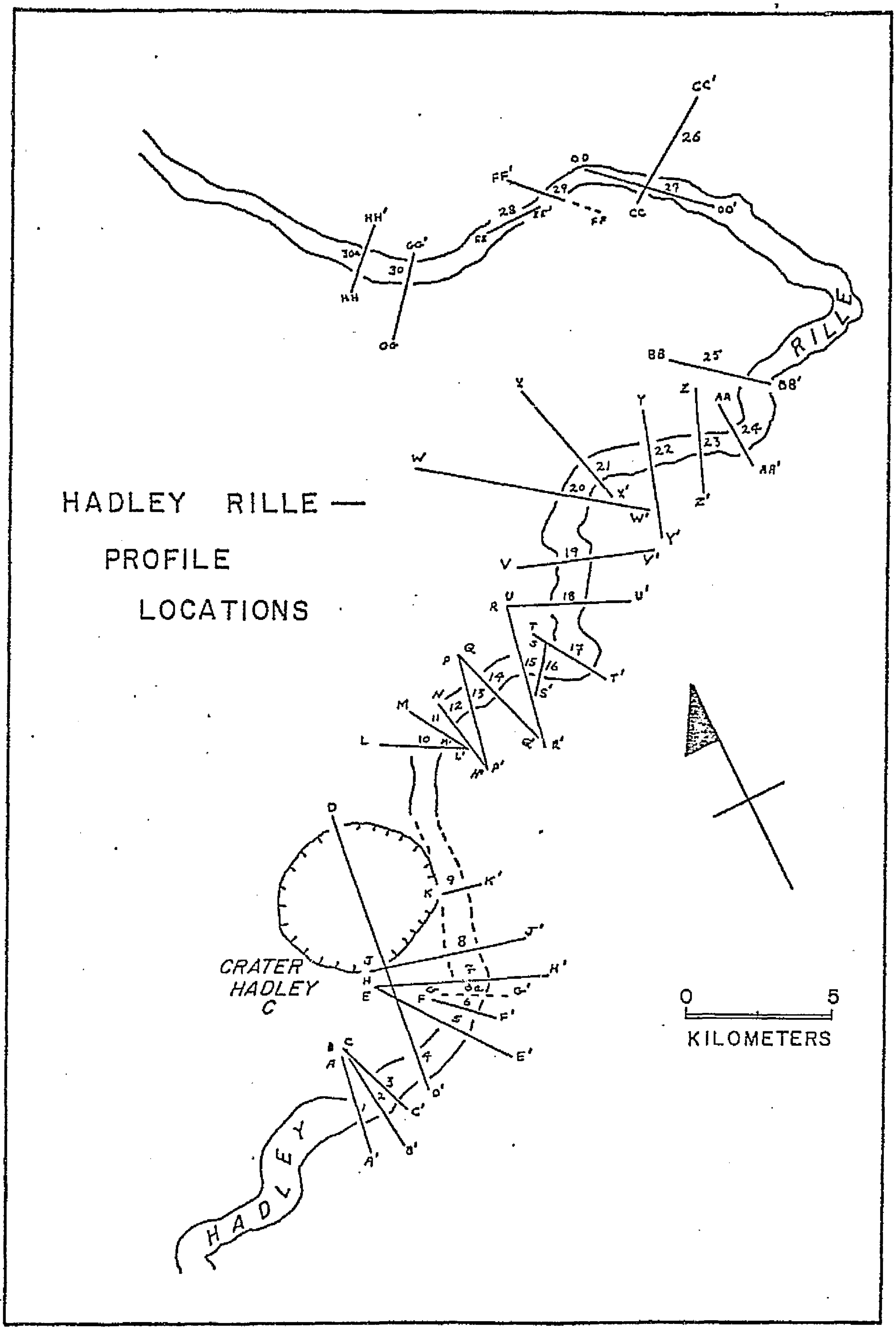

Fig. 4-5. Location map for profiles in figures 4-6 to 4-17.

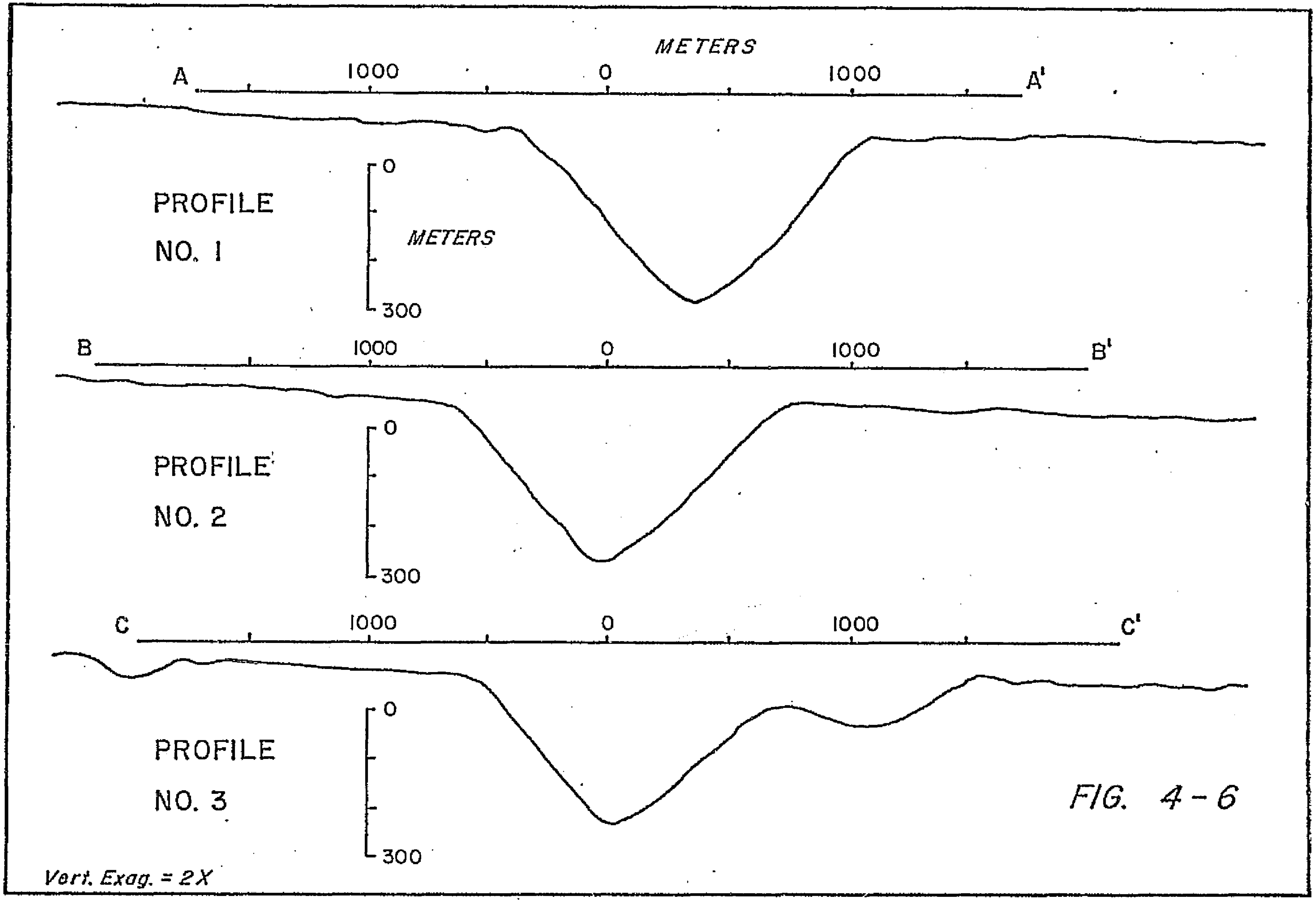
METERS
A
1000
0
1000
A'
PROFILE NO. 1
0
METERS
300
B
1000
0
1000
B'
PROFILE NO. 2
0
300
C
1000
0
1000
C'
PROFILE NO. 3
0
300
Vert. Exag. = 2X

FIG. 4-6

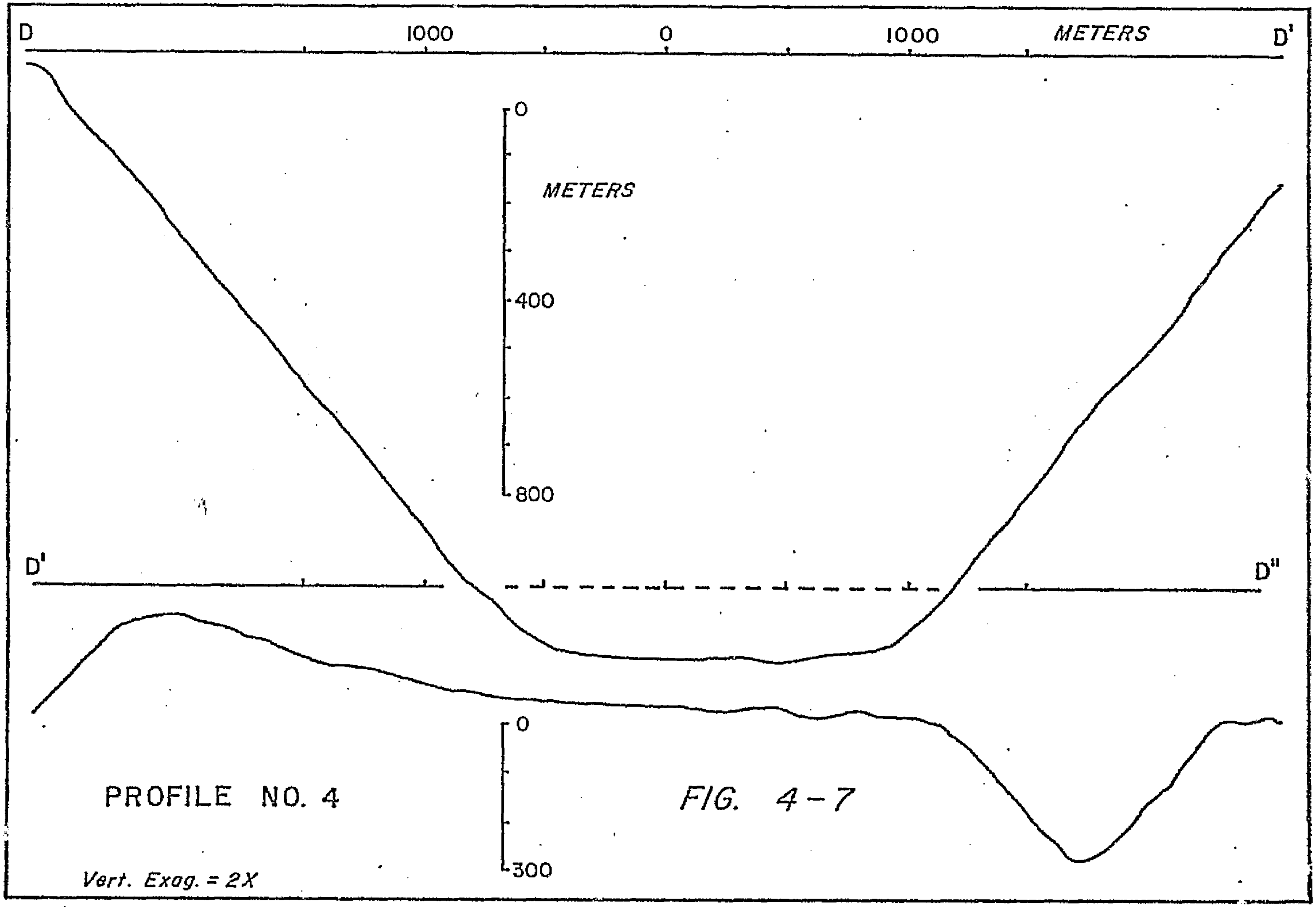
D
1000
0
1000
METERS
D'
0
METERS
400
800
D'
D''
0
300
PROFILE NO. 4
Vert. Exag. = 2X

FIG. 4-7

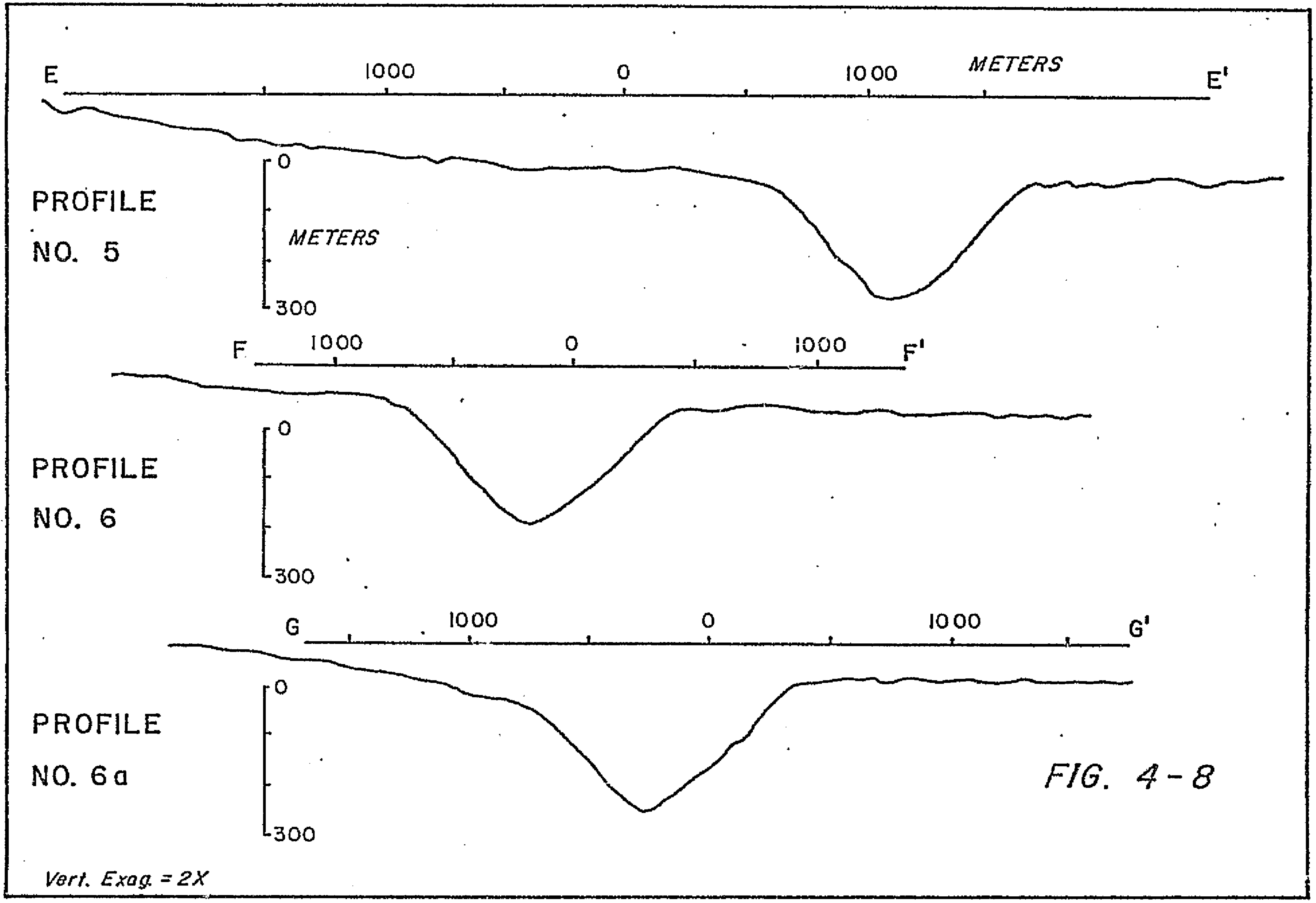
E
1000
0
1000
METERS
E'
0
METERS
300
PROFILE NO. 5
F
1000
0
1000
F'
0
300
PROFILE NO. 6
G
1000
0
1000
G'
0
300
PROFILE NO. 6a
Vert. Exag. = 2X

FIG. 4-8

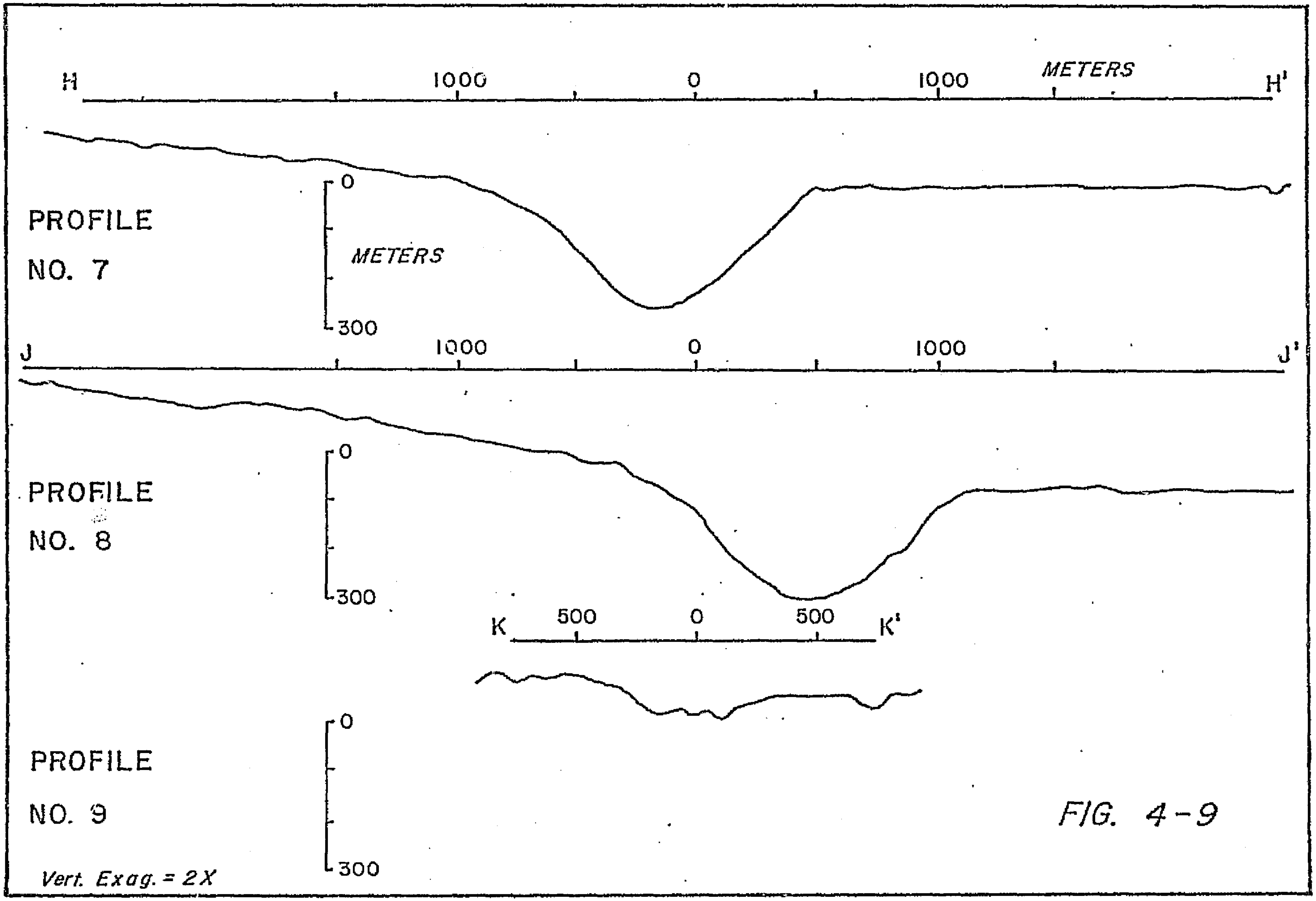
H
1000
0
1000
METERS
H'
0
PROFILE
NO. 7
METERS
300
J
1000
0
1000
J'
0
PROFILE
NO. 8
300
K
500
0
500
K'
0
PROFILE
NO. 9
300
Vert. Exag. = 2X

FIG. 4-9

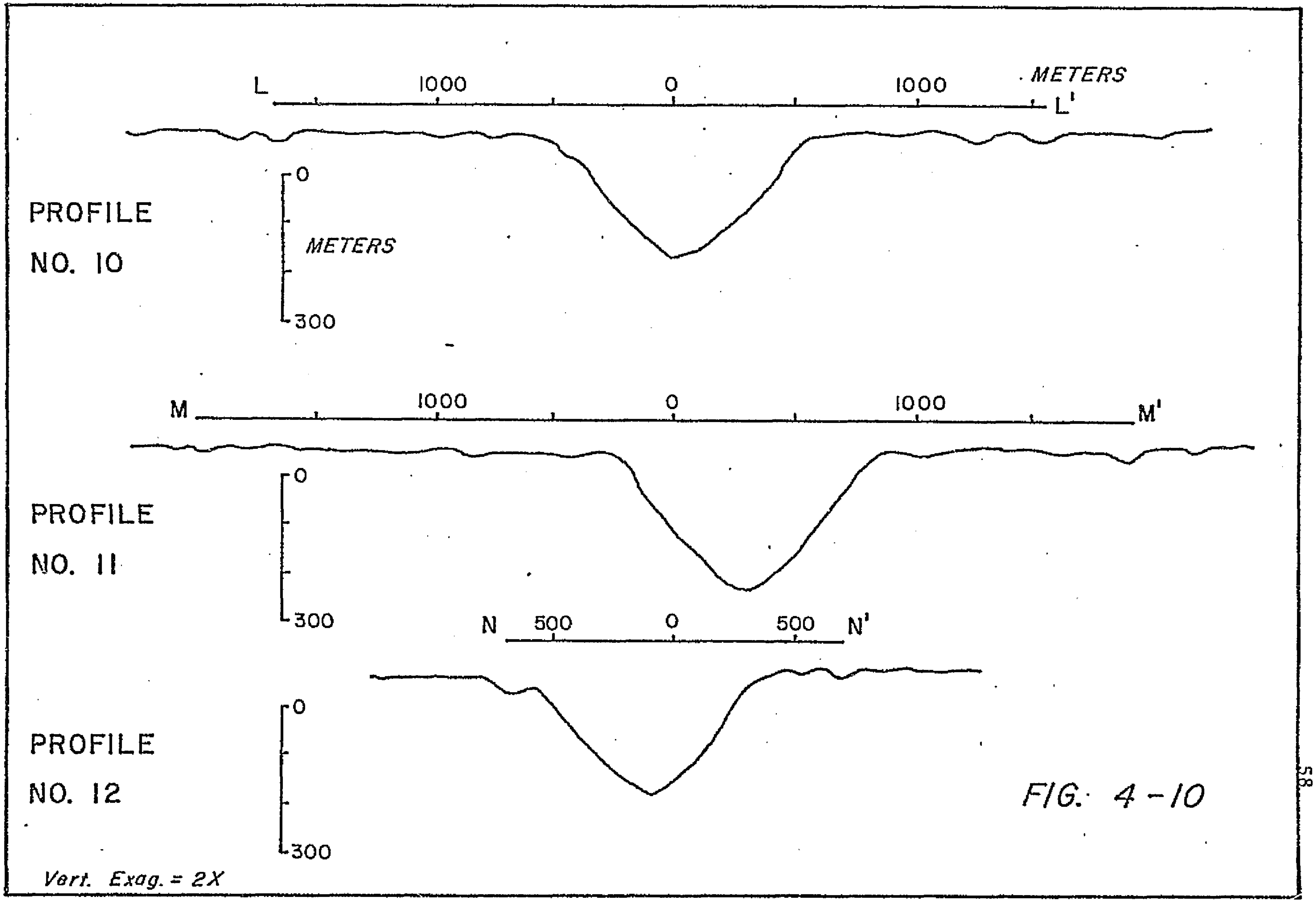
L
1000
0
1000
METERS
L'
PROFILE
NO. 10
0
METERS
300
M
1000
0
1000
M'
PROFILE
NO. 11
0
300
N
500
0
500
N'
PROFILE
NO. 12
0
300
Vert. Exag. = 2X

FIG. 4-10

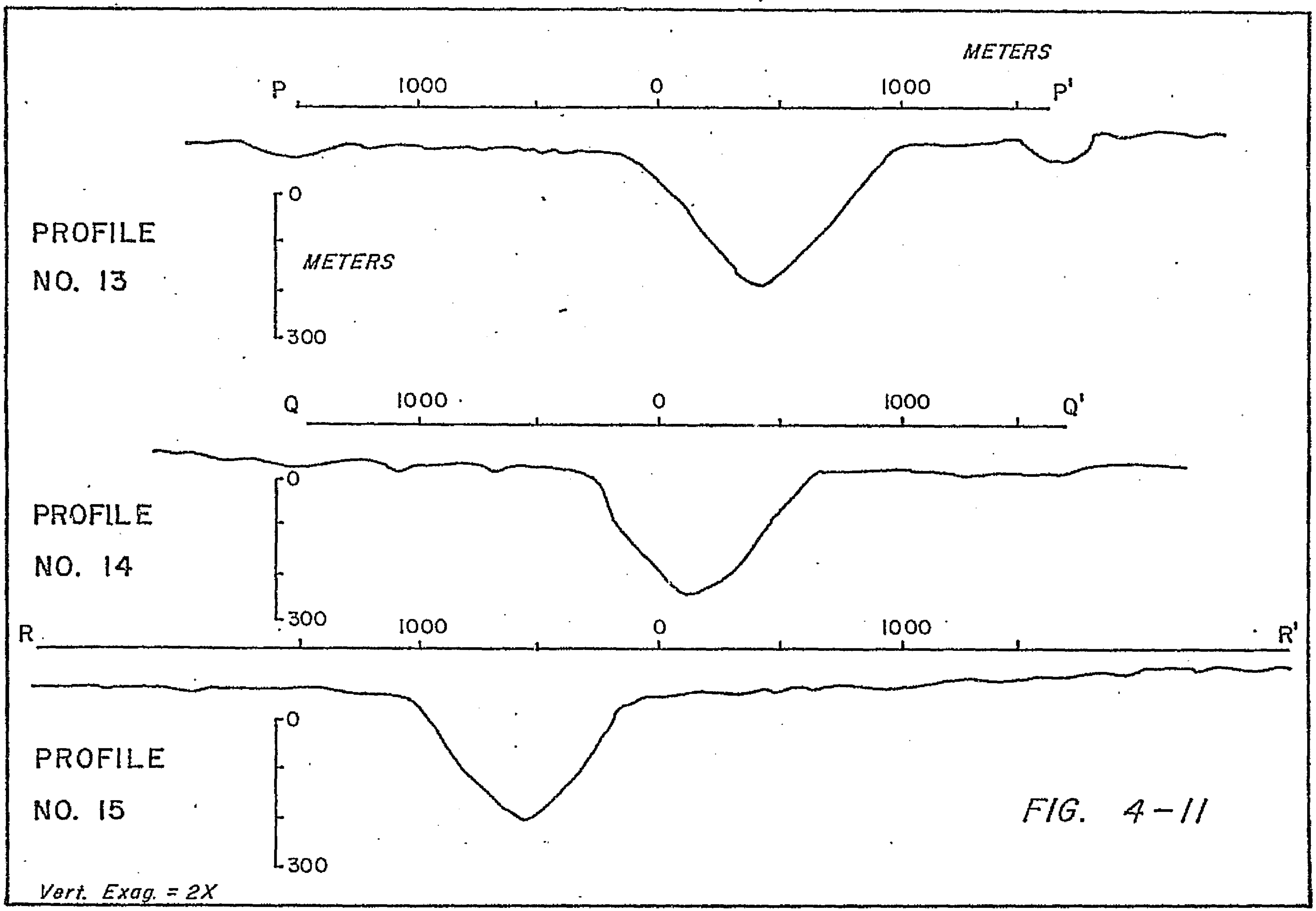
METERS
P
1000
0
1000
P'
PROFILE
NO. 13
0
METERS
300
Q
1000
0
1000
Q'
PROFILE
NO. 14
0
300
R
1000
0
1000
R'
PROFILE
NO. 15
0
300
Vert. Exag. = 2X

FIG. 4-11

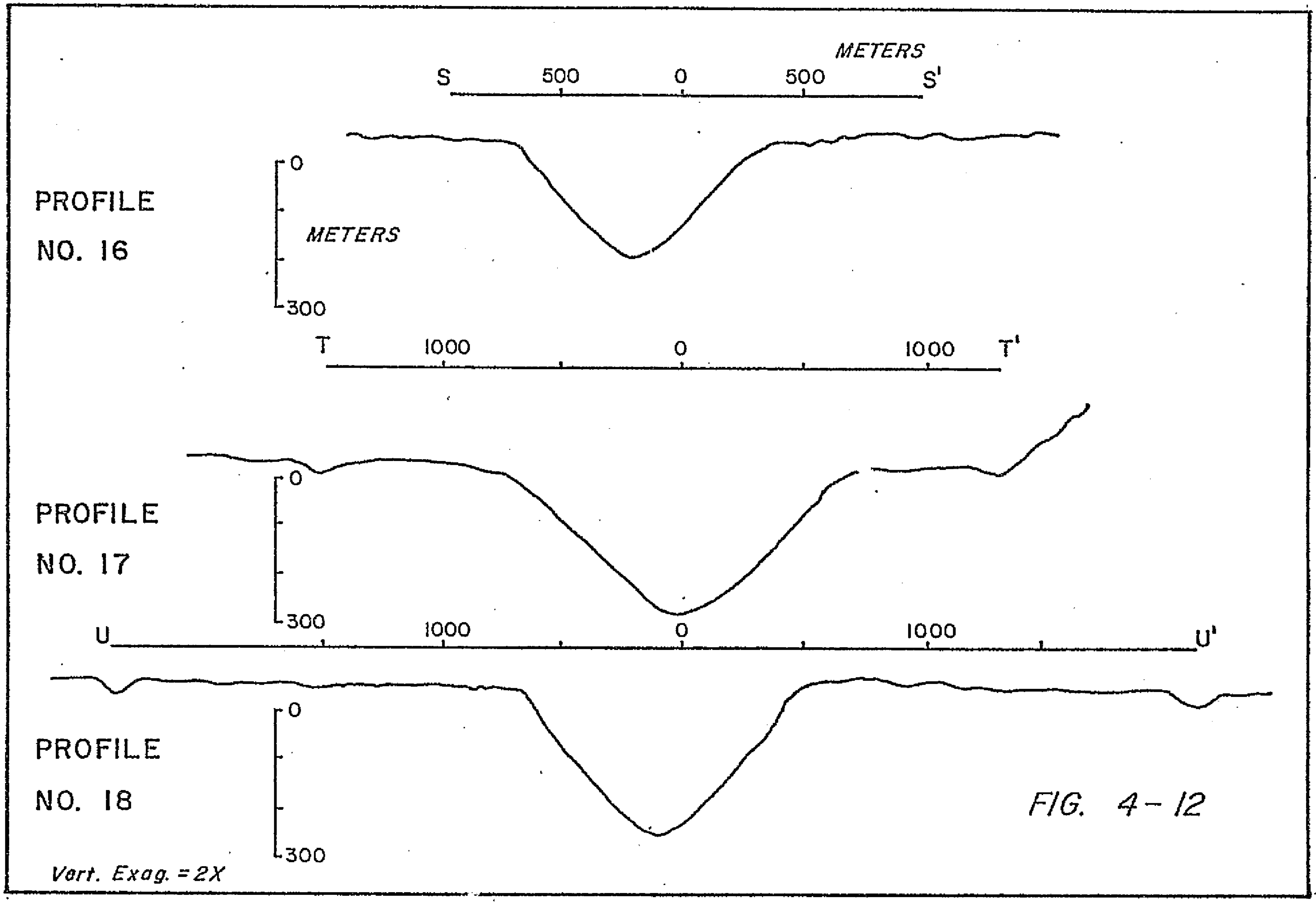
METERS
S
500
0
500
S'
0
PROFILE
NO. 16
METERS
300
T
1000
0
1000
T'
0
PROFILE
NO. 17
300
U
1000
0
1000
U'
0
PROFILE
NO. 18
300
Vert. Exag. = 2X

FIG. 4-12

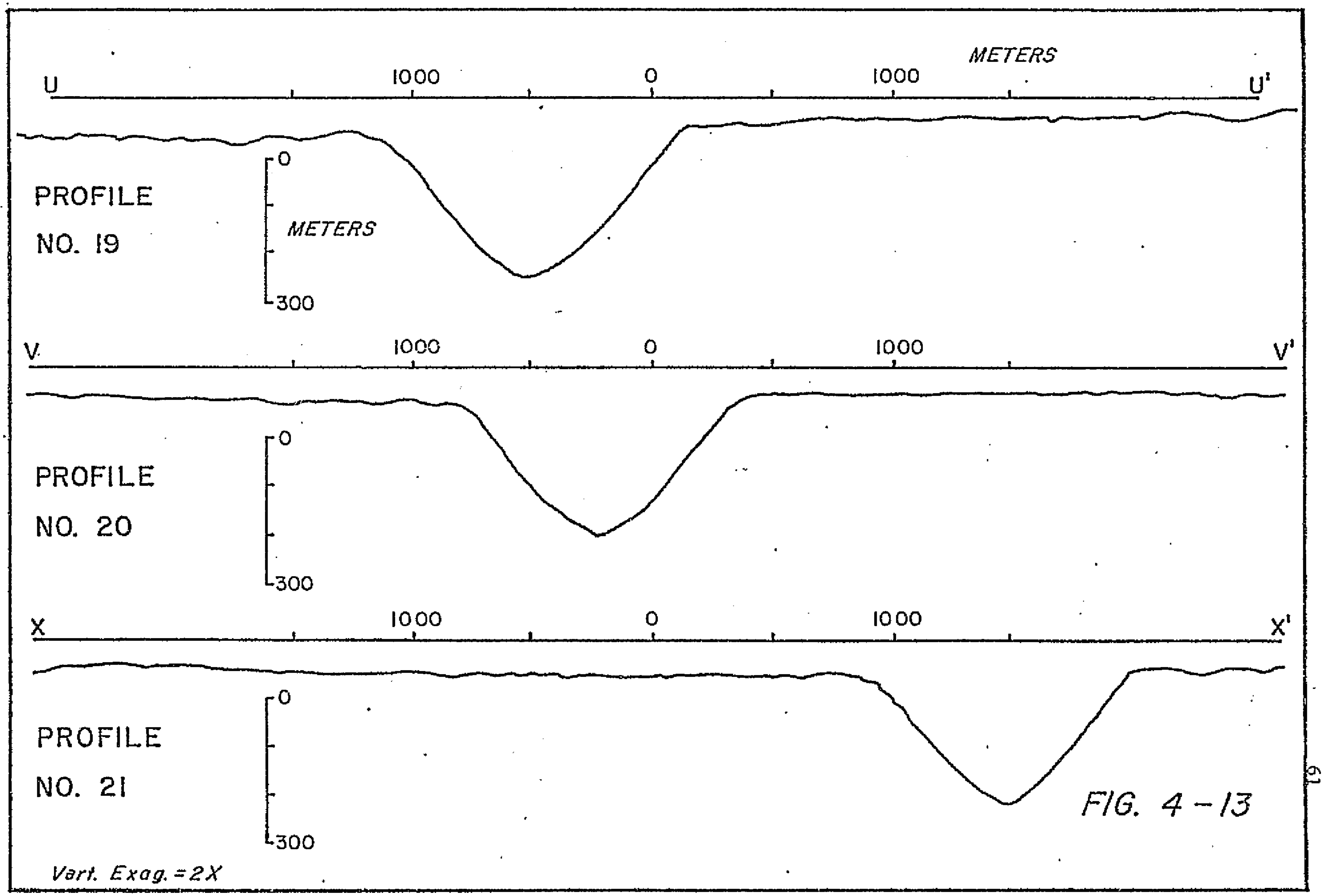
METERS
U
1000
0
1000
U'
PROFILE
NO. 19
0
METERS
300
V
1000
0
1000
V'
PROFILE
NO. 20
0
300
X
1000
0
1000
X'
PROFILE
NO. 21
0
300
Vert. Exag. = 2X

FIG. 4-13

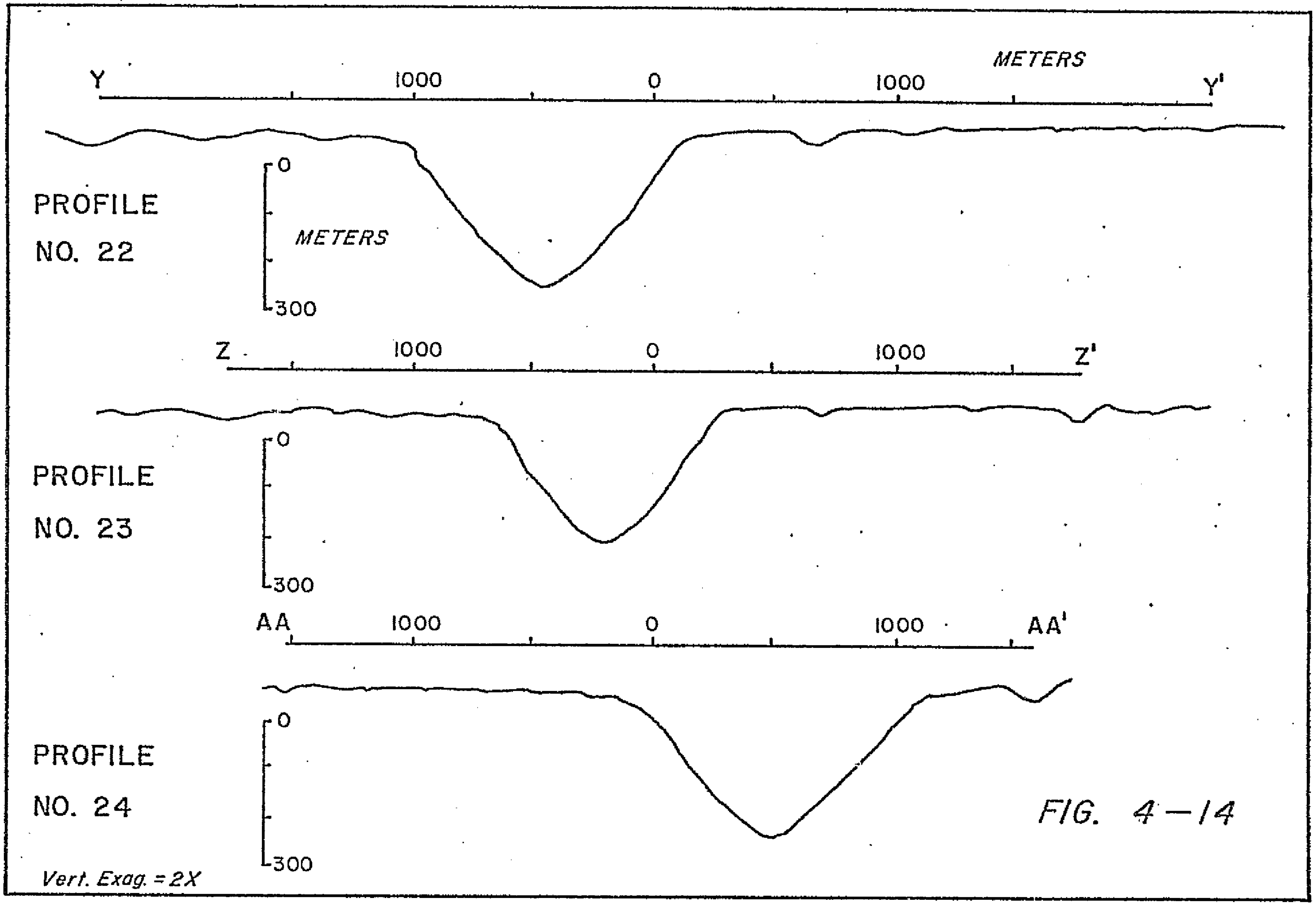
METERS
Y
1000
0
1000
Y'
PROFILE
NO. 22
0
METERS
300
Z
1000
0
1000
Z'
PROFILE
NO. 23
0
300
AA
1000
0
1000
AA'
PROFILE
NO. 24
0
300
Vert. Exag. = 2X

FIG. 4-14

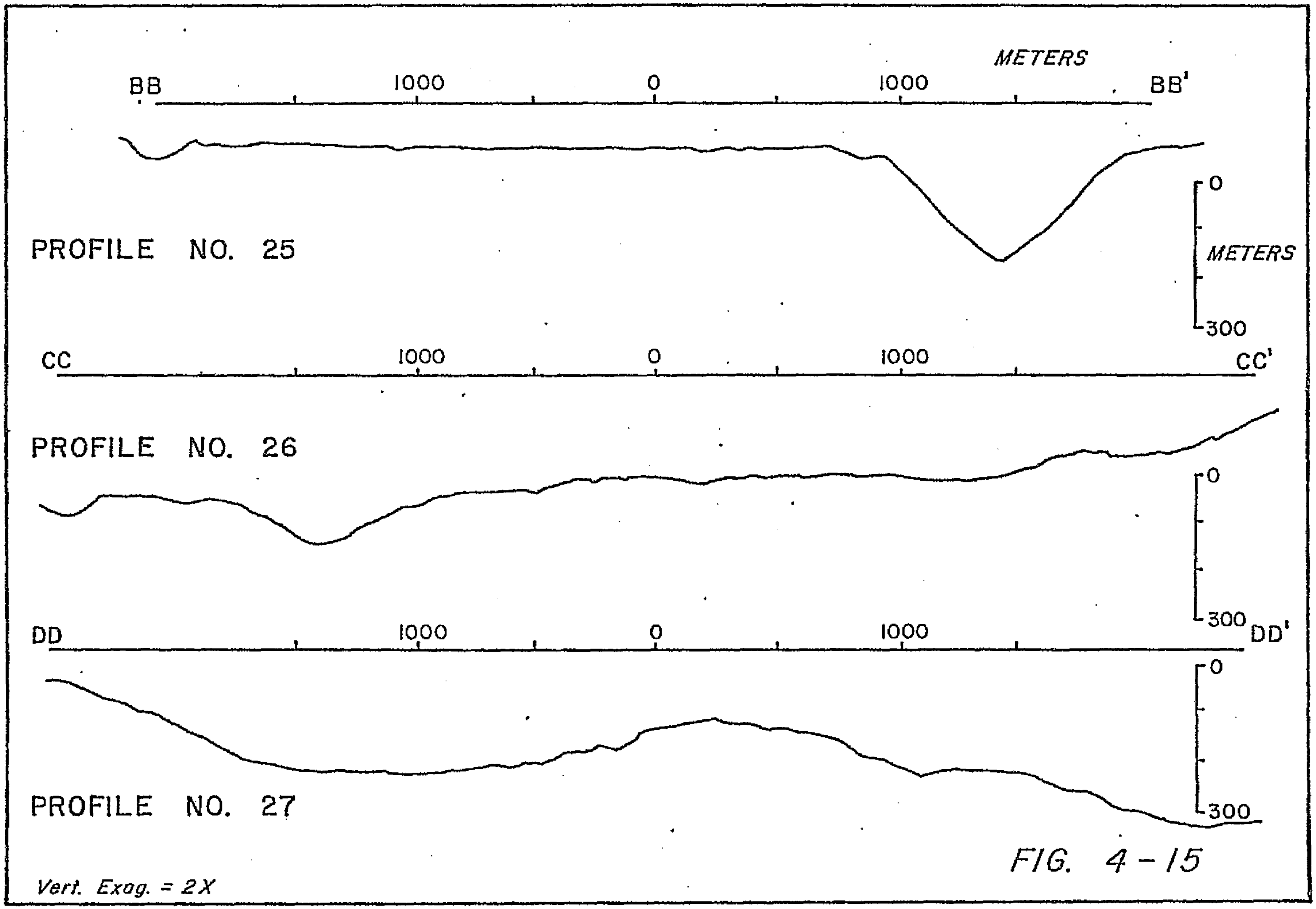
METERS
BB
1000
0
1000
BB'
0
METERS
300
PROFILE NO. 25
CC
1000
0
1000
CC'
PROFILE NO. 26
0
300
DD
1000
0
1000
DD'
0
300
PROFILE NO. 27
Vert. Exag. = 2X

FIG. 4-15

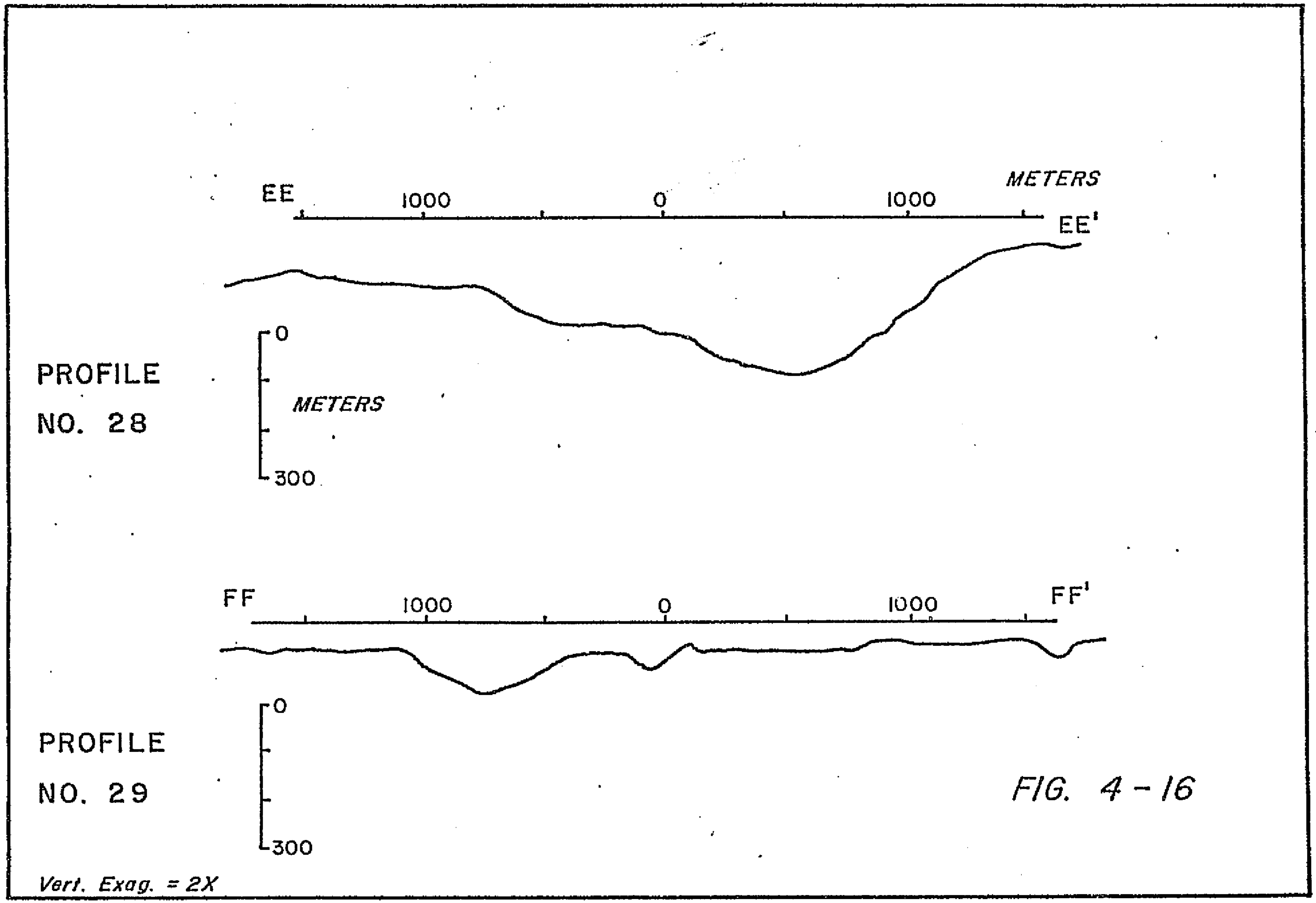
EE
1000
0
1000
METERS
EE'
0
METERS
300
PROFILE
NO. 28
FF
1000
0
1000
FF'
0
300
PROFILE
NO. 29
Vert. Exag. = 2X

FIG. 4-16

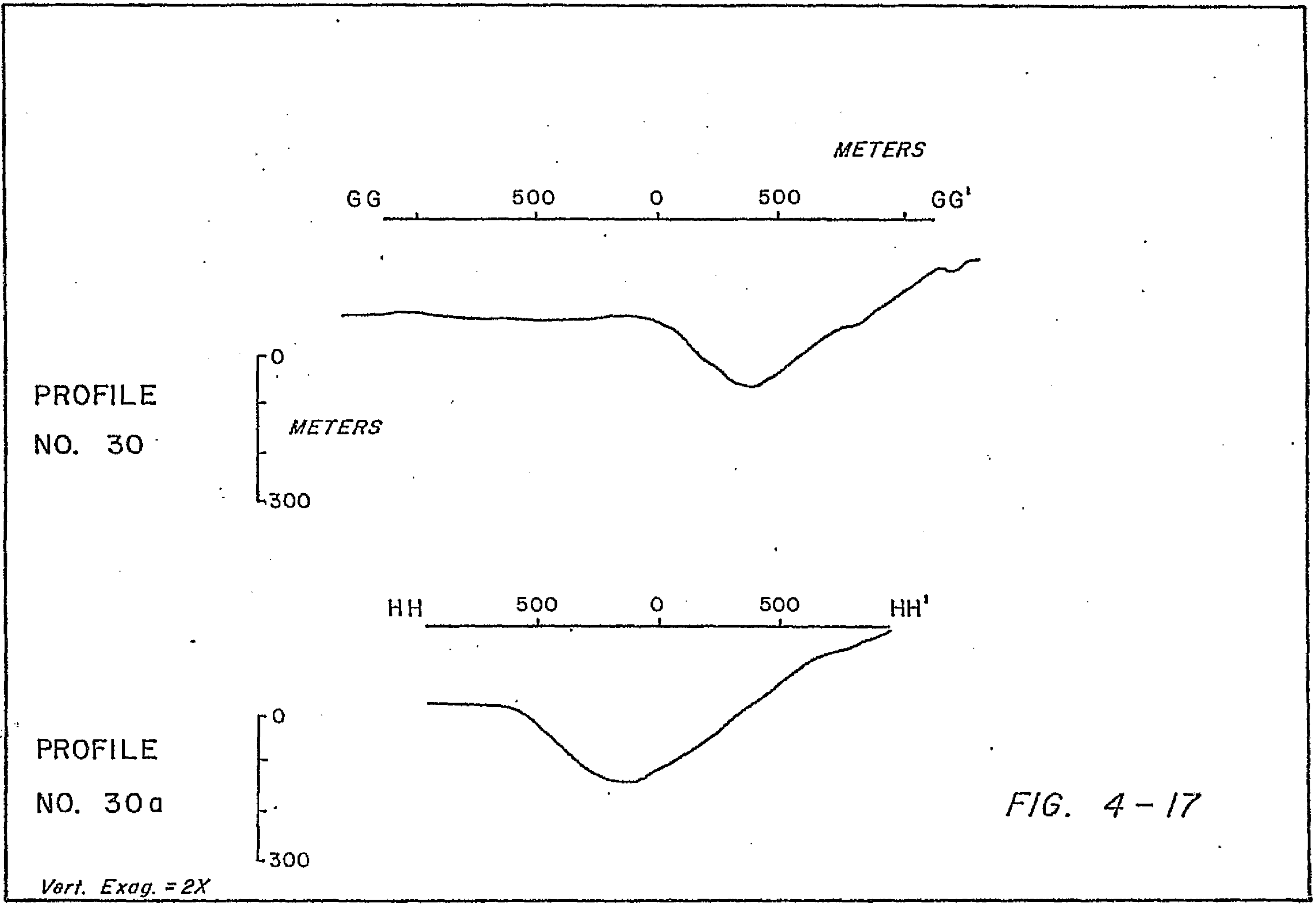
METERS
GG
500
0
500
GG'
PROFILE
NO. 30
0
METERS
300
HH
500
0
500
HH'
PROFILE
NO. 30a
0
300
Vert. Exag. = 2X

FIG. 4-17

is the basis of the discussion to be presented forthwith.

The southern cleft. The southern end of the rille connects to an arcuate depression with an approximate north-south orientation, with a length of about ten kilometers and a width of about two kilometers at its widest. Under the stereoscope, this is seen to be one of three connected depressions which resemble dissimilar canoes tied end to end, the southernmost two being progressively shorter than the first. Owing to the curvature of the forms, the chain of depressions crosses the Apennine Front and assumes a southwest azimuth. The final depression grades into the set of lineaments which borders the mountain block. Although the depressions are clearly connected, there is a distinct topographic barrier between them.

Concentric with and immediately adjacent to the northern depression is an additional similar depression with corresponding shape but with dimensions about one half as large. The north-south azimuth displayed by the two concentric depressions is visually and analytically (ch. 5) in discord with regional structures, although an extension of them may curve northeast along the edge of Bennett Hill. Such an extension would match the regional pattern of lineaments.

These forms cut both the mare surface and hilly material. It is not completely clear how the depressions actually cut the Apennine

Massif, Carr and El-Baz (1971) place them at the contact between the Block Mountains and post-uplift slump deposits. The walls show little outcrop which is notable considering the large amount of outcrop exposed in the rille. There is a distinct change of texture at the bottom of the northern depression which may represent an accumulation of transported debris. If so, the size of the accumulation indicates that there has not been much erosion from adjacent slopes.

The cross-sections of different depressions vary in that the concentric pair both appear V-shaped, the central one has a hummocky, flat bottom, and the southernmost appears somewhat U-shaped. The flat bottom in the central depression may represent the original bottom profile because talus deposits in other parts of the rille have not produced a flat bottom. There is no linear relationship between elevation and width along these depressions. Consequently, they cannot be interpreted as grabens as have certain other linear furrows on the moon (Baldwin 1971) .

The southern section. The rille emerges from the cleft-like depression in a tight S-curve which is the only segment of the rille which distinctly cuts pre-mare material. There is a peculiar mottled appearance to the rille wall where the rille appears to cut what has been mapped as Imbrium impact breccia (Carr and El-Baz, 1971). Measurements with the Kern PG-2 plotter [1] indicate that the channel cross-section here has the most asymmetric form found in the rille. The steepest slope of the transverse profile occurs on the outside of the curve.

Profile number 3 (fig. 4-6) is drawn across the channel about ten kilometers north of the cleft. At this location, a subdued crater about 800 meters in diameter intersects and cross-cuts the rille on the mountain side. A number of similar craters intersect at different places along the rille and their ejecta may be partially responsible for undulations in the rille bottom.

At the location of profile number 6a (fig. 4-8), there is a large

[1] This location was not included in the model used in the AS-11A plotter for reasons discussed in chapter 3.

(one kilometer long) block of material, visible only on panoramic photographs, which forms a downward step on the mare edge of the rille. The 50-meter-high escarpment between the block and the mare surface is obvious on the profile. This appears to be a slump or fault block which has truncated the bend in the rille. The strike of the escarpment corresponds to the structural trends in the region and the face of the escarpment aligns well with the fault which is assumed to bound the Apennine Front. There is a hint of a slight displacement on an extension of the same slip surface to the northeast across the rille. This feature may have resulted from remobilization of Imbrium event faults by the event which produced the nearby Crater Hadley C (fig. 2-3).

The Crater Hadley C on the mare side of the rille is the largest post-mare crater in Palus Putredinis being 5.6 km. in diameter. Its obvious overlap of the rille establishes its post-rille age without doubt. Although the rille is almost totally obscured next to the crater (profile 9, fig. 4-9), the ejecta has only covered the rille to a distance of about one half a crater diameter from the crater rim (profile 10, fig. 4-10). Many of the small craters on the mare surface here are assumed to be the result of secondary impacts after this event. It is notable that there is no pronounced increase in the number of craters in adjacent sections of the rille. Profile number 4 (fig. 4-7) is directly across Hadley C and emphasizes its flat bottom.

Profile number 14 (fig. 4-11) passes through a location where the wall of the rille is over-steepened in comparison with the other profiles, and the floor is abnormally flat. This has resulted in an asymmetric profile in a relatively straight section of the rille. This feature can be adequately viewed only in stereo under high magnification on film-based panoramic photographs. About three kilometers north of the profile number 14 location, there is a small, dark area in the rille bottom containing several well-defined craters. The appearance is similar to the pooled lava observed lying in the crater walls of some large craters[1].

Profile number 17 (fig. 4-12) is directly across a small radius curve which is comparable to the curves at the south end of the rille. This profile was plotted several times to check for asymmetric channel shape. The outside slope of the curve is concave in contrast to the opposite slope which is convex. This results in a steeper slope on the outside of the curve. These contrasting slopes could be interpreted as indicating either a cut bank on the outside of the curve or evidence of more effective meteorite erosion on the promontory which is present on

[1]For example, the Crater Aristarchus as seen on Lunar Orbiter V 199H.

the inside of the curve. Profiles numbers 22 and 23 (fig. 4-14) are across a straight section of the rille with particularly favorable illumination. This segment contains the most observable outcrop of any segment. The outcrop occurs on both sides of the rille with more on the mountain side, and extends one fourth to one third of the way down the rille wall for a distance of three kilometers along the channel. This contributes a distinct cliff and bench appearance to the mare side of the profiles and results in concave slopes on both sides of the rille. In the film-base versions of the pan photography, the rille walls in this section have a distinct fish bone or tartan appearance. It is difficult to pick out any particular lineament from the overall pattern, and the pattern may be an effect of illumination geometry. This problem is discussed in chapter 5.

At the end of this straight reach, the rille makes a series of tight turns which seem to be controlled by the Apennine Front. This is the most obvious example of topographic control of the rille, although control is evident at several other locations. It can be noted that the three sharpest turns in the rille occur where the channel is in contact with pre-mare material in the southern section.

On film-base panoramic photography, there are notably few boulders visible in the rille where it passes the Crater St. George, and outcrop if present at all is found only on the mare side. Evidently, there is a deposit of material in the rille here which has been eroded from the adjacent mountain block. Simple deposition does not explain the relative lack of outcrop on the mare side, however, especially considering that an obvious post-rille crater is present in the rille wall. A crater such as this produced abundant boulders at the Apollo-15 landing site (discussed below in detail).

The final bend of this sequence is a sharp turn to the northwest which becomes the general trend of the rille direction for the northern half of its length. The Apollo-15 landing site is located on the mountain side of the rille about one kilometer north of the turn. The high resolution ground-based photographs of this area will be discussed below.

To the northwest of the landing site, there is a cryptic feature which is not duplicated elsewhere along the channel. In a series of elongated forms of decreasing width, the rille tapers northward over a distance of about ten kilometers until the channel is almost completely closed. The rille then widens abruptly and assumes an unobstructed configuration. Some material has been thrown out of a recent bright-haloed crater on the mountain side at the sharp bend in the rille. The resultant ejecta blanket has obscured the original rille geometry somewhat and has also produced a few boulder trails on the rille walls. An explanation for this constriction is essential to an adequate hypothesis for rille genesis, and it is considered in some detail in chapter 7. Profiles number 26 (fig. 4-15) and number 29 (fig. 4-16) are across significant constrictions in this tapered section. Profiles number 27 (fig. 4-15) and number 28 (fig. 4-16) are along the rille bottom through the constriction.

The northern section. Just at the point where the rille assumes a normal configuration above the constriction, there occurs the first of four lineaments which intersect the rille within a 20 kilometer length of channel. These have been interpreted as tributary rilles (Greeley 1971) but were later mapped as faults (Carr and El-Baz, 1972). Profile number 26 (fig. 4-15) is drawn perpendicular to and across the lineament and also intercepts Hadley Rille obliquely at the constriction. Viewed in profile, the lineament is seen to be an escarpment with a height of about 15 meters. The appearance in cross-section and the obvious alignment with other local structures supports the view that this is a high-angle fault. This structure may have considerable significance in its relation to the constriction.

About three kilometers to the northwest from its intersection with the first escarpment, the rille encounters a second escarpment with a strike direction approximately perpendicular to the first. This northeast facing escarpment is in approximate alignment with the southwest face of Hill 305. At additional distances of four and then five kilometers along the rille, two more lineaments intersect the channel with orientations perpendicular to the rille and to Hill 305. Their cross-cutting relationship with the mare surface indicates post-mare filling tectonic activity.

In the vicinity of Hill 305, the rille traverses a stricture between two embayments of Palus Putredinis. Where the rille is adjacent to the hill slope, it becomes subdued and irregular in appearance. In profile (profiles numbers 30 and 30a, fig. 4-17), the bottom of the rille flattens, the width diminishes, and little outcrop is visible. The change in character of the rille where it abuts pre-mare mountains has been attributed by other authors (Howard and Head, 1972) to mass wasting from the mountains. This interpretation has been expanded at the end of this chapter to calculate a maximum rate of erosion from Hill 305, and a maximum erosion rate of 106 meters is indicated. The position of the rille relative to Hill 305 and the unusual linearity of the section of channel adjacent to the hill indicate topographic or structural control of the rille by the hill. At several places around the edge of Hill 305, there are benches of probable mare material clinging to the edge of the hill. These may represent high lava marks formed during mare filling. Swann et al. (1972) have reported similar marks at a height of 90 meters above the mare surface around the base of Mount Hadley.

North of Hill 305, the rille is positioned across one corner of Palus Putredinis. It ultimately ends about 25 kilometers northwest of the hill. This length is further from the 'shore' of pre-mare filling bedrock than any other rille segment. North of the straight section under Hill 305, the rille pattern becomes clearly sinuous for a channel length of ten kilometers, then abnormally straight for about eight kilometers, and finally continues in a sinuous pattern to the end. Immediately to the north of Hill 305, the rille assumes a subdued appearance and nearly disappears for a distance of about eight kilometers. Further north, the channel becomes more distinct, and the relief continually increases to the northern end.

The northern end of the rille intersects some of the segments of the arcuate system of furrows called the Fresnell Rille System. These are believed by most authors (ch. 5) to be surface expressions of the circum-Imbrium fault system. One prominent furrow about one kilometer wide ends abruptly at the rille and several other lineaments appear to intersect it less distinctly. An adequate hypothesis for rille origin should explain this association.

At its extreme northern end, the rille widens into a triangular depression about four kilometers long and three kilometers wide at its widest. The north edge of this depression is coincident with the contact between mare filling material and pre-mare hilly material. One irregular furrow which intersects the rille on the mare side is out of accord with the other structural directions and is surrounded with brighter material than the general mare surface. This appears to be a plumose structure from Autolycus or Aristillus rather than some feature related to the bedrock or mare surface structure. This indicates that at least one of the craters must post-date the rille.

Observations From Large Scale Ground-based Photographs:

During the Apollo-15 traverses, numerous ground-based photographs were taken of features around the landing site. Two focal lengths were used, 60 mm. for normal scale photo coverage, and 500 mm. for telephoto photographs. The photo stations were chosen to provide stereo coverage of many features and photographs of both scales can be assembled into mosaics, some of which are detailed in chapter 3. This section is a description of certain small scale features in the rille based on observations from those photographs.

The material visible within the rille at the landing site includes both outcrop and fragmented material which ranges in size from 30 meter boulders to probable clay size. Both the outcrop and the loose materials are quite variable in their appearance.

Swann et al. (1972) have discussed individual outcrops in some detail and have made a number of significant observations. This paragraph is a summary of their observations. The outcrop along the rille is discontinuous and it is difficult to trace a particular stratigraphic horizon from one outcrop to the next with certainty. The maximum depth of visible outcrop is 60 meters, but rocks collected from Dune Crater (fig. 2-4) suggest at least 100 meters of basaltic rock. Individual outcrops are clearly layered; all feature a massive layer, and many have thinner section above and/or below the massive one. It is possible to distinguish the different layers because different physical properties such as reflectance, appearance after weathering, resistance to weathering and mode of fracture give them different optical relief. There is a prominent near-vertical joint set, and this frequently cuts more than one layer. Other joint directions are observed locally but not as a general rule. A few places show possible columnar jointing. The layers in this vicinity have an apparent dip to the southwest suggesting that older materials are exposed north along the rille. The lower exposure of the outcrop seems to be associated with a slight topographic bench of problematical origin. These authors think that the evidence is insufficient to demonstrate that a series of separate lava flows are exposed in the rille wall. A comparison of these photographs with outcrops which I have observed in Iceland and northwest Canada suggests that the evidence for at least two flow units on photograph Apollo-15-12023 (fig. 4-19, discussion to follow) is compelling These authors also discuss the possibility that the rille is incised into the pre-mare surface, but find no direct evidence in the nature of a nonconformity.

In order to illustrate several additional important features of the rille wa-1, three sets of stereo photographs will be described here in detail (figures 4-19 to 4-25) These three sets have been chosen as being representative of the features visible on the entire set of 500 mm. photographs of the rille. The coverage of each pair is illustrated on figure 4-18, and identifying information for the stereo models is given in table

4-1. Some of the features to be described can only be discerned stereoscopically.

Table 4-1 Ground-based stereo models described in the text.

Stereo Model	Apollo-15 photographs	Camera location-ground station	Figure number
1	12023	9a	4-19
	12104 or	10	4-20
	12107	10	4-21
2	12058	9a	4-22
	12125	10	4-23
3	12056	9a	4-24
	12156	10	4-25

Features visible on the upper rille wall section. Stereo model number 1 (table 4-1) illustrates a typical upper section of the rille wall. This model includes extensive outcrop and debris. To the rear of the outcrop on the mare surface is a subdued crater about 50 meters in diameter with virtualln no boulder debris present on its rim. The mare surface behind the rille seems to be veneered with fine material with only an occasional nearly buried boulder visible. The rille wall has two obvious zones, an upper region containing well-displayed outcrop, and a lower section containing unconsolidated material ranging in dia-

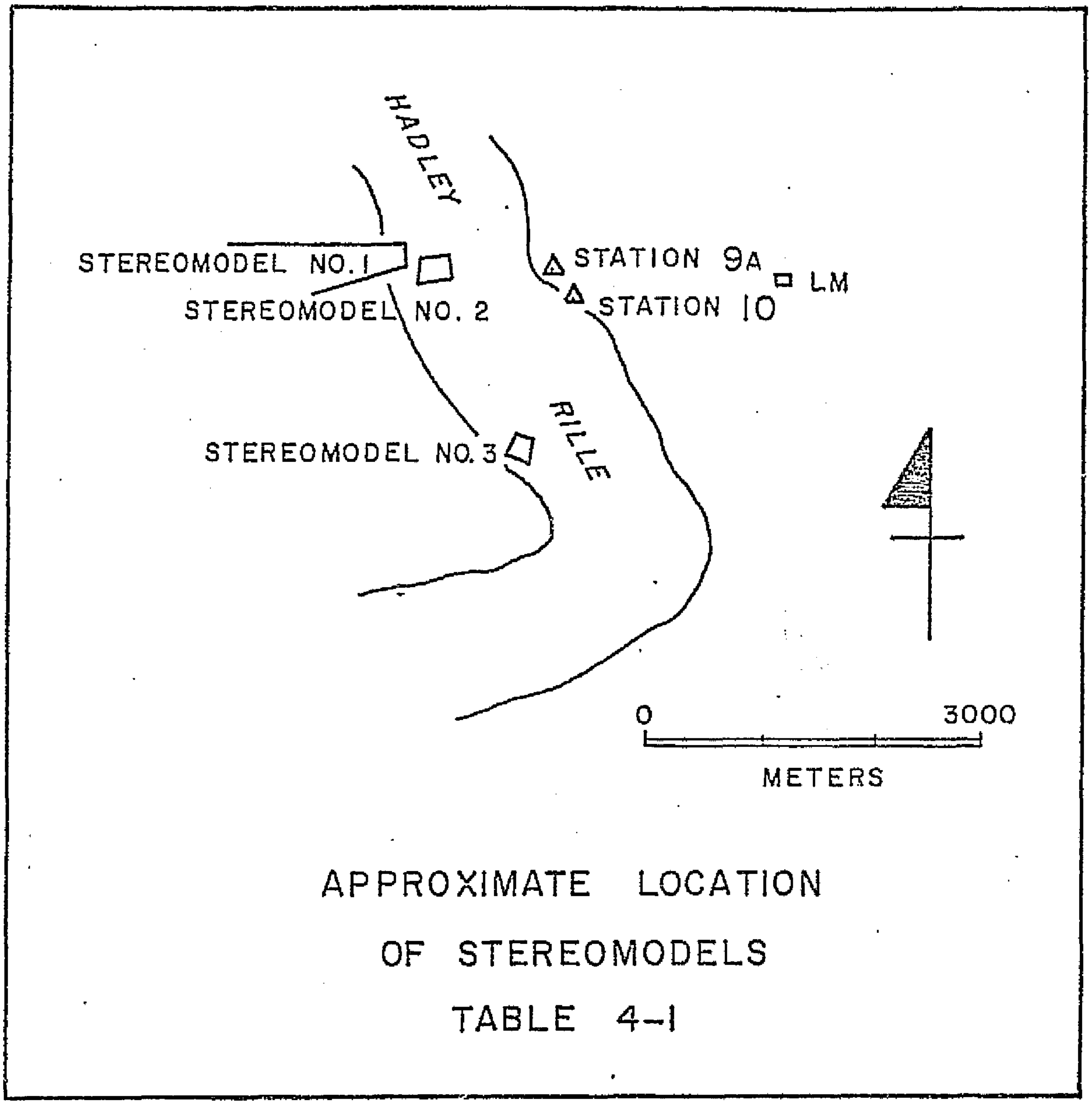

Fig. 4-18. Map to indicate the location of stereo models discussed in the text. The models are described in table 4-1.

meter from ten-meter boulders to fine material. Overlying the outcrop is a layer of regolith several meters in thickness which is a depth in agreement with regolith depths predicted from studies of crater morphology (Oberbeck and Quaide, 1967).

The outcrop has two clearly different zones. The upper unit is massive, light-colored material cut by oblique and vertical joints, the most obvious set being the oblique set. The joint spacing is irregular and relatively wide. The outcrop surface has both rounded and angular areas, but is predominently rounded.

The lower outcrop by contrast is more closely jointed. There are two prominent joint sets which have no correspondence to those in the overlying unit. There is a prominent sub-horizontal set and a well-developed, subsidiary near-vertical set. The horizontal joints divide the unit into very well-defined layers which closely resemble terrestrial depositional units. The vertical joint set suggests columnar jointing viewed from the edge. The lower unit is darker than the upper, has a more blocky surface appearance, but has a smoother face as a whole. The considerable difference in appearance, joint direction and joint spacing suggests that these two rock units have been emplaced at different times. Both outcrops have overhanging blocks jutting out from the surface a distance of several meters. There is partially developed cliff and bench topography on the upper part of the rille wall, presumably due to different characteristics of rock units. Debris has collected on a bench on top of the second unit, and a second accumulation has formed on a bench below this unit. The upper unit is cut by two notches which appear to have acted as conduits for talus fans on the bench below. These notches have an appearance similar to trails cut by soil movement which the author has observed in terrestrial alpine topography. However, the lunar trails are less pronounced than the terrestrial trails.

Poised on the rille lip above the highest rock unit is a collection of large-to-moderate-sized boulders. It is not clear how they achieved this stratigraphic position. They may have been ejected with regolith from the crater beyond the rille lip on the left side and now are a lag deposit after micro-meteroite erosion (or thermal creep-a mechanism to be postulated). It is not clear how material could be removed from beneath the rocks so as to leave them so precariously positioned. They might have been ejected from some other fresher crater in the vicinity although no such source is evident on the pan photography. There are several such places along the rille lip where boulders stand above outcrop, but in most cases, the boulders are partially buried and not free-standing as these are.

In order to compare the debris accumulations within the rille with similar features on the earth, observations and photographs were made at the B&M crushed stone quarry in Ashland, Mass. This site was chosen because the quarry stone is a greenschist which breaks into angular fragments similar to the lunar debris. The quarry slope accumulation in figure 4-26 is zoned so that the large fragments are at the down-slope side of the pile and fines have accumulated above. These accumulations form when a few large rocks slide or roll down the slope and stop to form a dam across the flow path and are followed by a flow of finer material to a position behind the dam. If more large fragments follow the fine material, they may have enough momentum to roll over the fine accumulation and thus come to rest toward the front of or even ahead of the heap. Evidently, this process can happen as a single event or as a succession of smaller events. This process requires no atmosphere or water. Several of the debris accumulations on the lunar photographs have a similarly zoned aspect. This is especially true of the boulders on the bench below the layered outcrop. Thus, a similar slope transport process is assumed to be responsible for this accumulation although it is not possible to speculate on the time rate.

There are a number of other debris accumulations which do not show a clear zonation. One such accumulation is on the left side of photo 12023 and is best viewed in stereo on the pair 12023-12107. It is not clear if these boulders are in their approximate original positions or if they were transported by some mechanism which did not cause zonation. They seem to overlie a layer of fine material which suggests transport to this locality. Perhaps the entire accumulation arrived in one ballistic event.

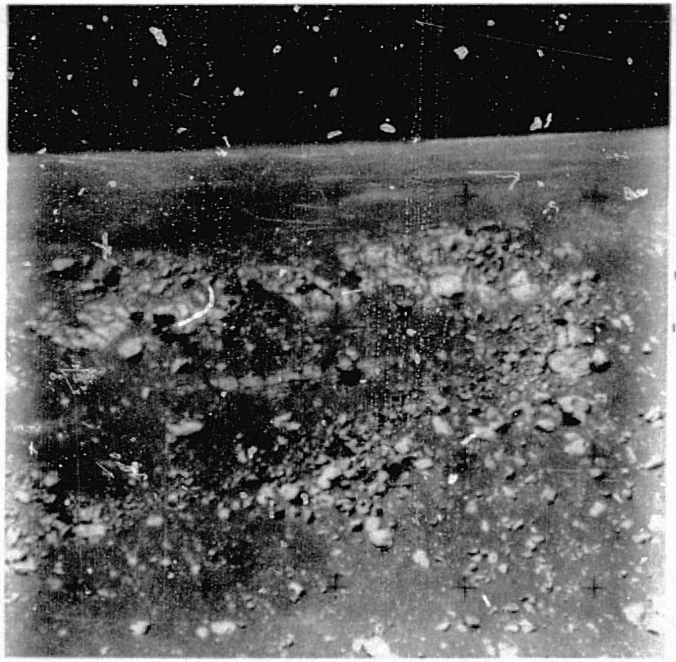

4-20

MODEL I L

15-12104

APOLLO HASSELBLAD 15-12104 NATIONAL SPACE SCIENCE DATA CENTER

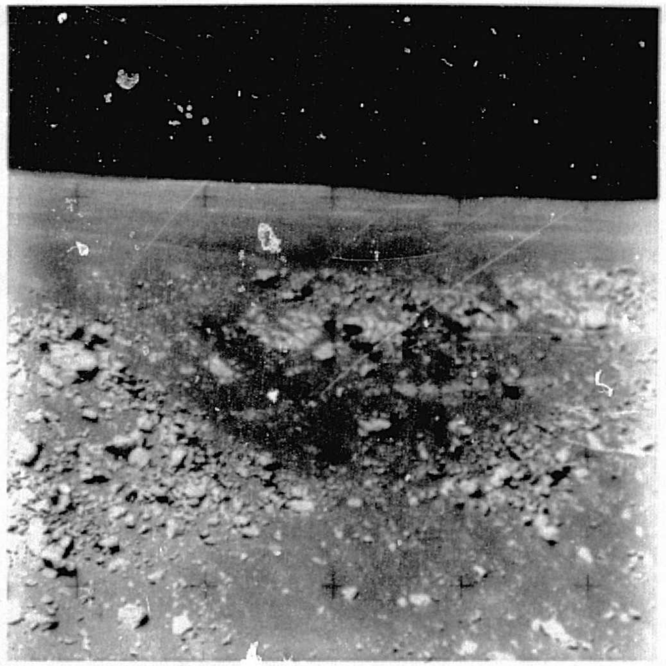

4-19

MODEL I R

15-12023

APOLLO HASSELBLAD 15-12023 NATIONAL SPACE SCIENCE DATA CENTER

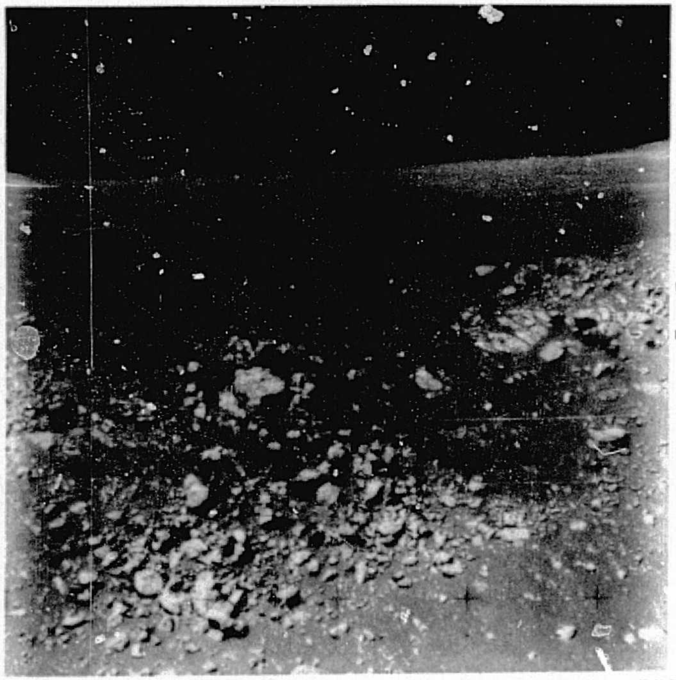

4-21

MODEL I L

15-12107

APOLLO HASSELBLAD 15-12107 NATIONAL SPACE SCIENCE DATA CENTER

Fig's. 4-19 to 4-26. The Apollo-15 ground based photographs (fig's. 4-19 to 4-25) are not spaced for stereo viewing, but may be cut for use with a mirror stereoscope. Some difficulty will be experienced because of scales which don't match. This might be resolved by elevating one edge of the stereoscope and refocusing. Figure 4-26 is placed out of sequence for comparison (see text).

4-23

MODEL 2 L

15-12125

4-22

MODEL 2 R

15-12058

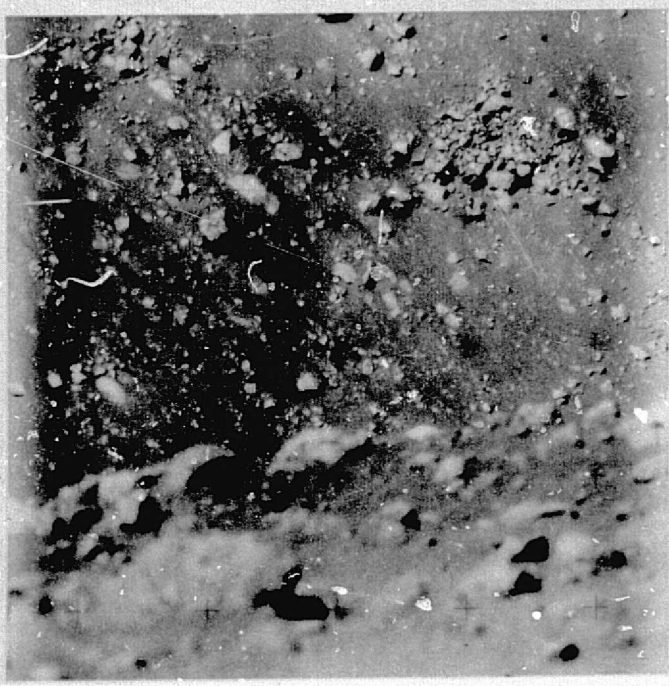

4-25

MODEL 3 L

15-12156

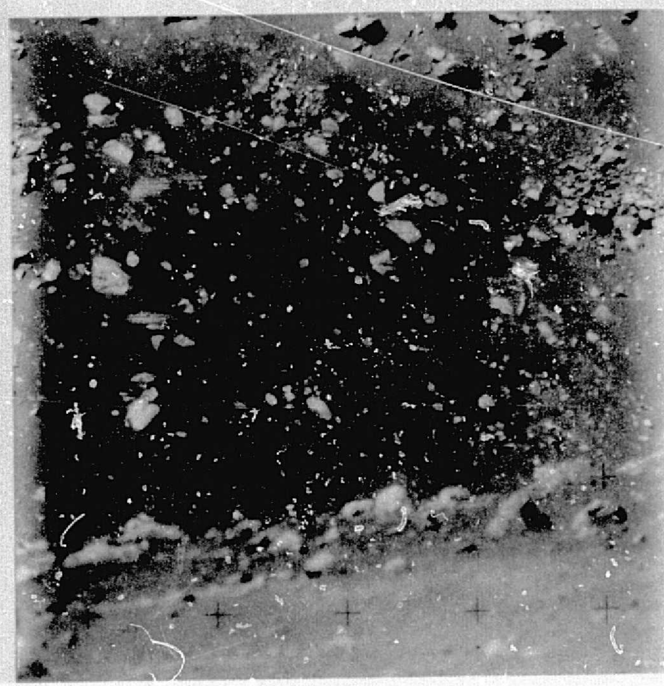

4-24

MODEL 3 R

15-12056

On the bottom one third of the stereo model, the slope takes on a different appearance which is characteristic of most of the photographed portions of the lower rille wall. At this level, there is no outcrop present and the talus contains fewer boulders in proportion to fine materials. The boulders which are present can be divided into two groups. One group consists of relatively dark-colored rocks which are angular and which rest on the surface with little or no filleting with fine material (Morris and Shoemaker, 1968) [1]. The other boulders are light in color, subdued or rounded in surface appearance, and are relatively buried or filleted. There seems to be a relative lack of partially buried boulders. This effect is more fully displayed on stereo pair 12056-12156 which constitute stereo model number 3 (table 4-1).

Recent cratering in the rille. The first stereo model (above) illustrates a general section of the rille wall. Stereo model number 2 (table 4-1) contrasts debris which is obviously recently generated with other materials on the slope.

[1]These authors have defined fillets as embankments of fine-grained material partially or entirely surrounding larger fragments in a report: Morris, E. C. and Shoemaker, E. M. (1968) Fragmental debris., Geology, Television observations from surveyor: Part II of Surveyor Project Final Report, JPL Tech. Rept. 32-1265, p. 69.

The crater in the center of the field of this stereo model is about 100 meters in diameter, fresh in appearance and has an obvious raised rim of ejecta. The floor of the crater is filled with angular boulders which are as large as twelve meters across. These were undoubtedly excavated by the cratering event. The present author has seen few boulders in natural situations as clearly angular as the large, pyramidal boulder on the rim of the crater on the uppper left side.

On the rim of the crater, there are many angular boulders, but in addition, there are many which are noticably less angular. The rim deposit is probably a mixture of newly excavated material with material from the pre-crater surface. Outside of the ejecta blanket, particularly well displayed on the left, there are accumulations of unzoned debris similar to those noted on the first stereo model. Above this accumulation, there is a section of the slope which contains nearly buried, subdued appearing boulders also similar to those noted on the prior model.

Three discrete stages of slope development seem to be represented by this debris. During the first stage, the relatively rounded, nearly buried boulders were formed and they were incorporated in a matrix of fines. During the second stage, the slightly rounded, unburied boulder accumulations formed. Finally, the cratering event produced the extremely angular, excavated boulders in and around the crater. It is not clear if the three boulder types result from distinct time-separated processes or if the three types represent a continuous process of slope evolution. The apparent absence of partially buried boulders and the dissimilar degree of rounding represented by each boulder type suggests that three distinct processes have operated at widely separated times.

Features visible on the central rille wall section. Stereo model number 3 illustrates a portion of the mid-slope section of the rille wall. At this level, there is no outcrop. There are few zoned debris accumulations although a small one is observed on the right side of the model. These photographs particularly illustrate the two oldest boulder categories. There are many thoroughly buried boulders, but many stand out on the slope. The number of one-half buried boulders is minimal.

It should be realized that the boulders in these photographs are comparable to the largest glacially transported boulders on earth. It is puzzling as to how they arrived at their present positions without breakage assuming they have been significantly moved at all. Some of the boulders on the rille slopes (sizes up to 30 meters across) are larger than the joint blocks in the outcrops in the outcrops above. A joint spacing this large in terrestrial volcanic rocks is certainly exceptional.

As illustrated by this photograph, most boulders within the rille have no well-defined boulder trails leading to their present positions.

There are a few boulder trails visible on panoramic photographs (example discussed previously in this chapter), but all are easily associated with recent cratering events. Evidently, most boulders have been emplaced by a process with one of the following characteristics:

1. The process did not form trails initially.

2. The emplacement took place so long ago that the trails have been erased by subsequent erosion.

3. The boulders are in continual movement in some process which is so slow that the rate of erasure of boulder trails exceeds the rate of boulder motion.

The movement of material down lunar slopes has usually been assumed to result from small impact events causing the saltation of surface particles. If the results of many impacts are considered, net movement of particles in a down-slope direction is the most probable result. Micrometeorites appear to be an important agent of weathering and erosion of the rille wall. For example, the banded boulder at the top of the talus accumulation on stereo model number 3 has evidently been differentially weathered to a relief of several decimeters by this mechanism. Another mechanism proposed by Gold (1966) assumes that particles which attain an electric charge on the lunar surface maintain the charge for a long period in the absence of an atmosphere. The resulting electrostatic attractions and repulsions may result in down-slope movement. This process has not been directly documented.

I would like to propose another possible mechanism for lunar slope transport which can be called thermal creep. Thermal expansion and contraction in response to cyclic solar exposure probably causes continual slight intergranular readjustments in the mass of regolith. On sloped surfaces, this would cause downhill movement with a slow time rate. Such a process would be particularly active below boulders because reflection of sun light by the rock to the surface in an area adjacent to the shadow of the rock would produce a high temperature gradient there, and thus, be more apt to result in differential movement. This could be largely responsible for the unexplained excavation which has been noted below rocks on lunar slopes and which is apparent on many buried rocks in this stereo model.

Characteristics of the Profiles:

In order that unusual profiles could be identified, several characteristics of each profile were examined to determine 'ordinary' appearance. These observations are summarized in table 4-2. The following general statements are based on the observed profile characteristics and an examination of each profile location using panoramic photographs.

1. The usual profile shape is a symmetric V-shape with a rounded bottom and mildly concave limbs.

2. U-shaped profiles are related to craters or adjacent mountain slopes which have probably contributed material to the rille.

3. There is no consistant evidence indicating natural leevees.

4. Asymmetry of profiles can be explained by various post-rille formation processes such as infilling by cratering or erosion from adjacent slopes. Some curved sections have distinct asymmetry suggestive of slip-off slopes and cut banks in stream channels. This could be equally well explained by more extreme weathering after rille formation on the sharp inside corner of the curve.

5. On the other hand, weathering and erosion may have destroyed asymmetries which existed after rille formation.

6. Much of the cliff and bench appearance is related to visible outcrop.

7. The mare surface slopes toward the mountain side in the southern extremity of the rille, toward the mare side around the landing site, but both sides of the mare slope in toward the rille in the mid-section of the southern rille segment.

8. The mare surface at the rille edge is higher on the mare side

Table 4-2. Observed profile characteristics.

Characteristic	Number of profiles with characteristic		
	Brewer[1]	Wu[2]	Total
Profile location			
Straight channel	14	4	18
Gentle curve	7	2	9
Sharp curve	6	0	6
Very sharp curve	1	1	2
Profile symmetry			
Symmetric	19	5	24
Asymmetric	8	3	11
Profile shape (based on appearance of bottom curve joining the two opposite slopes)			
V-shape (ex.: profile 6)	18	5	23
U-shape (ex.: profile 23) (the examples are borderline cases)	6	3	9
Cliff and bench topography			
Present on	5	N/A[3]	5
Possibly present on	7	N/A[3]	7
Mare slopes to the side			
Mountain	8	3	11
Mare	4	2	6
Both sides slope to rille	8	3?[3]	11
High side of rille			
Mare	7	1	8
Mountain	9	5	14
Even	3	2	5
Ill-defined	8		8

[1]Figures 4-6 to 4-17 this dissertation.

[2]Wu, S. S. C. et al. (1972) Photogrammetry of Apollo-15 Photography: in Apollo-15 Preliminary Science Report, NASA SP-289, Washington, D.C.

[3]Small scale makes judgment questionnable.

on southern profiles but higher on the mountain side around the landing site. The high side tends to be the mountain side at intermediate locations, but this is variable.

Calculation of Lunar Erosion Rate:

The probable infilling of the rille with material eroded from Hill 305 has been noted in this chapter. If one assumes that the channel in this section was originally similar to the remainder of the southern section of the rille, the amount of deposition can be calculated. This provides an estimate of the amount of erosion from Hill 305.

In order to accomplish this, the cross-sectional area of the rille was established for each profile location without an obvious disruption using a polar planimeter. These values were averaged to give the statistics in table 4-3.

Table 4-3. Results of channel cross-section calculations.

Profile numbers used in average:	1-8, 10-24 (24 in total)
Average cross-sectional area: (square meters)	18.4×10^4 M^2
Standard deviation	3.8×10^4 M^2
Standard error	$.8 \times 10^4$ M^2

By comparison, the two profiles across the rille under Hill 305 (Profiles number 30 and number 30a, Fig. 4-17) have values of 5.73×10^4 M^2 and 8.21×10^4 M^2 which when averaged, give 6.97×10^4 M^2.

Subtracting these two average values and computing pooled confidence limits, the amount of in-filling is calculated to be 11.3 x 10^4 M^2 $\pm$ 6.5 x 10^4 M^2. Over the 7.2 kilometer length of channel which profiles 26 and 31 seem to represent, this amounts to a volume of 8.1 x 10^8 M^3 $\pm$ 4.7 x 10^8 M^3. This volume has been shed from an area (orthogonally projected on metric photo without slope correction) of about 1.2 x 10^7 M^2. If the material in the rille is assumed to represent all the material which has been shed from the hill slope, this figure implies that at the 90% confidence level, there has been between 28 and 106 meters of erosion from the south slope of Hill 305. If a three billion year date is assumed for the age of rille formation (a data consistent with the mare basalt dates discussed in chapter 2), the maximum rate of erosion is found to be about 35 meters per billion years. There are obvious objections to this argument, but it suffices to establish an order of magnitude for the lunar erosion rate on an equilibrium slope during Eratosthenian and Copernican time.

CHAPTER V

THE STRUCTURAL SETTING OF HADLEY RILLE

On metric photos of the Apennine-Hadley region (fig. 5-1), numerous linear and sub-linear structural elements can be observed in map view. The question naturally arises as to the connection between these structures and Hadley Rille itself. A careful examination of metric photos indicates that a few structures (perhaps two) in highland areas can be extended to correspond with individual rille segments, but that no such correspondence is evident for most rille segments. It is necessary, therefore, to examine the region for more subtle relationships.

Structural Data Preparation:

In order to assemble a structural map and to acquire data for numerical analysis of structural trends, the following technique was adopted. A photomosaic of strips from metric photos 15-0991 to 15-0995 was assembled and glued to a hard backing (fig. 5-1). The mosaic was then examined strip by strip under the large format stereo viewer (described in ch. 3) using the appropriate stereo companion for each strip in turn. After a preliminary examination of the mosaic, a sheet of matte surface mylar, upon which the structures could be traced, was taped over the mosaic. Then, with the stereo viewer still in position, the structures were located, plotted on the mylar, and an identifying number was assigned to each. The matte surface mylar transmitted enough of the image from the mosaic that good stereo fusion was possible during the plotting. This allowed relief to be used as a primary criterion in distinguishing structures in addition to tone and textural differences.

This technique was developed by the author after reviewing reports describing difficulties in interpreting lineaments visible on Apollo-15 photography. In particular, Howard and Larsen (1972) have concluded after laboratory experiments involving the photography of random surfaces that illusionary lineament patterns may exist on much lunar photography. Characteristically, these patterns are most observable at low sun angle and appear to form a grid which is symmetrically disposed about the direction to the sun. The angle between the grid pattern and the surface projection of the sun vector varied from 15° to 55° increasing with the sun angle. The authors conclude that serious difficulty may be encountered distinguishing real and imaginary lineaments on low sun photography. Swann et al. (1972) have specifically studied the numerous small scale lineaments that appear on the

Apollo-15 ground-based photography and have published rose diagrams of the result. Most of the rose diagrams show a symmetry about the sun vector. They have concluded that it is not possible to definitively distinguish true lineaments from artifacts of lighting.

By using relief as a key factor in distinguishing lineaments, this bias is probably minimized. The photographs which were chosen are taken at intermediate sun angles of 21° (0995) to 26° (0991)[1]. These give adequate stereo relief and contrast but should exhibit fewer lighting artifacts than low sun photos. An additional advantage is that lineaments are not obscured by the relatively small shadows on these photographs.

A total of 181 structures were plotted. As the structures were being mapped, they were documentedas follows:

1. The azimuth of each of the elements was measured using the vernier anglehead of a K&E drafting machine. This method of accumulating angular data from graphics is rapid, accurate ($\pm \frac{1}{4}$ degree) and therefore has much to recommend it. It must be noted that no correction was attempted for the distortion of the structure azimuths due to relief of the terrain through which they pass. Long structures probably

[1]Lockheed Electronics Co., Inc. (1972) Apollo-15 Index of Mapping Camera and Panoramic Camera Photographs, NASA, Houston.

average to an approximately correct value and the most meaningful of the subsequent statistical tests emphasize the long-length structures.

2. The type of structure was noted and an appropriate map symbol was plotted. In addition, a numerical code was recorded to identify the structure type for each structure in the data set. The seven structure types into which all observed structures could be classed and the number of observations in each class are:

a. Apparent grabens (17 or 9.4%).

b. Edges of mountain blocks (22 or 12.5%).

c. Undifferentiated lineaments (97 or 53.6%).

d. Crater chains (17 or 9.4%).

e. Apparent volcanic relief features (14 or 7.7%).

f. Small local systems of fractures (11 or 6.1%).

g. The general trend of sinuous rilles (3 or 1.7%).

3. The relative relief of each structure was classed as follows:

a. Obvious relief features (e.g., Fresnell Rille system).

b. Easily seen on metric photos (southeast segment of Bradley Rille).

c. Can be found on monoscopic photo after a search (many

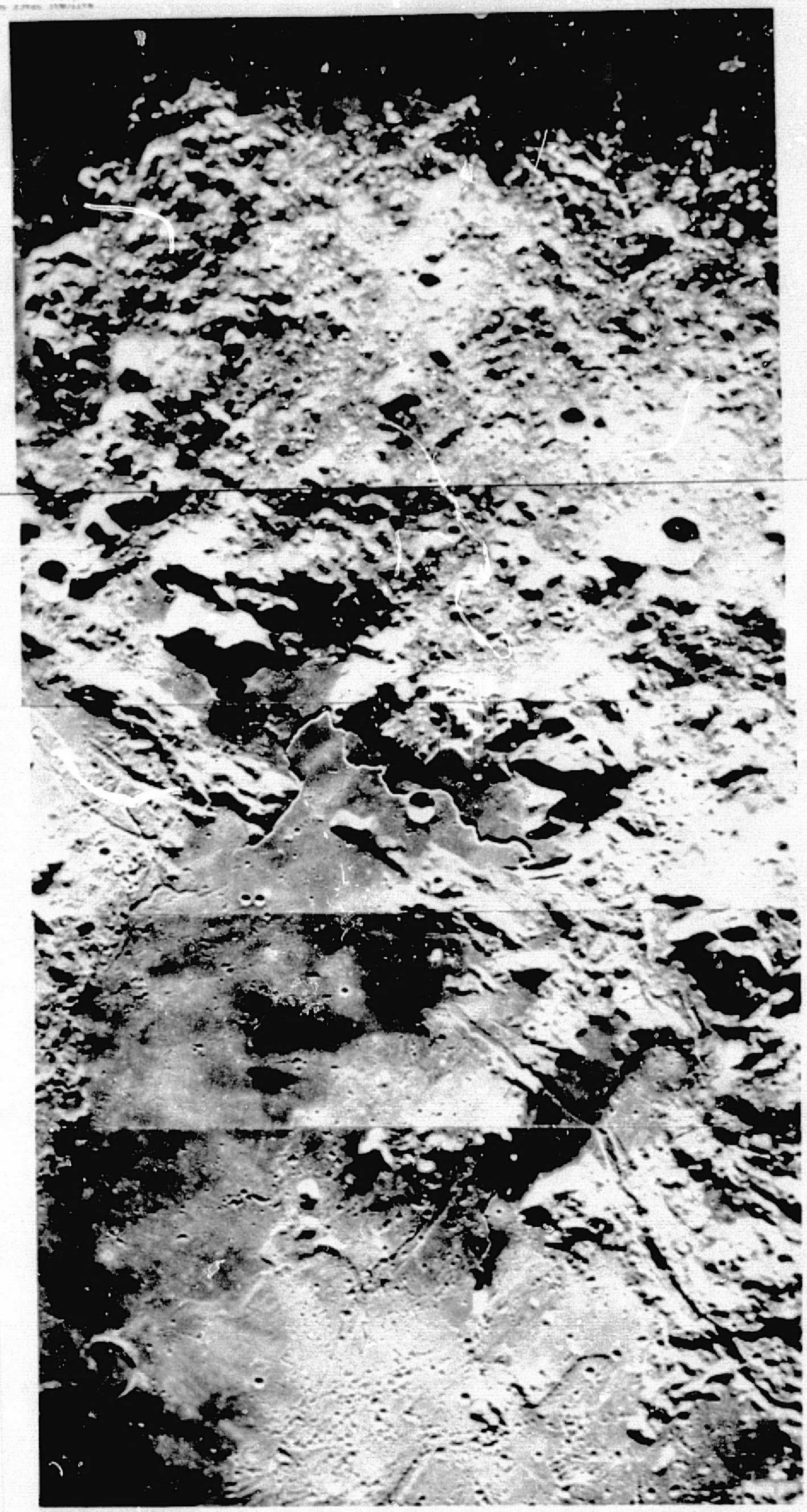

fig. 5-1. Mosaic of photographs, Apollo-15 metric 991 to 995 used for structural interpretation. Compare with fig. 5-2.

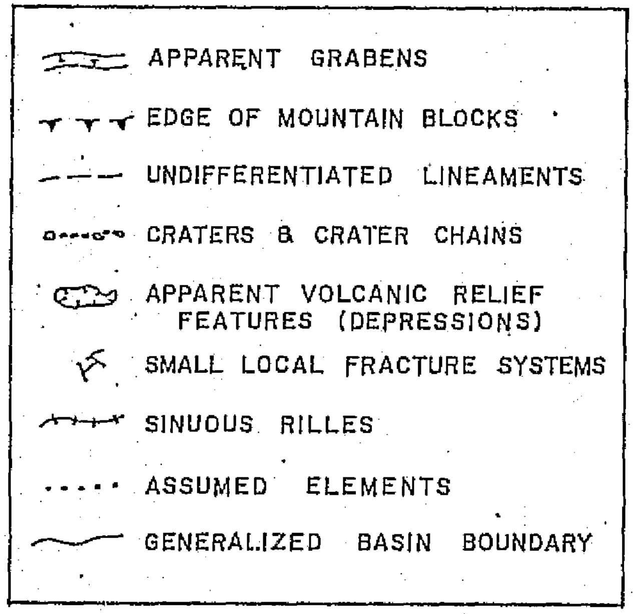

Fig. 5-2. Map illustrating structures surrounding Hadley Rille

STRUCTURES SURROUNDING HADLEY RILLE

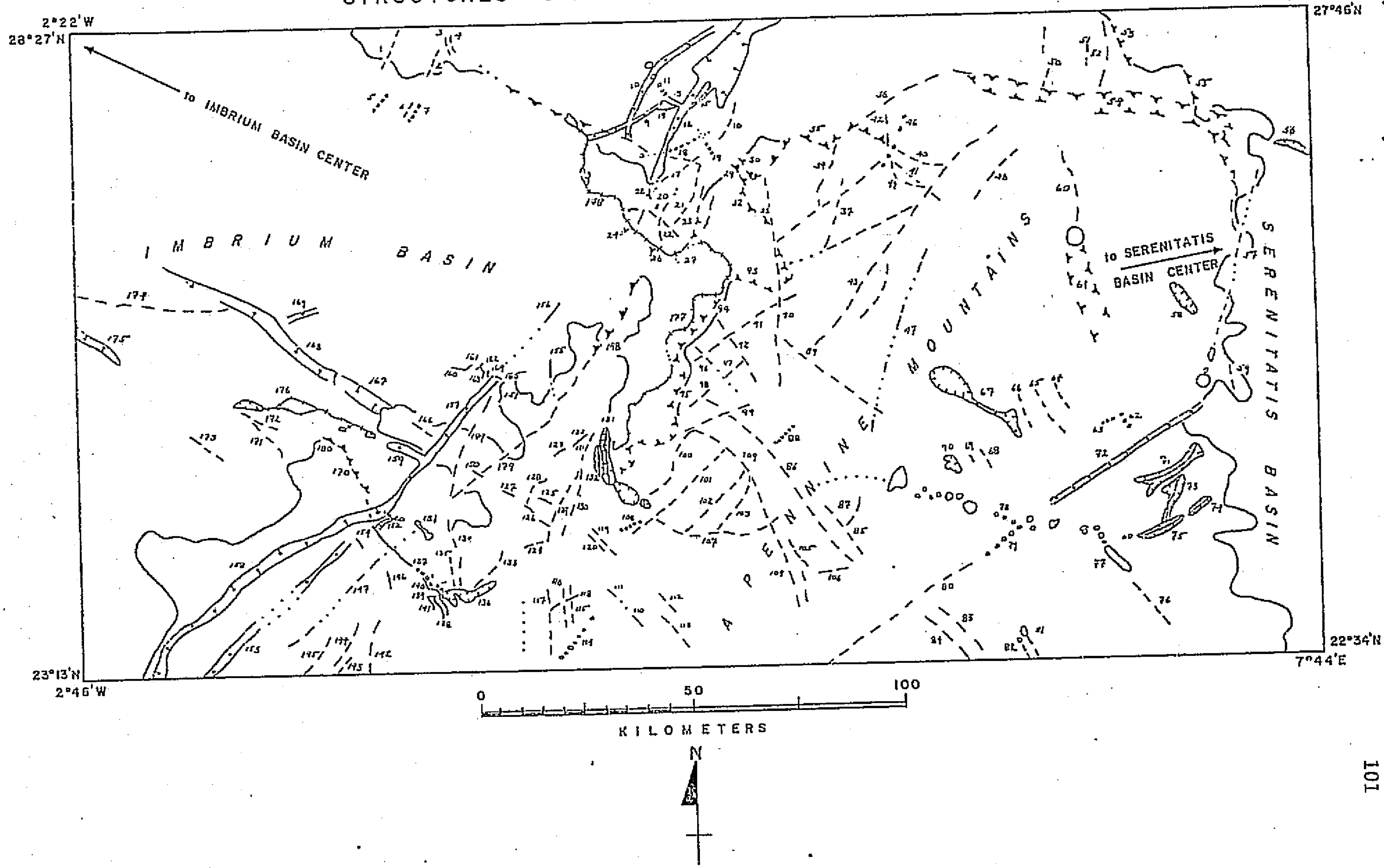

lineaments).

d. Only evident in stereoscopic model (no. 16).

4. The length of each structure was measured.

5. The linearity of each structure was indicated with a code number.

The map which resulted from these observations is reproduced as figure 5-2.

To complete the structural data, the position of the mid-point of each structural element was determined and recorded. This was accomplished by overlaying a metric grid on the map (fig. 5-2) to establish a reference system. The position of the grid relative to the lunar coordinate system was recorded so that the metric measurements could be transformed into lunar latitudes and longitudes. The completed structural data set is listed in appendix two.

Relationship of Structures to Adjacent Basins:

In chapter two, it was noted that the structures in the Apennine-Hadley region appear to be generally circumferential or radial to the Imbrium Basin, but that the preceding Serenitatis and Vaporum Basin-forming events must have affected the region as well. One use of the structural data is to examine the relationship between basins and structures.

Several authors have discussed the structures which are circumferential and radial to lunar basins:

Hartmann and Kuiper have published a series of papers discussing the gross structure of lunar basins. Hartmann and Kuiper (1962) is a report detailing the positions of concentric ring structures around all the telescopically observable lunar basins. Hartmann (1963) published a detailed study of the radial structures surrounding the Imbrium Basin. This paper also contains an extensive bibliography on the Imbrium Basin structures. The papers by Hartmann and Kuiper establish the existance of the concentric and radial patterns without doubt.

Carr and El-Baz (1971) consider the northwest facing scarpe of the Apennine Mountains to be a major structural boundary delimiting the edge of basin-fill deposits. They also suggest that basin-radial faults are to be found in the mountains outside the basin.

Mutch (1972) discusses the presence of concentric rilles surrounding the Humorum Basin.

Basin related directions. The present author decided to investigate the question of the relationship of these structures to the adjacent basins using a direct approach. A general equation was written which gives the azimuth from any point on a planetary surface to any other point given the latitude and longitude of the pair of points. The analysis of this problem which is given in appendix one yields the following result:

$$\mathrm{Cos}(AZ) = \frac{\mathrm{Sin}(L_2) - S \times \mathrm{Sin}(L_1)}{\mathrm{Cos}(L_1) \times (1 - S^2)^{\frac{1}{2}}}$$

where

$$S = [\mathrm{Cos}(L_1) \times \mathrm{Cos}(L_2)] \times [\mathrm{Cos}(W_2 - W_1) + \mathrm{Sin}(L_2) + \mathrm{Sin}(L_1)]$$

AZ is the desired azimuth from point 1 to point 2 (note that on a spherical surface that the azimuth is not the same as the back azimuth. Thus, some care must be taken to substitute variables correctly.)

L_1 and L_2 are the latitudes of points 1 and 2 respectively.

W_1 and W_2 are the longitudes of points 1 and 2 respectively.

Upon the completion of this analysis, a program was written to use this equation and the position data taken for the mid-point of each of the measured structures to compute:

1. The direction to the center of the Imbrium Basin from each structure.

2. The direction to the center of the Serenitatis Basin from each structure.

3. The directions at each structure location circumferential to each basin; that is, azimuths at 90° to the radial azimuths described in 1. and 2.

For purposes of this numerical experiment, the coordinates of the basin centers were estimated from the map by Wilhelms and McCauley (1971). The overall results of these calculations are listed in table 5-1 and displayed graphically in figure 5-3.

Table 5-1. Ranges of computed directions from structural elements in the Apennine-Hadley region radial and circumferential to the Imbrium and Serenitatis Basins.

Direction	Range of Values in the Region
Radial to the Imbrium Basin	N55.6W to N64.9W
Circumferential to the Imbrium Basin	N26.0E to N34.4E
Radial to Serenitatis Basin	N76.1E to N89.5E
Circumferential to Serenitatis Basin	N0.5W to N13.9W

<u>Classification of structures according to azimuth.</u> It can be seen that there is a considerable angular difference between these values;

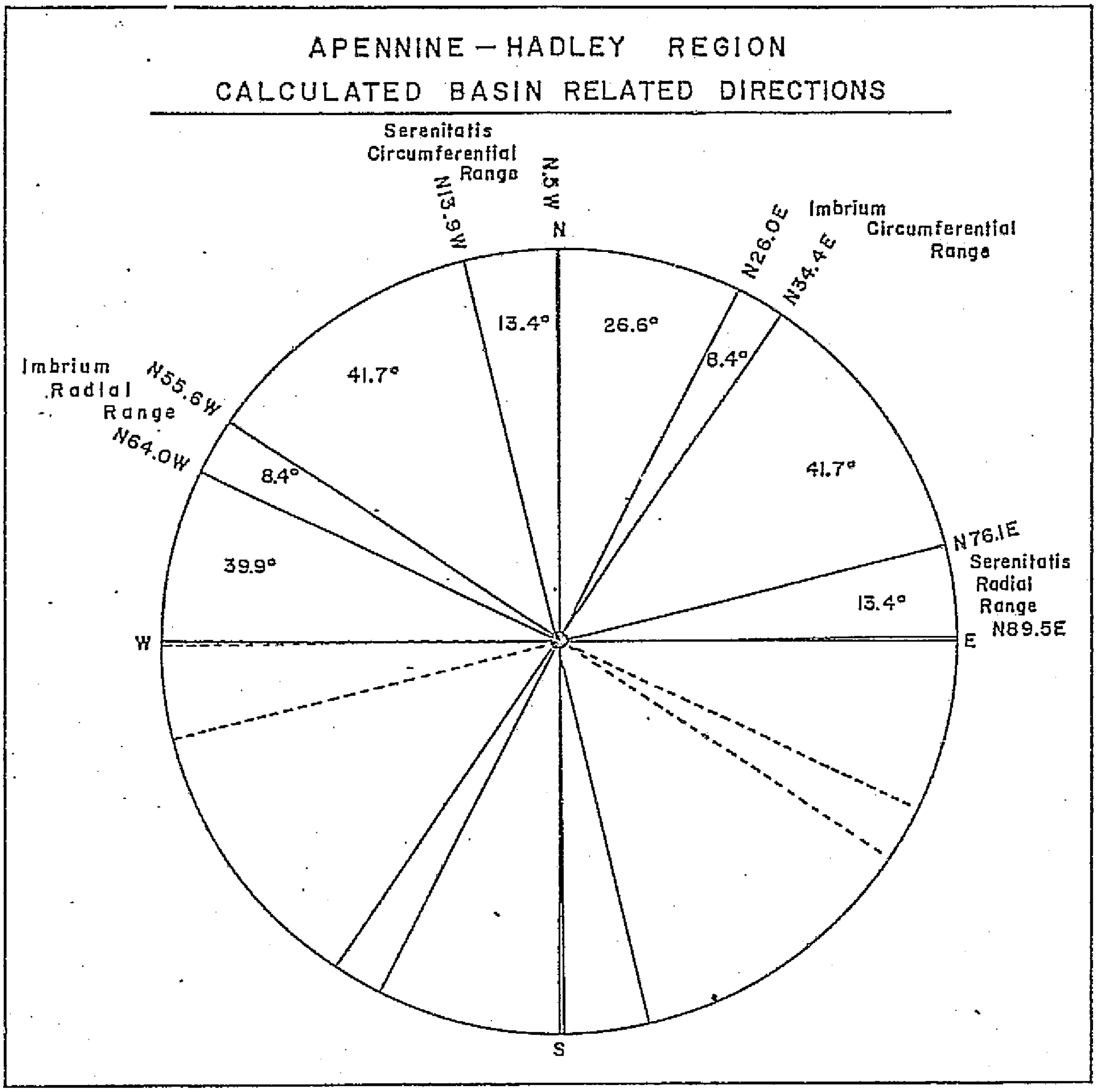

Fig. 5-3. Basin-related directions which form the basis of the structure classification by azimuth.

that is, Serenitatis-related directions do not correspond to Imbrium-related directions. This fact is presented graphically in fig. 5-3. Thus, the possibility arises that the measured structural azimuths might be classed and discussed in terms of which computed basin-related direction the measurements most closely approximate. If the Serenitatis radial directions through this region were similar, for example, to the Imbrium radial directions, such a classification would be impossible.

Accordingly, the computed azimuths from the center of each structure radial and tangential to each basin were compared to the azimuths which were actually measured for each structure. Then, the individual structures were grouped according to the basin direction with which they were most closely associated. The overall results are as follows:

1. Forty-eight (48) of the measured structure azimuths or 26.5% fall closest to the Imbrium radial direction (within $\pm$ 22°).

2. Fifty-five (55) of the structure azimuths or 30.4% fall closest to the Imbrium circumferential direction (within $\pm$ 25°).

3. Thirty (30) of the structure azimuths or 16.6% fall closest to the Serenitatis radial direction (within $\pm$ 24°).

4. Forty-eight (48) of the structure azimuths or 26.5% fall closest to the Serenitatis circumferential direction (within $\pm$ 24°).

Results of structural calculations. The numerical results of these calculations are presented in appendix two. In order to allow interpretation, the results have been summarized and presented in two formats. The first is graphical and the second is cartographic.

Histograms. Figure 5-4 contains three graphical displays of the set of structure azimuths. The bottom graph is a histogram with a 1° class width of the number of measured structures falling in each interval. Plotted above this is a second histogram of the same data grouped with a class width of 10°. Plotted at the top of the diagram is a graph which represents the 1° class width histogram except that the 1° frequency values have been smoothed according to Spencer's curve-smoothing technique. (The use of this formula is detailed in ch. 3.) It can be noted that the smoothed curve gives a much better representation of the oscillations in the frequency distribution than does the 10° class width histogram.

In order to display the results of the preceding numerical experiment, the ranges of the calculated basin-radial and basin-circumferential azimuths have been superimposed as vertical lines on the graphs. In addition, figure 5-4 indicates the range of measured structure azimuths which is associated with each of the four basin-related structural directions.

On the histograms (fig. 5-4), several significant factors are evident:

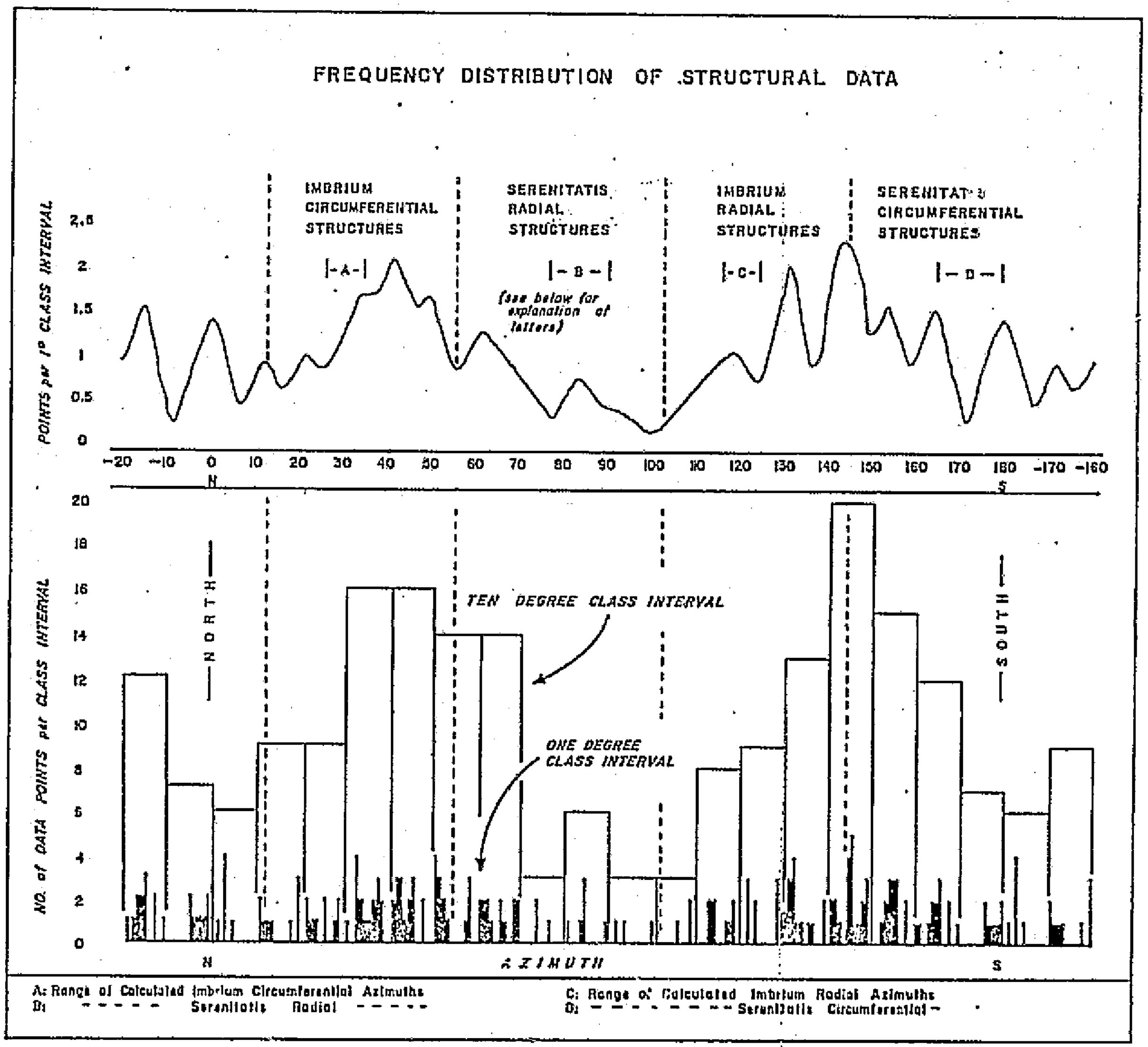
FREQUENCY DISTRIBUTION OF STRUCTURAL DATA
IMBRIUM CIRCUMFERENTIAL STRUCTURES
SERENITATIS RADIAL STRUCTURES
IMBRIUM RADIAL STRUCTURES
SERENITATIS CIRCUMFERENTIAL STRUCTURES
(see below for explanation of letters)
POINTS per 1° CLASS INTERVAL
NO. of DATA POINTS per CLASS INTERVAL
NORTH
SOUTH
TEN DEGREE CLASS INTERVAL
ONE DEGREE CLASS INTERVAL
AZIMUTH
A: Range of Calculated Imbrium Circumferential Azimuths
B: Serenitatis Radial
C: Range of Calculated Imbrium Radial Azimuths
D: Serenitatis Circumferential

FIG. 5 - 4

1. The Imbrium circumferential and the Serenitatis radial directions are represented by well-defined peaks. The structures with east-west azimuths are unusual in the lunar structural pattern. Elston et al. (1971) have noted a moon-wide absence of structures with an east-west strike.

2. The Imbrium radial direction is represented by a well-defined peak which is not as large as might be expected.

3. The Serenitatis circumferential direction seems to be represented by a trough, but an examination of the 1° class interval histogram indicates that several structures with a north-south strike constitute a peak.

4. A somewhat puzzling observation is that the largest peak on the smoothed curve, as well as both histograms, falls at the division between the Imbrium radial and the Serenitatis circumferential expected ranges at an azimuth of 144°.

These frequency distributions indicate only the number of points falling in each azimuthal class interval with no indication of the relative importance of the different structures. In order to give weight to the major structures, a smoothed curve showing the percentage of structure length falling in each azimuthal interval has also been prepared (fig. 5-7). Comparison of the two smoothed curves (figs. 5-7 and 5-4) illustrates the following points:

1. With one exception, all the major peaks are still present. The exception is at 12°.

2. The Imbrium-related peaks have become higher at the expense of the Serenitatis-related peaks. The east-west Serenitatis radial peak has become very small.

3. The peak at the boundary between Imbrium radial and Serenitatis circumferential ranges has considerably diminished.

Thus, in comparison, the structures which have azimuths associated with the Imbrium circumferential and radial directions are the structures with the most surface expression. This is what one would expect from the chronology of the region.

Interpretive structure maps. These graphs, while giving a good indication of the distribution of measured azimuths relative to basin-related directions, fail to illustrate individual relationships. In order to display which specific fractures appear to relate to each basin, two additional maps (figs. 5-5 and 5-6) have been drawn. The information for these figures was obtained with a program segment which listed for each structure the basin-related direction which its azimuth most closely approximates. (This is not to imply that all structures are basin-related—only that they have been so classed.)

APPARENT GRABENS

EDGE OF MOUNTAIN BLOCKS

UNDIFFERENTIATED LINEAMENTS

CRATERS & CRATER CHAINS

APPARENT VOLCANIC RELIEF FEATURES (DEPRESSIONS)

SMALL LOCAL FRACTURE SYSTEMS

SINUOUS RILLES

ASSUMED ELEMENTS

GENERALIZED BASIN BOUNDARY

Fig. 5-5. Structures apparently related to the Imbrium Basin.

IMBRIUM RELATED STRUCTURES

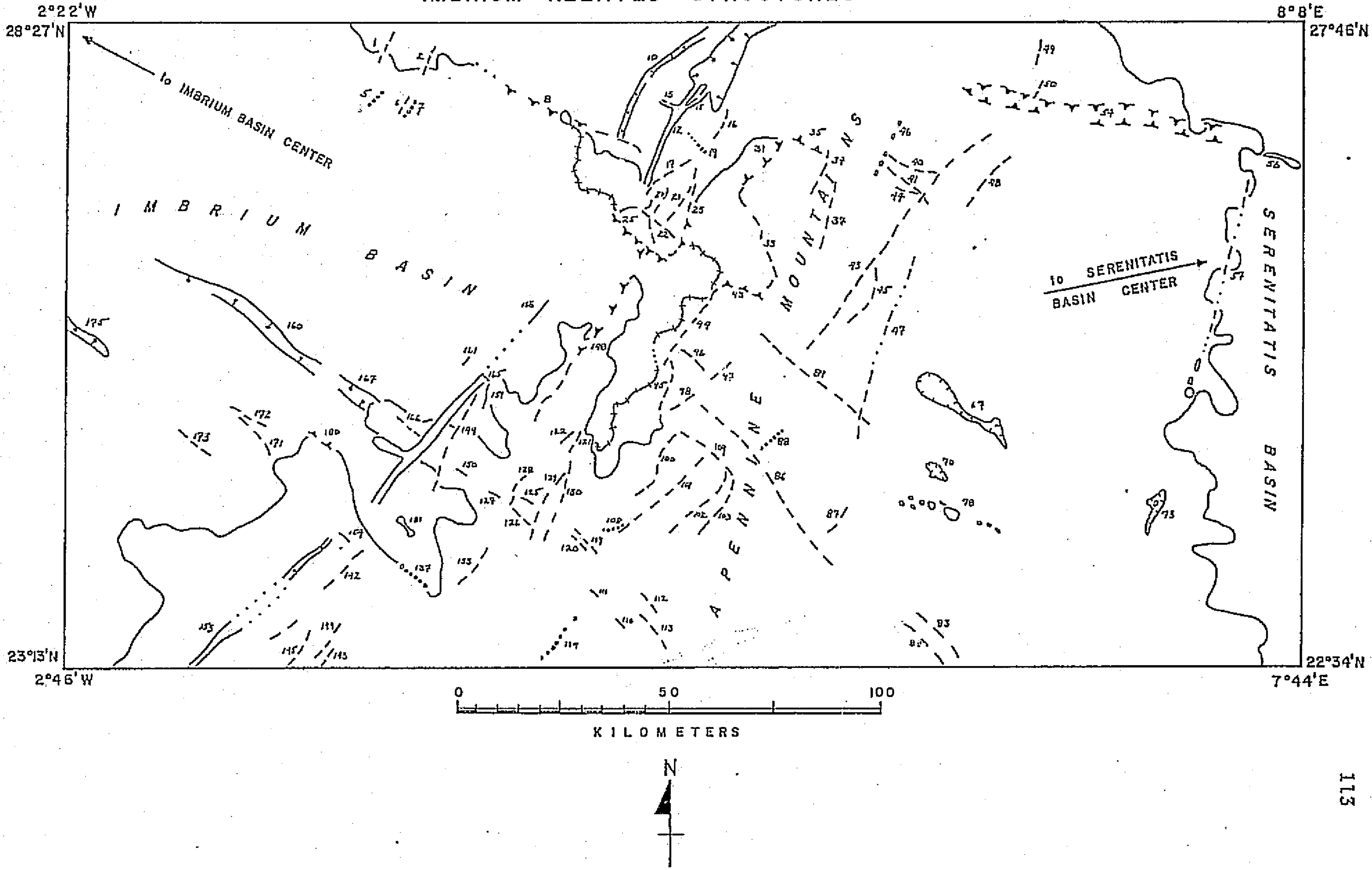

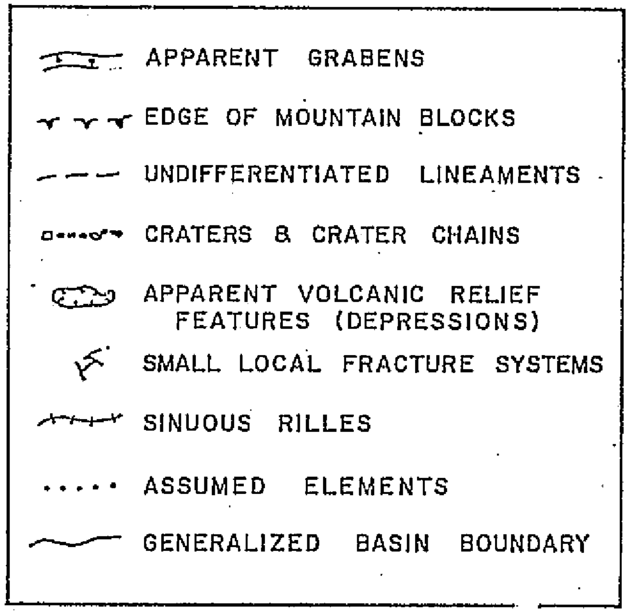

Fig. 5-6. Structures apparently related to the Serenitatis Basin

SERENITATIS RELATED STRUCTURES

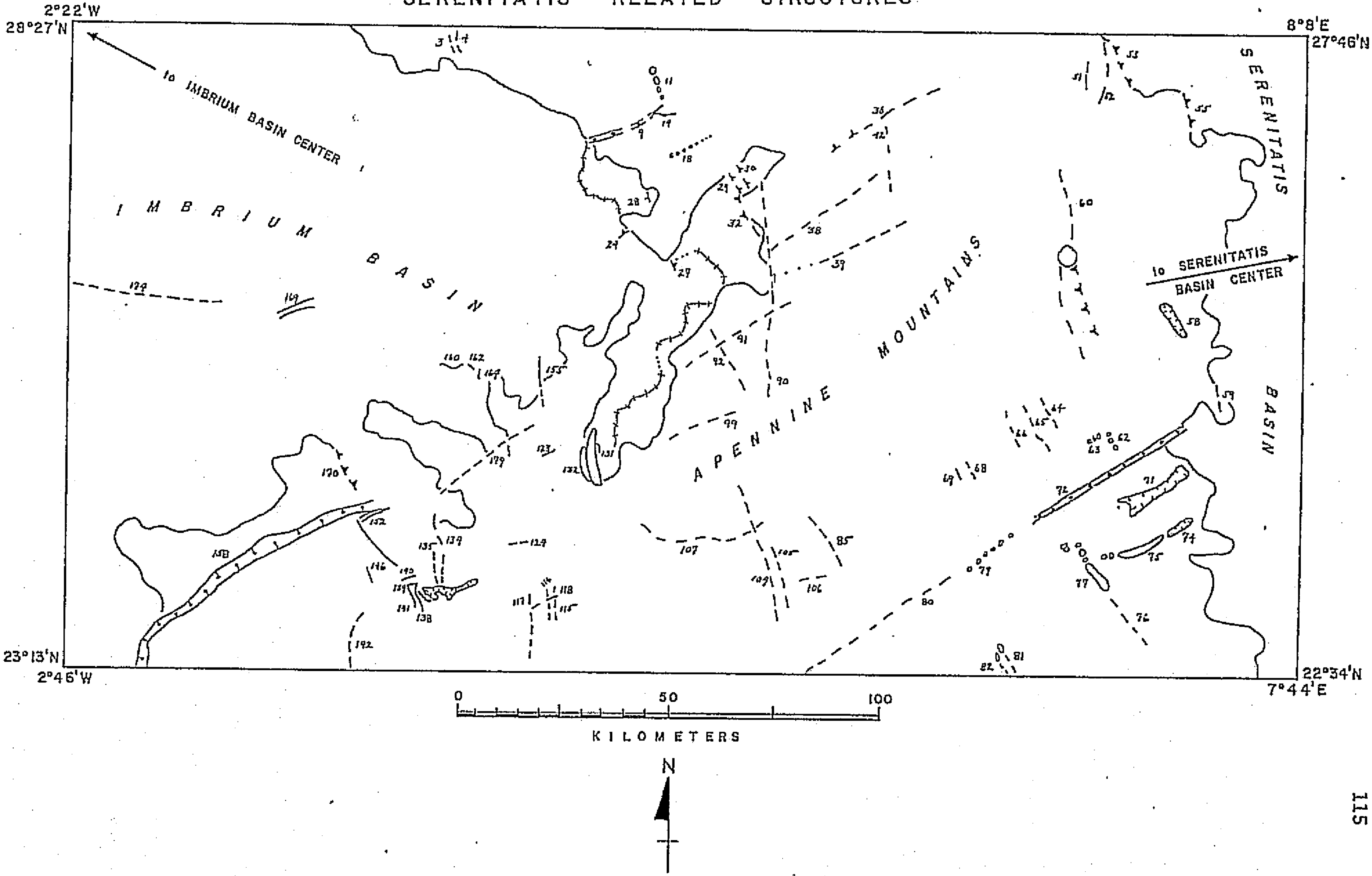

The maps were then prepared by tracing the structures related to each basin on separate sheets. Examination of these maps indicates the following:

1. Most of the major structures in the region appear to be Imbrium-related (fig. 5-5). Structure numbers 72, 80, 9, 158, 131, 132, and 90 on the Serenitatis map (fig. 5-6) are important exceptions to this rule.

2. However, there are significant Serenitatis-related structures even within the Imbrium Basin; for example, 158, 179, 169, 9 (fig. 5-6).

3. There is an important group of structures related to the Serenitatis radial direction which strike northeast across the Apennine-Hadley region. These include structure numbers 158, 80, 9, 79, 91, 99, 39, 38, 18 and other smaller structures (fig. 5-6).

4. The arcuate depression at the south end of Hadley Rille appears to be closely related by virtue of its orientation to the Serenitatis circumferential direction, both with respect to its strike and its concavity (fig. 5-6).

5. Post-mare filling fractures around Hill 305 (nos. 24, 27, 29 and 30) appear to be related to Serenitatis directions.

Conclusions. On the basis of these graphical and cartographic analyses, the following conclusions are postulated:

1. Although the major structures are Imbrium-related, many of the linear features in the Apennine-Hadley region are fractures related to the older Serenitatis event.

2. In particular, the arcuate depression at the south end of Hadley Rille is probably related to an old Serenitatis circumferential fracture which was subsequently obscured by Imbrium ejecta or the upthrusting of the Apennines.

3. Some of the post-mare filling structures around Hill 305 appear to be related to Serenitatis fracturing and therefore may represent much more extensive fractures than their limited surface expression implies.

4. If the Serenitatis event is still structurally evident in this region, the Vaporum event may be too. The Vaporum Basin has been thoroughly obscured by subsequent events so that it is not possible to accurately locate its center. It appears to be somewhat east of due south of Hadley Rille (fig. 2-1). If so, the Vaporum circumferential direction would roughly correspond to the Serenitatis radial direction and the Vaporum radial direction would correspond to the Serenitatis circumferential direction in the Hadley region. Thus, fractures on the Serenitatis-related map (fig. 5-6) could well be old Vaporum fractures which have subsequently been remobilized twice; once, by the Serenitatis event and finally, by the Imbrium event. Such a sequence of events could explain the frequency peak falling between the Imbrium radial and Serenitatis circumferential intervals on figure 5-4. The fractures

represented by this peak might never have been mobilized by the Serenitatis and Imbrium events if they had not been initiated by the Vaporum event.

Thus far, this chapter has discussed relationships betwe n structures and the surrounding basins. The relationship of the Hadley Rille to the structural setting remains to be discussed. This subject will be approached in two ways. First, the directions taken by various segments of the rille are compared with the structural azimuths measured in the region. Second, the density of structures in the region is investigated to show how the rille is related to the amount of assumed fracturing.

Comparison of Rille Directions With Structural Directions:

The author is aware of one detailed investigation of the relationship between the rille and surrounding structures. This was performed by Howard et al. (1972) who have published rose diagrams of predominant azimuths observed in the southern and northern section of the rille and compared these to the directions from the center of the Apennine-Hadley region radial and circumferential to the Imbrium Basin. They have concluded that in the southern section the rille shows no structural control, whereas there may be some control by Imbrium radial structures in the northern segment.

As should be evident from the preceding discussion, the structural situation in the region is more complex than a simple grid of Imbrium radial and circumferential azimuths. Therefore, a more detailed comparison seemed necessary. In the present study, the comparison has been carried out through the use of statistical tests on actual numerical data. Frequency distributions have also been plotted for visual comparison. Comparisons have been made between several classes of data which are described below.

Structural azimuths. Various sub-sets were extracted from the main set of structural data described earlier in this chapter. The extraction was accomplished by machine using the following technique:

1. Punched cards were prepared with a numerical code which detailed the characteristics (azimuth, length, structure type, relief, regularity) for each of the 181 measured structures.

2. A program was written to convert the descriptive parts of this data (structure type, relief, regularity) into a 20-digit binary number.

3. Selection cards were prepared, each of which also contained a 20-digit binary number. The number on each of these cards represents a combination of characteristics which characterizes a sub-set of the main structural data.

4. The binary numbers on the selection cards were read, compared for correspondnece with the internally generated binary numbers, and the azimuth and length of structures with characteristics which fit the specifications on the selection cards were stored for subsequent punching onto new cards. In this fashion, the lengths and azimuths of all the structures with any desired characteristics could be grouped as a data set for subsequent statistical comparison.

Rille azimuths. A set of azimuths and their associated lengths which characterizes the directions taken by the rille channel was obtained from a set of x-y coordinates of the rille obtained with the Mann comparator. This data is fully described in chapter six. The azimuths were computed by considering the rille to be a graph in x-y space and then computing the slope of lines connecting adjacent measured x-y points. These slopes were then converted to angles relative to north. There are 152 measured x-y coordinates which characterize the rille so that 151 azimuths were found between adjacent points. In addition to the azimuths, the distances between adjacent points were also tablulated. The resultant azimuth and length data sets were punched on cards for subsequent processing. Once the main set of rille azimuths was formed, two additional sub-sets were punched to characterize the northern and southern section of the rille separately. The southern azimuths and lengths are those between points 1 and 84 (fig. 6-2) and the northern sets run from points 84 to 152. This data is listed in appendix two.

Statistical comparisons of the data. The obvious non-normal distributions displayed by these data sets (figs. 5-7 and 5-8) makes the comparison of them meaningless if most simple classical parametric statistical tests are used. After some experimentation, the following approaches have been developed.

1. Comparison of frequency distributions. Frequency distributions have been formed from the various data sub-sets described above. The frequency distributions record the percentage of length of observed structures which fall into each 10° class interval; that is, the percent lengths are grouped into 18 azimuthal intervals between 0° and 180°. The 10° class width is greater than the irregularity in strike direction displayed by most individual structures. Some of these frequency distributions form the basis of the histograms (figs. 5-7 and 5-8).

Different frequency distributions have then been compared for:

a. Linear correlation.

b. Rank correlation.

using the Pearson product moment correlation coefficient and the Spearman rank correlation coefficient respectively. These two tests each yield a numerical correlation coefficient which allows the determination of the probability of a direct or inverse correlation between the frequency distributions. A positive results of these tests indicates that at a certain level of confidence, a correlation exists between the frequency distributions.

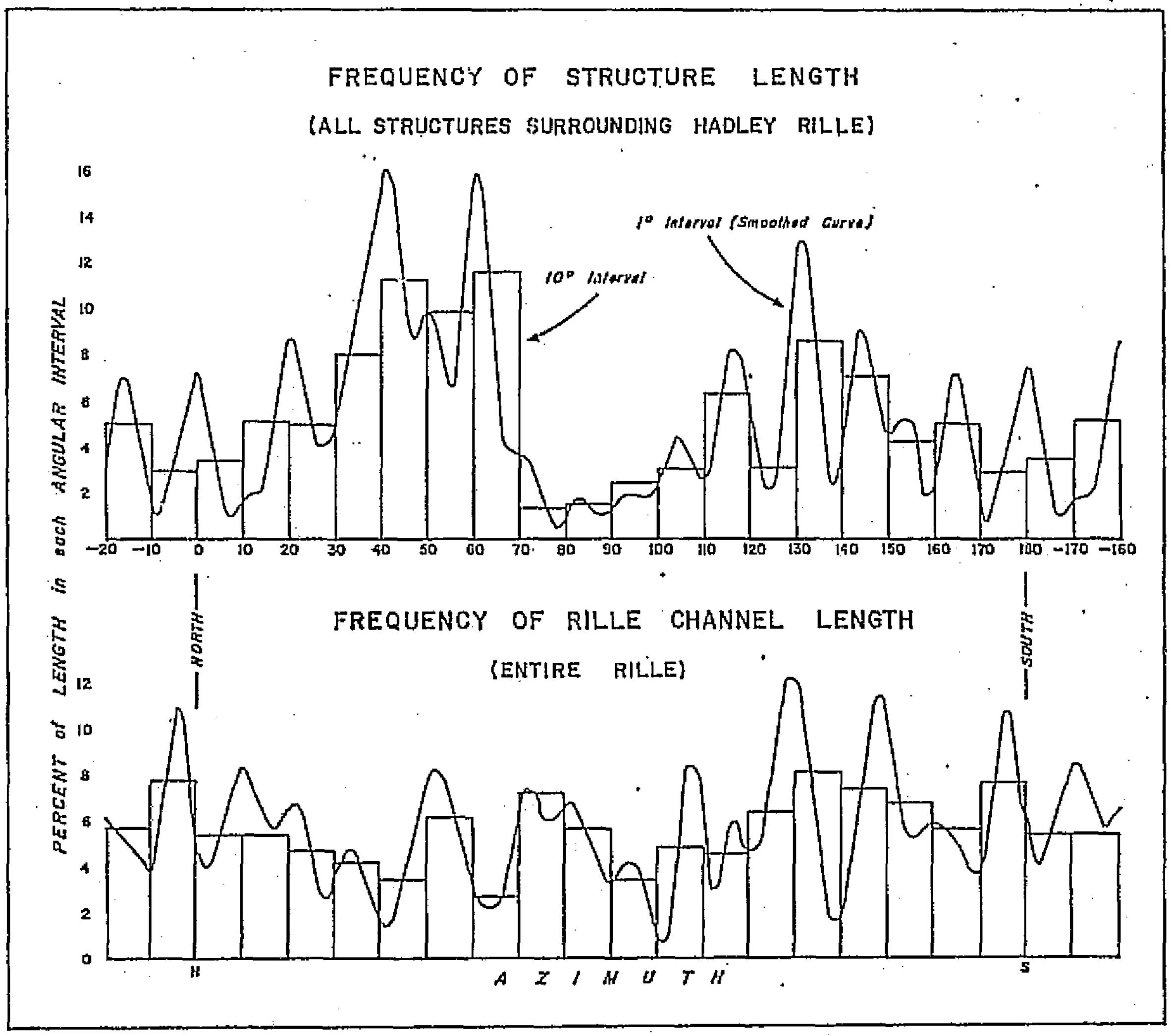
FREQUENCY OF STRUCTURE LENGTH
(ALL STRUCTURES SURROUNDING HADLEY RILLE)
1° Interval (Smoothed Curve)
10° Interval
FREQUENCY OF RILLE CHANNEL LENGTH
(ENTIRE RILLE)
PERCENT of LENGTH in each ANGULAR INTERVAL
NORTH
SOUTH
N
S
AZIMUTH

FIG. 5-7

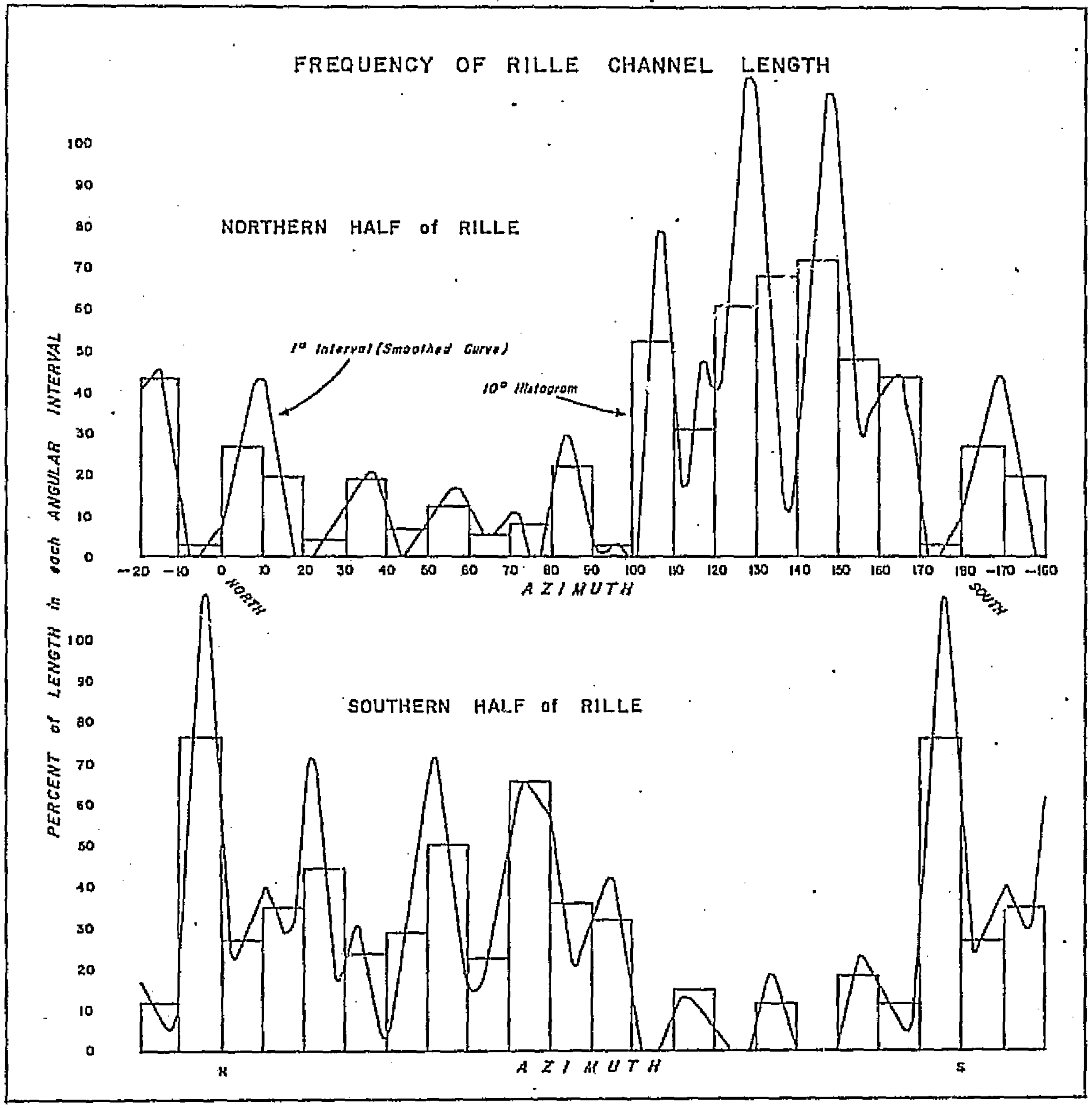
FREQUENCY OF RILLE CHANNEL LENGTH
NORTHERN HALF of RILLE
1° Interval (Smoothed Curve)
10° Histogram
PERCENT of LENGTH in each ANGULAR INTERVAL
AZIMUTH
NORTH
SOUTH
SOUTHERN HALF of RILLE
N
S

FIG. 5-8

2. Comparison of cumulative frequency distributions. Percent cumulative frequency distributions of the number of structures in each 1° azimuthal interval have been formed for the various data sub-sets. Different distributions have then been compared to find the maximum difference in cumulative frequency which occurs throughout the 0° to 180° azimuthal interval. This difference which is called the maximum deviation can be compared with theoretical distributions to determine the probability of finding the observed difference in two samples drawn from the same population. A positive result of this test indicates a small probability of observing the observed difference and thus can be taken as an indication of lack of correlation between the two samples. This test which is called Smirnov's maximum deviation test for identical populations has the following attribute according to Bradley (1968)[1].

"The present test is appropriate when the experimenter wishes to test the H_o[2] of identity against general alternatives of nonidentity and does not wish the sensitivity of the test to be concentrated upon one aspect of nonidentity (for example, different median value or

[1]Bradley, J. V. (1968) Distribution-Free Statistical Tests, Prentice Hall, Englewood Cliffs, New Jersey, p. 288.

[2]H_o is the null hypothesis—a postulate concerning the data which the experimenter can confirm or reject by statistical test.

unequal location - my note) at the expense of most others."

Thus, this appears to be a general test to detect dissimilarities in the overall characteristics of samples.

The essential difference between the correlation approach and the maximum difference approach is that the first assumes that no correlation exists and seeks to show the contrary, whereas, the second assumes a similarity between the two distributions and then expresses the probability of a difference. Thus, the two methods are complimentary. The first of the two tests is probably the most significant because of the emphasis placed on major structures by the accumulation of length values in the frequency distributions.

Summary of statistical tests. Table 5-2 is a summary of the significant tests which have been performed and an indication of the results. The table indicates the following generalizations:

1. No statistically significant direct or inverse correlation exists between the set of rille azimuths and any set of structure elements. The negative correlation coefficients obtained indicate that any correlation which does exist tends to be inverse; that is, rille azimuths have some tendency to follow directions not assumed by structures. Figures 5-9 is a scatter diagram illustrating the lack of correlation between the rille azimuths and the set of all structure azimuths.

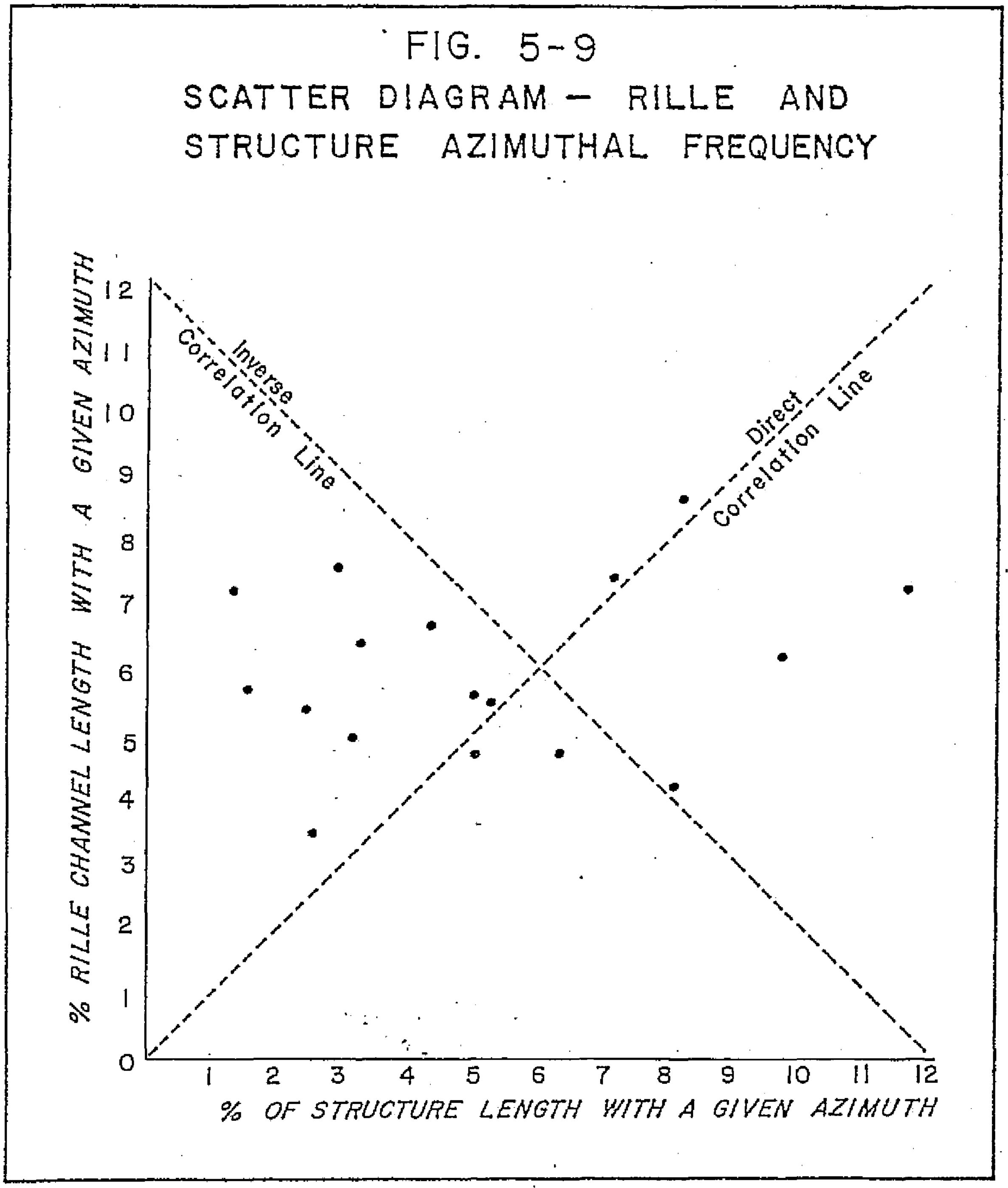

Fig. 5-9. Scatter diagram: % length of rille azimuth in a 10° azimuthal interval vs. % length of structure azimuths in the same interval.

2. Although there is no significant linear or rank correlation between the frequency distributions, the Smirnov test does not show a significant difference between the cumulative frequency distributions. An attempt was made to resolve the paradox of no correlation but also no significant difference by comparing cumulative frequencies of structure length rather than data points, thus weighting the effect of the major structures. Such tests gave significant differences at the 1% confidence level, but this approach may be inconsistent with the basic assumptions supporting the Smirnov test.

3. No correlation exists between either the north or south sections of the rille and any set of structural elements.

4. The Smirnov tests indicate that the north and south sections of the rille to have cumulative frequencies considerably different than the structure sets, in agreement with 3. above.

5. Azimuths displayed by the south half of the rille show a strong inverse correlation to those in the north. The Smirnov test indicates a very significant difference.

Thus, the statistics appear to indicate a general lack of correlation between the rille and surrounding structures. If the frequency distributions being compared were simple uni-modal distributions, this could be viewed as clear evidence of lack of structural control. However, the bi-modal structural distribution evidenced here (fig. 5-4) adds another degree of freedom to the situation which leads to two possibilities:

Table 5-2. Results of Representative Statistical Tests.

Comparison	Result[1]		
Whole rille compared with all structures	L.C.C. =	-.319	Inverse tendency, not significant
	R.C.C. =	-.256	Inverse tendency, not significant
	D =	.090	Not significant
North $\frac{1}{2}$ of rille compared with all structures	L.C.C. =	-.027	Not significant
	R.C.C. =	.091	Not significant
	D =	.208	Significant at 5%[2]
South $\frac{1}{2}$ of rille compared with all structures	L.C.C. =	-.205	Inverse tendency, not significant
	R.C.C. =	-.257	Inverse tendency, not significant
	D =	.248	Significant at 1%[2]
Whole rille compared with well-defined structures (total of 129, small, irregular, or indistinct excluded)	L.C.C. =	-.424	Inverse tendency, not significant
	R.C.C. =	-.263	Inverse tendency, not significant
	D =	.120	Not significant
North $\frac{1}{2}$ of rille compared with well-defined structures	L.C.C. =	-.162	Not significant
	R.C.C. =	.048	Not significant
	D =	.262	Significant at 1%[2]
South $\frac{1}{2}$ of rille compared with well-defined structures	L.C.C. =	-.125	Not significant
	R.C.C. =	.048	Not significant
	D =	.215	Significant at 2%[2]
Whole rille compared with all lineaments	L.C.C. =	-.183	Not significant
	R.C.C. =	-.126	Not significant
	D =	.089	Not significant

[1] L.C.C. = linear correlation coefficient; R.C.C. = rank correlation coefficient, and D = Smirnov's maximum deviation.

[2] Koch, G. S. and Link, R. F. (1970) Statistical Analysis of Geological Data, Vol. 1, Wiley, New York, appear to suggest that a 10% risk level is significant for geologic problems.

Table 5-2. Results of Representative Statistical Tests, cont'd.

Comparison	Result[1]		
North ½ of rille compared with all lineaments	L.C.C. =	−.128	Not significant
	R.C.C. =	−.192	Not significant
	D =	.265	Significant at 1%[2]
South ½ of rille compared with all lineaments	L.C.C. =	.012	Not significant
	R.C.C. =	.123	Not significant
	D =	.211	Significant at 5%[2]
North ½ of rille compared with south ½ of rille	L.C.C. =	−.774	Inverse correlation probable at 1%[2]
	R.C.C. =	−.809	Inverse correlation probable at 1%[2]
	D =	.423	Significant at 1%[2]

[1] Ibid.

[2] Ibid.

1. There may be no structural control over the rille in which case the statistical result is taken at face value.

2. One structure direction may give a predominating structural control to the extent that the other structure direction which appears as a hump in a structure frequency distribution has no correlative hump in a particular distribution of rille azimuths. This lack of correlation for one structure direction may yield a nonsignificant correlation coefficient even if total structural control existed in the other structure direction.

The next section is an examination of the graphical displays of the frequency distributions which allows some discrimination between these alternatives.

Graphical comparisons. Figures 5-7 and 5-8 are frequency distributions of the most significant data sub-sets. Two graphs have been prepared for each sub-set; one is a histogram with a 10° class interval and the other is a 1° histogram smoothed by Spencer's formula. In order to emphasize the major structures, these diagrams represent the percent of structure or rille segment length which is found in each azimuthal class. This is in contrast to fig. 5-4 which indicates the number of observations in each class. The histograms serve to give a gross comparison and the smoothed curves show more detail. This type of graphical display is used in preference to rose diagrams because Cartesian coordinates avoid the distortion of the wedge-shaped segments of a rose diagram (discussed in Harbaugh and Merriam, 1968)[1]. Also, the use of Spencer's formula is facilitated, and comparison between diagrams can be made easily by projecting vertically from one curve to the next.

An examination of these figures indicates the following points:

1. Peaks on the whole rille smoothed curve tend to correspond to troughs on the curve of all structures. This explains the tendency toward negative correlation observed between the whole rille and different structure sub-sets.

2. The whole rille distribution is far more diffuse than the clearly bi-modal distribution of structures.

3. The inverse correlation between the north and south sections is obvious.

4. The north segment of the rille displays a well-defined peak (70° wide, 100° to 170°) which grossly compares to the wider (100° wide, 80° to 180°) peak which represents southeast striking structures.

5. The southern segment displays a peak [110° wide or 350° ($= 170^\circ$) to 100°] which corresponds to the peak of northeast striking structures (60° wide, 10° to 70°), but the rille's histogram peak is about twice the width of the structure peak.

[1] Harbaugh, J. W. and Merriam, D. F. (1968) Computer Applications in Stratigraphic Analysis, Wiley, New York.

Examination of the photomosaic of the region (fig. 5-1) indicates a physical basis for these observations. The southern half of the rille occupies a valley which strikes northeast in the Imbrium circumferential direction. Because the rille occupies a longitudinal position in the valley, it is necessary that azimuths measured for this section should cluster in a diffuse group about the northeast direction. Because the structure azimuths appear so much more concentrated than the rille azimuths, it is felt that individual rille segments are not directed by bedrock structure in the southern section.

By contrast, the northern section does not occupy a well-defined valley. The fact that the northwest striking rille azimuths form a tighter cluster than the northwest grouping of the structure azimuths is therefore significant. An examination of the photomosaic indicates that Hill 305 is one structure element which effects obvious control over the rille. The segment adjacent to the Apollo-15 landing site (fig. 2-3) is a similarly directed sub-linear segment, but without obvious structural control. Because of this obvious control of one rille segment and the relatively tight grouping of rille azimuths about the Imbrium radial direction, it is felt that significant control of individual rille segments exists in the northern section of the rille. In the next chapter, it will be shown that the sinuosity of this section is less than that of the southern section. The relative straightness of the northern section is further evidence of some linear controlling factor. The possibility of structural control of the linear segment adjacent to the Apollo-15 landing site has some significance in interpreting the constriction in that section of the rille (ch. 7).

In summary, it appears that the diffuse distribution of rille azimuths representing the whole rille results from the summation of two more concentrated groupings corresponding to the northern and southern sections. The southern section is influenced by no direct structural control, but its azimuthal distribution as a whole is influenced by the rille's valley-central position. The tight grouping of the northern rille azimuths indicates control of individual segments by Imbrium radial elements. The strong inverse correlation between the azimuths of the two sections is a result of these two factors. This interpretation is consistent with the statistical and graphic evidence.

Fractures Associated With the Rille:

Although the course of the rille is for the most part not directed by pre-existing structures, such structures may in some way have been involved in the formation of the rille. In order to investigate the overall association of the rille with structures, a fracture density map (fig. 5-10) was prepared. This map is predicated on the assumption that all the observed structures with the exception of sinuous rilles represent fractures in the basement material. The map was drawn by overlaying a metric sampling grid on the original 19 x 37 cm. structure map (fig. 5-2). Then the total length of structures measured in millimeters in each 2 x 2 cm. block was measured and the result was recorded at the center of the block. The result was an array of numbers at 1 cm. vertical and horizontal intervals (since overlapping blocks were used) which was suitable for contouring. The resulting map (fig. 5-10) has contour lines which represent the length of observable fracture in the surrounding area. Because of the arbitrary scale of the metric photos which form the basis of the original map, the units of fracture density are arbitrary, but a value of 20 (indicating a length of 20 mm. in a 2 x 2 cm. square at map scale) indicates that on the ground, 16 kilometers of structure length can be expected in the surrounding 16 x 16 km. square.

These observations have been made concerning this map:

1. Only visible structures are mapped. Several processes have conspired to obscure structures—the most prominent of which is mare filling. This explains the major areas with zero structure density.

2. The highest structure densities are associated with the Bradley and Fresnell Rille systems.

3. A high density extends east from the Fresnell Rille system across Fresnell Ridge.

4. The constriction at the midsection of the rille is associated with the extreme structure density around Hill 305.

5. The arcuate depression at the south end of the rille is in a region of high structure density.

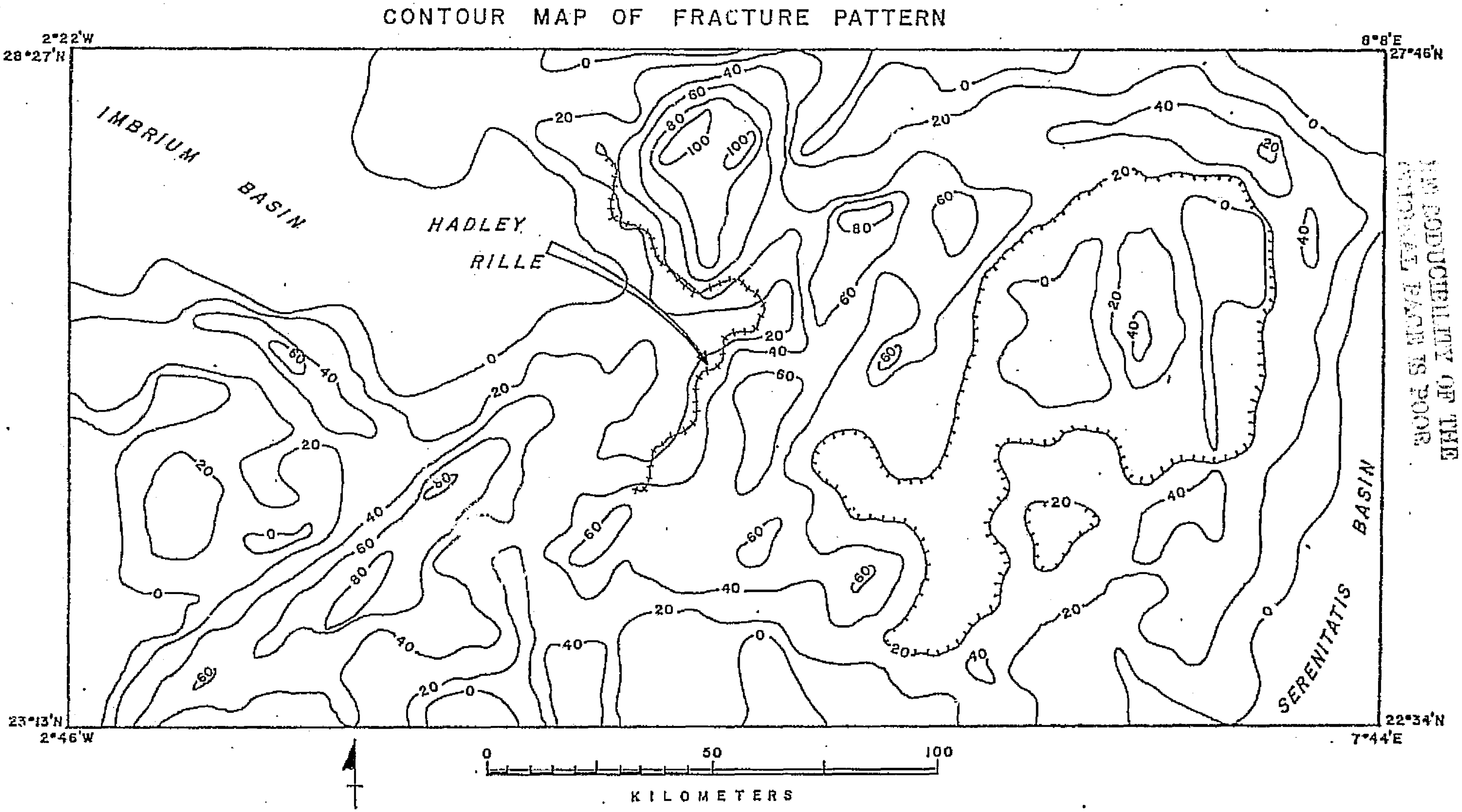

Fig. 5-10. Contour map of fracture pattern based on the relative length density of lineaments

Summary of Structural Relationships:

The preceding analysis indicates several pertinent relationships between the rille and its surroundings. The immediate vicinity has a complex set of fractures which are apparently related to at least two basin-forming events. The location of the rille itself is constrained by major structures, such as the faults bounding the Apennine Mountains. Some segments in the northern section seem to be directed by pre-existing structures. Some parts of the rille are associated with areas of high structure density. Particularly notable in this regard are the arcuate depression at the south end and the interruption northwest of the Apollo-15 landing site.

CHAPTER VI

NUMERICAL DESCRIPTION OF HADLEY RILLE

This chapter is intended to provide a numerical description of Hadley Rille. The first sections of the chapter discuss the determination of basic rille parameters: lengths, widths, depths, etc. This is followed by a discussion of derived relationships such as sinuosity, meander wave length, and width/depth ratios. These values are then compared with those found by other observers for other rilles. The final sections of the chapter discuss statistical relations and between parameters. Most of these relationships are presented graphically as well. Throughout this chapter, there is considerable emphasis on achieving a known degree of confidence; confidence limits are specified whenever possible, and a dual approach is used for deriving several conclusions. Data and calculated values not listed in the text will be found in appendix three.

Physical Dimensions of the Rille:

Several techniques have been used to measure lengths of rille segments, the width and depth at specific cross-sections and other numerical characteristics of the rille. This section is a summary of these results and techniques.

Gross lengths along the rille. The tip-to-tip extent of the rille and the length of several sub-sections have been established by direct measurement on metric photos M15-414 and N15-586. These are straight line map distances indicated on figure 6-1 and reported in table 6-1 which are intended to establish the gross size of the rille. These values were obtained by measuring the photo distances between point on paper base metric photos using a vernier caliper and converting to ground distances using the focal length and flight altitudes published by Lockheed Electronics (1972). On an undistorted vertical photograph,

$$\frac{\text{Ground distance}}{\text{Photo distance}} = \frac{\text{Flight height}}{\text{Focal length}}$$

which allows the determination of ground distances (Tewinkel, 1966). The photos were scaled by measuring the edges and computing the enlargement compared to the original metric format. The corresponding ground distances obtained from the two different photos agree to within ± 200 meters which probably represents the precision of the measurements. The accuracy, estimated to be about 2%, is probably limited by differential shrinkage of the paper, uncertainty in the flight height, possible tilt in the camera system and slight parallax due to the unevenness of the mare surface.

Table 6-1. Gross lengths of the rille.

Length (fig. 6-1)	Distance (AS15-414)		Distance (AS15-586)		Average value(km.)
	(mm. photo)	(km. gnd.)	(mm. photo)	(km. gnd.)	
a-b	95.80	76.5	95.0	76.6	76.6
a-c	90.80	72.5	90.0	72.6	72.6
b-c	5.60	4.5	5.55	4.5	4.5
d-e	10.20	8.1	10.10	8.1	8.1
f-g	shadow		18.3	14.8	——
a-h	60.40	48.2	59.55	48.0	48.1
h-c	63.00	50.3	62.60	50.5	50.4
h-b	68.70	54.9	67.65	54.6	54.8
j-b	33.45	26.7	j poorly defined		——

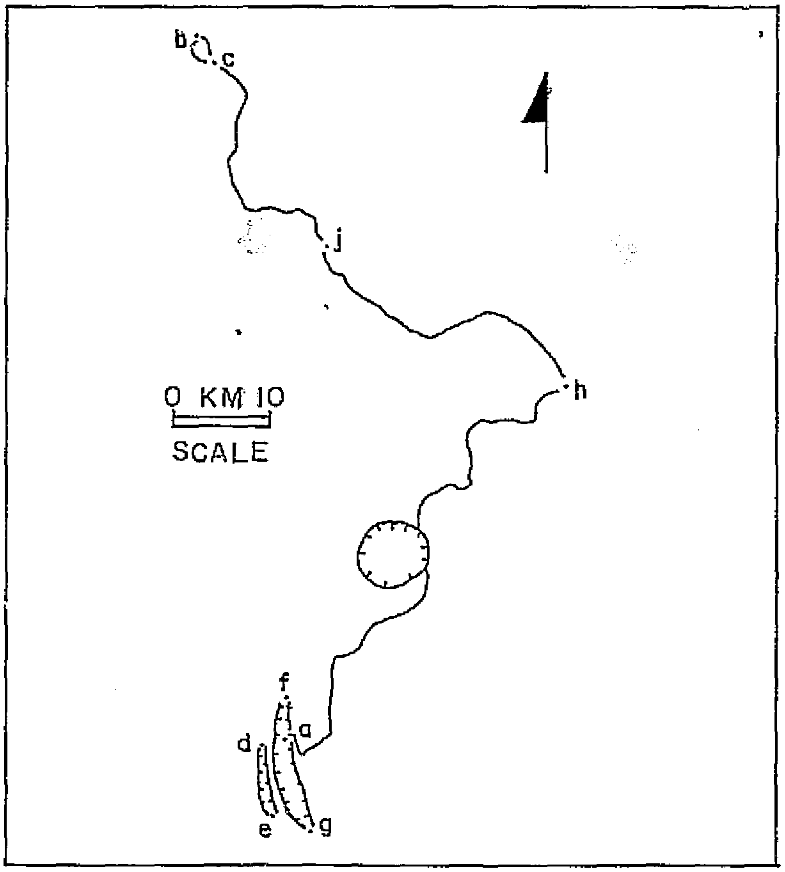

Figure 6-1. Location of length measurements reported in table 6-1.

Average width of the rille. To determine the average width of the rille and examine the relationship between width and other parameters, a set of measurements was made of x-y coordinates of pairs of points directly opposed across the rille at 152 locations along the rille. Figure 6-2 indicates the locations of these measurements. Since this data set is used for a number of calculations, its acquisition will be discussed in some detail.

Measurements were made on the Mann 1200-3 comparator (described in ch. 3) on film base photographs. The inherent accuracy of the Mann comparator is .001 mm. which corresponds to a ground distance of 10 meters. This is the same order as the resolution of the photographs so that no information is lost. The Mann comparator is not a stereoscopic instrument so the location of the edge of the rille was established by observing differences in texture, albedo, and tone. The photograph chosen for measurement was number 15-416 which displays the following characteristics:

1. It provides maximum contrast between the light reflected from the rille walls and that from the adjacent mare surface.

2. It minimizes the proportion of rille length which is obscured by shadows cast by the Apennines.

3. It provides adequate contrast in the relatively obscure northern portion of the rille where the east-west channel orientation results in poorer contrast than present in other segments.

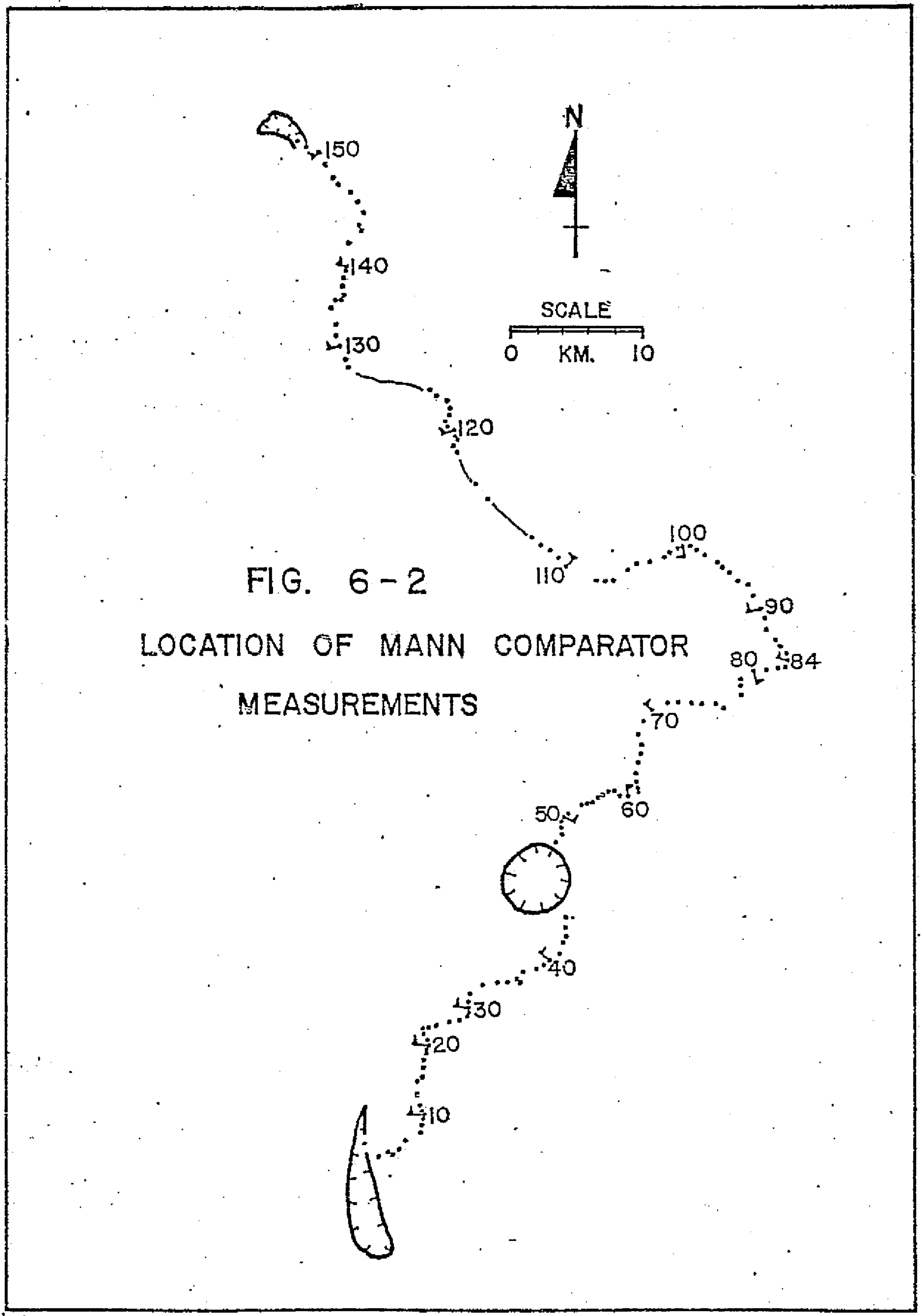

FIG. 6-2

LOCATION OF MANN COMPARATOR MEASUREMENTS

The measurement locations were neither randomly chosen nor equally spaced. In order to give the best graphic portrayal of the rille (fig. 6-4), the measurement locations were selected so that changes in the rille width could be accurately represented in the data. This data set leads to a valid width-distance graph of the rille, but it was necessary to extract randomly determined width measurements from these before calculating the average width.

This data set was resolved using an IBM 1130 computer. The program is a straightforward list of calculations based on the Pythagorean theorem which determines the distance between two points in x-y space. The calculations yielded the following information:

1. The width of the rille was calculated at each of the 152 measurement locations.

2. The distances along the rille channel between the locations of the 152 width measurements was calculated.

3. The cumulative distance along the channel from the south end of the rille to each measurement location was calculated.

4. Separate summations were made of the length of channel along which rille width increased and the length along which width decreased.

5. A calculation was performed to determine the azimuths of the channel center between successive width locations. These are the rille azimuths used for structural interpretation in chapter five.

The first of these items is used to compute the average width of the rille and the others are discussed subsequently.

The measured rille widths have values between 0.22 to 3.20 km. The largest values are observed at each end of the rille and appear to be due to the association of the rille with the arcuate fracture to the south and the angular depression to the north. If two kilometer segments are excluded from either end of the rille, the maximum width is found to be under 1.7 km. In the histogram of measured rille widths (fig. 6-3), all extreme values on the high side are at the ends of the rille. The minimum width of 0.22 km. occurs at the constriction near the Apollo-15 landing site. If this 8 km. length of unusually narrow section is excluded, the minimum width is found to be 0.52 km. The average of all measured widths (including extremes) is 1.11 km. The median value is 0.96 km. and the mode is 1.00 km. The standard deviation is 0.37 km. and the standard error is 0.03 km. A listing of all values is found in appendix three.

As discussed above, these measurements are not at randomly selected locations, and therefore, the simple arithmetic average is suspect. In order to find a 'true' average to characterize the rille, two approaches were used and the results are in substantial agreement, although slightly less than the arithmetic average reported above.

1. The map area of the rille was computed using the 152 computed widths and the 151 intervening lengths as factors in the trapazoidial rule. The average width was computed by dividing the area thus derived

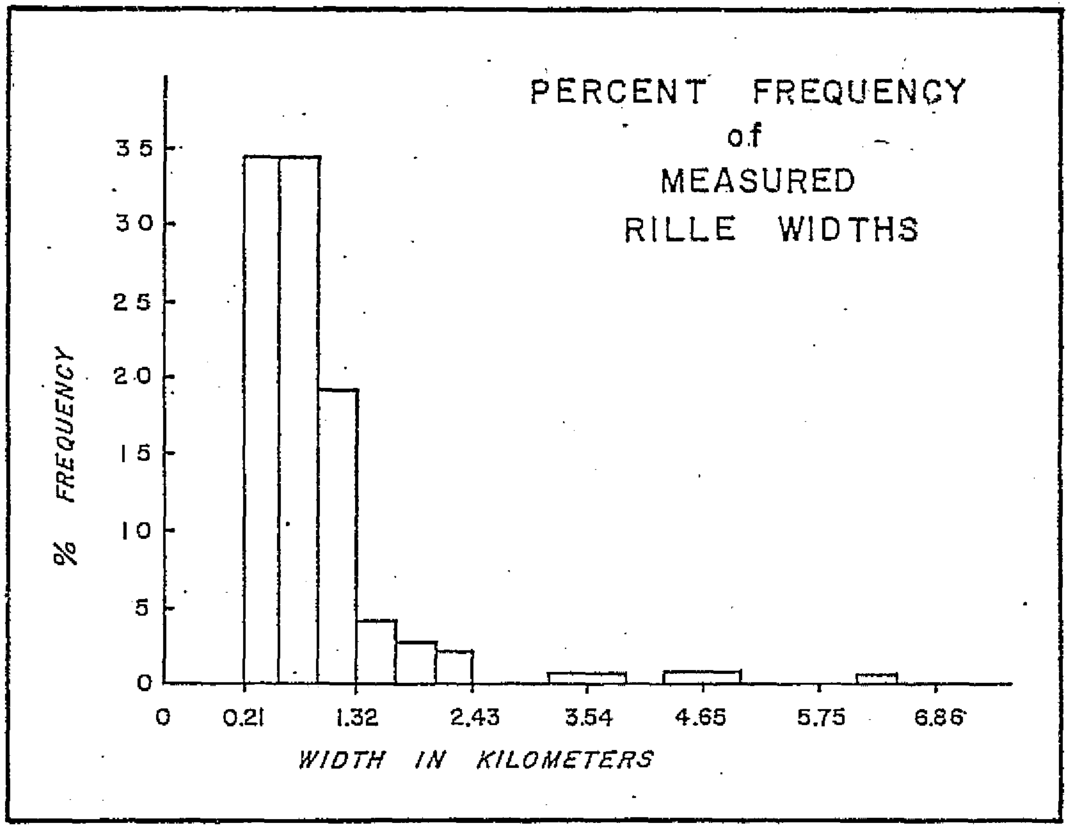

Fig. 6-3. Histogram of widths measured across Hadley Rille.

by the total channel length. The effect of this process is to weight the width measurements by the channel length which they represent. This gives an average width of 1.081 km. The same standard error of 0.03 probably applies indicating a 90% probability that the 'true' average width falls in the range 1.08± 0.05 km.

2. A graph of rille width vs. distance along the channel was constructed (fig. 6-4). Forty random numbers were drawn from a random number table (Koch and Link, 1970)[1] and multiplied by an appropriate constant to give a randomly determined abscissa with which to enter the graph. Three gaps in the data set due to shadowing and the crater, Hadley C, were assigned to a width value equal to the average of 10 values, 5 on either side of the gap. Finally, all the ordinates corresponding to the random numbers were averaged for an average width. The average obtained from this approach is 1.084 km. with standard deviation 0.26 and standard error 0.04 yielding a 'true' average width 1.08± 0.07 km. at the 90% confidence level.[2]

In addition to the width calculations for the whole rille, the

[1]Koch, G. S. and Link, R. F. (1970) Statistical Analysis of Geological Data, Vol. 1, Wiley, New York, p. 339.

[2]It must be mentioned that these two approaches are not independent since the graph (fig. 6-4) is a graphical solution of the trapazoidial rule. The second serves to establish a confidence limit more securely than the first, however.

FIG. 6-4

WIDTH AND CURVATURE VARIATION WITH DISTANCE

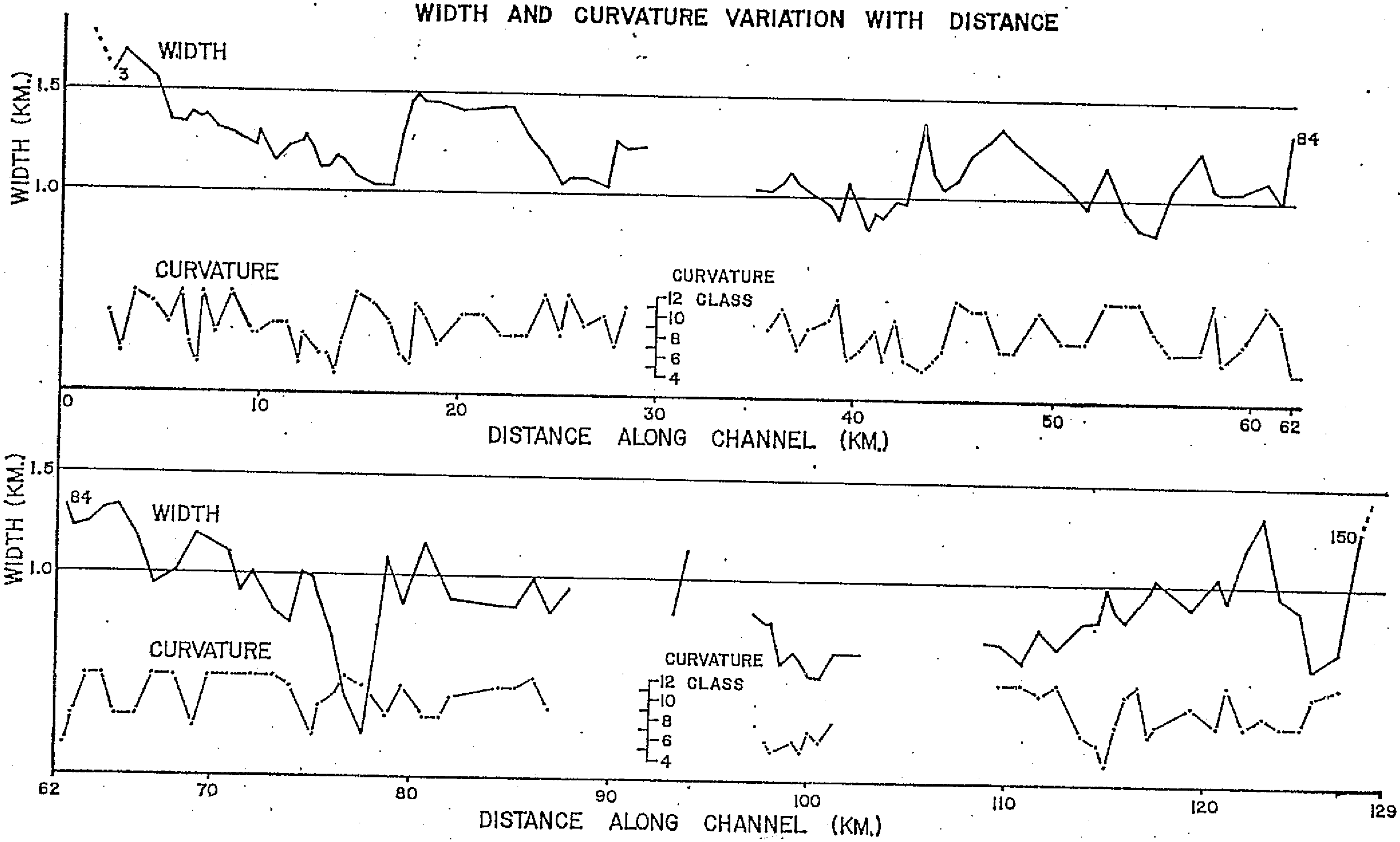

first method of averaging was employed to find average widths for several sub-segments of the rille. These are reported in table 6-2, which is keyed to figure 6-2.

Depth of the rille. The depth determination for the rille is less direct than the determination of other parameters because the whole rille could not be covered by the pan photography used with the AS-11A plotter. In the southern portion of the rille, the depth could be measured directly from profiles, but in the north, it has been estimated from the width measurements and the width to depth ratio, determined for the southern section.

For purposes of definition, the depth of the rille in the profiled section is taken as the depth below the surrounding mare surface. For most profiles, this is defined by laying a straight edge across the profile so that it touches the mare surface on either side. The depth is the vertical distance from the bottom of the rille to the straight edge. On a few profiles, one side does not exhibit a well-defined mare surface and best judgment prevailed. The measurement accuracy is judged at $\pm$ 2 mm. or $\pm$ 10 meters at the 1:5000 vertical profile scale. This is about the same as the standard error of the measurements and much less than the variability of the data which suggests that the method is adequate. The profile locations are semi-random (although dependent on sun vector directions) so the depth data set was considered to be unbiased. Depth values range from 363 meters to 200 meters, although these two values appear to be outliers. The average depth

Table 6-2. Basic rille parameters. Location numbers and letters specified in the left column are keyed to figures 6-2 and 6-1 respectively. All distances are in kilometers. Confidence limits are specified where possible and are at the 90% level.

Location	Point-to-Point Ground Distance	Average Width	Average Depth	Length of Channel	Sinuosity	Channel Volume(km.^{3})
1-152, a-b	76.5±0.8	1.08±0.07	0.25±0.04	129.7	1.68	17.6±16%
1-151, a-c	72.6±0.7			128.8		
1-84, a-h	48.1±0.5	1.23	0.29±0.04	62.6	1.28	11.0
84-151, h-c	50.4±0.5			66.3		7.0
84-152, h-b	54.8±0.5	0.95	0.22±0.04	67.2	1.23	
117-151, j-b	26.7±0.3			31.6		
1-45		1.39		29.3		
46-84		1.08		27.5		
84-117		0.93		34.7		
117-132		0.94		15.3		
34-88 (profiled section)		1.13	0.273±0.13	44.0		6.8±6%
Northern depression				4.5±0.2		
Southern depression				10.1±0.2		

of the rille in the profiled region is 273 meters with a standard deviation of 37 meters and a standard error of 7 meters. By application of the t-statistic, the 90% confidence interval is found to range $\pm$ 13 meters from the mean. A listing of all the depth values is found in appendix three. Figure 6-5 is a histogram of the measured depth values, and figure 4-5 indicates the profile locations.

The northern section of the rille is so obviously different from the southern section that it would doubtlessly be in error to assign to it the same average depth calculated for the profiled section. If we assume that the same width/depth ratio is assumed to hold for the northern section as for the south, an approximate average can be calculated because:

$$\text{average depth} = \frac{\text{average width (from Mann comparator data)}}{\text{average width/depth ratio (from profiles)}}$$

The bottom of the rille in the north appears flat which implies that width/depth is probably greater than in a V-shaped section. Thus, this scheme will probably give a maximum value.

The average width in the northern section is seen in table 6-2 to be 0.93 km. The average width/depth ratio for the southern section is 4.30 ± 0.75 at the 90% confidence level (see width/depth ratio to follow). Thus, the average depth in the northern section is estimated to be 220 meters with an uncertainty of about $\pm$ 40 meters. This diminished depth is in accord with stereo observations of the section. Using the same technique, the whole southern section (not limited to the profiled

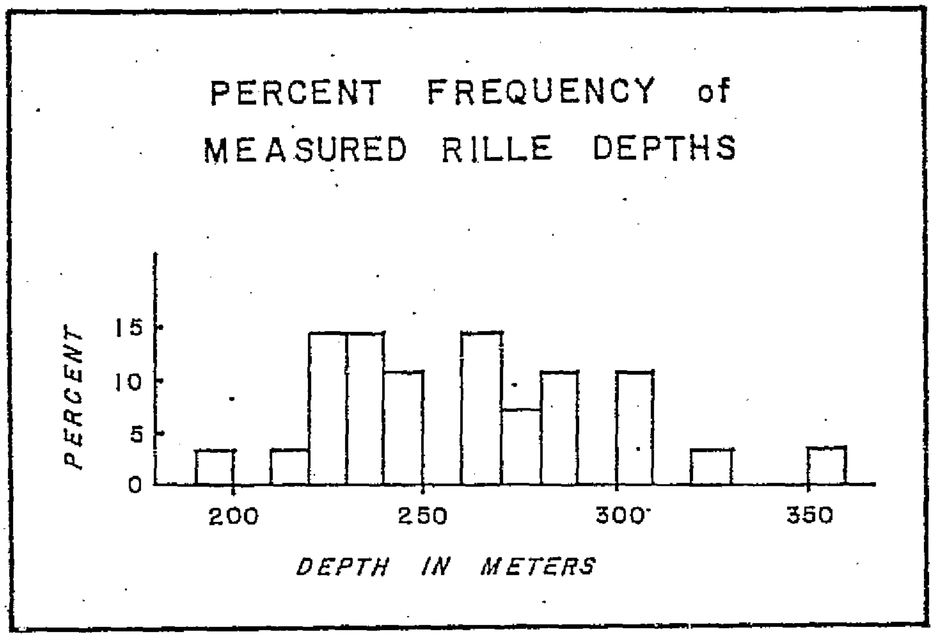

Fig. 6-5. Histogram of depths measured from Hadley Rille profiles.

section) has an average depth of 286 $\pm$ 40 meters, and the rille as a whole 251 $\pm$ 40 meters.

Length of channel. By suitable manipulation of the Mann comparator coordinate data, the total length of rille channel was calculated. Specifically, the center of the rille is found at each measurement location by averaging the coordinate locations on either side. Then the distance between adjacent center positions is calculated using the Pythagorean theorem. Finally, these distances are summed to provide the total length of channel. Using this technique, the total length of channel is found to be 129.7 km. The lengths of several shorter segments are detailed in table 6-2. A listing of the cumulative lengths is found in appendix three.

Area of the channel cross-section. The cross-sectional area of the channel at uninterrupted profile locations was measured directly using a polar planimeter. This essentially straightforward procedure yielded an average area of .184 $km.^2$ Profile numbers 1 to 24 excluding number 9 (ch. 4) were used for this average. The standard deviation of this data set is .038 $km.^2$ and the standard error is 0.008 $km.^2$ indicating a 90% confidence interval of + 0.013 $km.^2$ about the mean or 7.2%. Appendix three contains a listing of all measured values.

Curvature. Several attempts were directed toward measuring the curvature of the rille at different locations. Most of these were inadequate because the resolution of the method was poor, the location where the curvature was being measured was ill-defined, or complications in mathematical analysis made the result meaningless. Finally, the following technique evolved:

1. The x-y coordinates of the Mann comparator data were drawn up as a map of the rille (fig. 6-2) at an original scale of 1 cm. to 1 km.

2. A plexiglass template was constructed containing concentric circles. The radius of the circles increased geometrically according to the arbitrary equation:

$$\text{radius (class } n) = 2 \times 2^{(n-1)/2} \text{ expressed in milimeters}$$

that is, a class 1 circle has a radius of 2 mm., class 2 is $2 \times 2^{1/2} =$ 2.82 mm., etc. A total of 11 circles were drawn with radius from 2 mm. ($n = 1$) to 64 mm. ($n = 11$) although the smallest class subsequently utilized was class 4.

3. The template was overlain successively on each of the numbered points on the map in such a way that each of the adjacent points fall on or within a circle, the circumference of which was touching the central point.

4. The template was translated until the maximum diameter circle was found in which this condition prevailed. The central point was then assigned the curvature class represented by that circle.

The spacing of the points on the x-y plot (fig. 6-2) is sufficiently close that this technique appears adequate to characterize the curvature. A few points have long gaps separating them and these were deleted from the analysis, as were the end points on the plot. The deleted points are obvious on the graph of curvature vs. distance along the rille (fig. 6-4). The results of this experiment are shown in table 6-3.

Table 6-3. Summary of curvatures measured on Hadley Rille.

Curvature class (n) $Y_n = 2 \times 2^{(n-1)/2}$	Radius of maximum circle (km. on the ground)	Number of points in class
3	.4	0 (class 3 and lower)
4	.57	2
5	.8	8
6	1.13	14
7	1.60	17
8	2.26	25
9	3.20	14
10	4.53	13
11	6.40	15
12	all larger to straight line	33

The distribution is clearly bi-modal with centers at class 8 and class 12. The grouping above the class 8 curvatures represents the loops in the sinuous rille, and the class 12 peak probably represents the inflection points between curves. The median value of radius of curvature (which is an estimate of the average) excluding the straight values falls at 2.02 km.

Volume of the rille channel. The volume of the rille channel can be estimated by calculating the volume of the triangular prism with the width, depth and length of channel measured for the rille. This is given by:

$$\text{Volume} = \frac{\text{Average Width x Average Depth x Length of Channel}}{2}$$

Extracting the appropriate measurements from table 6-2, the volume of the rille as a whole is found to be:

$$\text{Volume} = \frac{1.08 \times 0.251 \times 129.7}{2} = 17.6 \text{ km.}^3$$

The greatest uncertainty is in the value of the average depth. This uncertainty is estimated to be $\pm$ 16% which stands as the uncertainty in the value of the volume.

As a partially independent check on the volume calculation, the volume of channel in the profiled section of the rille was calculated directly from the average channel cross-sectional area. This value compares with the volume calculated for the same section using the triangular approximation as follows:

Method	Profiled Section - Calculated Volume
Triangular approximation of cross-sectional area	6.8 km.^{3}
Cross-sectional area measured on profiles	8.1 km.^{3}

An examination of the profiles (ch. 4) shows that the cross-section is not precisely triangular because of concavity of the rille walls. If it is assumed that the cross-sectional area approximation of the volume in the profiled section is correct and that the triangular approximation yields the same proportionate error in the whole rille calculation as in the profiled section, a corrected whole rille volume may be calculated. This is accomplished by scaling the volume calculated by the triangular method as follows:

$$\text{Volume corrected value} = \frac{8.1 \text{ km.}^3}{6.8 \text{ km.}^3} \text{ values from above check} \times 17.6 \text{ km.}^3 \text{ value from triangular approximation}$$

This increases the calculated rille volume to 20.1 km.^{3}. This volume which just falls within the 16% uncertainty reported above is the best value which can be calculated from the present data.

Summary of basic parameters. Hadley Rille is seen in table 6-2 to be a major land form. It is comparable in width (1 km.) to a large terrestrial river, although its length is shorter than terrestrial rivers of this width. The estimated 20 km.^{3} volume of the channel could be represented by a sphere of 3.4 km. diameter or by a block 50 km. x 50 km. x 10 meters deep. One of the most puzzling aspects of Hadley Rille and lunar rilles in general is the lack of an associated depositional form such as an alluvial fan or flow-lobe representing material removed from the channel.

Derived Parameters:

Using the characteristics reported above as a base, it is possible to derive several other values which also characterize the rille.

Sinuosity. The sinuosity of a river channel is best defined as the length of the talweg divided by the straight line distance between end points (Scheidegger, 1970) . Thus, for the rille the sinuosity is defined:

$$\text{Sinuosity} = \frac{\text{length of channel segment}}{\text{straight line distance between end points}}$$

For purposes of this calculation, both the lengths were calculated from the Mann comparator data (app. 3). The sinuosity for the rille as a whole is 1.68 but the individual values for the northern and southern segments (dividing the rille at point 84, fig. 6-2) are 1.28 and 1.23 respectively. This indicates that the bend at point 84 foreshortens the end-to-end distance and results in an uncharacteristically high overall sinuosity.

Width/depth ratio. An initial attempt was made to compute width to depth ratios for each profile location by using the width and depth data previously described. Finally, it was decided that a more accurate value could be calculated in the following manner:

1. An accurate tracing was made of each profile at the original 2x vertical exaggeration.

2. Each tracing was set up in a level orientation on a drawing board. A 30° triangle was placed over each slope on each profile to

determine the point on the rille wall where the slope angle first exceeded 30° (at 2x vertical exaggeration). This is a point near the rille lip on most profiles.

3. The rille width is then arbitrarily defined as the distance between the two so defined points on each profile, and the depth is the vertical distance from the bottom point on the profile to the line connecting the two points. This construction is illustrated on figure 6-6.

4. The width/depth ratio, correcting for the 2x vertical exaggeration, is found:

$$\frac{\text{Width}}{\text{Depth}} = \frac{\text{Measured width}}{\text{Measured depth}} \times 2$$

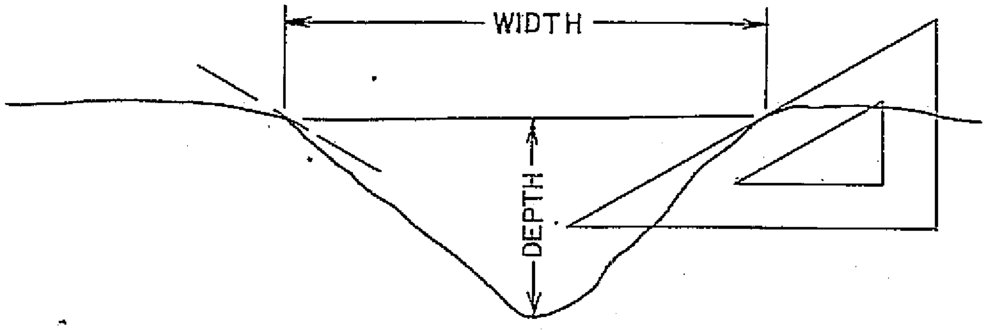

Figure 6-6. Geometric construction used to find width/depth ratio.

The advantage of this method is that whereas the width and depth so defined may be inaccurate, the geometry of the construction indicates that they are inaccurate in proportion. Therefore, the resulting ratio is an adequate characterization. The average ratio is 4.30 with standard deviation 0.44 and standard error 0.09. This indicates the 'true' average value to be in the range 4.30 ± 0.15 at the 90% confidence level. Individual values are listed in appendix three.

The width to depth ratio (with a 2x vertical exaggeration) is numerically equal to twice the cotangent of the depression angle from the rille lip to the bottom. These angles are an approximation of the wall slope angles, although the concave aspect of the profiles makes the maximum slope angles somewhat greater than these. The depression angles are found to range from 19.2° to 28.2°. The angle corresponding to the average width/depth ratio is 22.8°. At a 2x vertical exaggeration, the angles are roughly twice these values so the 30° triangle used as described provides a good definition of the rille lip as illustrated in figure 6-6.

Harmonic analysis. The wave-like character of the sinuous rilles suggests an examination using harmonic analysis. Such an examination has been completed for Hadley Rille using a Fourier cosine series. The purpose of this numerical experiment is:

1. To determine the spectral distribution of the irregular line which represents the rille so that it can be compared to the spectral curve for a terrestrial river.

2. To determine a suitable length to use for the 'meander wave length' of the rille.

The mechanics of this method of function approximation are discussed in chapter three.

Harmonic analysis approximates the rille pattern with a function which is composed of the sum of simple cosine waves of varying frequency and amplitude (Gaskell, 1958) . The rille pattern can be decomposed into its constituent cosine waves by listing the square root of the power spectrum (defined in ch. 3) for the series. In the case of the cosine series, this is merely the absolute value of the Fourier coefficients. Thus, each value in the root power spectrum equals the amplitude of one of the constituent cosine waves. These values can then be examined to determine which particular frequencies are important in the composition of the rille pattern.

It is analytically possible to calculate as many terms for the series as there are data points in the data set. In this case, the shortest wave length examined would be L/n_o where L is twice the length of the rille segment being examined, and n_o is the number of data points.

However, the data set cannot represent oscillations with a wave length similar to the data spacing. This problem is known as aliasing (Blackman and Tukey, 1959) . By limiting the number of terms in the series to $n_o/2$, it is assured that there are at least two data points on each hump of the shortest wave length spectral component being examined. This is the cosine term with wave length equal to $2L/n_o$ which in the case of the rille is about the same as the rille width. Secondly, if the short wave length terms are examined, they are found to have amplitudes less than the resolution of the data. This appears to be true for terms with a wave length shorter than $4L/n_o$. Thus, the spectral analysis has been limited here to the first $n_o/4$ terms since there seems little point in requiring the Fourier analysis to search for components not reliably represented in the data. The shortest wave length (which corresponds to the $n_o/4$th term) is about $2\frac{1}{4}$ kilometers long, or about twice the rille width.

The data set for the harmonic analysis was acquired using the Mann comparator. The method was similar to that described earlier in this chapter with a few important exceptions. The writing of a Fourier series requires data which is equally spaced along the x-axis. Therefore, the x-coordinate of the comparator was incrementally advanced and the associated y-values were read. The value of the x-increment was 0.250 mm. which corresponds to a ground distance of 0.28 km. The Fourier cosine series can only approximate single valued functions. Therefore, it was necessary to use separate data sets for the north and south sections and compute a separate series for each. x and y-values were read for the center of the rille in the north section and both the center and the mare edge were read in the south. Both of the southern sets give substantially the same spectral components. The rille center spectral curve is reported here so that the curves reported for the north and south sections of the rille have a common basis. There were 159 data points in the northern section and 153 points in the south.

The root power spectrum for the two rille sections is listed in appendix three along with other calculated parameters and data for the harmonic analysis. Figure 6-7 is a semi-log graph of the power spectrum as a function of wave number (n) for both rille sections. The graph displays obvious peaks corresponding to the important cosine terms of different wave lengths and there is a good correspondence between the wave lengths of important terms in the two different sections. This correspondence is illustrated in table 6-4 which lists the peak-forming wave lengths for each section of the rille.

Figure 6-8 is a third graph which is the result of the spectral

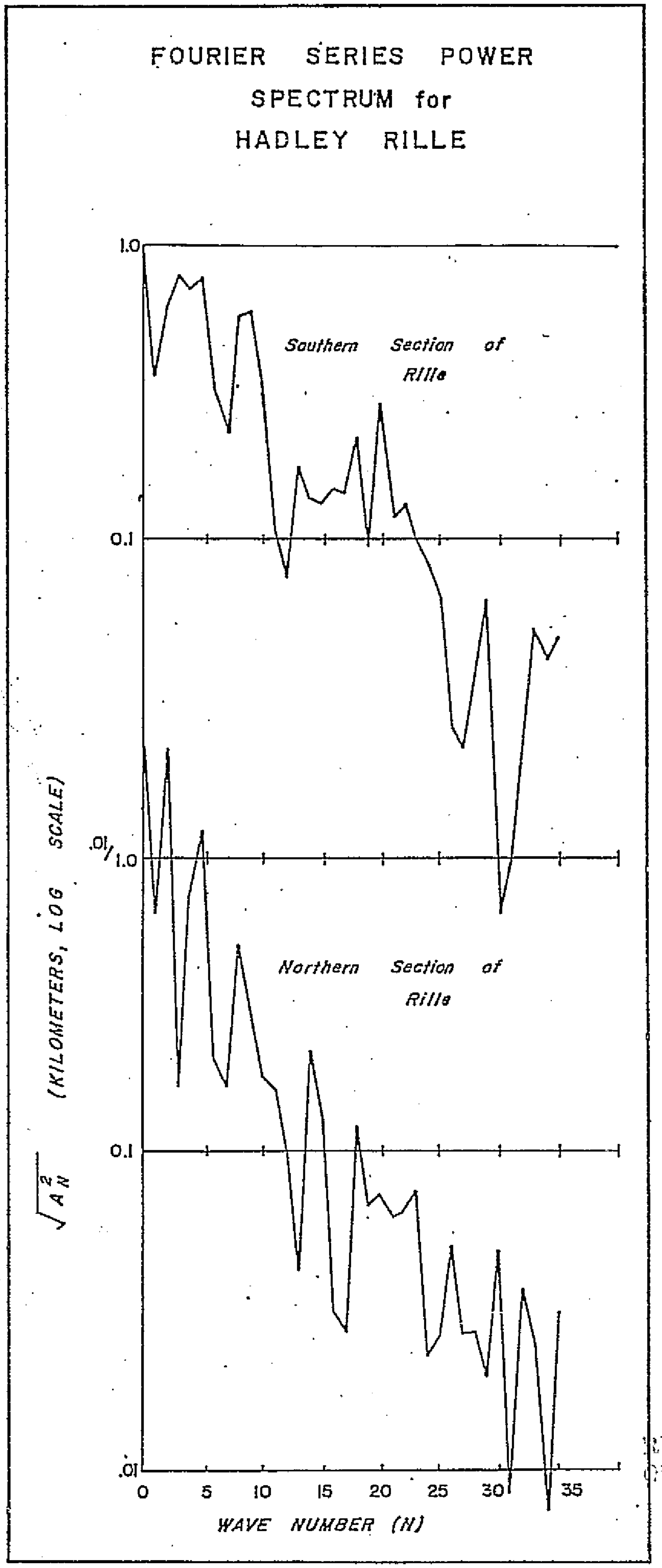
FOURIER SERIES POWER
SPECTRUM for
HADLEY RILLE
Southern Section of
Rille
Northern Section of
Rille
1.0
0.1
.01/1.0
0.1
.01
0
5
10
15
20
25
30
35
WAVE NUMBER (N)
$\sqrt{A_N^2}$ (KILOMETERS, LOG SCALE)

FIG. 6-7

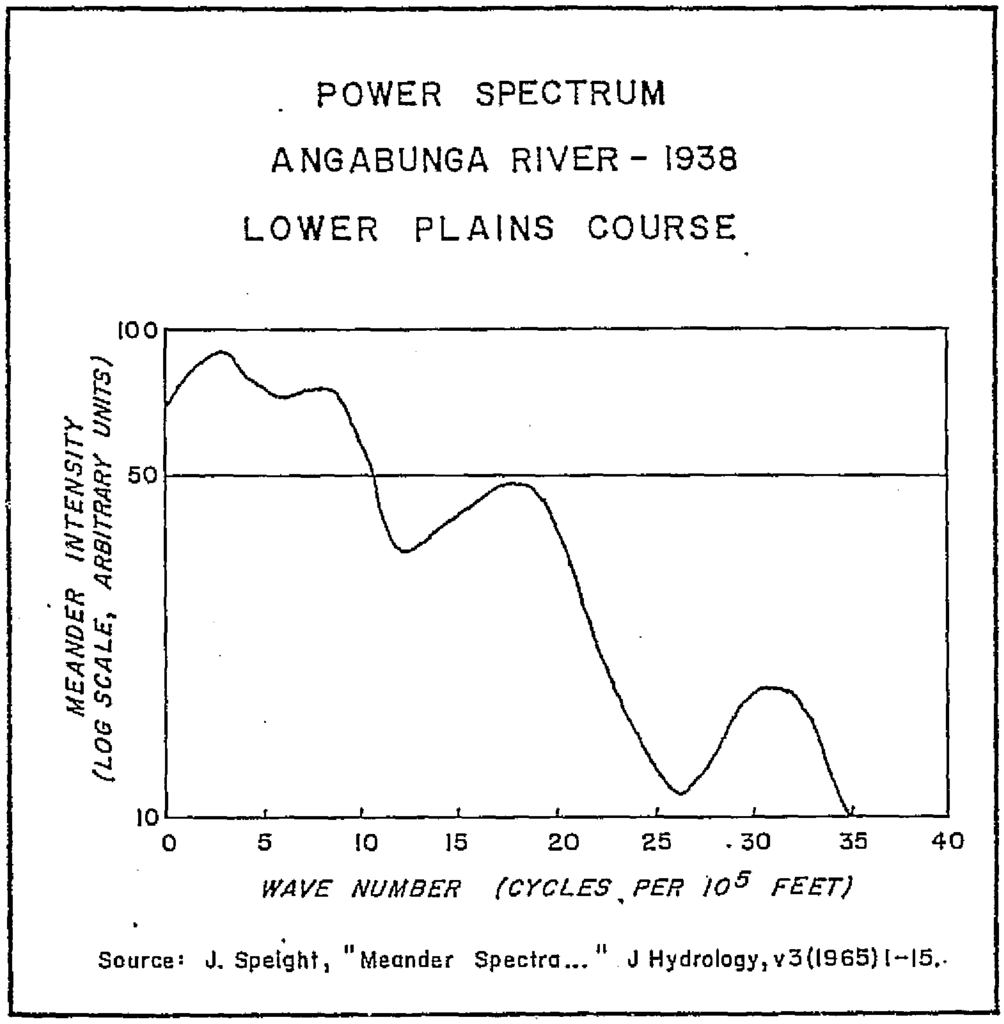

Fig. 6-8. Power spectrum of a terrestrial river.

analysis of a terrestrial river by J. G. Speight (1965) . This is a study of the Angabunga River in the Territory of Papua New Guinea. This particular river "was chosen for study because of its long, unobstructed and undisturbed alluvial plains course and its highly developed, rapidly changing meander pattern" (p. 2). Speight's analysis was carried out by an autocorrelation method (discussed in Scheidegger, 1970) which is different from the approach reported here. The autocorrelation method provides a more accurate spectral curve, particularly at the long wave length end of the spectrum, and gives a much smoother curve. However, it requires larger data sets than are available here, and the measurements are of a much different sort. Because the two methods are significantly different and because all the physical parameters of the two geologic situations are so completely separate, it appears impossible to make a meaningful direct comparison between the two studies. However, certain qualitative similarities can be mentioned.

1. All three spectral curves have several important long wave length peaks. The importance of peaks diminishes rapidly as wave length increases (figs. 6-7 and 6-8).

Table 6-4. Wave numbers with peak-forming spectral intensities. These are peaks which are graphically displayed on figure 6-7. There is a clear similarity between the long wave length intensities.

	Wave Number																													
	1	2	3	4	5	6	7	8	9	10	11	12	13	14	15	16	17	18	19	20	21	22	23	24	25	26	27	28	29	30
South Section Points 1-84, Fig. 6-2			X	X	X			X	X				X					X		X		X						X		
North Section Points 84-152, Fig. 6-2		X		X	X			X						X				X		X			X			X				X

2. The broad, smooth peaks in Speight's curve appear somewhat similar to the broad, irregular peaks from the cosine series. The scaling difficulties make it impossible to postulate a direct peak-to-peak correlation.

Choice of meander wave length. An examination of the metric photography (fig. 4-1) does not allow a satisfactory determination of the 'meander wave length' of the rille. This follows from three factors:

1. The meander wave length of a river is an ill-defined quantity, the value of which has in the past depended upon the observer's subjective interpretation of the river pattern.

2. There is a legitimate question as to whether the rille should be defined as 'meandering' at all because the value of its sinuosity is relatively low. One discussion of a meandering river (Leopold, Wolman and Miller, 1964) seems to suggest that the sinuosity of meandering rivers ought to be greater than 1.5 although some variation about this value is allowed. The sinuosity of the rille as a whole was seen to be well in excess of this (1.63), but the individual north and south sections had values which were substantially less (about 1.25).

3. The northern section of the rille has a pattern which is not smoothly sinuous, perhaps as a result of the structural control discussed in chapter five. Thus, it is not obvious how to include this section in an estimate of the meander wave length. Although the southern section is sinuous, a visual estimate gives between three and five full meander cycles depending on interpretation.

Thus, an examination of the spectral peaks is suggested to objectively find an appropriate meander wave length with a value which fits between three to five cycles in the southern section of the rille. The southern section (as viewed by the harmonic analysis) is 42.6 km. long. This means that spectral components with wave lengths between 8.5 km. ($n = 10$, or 5 cycles in the interval) and 14.2 km. ($n = 6$, or 3 cycles in the interval) must be examined. Table 6-5 lists the wave numbers (n), wave lengths and spectral intensities[1] of all the spectral components with wave lengths in this range. Two possible values for the meander wave length have been estimated by the following methods; the results are in substantial agreement:

1. It is seen that wave numbers 8 and 9 in the southern section and wave number 8 in the northern section have spectral intensities

[1]The value of the root power spectrum corresponding to a given wave length is here called the spectral intensity of the wave length.

about twice as high as the other components in the range. An average of the corresponding three wave length values gives an estimated meander wave length of 10.8 km.

2. A second estimated value has been calculated by weighting each wave length in the range by its spectral intensity and calculating the weighted average. This gives a value of 10.5 km. in close agreement with the simple average above. Both the north and south data sets were used in the weighted average. This average seems to make best use of the data and it is therefore accepted as the meander wave length.

Leopold and Wolman (1960) have investigated the relationship between river meander wave lengths and channel widths and also meander wave lengths and radius of curvature of the meanders. They have reported that the following equations hold for terrestrial stream channels:

$$\text{Meander wave length} = 10.9 \times \text{width}^{1.01}$$

$$\text{Meander wave length} = 4.7 \times (\text{radius of curvature})^{0.98}$$

If these equations are solved using the average rille width (1.08 km.)

Table 6-5. Calculation of meander wave length – weighted average.

	SOUTH SECTION			NORTH SECTION		
Wave Number(n)	Wave length (km.)	Intensity (relative)	Product	Wave length (km.)	Intensity (relative)	Product
6	14.18	32	453.76	Outside range of consideration		
7	12.16	23	279.68	12.64	21	265.44
8	10.64	58	617.12	11.06	63	696.78
9	9.46	60	567.60	9.83	37	363.71
10	8.51	35	297.85	8.85	23	203.55
11	Outside range of consideration			8.04	20	160.80
	Sum	208	2,216.01	Sum	164	1,690.28

Totals for both rille sections:

Total of intensities = 372

Total of products = 3,906.29

$$\text{Weighted average Wave length} = \frac{\text{Product total}}{\text{Intensity total}} = \frac{3,906.29}{372} = 10.5 \text{ km.}$$

and the estimated median radius of curvature (2.02 km., estimated from table 6-3), the calculated meander wave lengths are found to be:

From width equation, wave length = 11.78 km.

From radius equation, wave length = 9.36 km.

Both these values seem remarkably close to the rille value of 10.5 km. and are well within the spread of the data reported by Leopold and Wolman (1960) .

<u>Hadley Rille compared to other lunar rilles</u>. It is now possible to compare the overall characteristics of Hadley Rille with other lunar rilles. Schubert, Lingenfelter and Peale (1970)[2] have published histograms of length, width, width/length ratio, meander wave length and meander wave length/width ratio based on a sample of about 130 rilles. In order that Hadley Rille can be best compared with other rilles, these diagrams have been recast as cumulative frequency diagrams. The position of Hadley Rille was then plotted on each. This allows the position of Hadley Rille relative to other rilles to be easily examined. The five cumulative frequency diagrams

are shown in figures 6-9 to 6-13. The following observations can be made:

1. The width and length of Hadley Rille are exceeded by only about 16% of the rilles so it is a relatively large rille.

2. Its width/length ratio falls close to the median value, so the rille is 'average' in this sense.

3. Its meander wave length is longer than any found in the Shubert et al. (1970)[1] report in which a maximum meander wave length of 7 km. is mentioned. The meander wave length/width ratio is also an extreme value.

Thus, the meander wave length of this rille appears to be an anomolous characteristic in comparison with other rilles.

Relationships Between Rille Parameters:

Thus far, the gross numerical characteristics of the rille have been investigated. The remainder of this chapter is devoted to describing several relationships which appear to exist between parameters.

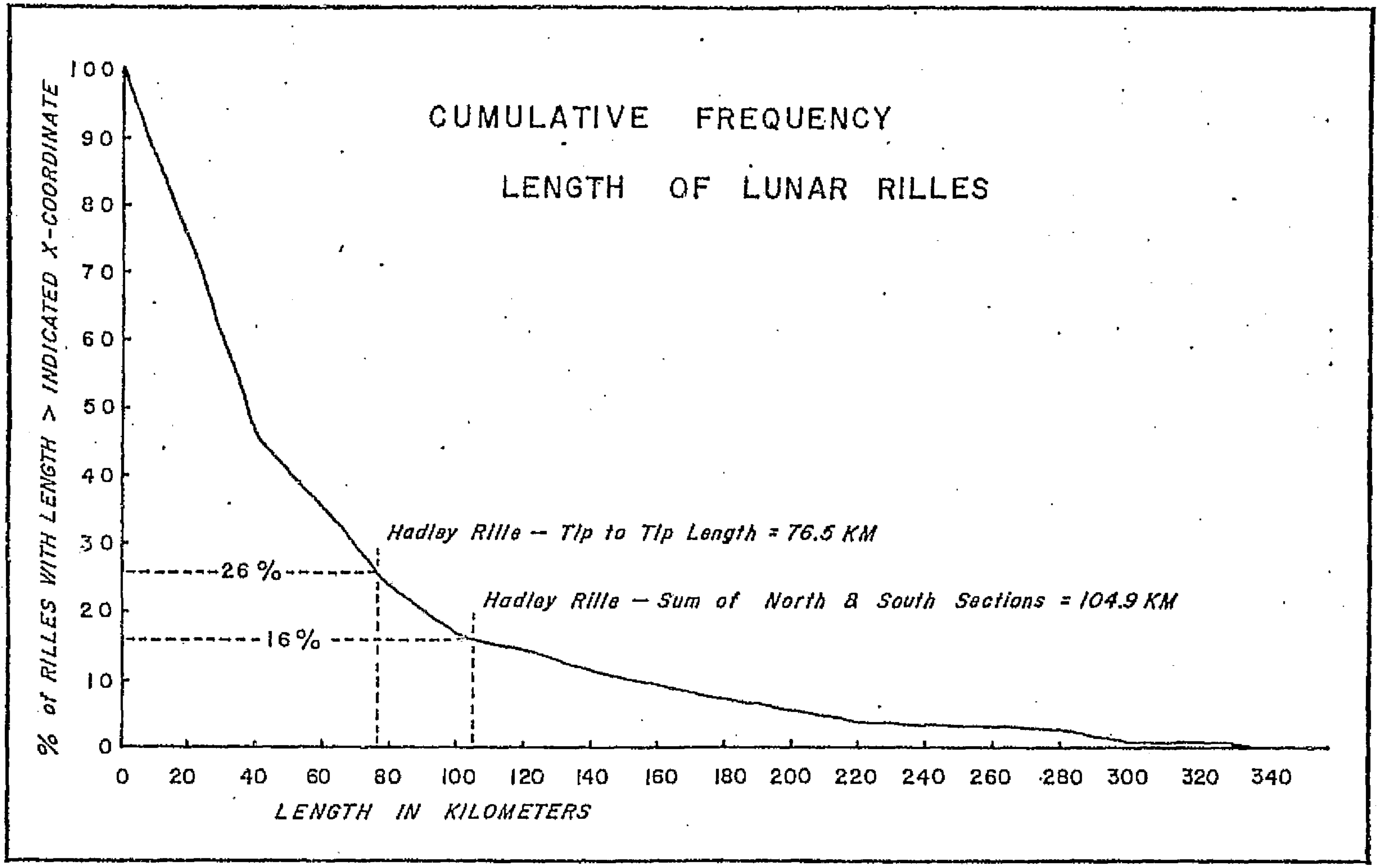

CUMULATIVE FREQUENCY
LENGTH OF LUNAR RILLES
% of RILLES WITH LENGTH > INDICATED X-COORDINATE
100
90
80
70
60
50
40
30
20
10
0
Hadley Rille — Tip to Tip Length = 76.5 KM
Hadley Rille — Sum of North & South Sections = 104.9 KM
26 %
16 %
0 20 40 60 80 100 120 140 160 180 200 220 240 260 280 300 320 340
LENGTH IN KILOMETERS

FIG. 6-9

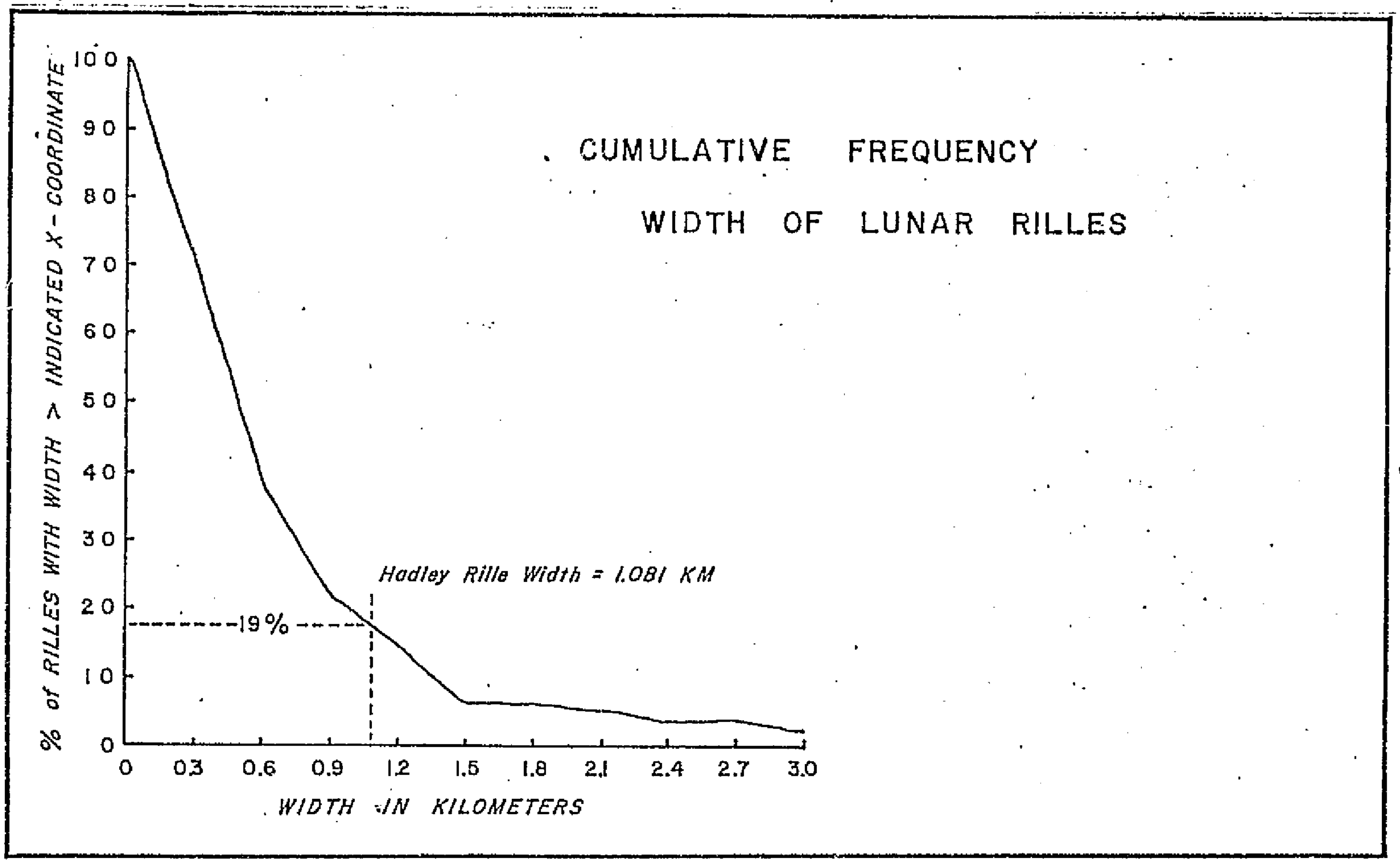
CUMULATIVE FREQUENCY
WIDTH OF LUNAR RILLES
% of RILLES WITH WIDTH > INDICATED X-COORDINATE
100
90
80
70
60
50
40
30
20
10
0
Hadley Rille Width = 1.081 KM
19%
0
0.3
0.6
0.9
1.2
1.5
1.8
2.1
2.4
2.7
3.0
WIDTH IN KILOMETERS

FIG. 6-10

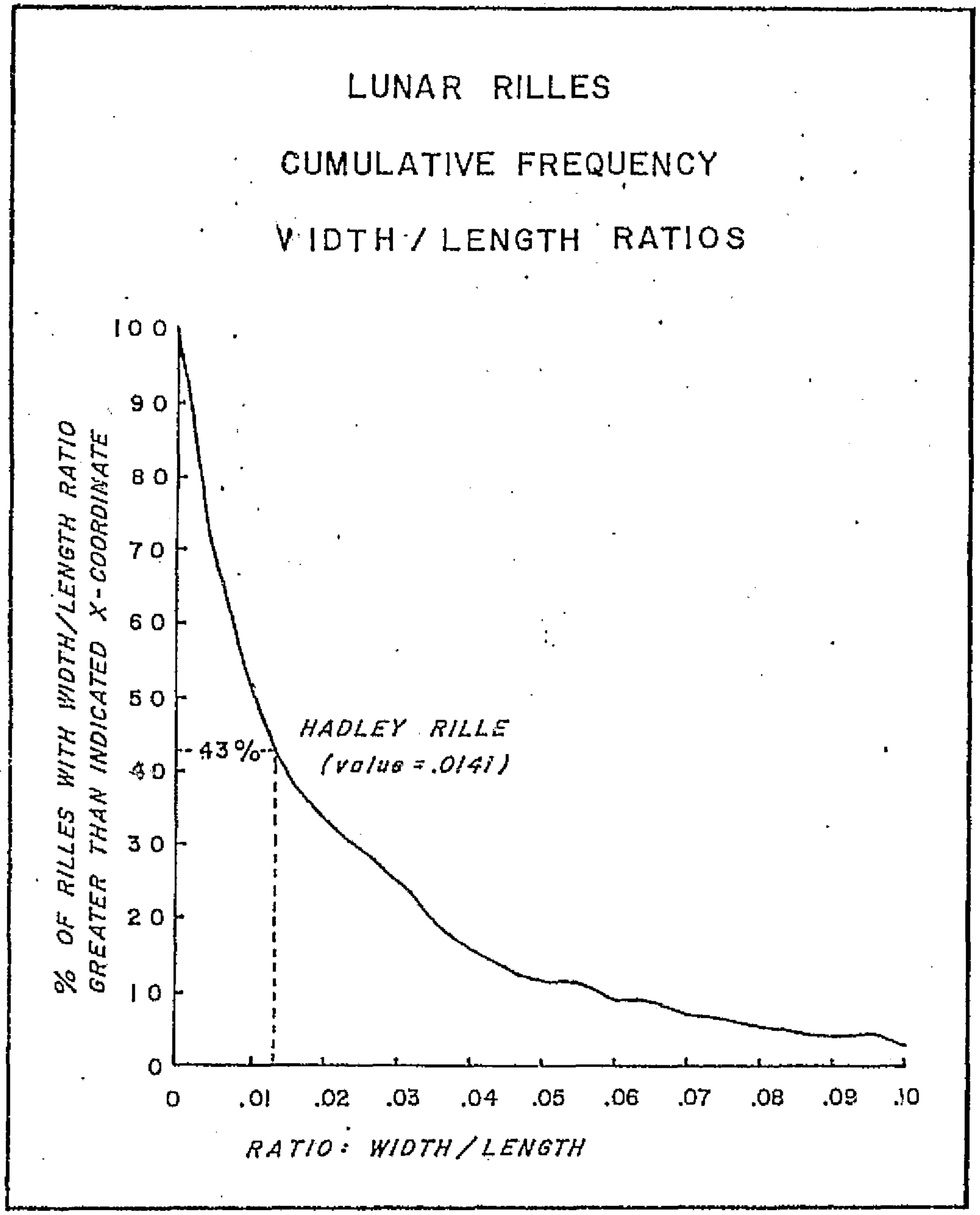
LUNAR RILLES
CUMULATIVE FREQUENCY
VIDTH / LENGTH RATIOS
% OF RILLES WITH WIDTH/LENGTH RATIO GREATER THAN INDICATED X-COORDINATE
100
90
80
70
60
50
40
30
20
10
0
43%
HADLEY RILLE
(value = .0141)
0
.01
.02
.03
.04
.05
.06
.07
.08
.09
.10
RATIO: WIDTH/LENGTH

FIG. 6 – 11

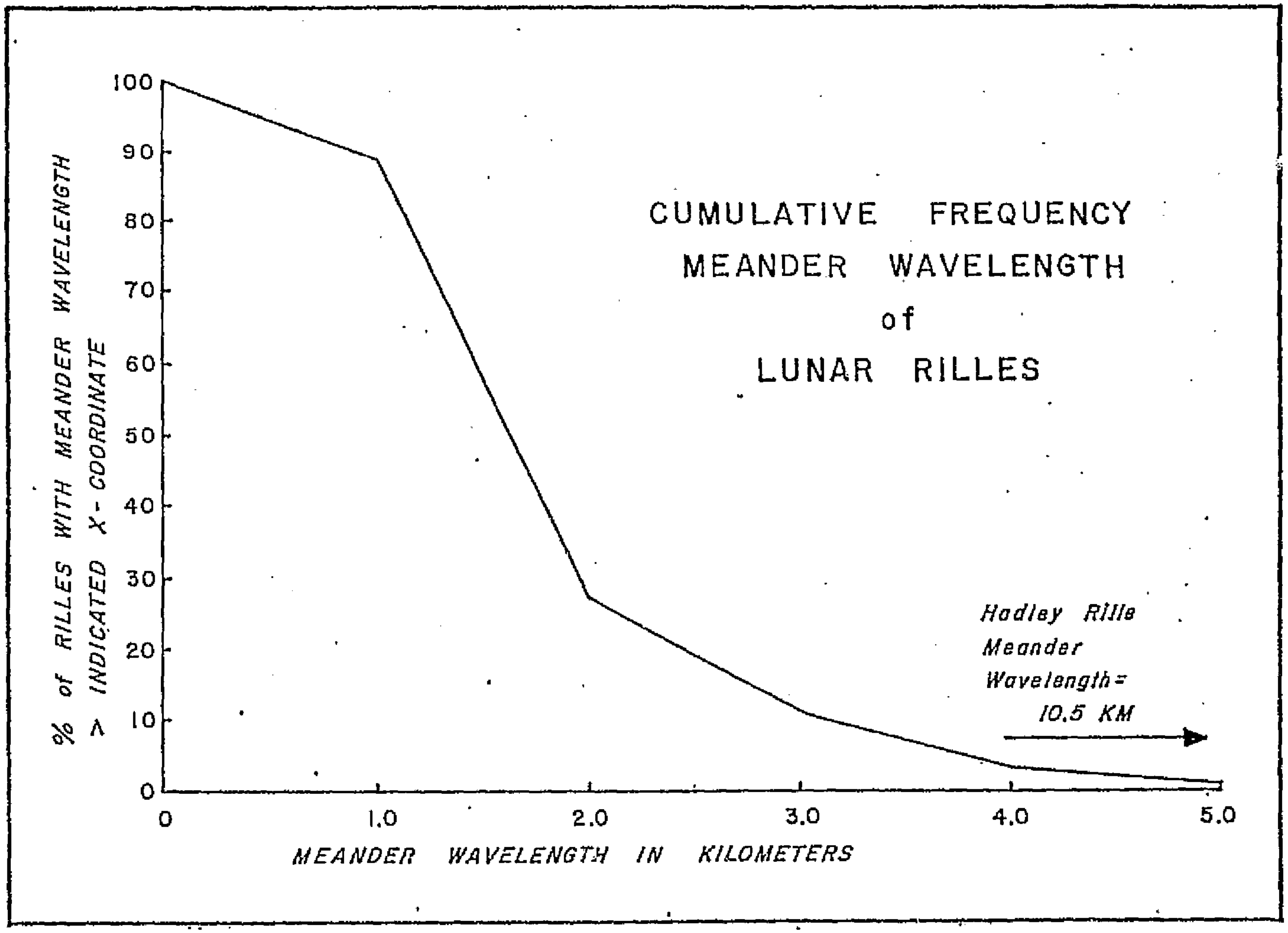
CUMULATIVE FREQUENCY
MEANDER WAVELENGTH
of
LUNAR RILLES
% of RILLES WITH MEANDER WAVELENGTH
> INDICATED X - COORDINATE
MEANDER WAVELENGTH IN KILOMETERS
Hadley Rille
Meander
Wavelength =
10.5 KM
100
90
80
70
60
50
40
30
20
10
0
0
1.0
2.0
3.0
4.0
5.0

FIG. 6 – 12

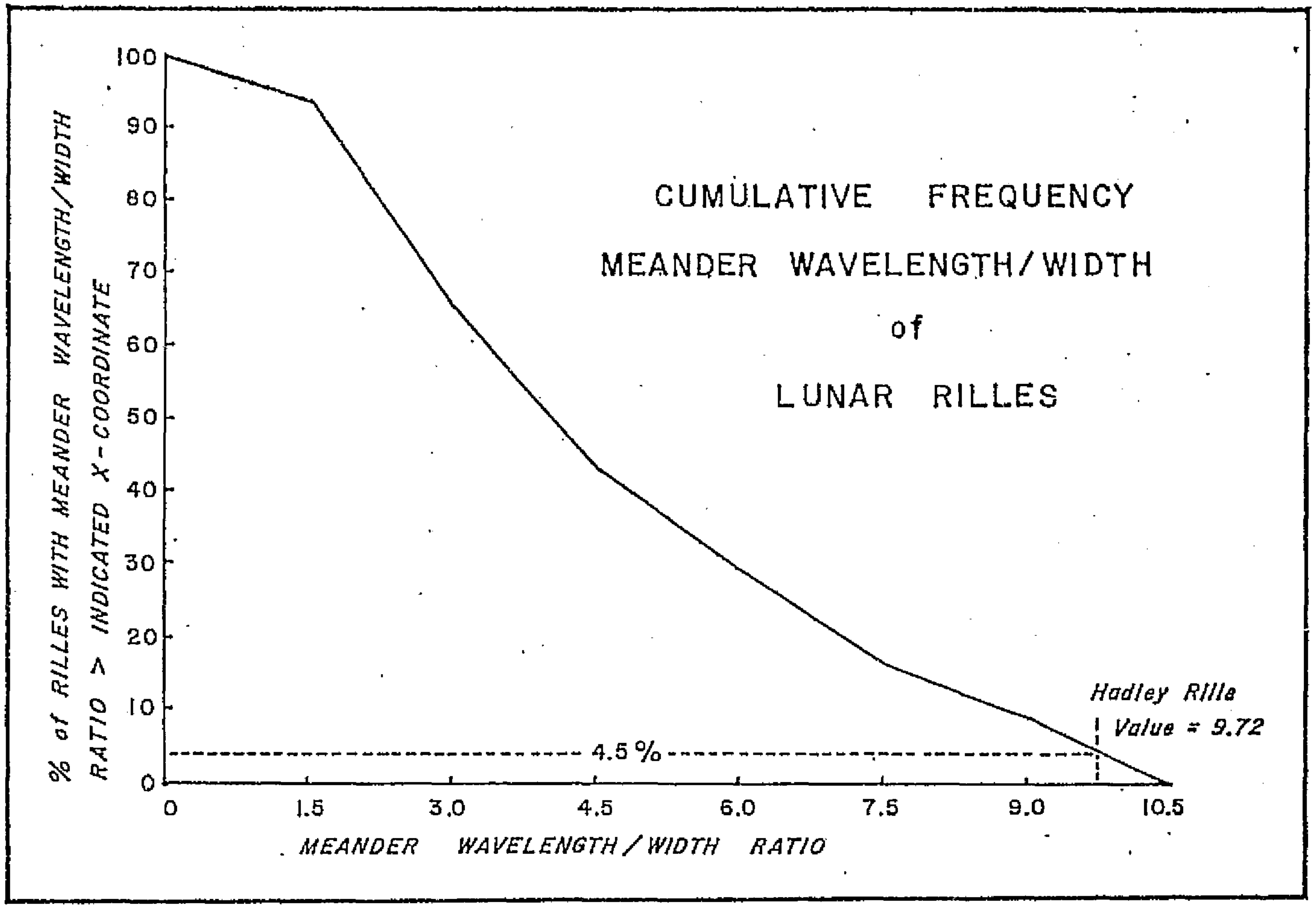
CUMULATIVE FREQUENCY
MEANDER WAVELENGTH/WIDTH
of
LUNAR RILLES
% of RILLES WITH MEANDER WAVELENGTH/WIDTH
RATIO > INDICATED X-COORDINATE
MEANDER WAVELENGTH/WIDTH RATIO
Hadley Rille
Value = 9.72
4.5 %
100
90
80
70
60
50
40
30
20
10
0
0
1.5
3.0
4.5
6.0
7.5
9.0
10.5

FIG. 6-13

Relation between width of rille and distance along channel. Figure 6-4 is a graph of the rille width as a function of distance along the channel. It is based on the same data set that was used to determine the average width of the rille. It is reasonably evident on this figure that rille width is a northward, decreasing function of length along the channel. For example, if one chooses the maximum and minimum peaks in 15 kilometer segments of the rille, these seem to diminish systematically between one 15 kilometer segment and the adjacent one to the north. This rule holds except for the northwestern 15 kilometers of the rille where the width appears to increase again.

In order to statistically test the conclusion that such a width decrease exists, the following experiment was performed: 38 pairs of 3-digit, random numbers were drawn from a random number table (Koch and Link, 1970) . These were multiplied by a scale factor to give new figures which could be used as distances along the rille channel with which to enter the width distance graph. In this manner, randomly selected pairs of widths were located on the width distance graph, and it was noted if the northernmost width or the southernmost width was the largest. In 38 trials, the southern width was the largest in 28 trials while the northern width was largest in only 10 trials. By application of the 50% probability test (Langley, 1970) , it is found that this outcome could occur less than 1% of the time if there is an equal probability of the largest value occurring to the north. Therefore, it is concluded that there is a well-displayed and statistically significant tendency for the rille width to decrease to the north.

The general aspect of the width-length curve (fig. 6-4) appears similar to the tooth pattern of a carpenter's rip saw which has an abrupt increase in amplitude followed by a gradual decrease and then another abrupt increase. In the case of the rille pattern, the abrupt increases appear to take place about every 15 kilometers. In order to indicate this sort of asymmetry, the program which resolved the width data included a segment which summed:

1. The length of channel along which a north-bound observer would note increasing width.

2. The length of channel along which a north-bound observer would note decreasing width.

3. The length along which no measurable change (according to the data) takes place.

The results of these calculations for the rille as a whole are as follows:

1. Width increases northward for 54.1 km.

2. Width decreases northward for 74.9 km.

3. No change occurs for 0.7 km. (considered negligible)

The ratio of the first two parameters is found:

$$\frac{\text{Length along which northward decrease occurs}}{\text{Length along which northward increase occurs}} = 1.38$$

In addition to the calculation for the whole rille, this ratio was calculated for several sub-sections of the rille with the results indicated in table 6-6.

Table 6-6. Ratio of length of channel showing width increase to the length showing width decrease as viewed by a north-bound observer in the rille. Point location numbers in the last column correspond to figure 6-2.

Between points	Ratio
1-152	1.38
1-84	1.81
84-152	1.09
1-108	1.65
108-152	1.05
1-124	1.94
124-152	0.42

Thus, it is seen that the described asymmetry is evidently quite characteristic of the southern 100 kilometers of the rille, but may not be characteristic of the northern 28 kilometers.

In order to assure that the observed ratios were not the result of the fortuitous selection of the end points, another experiment was performed. In this experiment, twenty segments, each of 15 kilometers length were selected using random numbers, and the ratio described above was calculated for each segment. Some statistics of the results follow:

Arithmetic average ratio	(m)	– 1.63
Standard deviation	(s)	– 0.78
Standard error	(s/n)	– 0.175 (n = number of data points)

By computing the t-statistic, the probability that the 'true' average value of this ratio might be less than any specified value (M) can be assessed. If the true value has a significant probability of being less than 1., the supposed rip-saw appearance of the curve cannot be assumed. The t-statistic is computed from the preliminary statistics as follows:

$$t = \frac{n \times M - m}{s} = \frac{20 \times 1 - 1.63}{0.78} = 3.61$$

Comparing this value with those in a table of t-statistics (Crow et al., 1970) , the probability that the ratio is less or equal to 1. i.

seen to be less than 0.2%. Therefore, there is a high probability that the average is greater than 1., and the asymmetry described above is assumed to be characteristic of the rille.

In order to informally illustrate the cyclic behavior of the width-length data set, a smoothed curve (fig. 6-14) of width vs. location number was generated using Spencer's formula (described in ch. 3 and ch. 5). It was not possible to plot a width-distance curve (that is, a smoothed version of fig. 6-4) using this method because Spencer's formula requires data which is equally spaced along one axis. Therefore, ground distance has been approximated by measurement location number to provide equally spaced data for the horizontal axis of the smoothed curve (fig. 6-14). Spencer's formula uses ten data points at either end of the data set which are not reproduced on the smoothed curve (discussed in ch. 3). This explains why there are only 132 data points present on the smoothed curve (fig. 6-14) compared to the 152 points present in the original data set and on figure 6-4.

Six peaks appear on the smoothed curve and they are remarkably evenly spaced. The smoothed curve gives a good impression of the general decrease of width with distance northward along the rille, and of the rip-saw pattern described above.

<u>Relationship between width and depth</u>. The relationship between width and depth of Hadley Rille has been studied graphically by Howard

C-3

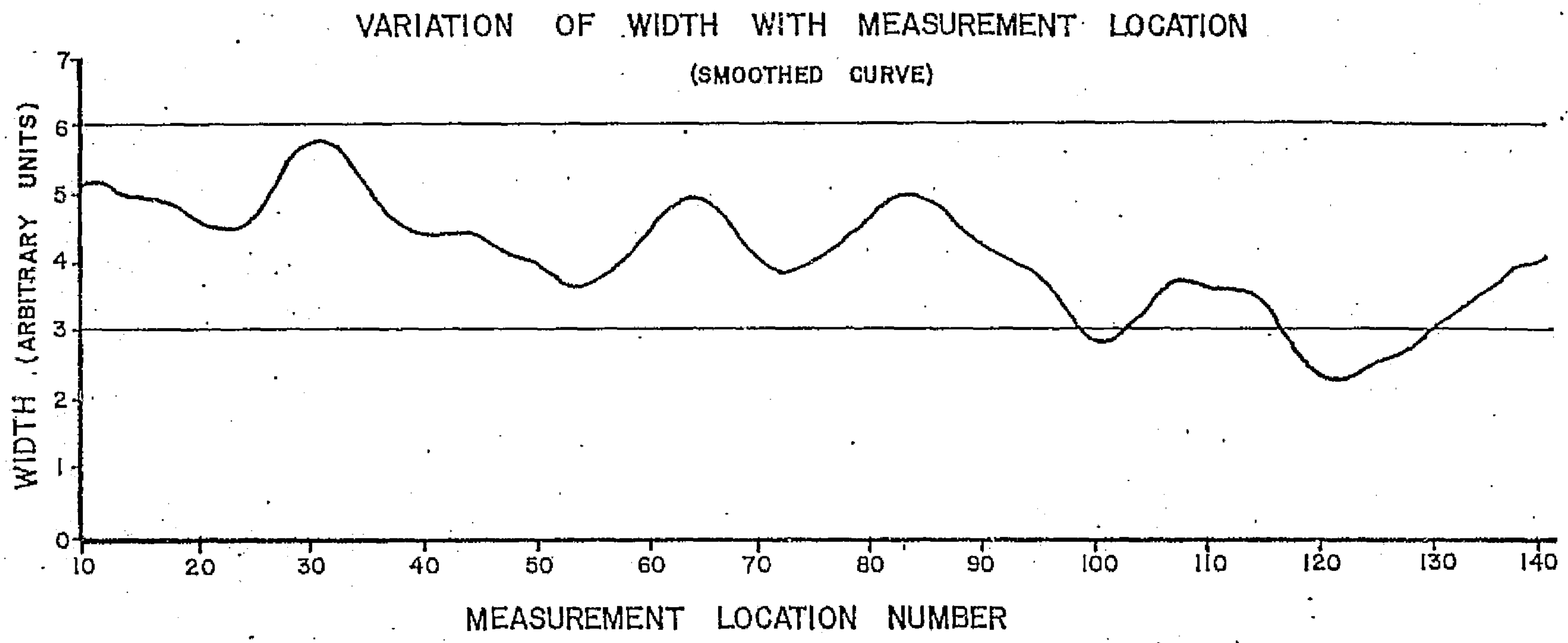

Fig. 6-14 Graph: width of rille vs. measurement location number smoothed by Spencer's formula.

et al. (1972). They conclude that width and depth are directly correlated from measurements taken from a central segment of the rille near the Apollo-15 landing site. The length of channel which they examined was 41.9 km. A similar study has been completed here using the width and depth measurements taken to compute the width/depth ratio.

Figure 6-15 is a graph of rille depth vs. rille width for 24 profile locations (profile numbers 1-24 excluding number 9 which is in a location obscured by crater, Hadley C). There is an obvious tendency for depth to increase with width. In order to check this relationship statistically, a rank correlation test (discussed in ch. 5) was performed on this data. The sum of the squared rank differences for the 24 data points was 604. Check of a squared-difference table (Langley, 1971) indicates correlation at better than the 1% level in agreement with Howard's study. The high degree of correlation indicates that when other factors show a relationship with rille width, they also probably show a similar relationship with rille depth.

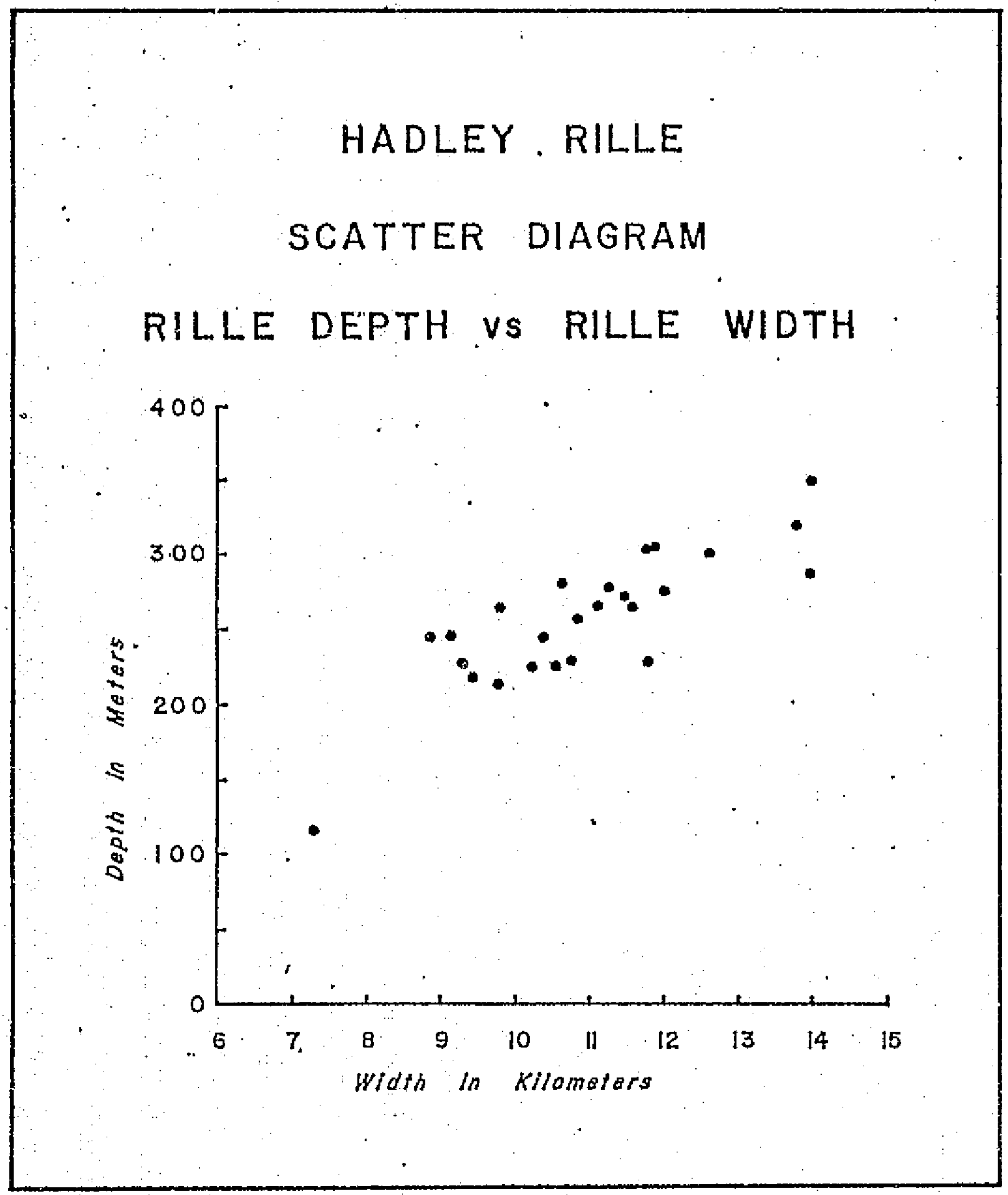

Fig. 6-15. Scatter diagram of rille depth vs. rille width at a location. Data from profiles, ch. 4.

Relationship between rille width and direction of channel. In order to investigate a possible relationship between the width of Hadley Rille and the direction of its channel, figure 6-16 was prepared. The widths on this scatter diagram are those calculated for the width-distance graph (fig. 6-4). The azimuths used here were measured directly from figure 6-2 using a K&E drafting machine. The straight edge of the drafting machine was placed tangent to the curve of the rille at each of the width locations, and the channel azimuth relative to north was read directly on the machine's protractor head. The azimuth readings thus obtained are probably correct within $\pm 3^{\circ}$ except in small radius corners where the location of the tangent is difficult to define. In these places, the values are probably $\pm 10^{\circ}$. The compilation of this set of azimuths was necessary to find the channel direction at each measurement location. This is a different value than those calculated from one location to the next and used for structural interpretation in chapter five.

The disperse appearance of the scatter diagram (fig. 6-16) indicates that no correlation is present between rille width and channel azimuth for the rille as a whole. However, there are several sequences of points along the channel which do seem to demonstrate an inverse correlation between increasing azimuth and channel width. These points have been replotted on figure 6-17. These sequences were selected after searching for related sequences of figure 6-16. In order to check for correlation, the Spearman rank correlation test (discussed in ch. 5) was applied with the following results:

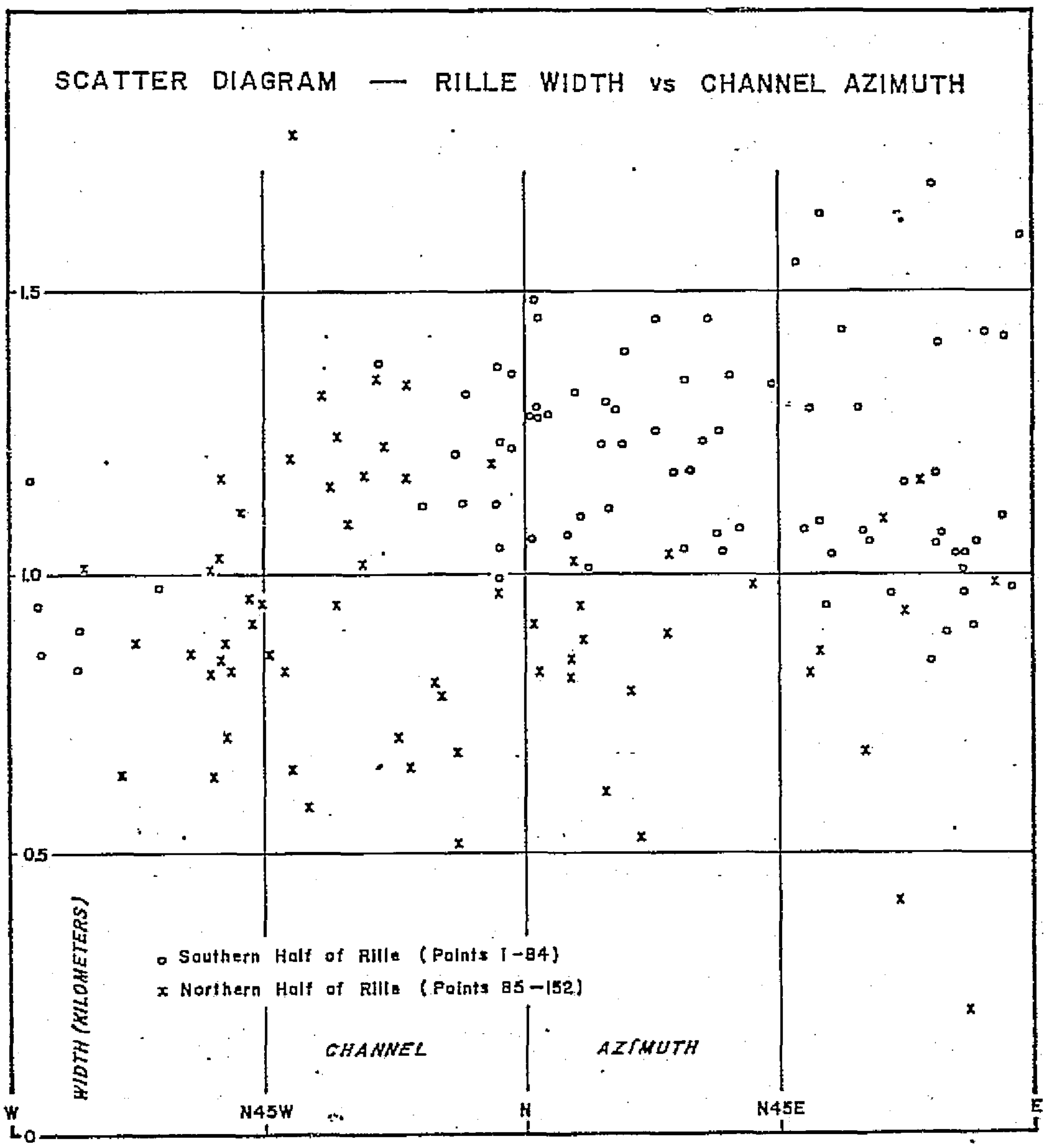

Fig. 6-16. Scatter diagram of rille width vs. azimuth of channel at the width measurement location. This diagram is for all the Mann comparator data locations, fig. 6-2.

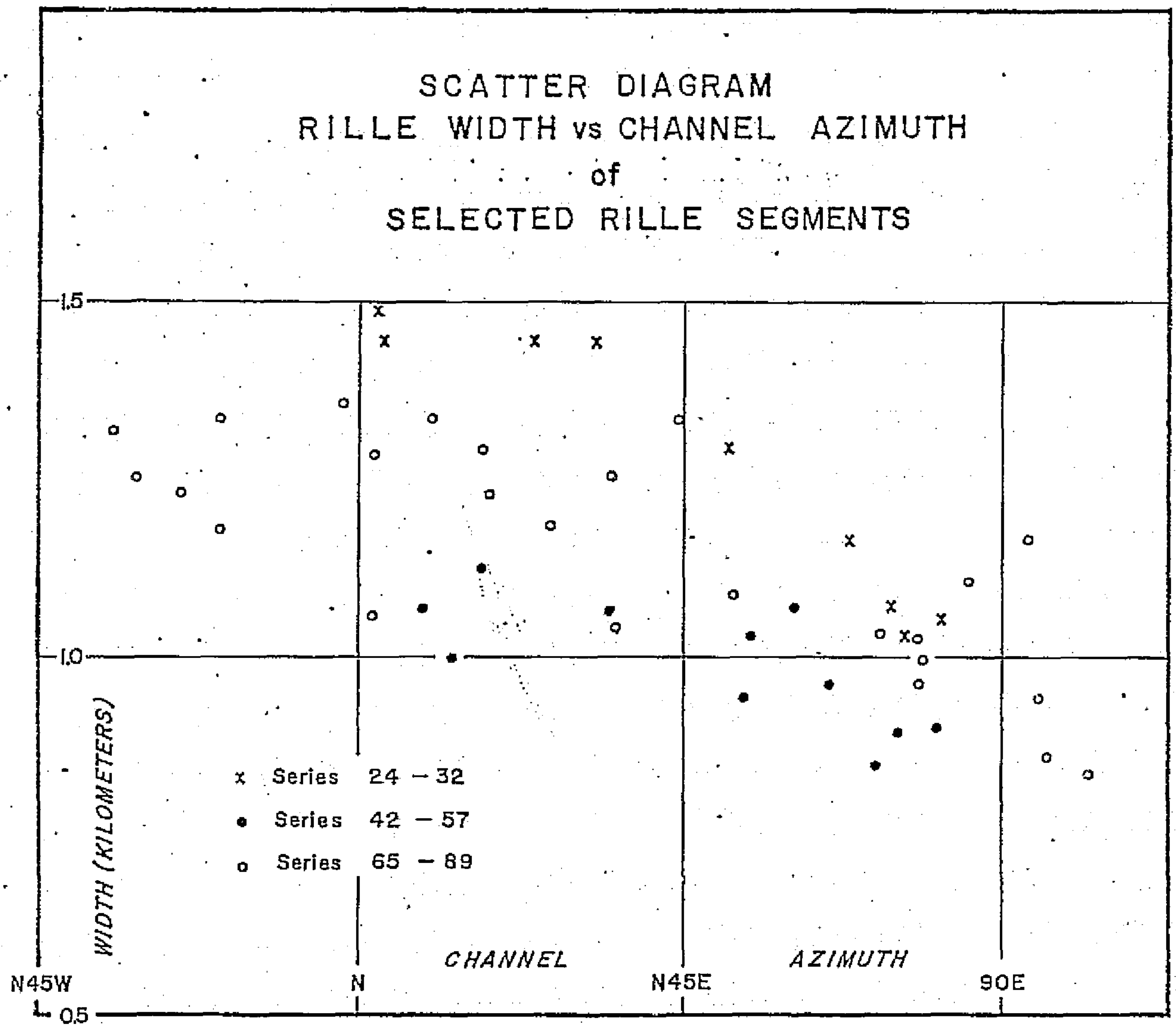

Fig. 6-17. Scatter diagram of rille width vs. azimuth of channel for selected rille segments. The specific locations of the three series which are plotted above can be determined from fig. 6-2.

Sequence (location numbers, Fig. 6-2)	Result
24-32	The probability of finding this sequence in a set of unrelated figures is between 1% and 5%. Therefore, the result is probably significant.
65-89 also 47-62	The probability of finding this sequence in a set of unrelated figures is less than 1%. Therefore, the results are statistically significant.

Two other sets of numbers were checked for correlation, one chosen from the scatter diagram and one selected at random. These results are as follows:

Sequence	Result
13-22	This set is a set of 10 points selected at random. The probability of finding this sequence in a set of pairs of unrelated figures is greater than 10%; therefore, the result is statistically insignificant.
118-143	This set was chosen from examination of the scatter diagram as a group which has a possible direct correlation. The probability of finding this sequence in a set of unrelated figures is greater than 10%; therefore, the result is statistically insignificant.

Several observations can be made concerning these apparent relationships:

1. All the statistically significant sequences occur in the southern part of the rille. The general appearance of the rille in the south is much sharper and well defined than the northern section. The general appearance of the north section suggests that it has been filled either as the final event in the rille formation, or in some subsequent event. Either occurrence would probably obliterate any pre-existing

width-azimuth relationship.

2. The three sequences of points over which these correlations hold all encompass at least one curve in the rille (fig. 6-2) and each sequence contains a local maximum and minimum point on the width-distance curve (fig. 6-4). Thus, a wide range of widths and azimuths are present in these figures.

3. The sequence of locations 65-89 occurs in a segment of the rille which contains four separate curves and which contains two local maxima and one minimum point on the width distance curve. This 15-kilometer segment of rille channel is also in the section of the rille with the best preserved appearance. Thus, the excellent correlation obtained here is the most significant of the three.

Relationship between width and curvature. A number of attempts to relate width and curvature at a point in the rille were undertaken with no positive result. Finally, a graph representing the curvature class at each point was added to the width distance graph (fig. 6-4) to display any possible relationship. It is reasonably apparent on this figure that there is no direct correlation at a point. The two graphs were then examined for correspondence in shape rather than for corresponding peaks. It appeared possible that a less obvious similarity does exist. This is the possibility that slopes of the two graphs correspond in sign but that slopes on the width graph are displaced about two kilometers to the north along the rille from the corresponding slopes on the curvature graph.

In order to test such a relationship, the following approach was devised. Approximately 100 random numbers were extracted from a random number table (Koch and Link, 1970) . These were multiplied by an appropriate constant to yield a number which could be used to enter the curvature-distance graph at a point between the south end of the graph and a point two kilometers short of the extreme northern end of the graph. The sign (positive, negative or zero) of the slope of the curvature-distance graph was noted. The sign of the slope of the width-distance graph at a point two kilometers north along the rille was similarly noted. The signs of the slopes of the two curves must match in one of the three following ways:

1. Both slopes could have a similar sign.

2. Both slopes could have opposite sign.

3. The result is indeterminate if one slope has a zero slope or if the randomly chosen ordinate occurs at a break in one of the curves.

The results of this experiment were treated using the 50% probability test. This test assumes that there is an equal probability of observing either similar or dissimilar signs in the parent population from which the sample was drawn and calculates the probability of finding the observed numbers if the assumption is true. If the test yields a low probability, it is an indication that width and curvature tend to increase together with a two kilometer offset along the rille. In performing this test, it is acceptable to discard data falling into the third category; the rationale behind this and behind the test as a whole is discussed in a book by Langley (1971). The test has yielded the following result:

Number of matched signs	Number of opposite signs	Total
37	21	62

The probability of this result is between 1% and 5% so in a statistical sense, the proposed relationship is probably significant.

From a physical point of view, this result may be important. A relationship between channel geometry at one channel location and the geometry at a location displaced along the channel suggests flow in the rille as a causual mechanism.

Summary:

The numerical and statistical characteristics of Hadley Rille have been explored in this chapter in some detail. For the most part, the results in this chapter have been left as numbers which characterize the rille without further discussion. The conclusions which can be drawn from these results and the results of chapters four and five are the subject of chapter seven.

CHAPTER VII

THE ORIGIN OF HADLEY RILLE

This chapter is a discussion of the origin of Hadley Rille. The first section is a review of mechanisms which have been proposed for rille formation. This is followed by a summary of the primary objections to each, both in general terms and with regard to the characteristics of Hadley Rille. Finally, a mode of origin is proposed for Hadley Rille which appears to conform well with the observations carried out in this study.

Review of Rille Forming Mechanisms:

Mechanisms dependent on geologic structure. Structurally dependent hypotheses for rille formation fall into two groups. One group supposes that the rille are actual structural features and the second requires the presence of an underlying fracture system.

Elger (1895)[1] and Goodacre (1931)[2] suggested that all lunar rilles (not only the sinuous rilles) are shrinkage cracks associated

[1]Elger, T. G. (1895) The Moon, George Phillips & Son, London.

[2]Goodacre, W. (1931) The Moon With a Description of Its Surface Formations, Pardy & Son, Bornemouth, England.

with the cooling of lava. Nasmyth and Carpenter (1874)[1] performed an interesting set of experiments with hollow glass spheres and concluded that all lunar rilles are tension fractures from internal pressures. Shaler (1903)[2] concluded that all lunar rilles are tectonic and not of fluid flow origin. These authors do not specifically mention sinuous rilles, and it is not clear if they were aware of them. Fielder (1960)[3] suggested that the straight lunar rilles are faults which have been subsequently intruded by dikes. The intrusion is assumed to be accompanied by the formation of a depression over the dike due to tension and thinning in overlying material. Quaide (1965)[4] suggested that the sinuous rilles are sinuous tension fractures, although in subsequent articles (below) he has abandoned this view.

Schumm (1970)[5], prompted by Mills' (1969)[6] experiments and several

[1]Nasmyth, J. and Carpenter, J. (1874) The Moon Considered as a Planet, a World and a Satellite, 2nd ed., John Murrary, London.

[2]Shaler, N. S. (1903) A Comparison of the Features of the Earth and Moon: Smithsonian contributions to knowledge, Vol. XXXIV, Washington.

[3]Fielder, G. (1960) A theory of the origin of lunar rilles: Sky and Telescope, Vol. 19, p. 334-337.

[4]Quaide, W. (1965) Ridges, rilles and domes, clues to maria history: Icarus, Vol. 4, p. 374.

[5]Schumm, S. A. (1970) Experimental studies on the formation of lunar surface features by fluidization: G.S.A. Bull, Vol. 81, p. 2539.

[6]Mills, A. A. (1969) Fluidization phenomena and possible implications for the origin of lunar craters: Nature, Vol. 224, p. 863-866.

earlier investigations, performed a series of experiments exploring the behavior of powdered materials when they are fluidized by gas emitted from a sub-surface slit. Based on these studies, he postulated that sinuous rilles could be formed by gases passing up fractures in the lunar crust through a mantle of regolith. This view is supported by McCall (1970)[1] who bases his arguments on field examination of terrestrial volcanic blow holes. It is also probably supported by Hapke and Greenspan (1970)[2] who have observed anomolously high crater densities in the bottoms of some rilles.

Mechanisms which require fluid motion. The remaining hypotheses all depend on fluid flow. The difference between different proposals depends on the nature of the fluid, its source, and precisely how it flows.

A. Ash flow. Cameron (1964)[3] proposed that the fluid medium is a fluidized ash in the form of a nuée ardente. She based this conclusion on a comparison of telescopic photos of rilles with nuée ardente channels formed on earth.

[1]McCall, G. J. H. (1970) Lunar rilles and a possible terrestrial analogue: Nature, Vol. 225, p. 714.

[2]Hapke, B. and Greenspan, B. (1970) Crater densities in the vicinity of lunar sinuous rilles: EOS 51, p. 346.

[3]Cameron, W. S. (1964) An interpretation of Schroeter's Valley and other sinuous rilles: J.G.R., Vol. 69, p. 2423.

B. Water. Some older studies concluded that rilles are fluvial erosion channels. Pickering (1903)[1], who is credited with the discovery of the sinuous rilles, felt that they are drainage channels from hot springs associated with volcanic activity. He also suggested the presence of ice and snow on the moon although he realized that the lunar atmospheric pressure is near zero. Pickering was preceded by Neison (1876)[2] who did not recognize sinuous rilles, but felt that all lunar rilles are abandoned river valleys. One modern selenologist (Gilvarry, 1969)[3] has steadfastly believed in the presence of an ancient hydrosphere with a depth of up to two miles, but has argued that lunar hydraulic channels would be very shallow. This conclusion is based on a dimensional analysis of terrestrial hydraulic geometry to determine the effect of the lower lunar gravity on channel form.

Although the past existence of lunar surface water is presently viewed as improbable by most selenologists, a number of recent arguments are based on surface or near-surface ice. Urey (1967)[4] suggests

[1]Pickering, W. H. (1903) The Moon, Doubleday Page & Co., New York.

[2]Neison, E. (1876) The Moon and the Condition and Configuration of its Surface, Longmans, Green & Co., London.

[3]Gilvarry, J. J. (1969) Geometric and physical scaling of river dimensions on the earth and moon: Nature, Vol. 221, p. 533.

[4]Urey, H. C. (1967) Water on the moon: Nature, Vol. 216, p. 1094.

that the lunar maria are underlain by ice and that the rilles were eroded by ice streams. This idea may be based on the suggestion by Gold (1961)[1] that if water was initially present on the moon, a permafrost layer must now exist at depth. Smoluchowski (1968)[2] performed detailed calculations to show that water could be retained on Mars, even at low atmospheric pressure, because a protective ice cover would form on the surface. This possibility was extended to the lunar environment by Shubert, Lingenfelter and Peale (1970)[3] who calculated that sublimation of the lunar ice would cease after a sufficiently thick accumulation of rock debris collected on the ice surface. They concluded that the rilles were formed when an impact event shattered the ice layer and underlying water flowed to the surface. The water then was supposed to have flowed in an ice-capped stream to form the rille. These authors have also performed calculations to indicate that a reasonable amount of water could erode a rille-size channel in a reasonable amount of time. In terms of analytical justification, Shubert's paper is one of the most persuasive to date.

C. Lava. Another group of recent hypotheses are based on lava

[1]Gold, T. (1961) Permafrost on the moon: J.G.R., Vol. 66, p. 2531.

[2]Smoluchowski, R. (1968) Mars: retention of ice: Science, Vol. 159, p. 1348.

[3]Schubert, G., Lingenfelter, R. E. and Peale, S. J. (1970) The morphology, distribution and origin of lunar sinuous rilles: Rev. of Geophy. and Spa., Vol. 8, p. 199.

as the fluid medium. The best supported of these is the argument by Oberbeck, Quaide and Greeley (1969)[1] which proposes that the rilles are collapsed lava tubes which formed originally in the mare basalt flows. This argument is based on terrestrial analogues and calculations which show the dimensions of the roof span possible under lunar gravity. The lava tube hypothesis is supported by Murray (1971)[2] in an article which compares lunar and terrestrial forms. Cruikshank and Wood (1972)[3] compare the lunar rilles with Hawaiian volcanic features and conclude that the lava tube origin is likely. Greeley (1971)[4] compares features in the Marius Hills of the moon with terrestrial forms and concludes that these specific rilles are collapsed lava tubes. Hatheway and Herring (1970)[5] have completed a detailed geomorphic study of lava tubes in New Mexico specifically for comparison with lunar rilles. They have reported the basic characteristics of the lava tubes, but are unwilling to assign a lava

[1]Oberbeck, V. R., Quaide, W. L. and Greeley, R. (1969) On the origin of lunar sinuous rilles: Modern Geology, Vol. 1, p. 75.

[2]Murray, J. B. (1971) Sinuous rilles: in Geology and Physics of the Moon, Fielder, G., ed., Elsevier, New York, p. 27.

[3]Cruikshank, D. P. and Wood, C. A. (1972) Lunar rilles and Hawaiian volcanic features: possible analogues: Moon, Vol. 3, p. 412.

[4]Greeley, R. (1971) Lava tubes and channels in the lunar Marius Hills: Moon, Vol. 3, p. 289.

[5]Hatheway, A. W. and Herring, A. K. (1970) Bandera lava tubes of New Mexico and lunar implications: C.L.P.L. 152, Vol. 8, p. 299.

tube origin to the lunar rilles without further investigation. Green (1969)[1] with considerable optimism suggests that uncollapsed lava tubes would be suitable lunar shelters.

Most of the above authors feel that flow may have alternated between the closed lava tubes and open channels depending on the width of the flow and the thickness of the roof support. Turner (1973)[2] has prepared a model of the eastern segment of Schroeter's Valley and concluded that the valley may be an open channel. This study is based on lunar orbiter imagery. Mutch (1972)[3] also suggests that flow in open channels is a possible origin, and further suggests that the direction of flow cannot be established a priori.

Two additional papers by Leonardi (1971)[4] and by Burke, Brereton and Muller (1970)[5] have given overall reviews of the problem and have concluded that present evidence is insufficient to provide a unique solution, if indeed there is a unique origin for all sinuous rilles.

[1] Green, Jack (1969) Terrestrial analogs: water on the moon, Presentation at the North American Rockwell Science Center, Jan. 16, 1969.

[2] Turner, R. (1973) A model of the eastern portion of Schroeter's Valley: C.L.P.L., Vol. 10., No. 195, p. 81.

[3] Mutch, T. A. (1972) Geology of the Moon, Princeton University Press, New Jersey, p. 301.

[4] Leonardi, P. (1972) Winding and meandering furrows on the lunar surface: Modern Geology, Vol. 31, p. 151.

[5] Burke, J. D., Brereton, R. G., and Muller, P. M. (1970) Desert stream channels resembling lunar sinuous rilles: Nature, Vol. 225, p. 1234.

It has been strongly suggested by Mather (1971)[1] that the sinuous rilles may have several diverse modes of origin.

Examination of Hypotheses:

The above hypotheses may now be assessed with regard to both the lunar geologic environment and the geomorphic characterization of Hadley Rille presented in chapters four, five and six.

Water-dependent hypotheses. Hypotheses requiring the presence of water appear the least plausable. Experimental studies (Adler and Sallisbury, 1969)[2] indicate that water in a vacuum flows across the surface rather than flowing in channels, and produces a hummocky topography. Anders (1970)[3] has shown analytically that water on the moon is incompatible with an accretionary origin. O'Keefe (1969)[4] has shown that large craters would rapidly be obliterated by plastic flow if large amounts of ice exist at depth within the moon. Gilvarry (1969)[5]

[1]Mather, K. F. (1971) Personal communication.

[2]Adler, J. E. M. and Sallisbury, J. W. (1969) Behavior of water in a vacuum: implications for "lunar rivers": Science, Vol. 164, p. 589.

[3]Anders, E. (1970) Water on the moon?: Science, Vol. 169, p. 1309.

[4]O'Keefe, J. A. (1969) Water on the moon and a new non-dimensional number: Science, Vol. 163, p. 669.

[5]Ibid., p. 533.

has calculated that open channels containing flowing water would be shallow and wide rather than deep as is the rille. The most serious objection to lunar water is the lack of any evidence of it in lunar samples. No hydrated silicates have been found in any of the lunar samples (Keil, et al., 1970)[1], Mason and Melson, 1970[2] and numerous studies published in the proceedings of the first, second, third and fourth lunar science conferences[3]). In fact, Apollo-16 samples contain Lawrencite ($FeCl_2$) which is highly unstable in a hydrous environment (Taylor, Mao and Bell, 1974)[4]. The absence of hydrated minerals in porphyritic or phaneritic rocks suggests that no water was present during crystallization at depth within the moon.

With specific reference to Hadley Rille, the absence of any associated depositional form is unexplained. Urey's (1967)[5] unique suggestion that the rille was formed totally by ice which has since sublimed

[1]Keil, K., et al. (1970) Mineral chemistry of lunar samples: Science, Vol. 167, p. 597.

[2]Mason, B. and Melson, W. G. (1970) The Lunar Rocks, Wiley, New York.

[3]Published by Geochimica and Cosmochimica Acta, MIT Press, Cambridge.

[4]Taylor, L. A., Mao, H. K. and Bell, P. M. (1974) Identification of the hydrated iron oxide mineral akaganeite in Apollo-16 lunar rocks: Geology, Vol. 2, p. 429.

[5]Ibid.

is a mechanism which should have left some morainal forms. It is difficult to see how any water-related mechanism could form a channel with a depression at each end. Water provides no explanation for the central constriction. Schubert's (1970)[1] hypothesis evidently requires an impact crater at one end of the rille, and no such crater is observed on Hadley Rille. Fluvial channels in a terrestrial environment appear as braided streams if the sinuosity is as low as Hadley Rille's sinuosity (Leopold, 1960)[2] but no braided channels are apparent. It is difficult to explain how such a well established sinuous form as the south section of Hadley Rille could have had a fluvial origin without the formation of numerous meander scars and abandoned channel segments.

Hypotheses dependent on structure. Hypotheses requiring a directly controlling geologic structure also have serious objections. The parallelism of the edges of sinuous rilles throughout a tortuous course (ch. 4) evidently eliminates simple faulting from consideration. The intrusion of a sinuous dike is possible only if a yet undescribed mechanism for sinuous crack formation is discovered. The strongest hypothesis which requires structural control appears to be Schumm's (1969)[3]

[1] Ibid.

[2] Leopold, L. B. and Wolman, M. G. (1957) River channel patterns: braided, meander and straight: U.S.G.S. Prof. Paper 282-B, p. 59.

[3] Ibid.

proposal requiring a fludized regolith.

This mechanism seems unlikely in the case of Hadley Rille because of the absence of fractures in the adjacent highlands which line up directly with rille segments (ch. 4). The overall discordance of most rille segment azimuths with regional structures (ch. 5) also suggests lack of control by specific underlying fractures. The partial structural alignment of the northern segments of the rille seems best explained as a diversion of the rille by topography rather than alignment with a linear vent. The thin mantle of regolith over bedrock (ch. 4) does not seem to allow a thick enough fluidized bed to form a rille as deep as is Hadley Rille. The raised edges on Schumm's (1970)[1] experimental models are noticeably absent on Hadley Rille (fig. 4-7). Furthermore, the textures of the rocks found near the rille appear to be best explained as lava flows rather than pyroclastic debris (ch. 2).

Ash flow hypothesis. The pyroclastic ash flow hypothesis of Cameron (1964)[2] is similarly out of accord with the petrologic evidence. Lavas with the chemistry of the Hadley Rille rocks have been shown to have exceptionally low viscosity (Murase and McBirney, 1970)[3] whereas nuée ardente flows are typically viscous compositions. Nuée ardente

[1] *Ibid.*

[2] *Ibid.*

[3] Murase, T. and McBirney, A. R. (1970) Viscosity of Lunar Lavas: Science, Vol. 167, p. 1491.

flows are found to contain 55% to 65% silica (Ollier, 1969)[1] whereas the lunar rocks are typically less than 45% silica. Also, the mechanics of a nuée ardente flow may require an atmosphere (Holmes, 1965)[2]. The nuée ardente channels depicted by Cameron appear to have a much more disperse and distributive aspect than the Hadley Rille channel.

Lava tube hypothesis. The most widely held hypothesis at present appears to be the collapsed lava tube mechanism. Although the general character of the rilles and the petrologic evidence seem to favor this view, there are as yet important unexplained objections.

A. Geomorphic objections. According to Oberbeck (1969)[3], the breadth of a lava tube roof arch might reach 500 meters under extremely optimal conditions, and erosion could subsequently widen the rille to twice that width. However, Hadley Rille displays widths considerably in excess of 1 km. throughout much of its southern extent (fig. 6-4). Furthermore, the estimated rate of erosion calculated in chapter four indicates that 200 meters of additional widening after roof collapse of the lava tube would be an extreme value. Assuming this much erosion, the rille, according to Oberbeck's roof span calculation, should not be more than 700 meters wide. The appearance of the rille wall at

[1] Ollier, C. (1969) Volcanoes, MIT Press, Cambridge.

[2] Holmes, A. (1965) Principles of Physical Geology, 2nd ed., Ronald, New York, p. 308.

[3] Ibid.

the Apollo-15 landing site strongly suggests a sequence of lava flows (ch. 4) and the petrology of the Apollo-15 rocks suggests at least four flows (ch. 2). However, terrestrial lava tubes have a vertical dimension entirely within a single flow (Hatheway and Herring, 1970)[1]. If Hadley Rille was vertically contained within a single flow, the flow must have been at least 400 meters thick. For comparison, the thickest flow in the Columbia River basalts is only 120 meters thick and the average thickness of these flows is about 10 meters. A thickness of 400 meters for lunar flows is a clear contradiction to the low viscosity of the lavas (Murase and McBirney, 1970)[2], the lower cooling rate implied by an environment without atmospheric convection or rain and the absence of coarse grained rocks which should have formed at the Apollo-15 site due to slow cooling in such a massive flow (discussion of cooling history to follow). If the entire rille, vertically and horizontally is contained within one lava flow, the flow dimensions must be about 100 km. by 30 km. by 400 meters deep (surface area estimated from fig. 4-1). This yields a flow volume of 1200 km.^{3}, a truly tremendous outpouring. A listing of large terrestrial lava flows (Holmes, 1965)[3] lists a 43 km.^{3} flow as the largest value which suggests that the 1200 km.^{3} value is far larger than expected on earth.

[1] Ibid.

[2] Ibid.

[3] Ibid.

The appearance of Hadley Rille is also in discord with lava tube morphology. According to Hatheway and Herring (1970)[1], lava tubes attain a sinuous appearance when diverted by pre-existing topography. Hadley Rille displays its most sinuous appearance in the southern section where topographic control is evidently the least. Published maps (e. g., Greeley, 1971)[2] indicate that terrestrial rilles have a less sinuous appearance than Hadley Rille and lava tube bends appear more abrupt than the Hadley Rille curves. Also, lava tubes appear to end in a distributary system or a flow lobe, not a depression. In a second article, Greeley (1971)[3] notes that lava tubes occupy topographic highs. Using profiles of Hadley Rille based on Lunar Orbiter imagery, he indicates that Hadley Rille is so positioned. The profiles drawn for this study (ch. 4) are in strong disagreement with Greeley's profiles in this respect as are the profiles of Wu, et al. (1972)[4]. The obstruction northwest of the Apollo-15 landing site, interpreted as an uncollapsed segment of a lava tube shows no evidence of a cave

[1] Ibid.

[2] Greeley, R. (1971) Lava tubes and channels in the lunar Marius Hills: Moon, Vol. 3, p. 302.

[3] Greeley, R. (1971) Lunar Hadley Rille: considerations of its origin: Science, Vol. 172, p. 722.

[4] Wu, S. et al. (1972) Photogrammetry of Apollo-15 photography: in Apollo-15 Preliminary Science Report, NASA SP-289, p. 25-36.

entrance and is adjacent to a region of high fracture density (ch. 5) and recent (post-rille) tectonic activity (ch. 4). It thus appears unlikely that this segment of all possible segments is a likely location for an uncollapsed cavern.

B. Objections based on cooling history. The strongest objection to a lava tube origin appears to this author to be an estimate of the cooling history of the flow. In a flow thick enough to contain Hadley Rille, two possibilities seem to exist for the mode of cooling.

1. Radiation from the top of the flow cools the surface so that dense material forms and sinks. This situation results in the formation of convection cells in the flow which contually subduct large rafts of solidified lava as soon as they form, and fresh, hot liquid material is brought to the surface. This behavior has been observed in lava lakes in Hawaii (Duffield, 1972)[1]. Under these conditions, the lava mass probably maintains a fairly uniform temperature throughout because of the mixing. An absolute minimum time for cooling under these conditions can be calculated as follows:

Assume:

a. That the only heat loss from the lava is radiation to the sky which is at $0^{o}K$.

[1]Duffield, W. A. (1972) Kilauea Volcano provides a model for plate tectonics: Geotimes, Vol. 17, p. 19.

b. That the only energy released is from simple cooling of the liquid and that no phase transformations occur. The energy released through crystallization would probably increase the cooling time considerably.

c. The sample cools from 1650 to 1375 degrees Kelvin. These values approximate the crystallization range of lunar basalts according to the experiments by Murase and McBirney (1970)[1].

d. That convection in the liquid proceeds until the basalt is completely solid and the melt is a uniform temperature during cooling as a result of the convection. If convection ceases, then conduction through the flow becomes the dominant cooling process which slows cooling considerably as seen below.

e. Assume an emissivity of 1.0 or black body radiation. This gives a maximum cooling rate.

Heat radiated from the surface of the flow under these conditions is equal to: (McAdams, 1954)[2]

$$Qr = \nabla T^4 A dt$$

[1] Ibid.

[2] McAdams (1954) Heat Transmission, McGraw-Hill, New York, p. 59.

where:

Qr = Heat radiated (cal)
∇' = Boltzman constant (= 4.88×10^{-9} cal/cm.^{2} hr. ^{o}K)
T = Temperature (^{o}K)
dt = Time increment (hr.)
A = Surface area of flow

The heat lost from the flow through cooling is found

$$Q_L = ADC_p dTp$$

where:

Q_L = Heat lost
D = Depth of flow (taken as 400 meters)
A = Surface area of flow (note that A x D = the flow volume)
dT = Incremental temperature change
C_p = Specific heat (approximated at 0.35 cal/gm. the value for quartz at 1600 ^{o} C)
p = Density of liquid (estimated to be 3 gm./cm.^{3})

Then, the heat radiated = -heat lost to flow or

$$\gamma T^4 A dt = -pADC_p dT$$

which yields upon rearrangement:

$$\int_{T_i}^{T_f} \frac{dT}{T^4} = -\int_{t_i}^{t_f} \frac{\gamma dt}{pDC_p}$$

Integrating between initial and final temperatures (T_i and T_f or 1650K and 1375K) and starting and ending times (t_i and t_f) gives upon rearrangement the elapsed time for cooling between two temperatures:

$$\text{elapsed time} = \Delta t = \frac{pC_p D}{3\sigma}\left[\frac{1}{T_f^3} - \frac{1}{T_i^3}\right]$$

Substituting values to find the cooling time under the stated assumptions:

$$\Delta t = \left[\frac{3\ \text{gm./cm.}^3\ .35\ \text{cal./gm.}\ 4 \times 10^4\ \text{cm.}}{3(4.88 \times 10^{-9}\ \text{cal./cm.}^2\ \text{hr}\ {}^\circ\text{K}^4}\right]\left[\frac{1}{1375^\circ\text{K}} - \frac{1}{1650^\circ\text{K}}\right]$$

$= 465$ hours or 19 days minimum

2. If the convection process is initially inoperative, or if cooling by radiation increases the viscosity of the flow to the extent that the rafted material no longer is subducted, then a crust will form. Murase and McBirney (1970)[1] feel on intuitive grounds that a crust accompanied by a still liquid flow beneath is conducive to the formation of lava tubes. However, let us examine the cooling behavior of a 400-meter-thick flow at a temperature of 1500°K (midway in the cooling range) which has accumulated a 20-meter-thick crust on its surface. This crust thickness is only about 1/3 of the roof thickness postulated by Oberbeck, *et al.* (1969)[2] as being necessary for large lunar lava tubes.

Assume:

a. No phase transformation as before.

[1] *Ibid.*

[2] Oberbeck, V. R., Quaide, W. L. and Greeley, R. (1969) On the origin of lunar sinuous rilles: Modern Geology, Vol. 1, p. 75.

b. That the surface temperature of the slab is absolute zero. This gives a maximum possible temperature gradient across the slab and the highest possible value for conducted heat.

c. The temperature drop is one Kelvin degree and only temperature changes in the liquid are considered.

d. The specific heat of the liquid is 0.35 cal./gm. as before.

e. The heat conductivity of the solid crust is 14.4 cal./cm. hr. ^{o}K. This value is in accord with experimental values found at high temperatures by Murase and McBirney (1970)[1].

f. No temperature gradients exist within the material under the solid crust, that is, only the thermal r sistance of the crust is being considered.

g. The lava sheet is effectively infinite in horizontal dimension compared to thickness, thus, only heat conducted out of the surface is considered.

Then:

$$Q_c = -AK \frac{T_t - T_b}{d} \Delta t$$

[1]Murase, T. and McBirney, A. R. (1970) Thermal conductivity of lunar and terrestrial igneous rocks in their melting range: Science, Vol. 170, p. 165.

Where:

Q_c = Conducted heat
A = Surface area
K = Thermal conductivity
T_c = Temperature at surface of crust (= $0^\circ K$)
T_b = Temperature at base of crust (= 1500° K)
Δt = Elapsed time
d = Thickness of crust (= 20 meters)

As before, the heat loss within the liquid mass is given by:

$$Q_L = ADC_p \Delta Tp$$

where

ΔT = temperature change within the liquid during time Δt (taken as 1° Kelvin for discussion)

Setting the heat released to the heat lost:

$$-AK \frac{(T_t - T_b)}{d} \Delta t = ADC_p \Delta Tp$$

so that

$$\Delta t = \frac{-d}{K(T_t - T_b)} DC_p \Delta Tp$$

Substituting values to find the time for a 1° temperature loss, we find:

$$t = \frac{-2000 \text{ cm. x } 4 \times 10^4 \text{ cm.}}{14.4 \text{ cal./hr. cm.}^\circ K \ (0-1500)^\circ K} \times .35 \text{ cal./gm.}^\circ K \times 1^\circ K \times 3 \text{ gm./cm.}^3$$

$$= 3889 \text{ hours}/^\circ K = 162 \text{ days}/^\circ K$$

Thus, if a 400-meter-thick flow of low viscosity lava could form at all, it would probably have the following cooling history:

a. An eruptive phase would be coincidental with lateral flow of lava until the lava became ponded by surrounding topography.

b. The ponded material would develop convection cells and very rapid cooling would proceed for several weeks. Convection apparently goes on for a year or so at Kilauea (Duffield, 1972)[1]; the assumptions in the preceding analysis probably decrease the calculated time considerably.

c. At some point, a solid crust would form with increasing viscosity of the cooling liquid. Cooling would then be controlled by conduction through the crust and would slow drastically. The remaining material under the crust would remain plastic for at least 50 years (100^{o}K temperature drop x $\frac{1}{2}$ year per degree drop).

It appears to this author from personal observations of existing Icelandic lava tubes and from the descriptions of other authors (Ollier, 1969[2]; Greeley, 1971[3], and Hatheway and Herring, 1970[4]) that

[1] Ibid.

[2] Ibid.

[3] Greeley, R. (1971) Observations of actively forming lava tubes and associated structures, Hawaii: Modern Geology, Vol. 2, p. 207.

[4] Hatheway, A. W. and Herring, A. K. (1970) Bandera lava tubes of New Mexico and lunar implications: C.L.P.L. 152, Vol. 8, p. 299.

lava tube formation is a short-term dynamic process which takes place in a solidifying lava crust. Both of the above modes of cooling seem incompatible with lava tube formation. The vertical movements in the liquid during convection effectively prohibit continuous lateral motion in lava tubes. After the solid crust formed, the underlying liquid would stay mobile for years. If any large lava tubes should develop early in the history of the flow, they must certainly become closed by lateral movement of plastic material under the crust. Therefore, one is forced to the conclusion that large lava tubes in deep flows of ponded lava are unlikely.

Proposed Origin of Hadley Rille:

What follows appears in the context of this study to be a reasonable explanation for the origin of Hadley Rille. It is certainly not regarded as the only possible origin, but it is an explanation which is consistent with the important observations which have been made in this study.

Fluid flow mechanism. Several lines of evidence point to fluid flow as the originating agent.

1. The parallelism of the channel edges is most easily explained by fluid flow (ch. 4).

2. The diversion and change in character of the rille where it encounters topographic obstructions is characteristic of terrestrial stream channels (ch. 4).

3. The meander wave length/width ratio is appropriate for a fluid channel (ch. 6).

4. Where channel asymmetry occurs in profile view, it is such as to suggest cut banks and slip-off slopes (ch. 4).

5. The width asymmetry with distance along the channel (rip-saw pattern, ch. 6) suggests a lateral flow. This asymmetry appears somewhat analogous to the various types of ripple marks produced by translation flow. This is not to suggest that the mechanism producing the width-length asymmetry is necessarily the same as that producing sedimentary structures.

6. The statistically significant relationship between rille width and rille curvature 2 km. further along the channel suggests fluid flow as a possible mechanism to produce this offset (ch. 6).

Probable fluid. Geologic considerations indicate that lava is the fluid. Palus Putredinis is a closed, or nearly closed, basin (ch. 2). Therefore, a local source for the mare basalts is indicated. The basement structure close to the rille has been shown (ch. 5) to contain fractures which have probably been remobilized by several impact events, thus many large and deep fractures probably exist. These provide likely conduits for the mare basalts. The fracture density at the south end of the rille (fig. 5-10) is relatively high which places the arcuate depression which terminates the rille in a likely site for a volcanic vent. The direction taken by the long dimension of this depression falls very close to the Serenetatis circumferential direction (ch. 5) indicating that it may be related to a well developed fracture. There are no evident cross-cutting relationships which divorce the time of rille formation from the emplacement of the mare basalts (ch. 2 and ch. 4) so the events can be presumed to be contemporaneous. The petrology of the Apollo-15 rocks suggest very fluid lavas rather than pyroclastic materials (ch. 2 and previous discussion in this chapter). The apparent absence of water on the moon leaves few fluid alternatives to lava.

Direction of flow. It has been generally assumed by authors favoring a fluid mechanism that the flow direction through Hadley Rille was from south to north. There is little topographic evidence to support this view. The lunar orbiter camera orientation information is usually inadequate to establish relative elevation differences on the mare surface because the lunar orbiter maps are estimated to be correct only to ± 250 meters at the 90% confidence level. However, the premission lunar orbiter-based map (TOPCOM, 1970)[1] clearly indicates that the rille bottom has a consistent slope to the south and that bottom of the rille at the northern extremity is as much as 700 meters higher than the rille bottom in the south. This difference appears to be well outside the error limits of the map. In an attempt to determine the slope of the channel bottom based on Apollo-15 metric information,

[1] After the completion of this report, the author obtained NASA Lunar Topographic Orthophotomap HADLEY, sheet LT041B4, scale 1:250000 based on Apollo 15 metric photos, and also NASA Lunar Topophotomaps 41B4S1 APOLLO 15 LANDING AREA, 41B4S2 RIMA HADLEY CENTRAL, and 41B4S3 RIMA HADLEY SOUTH; scale 1:50000 based on Apollo 15 metric and pan photos. These maps were prepared by the Defense Mapping Agency Topographic Center, Wash. D.C. The magnitude and direction of rille channel slope indicated by these maps is in excellent agreement with the measurements reported here

spot elevations were taken for this study on the AS-11A analytical plotter. These are plotted on figure 7-1. This information must be taken as only an indication of the slope direction and not interpreted numerically. To produce a valid numerical value for the slope and to confirm this graph, it would be necessary to establish several models in the analytical plotter and treat the resultant slope data statistically. However, this graph, which is the best available information, also indicates that the rille bottom has a well defined slope to the south. In terms of rille morphology, this is an entirely reasonable view because the widest end of the rille is then the downstream end in accord with most fluid channels.

Postulated origin. On this basis, it is postulated that Hadley Rille is a channel which has returned lava to the vent from which it was originally extruded. In Hawaiian volcanic flows, ponded lava back flows into the vent from which it initially came at a rate which is several times the extrusion rate (Holmes, 1965)[1]. If one assumes a similar process on the moon, it provides a rational explanation for many of the observations which have been made in this study:

1. Material which flowed in the channel has returned below the lunar surface. The puzzling absence of any depositional form at either end of the rille representing the 20 $km.^3$ volume of the rille channel

[1] Ibid.

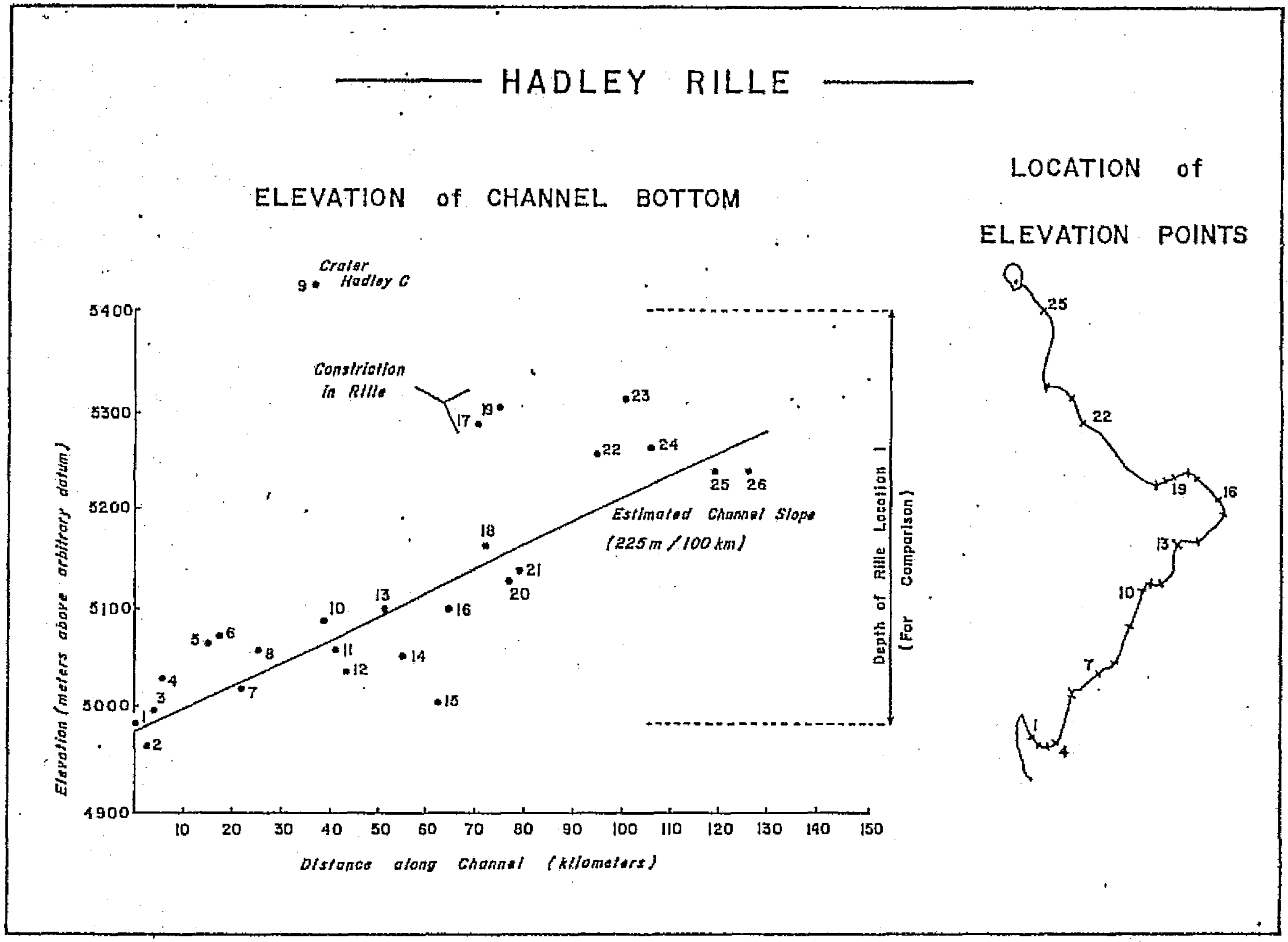

Fig. 7-1. Spot elevations in the bottom of the channel of Hadley Rille indicating the direction of channel slope.

(ch. 6) is thus explained.

2. The layered deposits displayed in the rille wall represent a series of flows (ch. 4). Outpourings probably came successively from the southern fracture and spread out over the land surface. After each eruption, backflow occupied the rille channel and drainage into the vent proceeded. Successive flows 'plated' successive layers on the surface of Palus Putredinis, each layer being tens of meters thick. As additional flows were deposited, the rille banks became higher and the rille became deeper. Each individual flow was considerably less than the 1200 $km.^3$ required by a lava tube hypothesis. An important feature of this mechanism is that the individual eruptions are relatively small and represent energy expenditures observed on earth (see Volumetric Consideration below).

3. The high lava marks (ch. 4 and Swann, et al., 1972)[1] represent the maximum level of lava which was ever present. Withdrawal subsequently left the surface at its present elevation.

4. Underlying the mare basalts adjacent to the Apennine Mountains there must be a layer of talus which was shed from the mountains during the 500,000,000-year interval between the Imbrium event and mare filling (ch. 2). Back flow through the rille could probably erode a channel

[1]Swann, et al. (1972) Preliminary geologic investigation of the Apollo-15 landing site: Apollo-15 Preliminary Science Report, NASA SP-289.

into this unconsolidated material. One might then expect to find pre-mare talus under a thin veneer of lava in the bottom of the rille. Some of the talus may have been subsequently exposed by impact gardening of the rille bottom, and may now be visible as the rounded, half-buried boulders noted in chapter four. Down cutting into unconsolidated material might also explain the V-shaped profile in the southern section of the rille.

5. With each additional flow, the rille channel would become more and more permanent because after each eruption, the rille would become larger. The larger thermal mass in the rille would make it successively less probable that the lava would congeal in the channel before the back flow process became complete. It is quite unlikely that the rille would change its channel under these conditions to melt down through previously congealed flows. Thus, we see no meander scars or cut-offs. Tributaries, if they existed at all, would be associated with single flow units. They would be obscured by successive flows and not survive.

6. The association of the rille with the Fresnel Rille system to the north probably occurred because the Hadley Rille drained lava which originally filled the pre-existing Fresnel Rille system. Lava in the Fresnel Rille system would stay liquid long enough for the draining to take place because the ponded lava in the Fresnel Rille was too thick to cool as rapidly as that on the nearby mare. The depression at the north end of the rille appears to be a lava pond which

was drained by the rille. The presence of sources of lava such as these at the upstream end of the rille might be an important factor in keeping the rille channel open during cooling of the whole flow. If so, the association of the rille with the depression would be inevitable rather than happenstance.

7. The structural control of the northern section of the rille (ch. 5) appears to have come about because the lava in this location was less deep. This could be due to the distance of this section from the vent and/or because of a higher elevation of the pre-mare surface at this end. As a result, the rille appears to have been superimposed over pre-existing topography. As noted below in the discussion of the rille constriction, similar topographic control probably occurred around the Apollo-15 landing site. The well-defined cut through Hill 305 which aligns with the rille channel in this segment is a suggestion of this control.

8. Pronounced natural levees would not be expected because ponded lava adjacent to the rille would congeal to maintain a relatively level land surface. This is in accord with the profiles (ch. 4).

9. Once established, the rille would act as an effective distributary system to move lava to <u>and</u> from the vent. Thus, flow lobes would not be directly associated with the vent. Flow lobes in Palus Putredinis are difficult to define at all.

10. The obscured channel between Hill 305 and the Fresnel Rille

may have developed because the Hadley Rille channel was not adequate to drain the last flow from this region before the lava congealed. Lava reaching this region would be relatively cool by the time of its emplacement because of its distance from the vent to the south.

11. This hypothesis is attractive from a stratigraphic point of view. The overall aspect of the rille indicates that its formation was associated with the end of volcanic activity in the Palus Putredinis region. According to this mechanism, the final volcanic event in the region was the withdrawal of lava through the rille.

Volumetric considerations. In order for this mechanism to be operative, an adequately large sub-surface chamber must exist without roof collapse while the lava is returning. Otherwise, a caldera would presumably form around the vent. Oberbeck, Quaide and Greeley (1969)[1] have investigated the roof support over a lava tube and determined the following equation:

$$l = \left(\frac{4}{3} \times \frac{sd}{pg}\right)^{\frac{1}{2}}$$

where:

l = Length of span
s = Tensil strength of rock = 6.9×10^7 degrees/cm.^{2}
d = Roof thickness
p = Mass density of rock
g = Acceleration of gravity

[1] Ibid.

This equation can be used to make an order of magnitude estimate of the diameter of magma chamber which could exist unsupported on the moon without collapse. This calculation should provide a minimum diameter because a spherical form with an arched roof is considerably stronger than the simple beam for which this engineering equation was developed. Table 7-1 shows the results of these calculations. The calculated volumes are volumes of spheres with diameters equal to the calculated roof spans.

Table 7-1. Calculated magma chamber sizes.

Depth to Chamber (km.)	Diameter of Roof Span (km.)	Implied Volume ($km.^3$)
1	1.4	1.3
10	4.3	43.
50	9.7	480.
100	13.6	1300.

These values which are based on an over simplified model and which assume no change in material properties with depth can only suggest an order of magnitude for the magma chamber size. However, if the flow units presently in Palus Putredinis are 30 km. by 100 km. by 30 meters thick (the first two dimensions seem reasonable from metric photography and the last from the rille wall stratigraphy), the total volume is 90 $km.^3$. If four times this volume originally erupted, 3/4 of it having returned to the magma chamber, the total erupted volume would be 360 $km.^3$. It appears from the above that a chamber to hold this volume could exist without collapse at a depth of less than 50 km.

This appears to be a reasonable depth for lava to originate on earth (Holmes, 1965)[1]. However, the higher gravity on the earth would presumably cause roof collapse and the formation of a caldera.

The 360 km.^{3} volume mentioned above is the approximate volume required to form the previously noted high lava marks in Palus Putredinis. This is eight times the volume of the previously noted large Icelandic flow. Approximately the same amount of energy would be required to lift these two flows from equivalent depths in their respective gravitational fields, so that from a physical point of view, lunar flows this size seem reasonable.

Morphology of the rille constriction. In the rille channel northwest of the Apollo-15 landing site, there is a constriction which is an apparent obstacle to lateral flow (ch. 4). This, therefore, requires a detailed examination. This feature has been interpreted by Greeley (1971)[2] as an uncollapsed portion of a lava tube. This interpretation is based upon the appearance of part of the constriction which is similar to depressions formed by cave and lava tube roof collapse. Figure 7-2 is an interpretive sketch of the construction drawn as an overlay

[1]Holmes, A. (1965) Principles of Physical Geology, 2nd ed., Ronald, New York, p. 308.

[2]Greeley, R. (1971) Lunar Hadley Rille: Considerations of its origin: Science, Vol. 172.

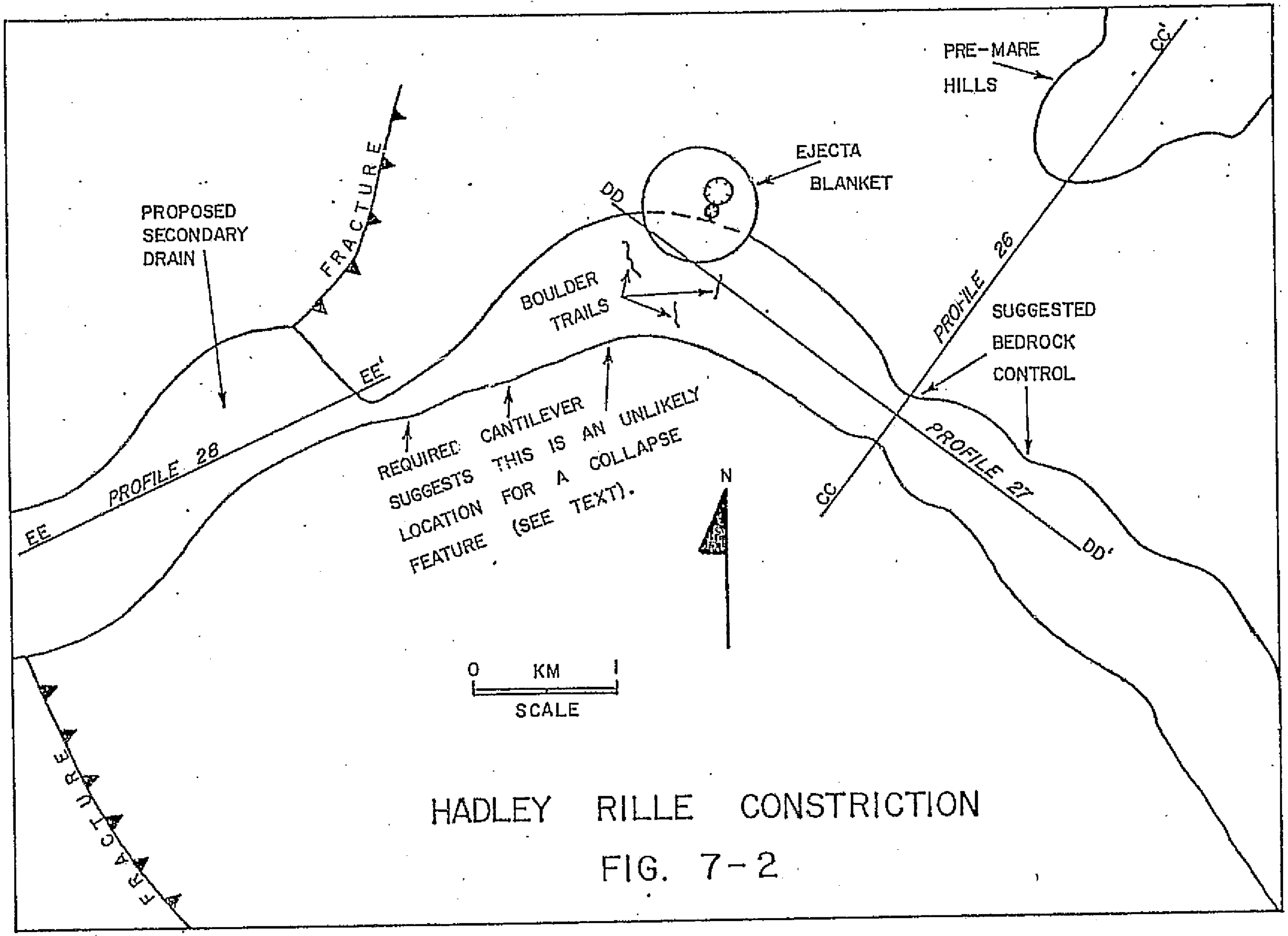

HADLEY RILLE CONSTRICTION

FIG. 7-2

on rectified pan photograph 15-9377. This illustrates alternative possibilities for the appearance of this section.

The narrowest part of the constriction (fig. 7-2) is not bowl-shaped at all, but is seen to gradually taper over a distance of several kilometers until the rille is almost totally closed. A long, narrow breach as suggested by this section is an unlikely mode of cavern roof collapse. When the cavern roof is intact, the roof structure can be approximated as a simple beam (Greeley, 1971)[1], However, if a small, central portion of the roof were to collapse, the remaining structure would resemble two cantilever beams, each projecting toward the other from opposing walls. The maximum bending moment in the cantilever is twice the moment in the simple beam and the location of the maximum moment moves from the center (in the simple beam) to the wall (in the cantilever). This occurs even though the cantilever length is only ½ the length of the original beam. (Fuller and Johnston, 1919[2], or most textbooks on engineering mechanics). Thus, the cantilever is not apt to remain intact. The collapse depressions over lava tubes tend to be elliptical in form, and the width of the ellipse is similar to the tube width (photo in Murray, 1971)[3]. This form minimizes the

[1] Ibid.

[2] Fuller, C. E. and Johnston, W. A. (1919) Applied Mechanics, Vol. 2, Wiley, New York, p. 122.

[3] Ibid.

length of cantilevered projections from the wall. The tapered section of the constriction (labelled on fig. 7-2) appears in violation of this principle. The obvious post-rille faults passing close to this location also make this an improbable site for an uncollapsed cave roof.

The bowl-shaped appearance of other parts of the constriction could also result from mechanisms other than collapse, for example:

1. The minor constriction in the rille wall at the sharp bend (fig. 7-2) is caused by ejecta from a post-rille crater. Boulder trails in the rille are clearly related to this event.

2. The bowl nearest the Apollo-15 landing site may have occurred when the rille was superimposed on the pre-mare surface. The alignment of this segment with the Imbrium radial direction and with a lineament through Hill 305 suggests control by pre-mare topography. The humps in the rille bottom which form the edges of the bowl are aligned with nearby pre-mare hills. Figure 7-3 is a transverse profile at one of the humps and over one of the hills. If the present slope of the hill is extended, it passes less than 100 meters under the rille bottom. This suggests that the rille was superimposed on this pre-mare hill (fig. 7-3).

<u>Origin of the rille constriction</u>. A possible explanation for this constriction is that it results from a secondary lava drain. The drain itself is postulated at the intersection of the two post-mare fractures (fig. 7-2). Reference to the structure density map (fig. 5-10) suggests that this location is one of the most highly fractured areas

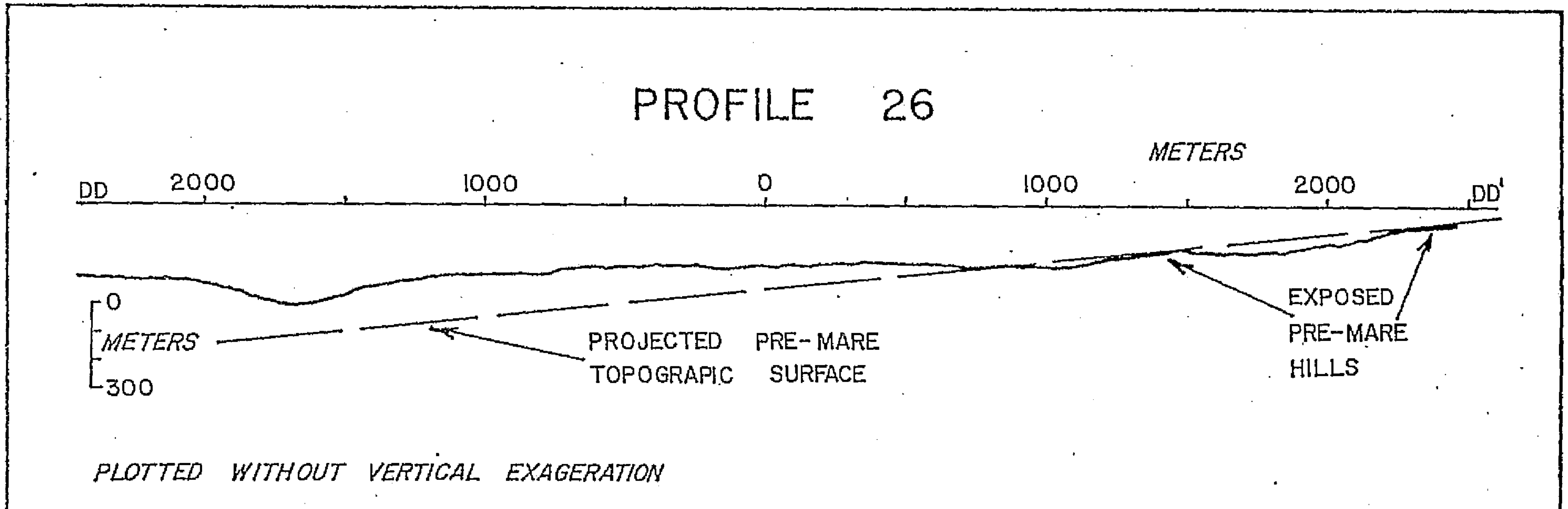

FIG. 7-3

Fig. 7-3. Profile across the rille at the constriction indicating possible bedrock control.

in the region and is thus a likely location for lava conduits. Eruptions of the volcano, Kilauea Iki, in Hawaii have occurred 30 to 40 miles from the main caldera, although land movements indicate that they are associated with a magma source underlying the caldera (Holmes, 1965)[1]. Considering the low lunar gravity, and the low thermal conductivity of lunar rocks, it seems reasonable that the conduit to a secondary vent could remain open for reverse flow black to the main magma chamber. The rille channel downstream from the drain would carry a diminished flow resulting in an altered channel geometry. The depth and shape of the channel downstream from the drain would be controlled by the pre-mare topographic surface, which is evidently not far below the lava surface. The shallow depth of lava here is indicated by the structural alignment of the rille (ch. 5). Figure 7-4 is a longitudinal profile along the rille through the constriction. The slope of the channel toward the south end of the rille is in accord with fluid flow to the south toward the main vent. Figure 7-5 is a profile through the supposed drain and indicates its shape. The profile lines are indicated on figure 7-2 and on figure 4-5.

Terrestrial-lunar comparison. The geologic evidence suggests that Hadley Rille is a fluid flow channel resulting from the flow of lava. It is postulated that the flow occurred as a back flow into the vent which originally extruded the flow. Because similar large back

[1] Ibid.

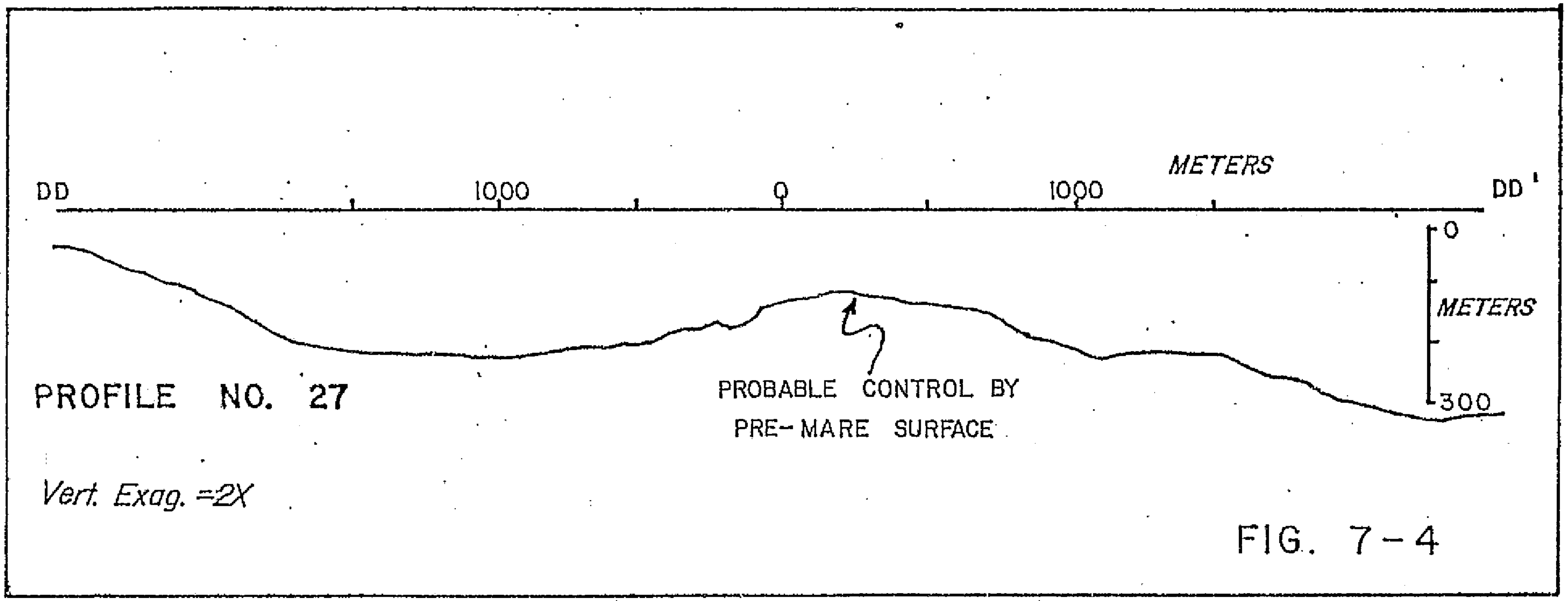

Fig. 7-4. Longitudinal profile of the rille channel bottom through the constriction.

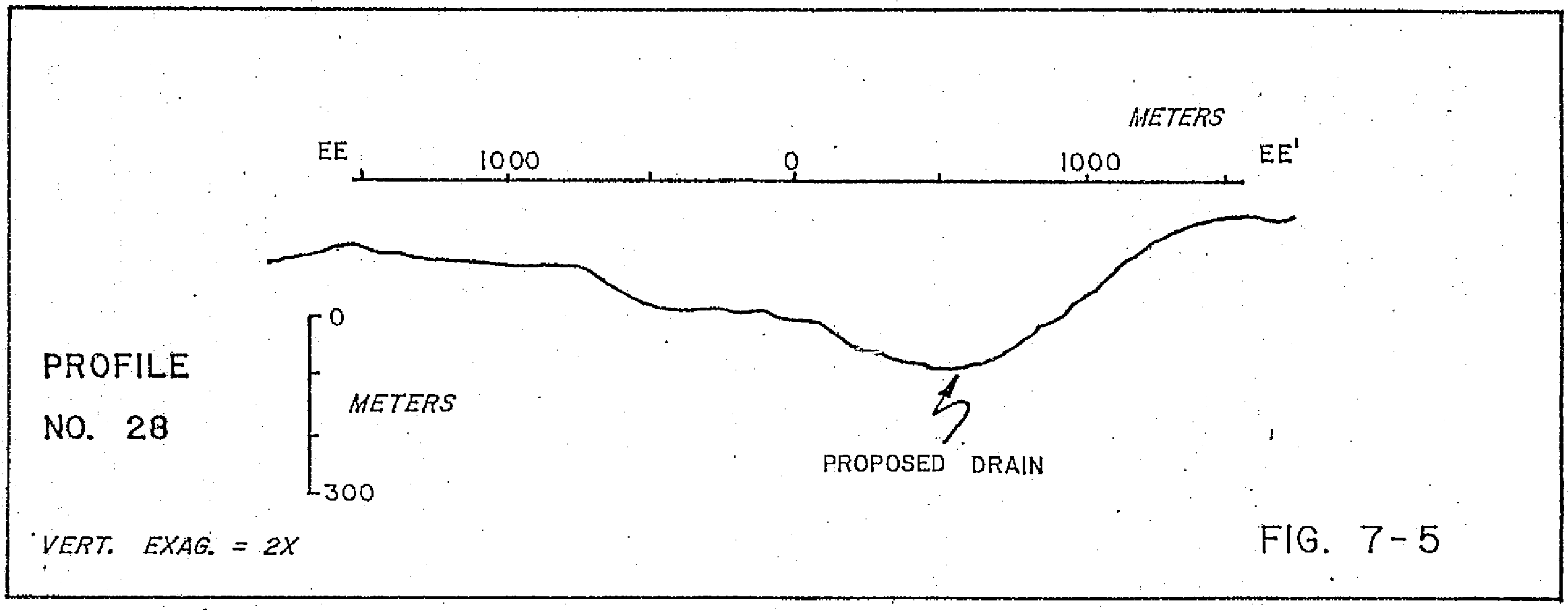

FIG. 7-5

Fig. 7-5. Longitudinal profile of the rille channel bottom west of the constriction indicating location of proposed drain.

flow channels are not generally recognized on earth, it is necessary to discuss dissimilarities between the two environments. There are several factors which may inhibit the formation of such channels in the terrestrial environment:

1. A large, flat region is required for such a channel to develop. Most present day terrestrial lava flows occur on the continental margins in mountainous regions. This may effectively prevent rille formation.

2. The vent must be at or below the same elevation as the flow surface. Most such vents on earth are under water. Visible terrestrial volcanoes have a raised vent area. This can be explained by the high viscosity of terrestrial lavas compared to lunar lavas.

3. Calderas and other collapse features which are apt to divert the flow are common in the terrestrial gravitational field.

4. Cooling of terrestrial lavas is faster because of atmospheric convection and rainfall. Cooling of underwater eruptions is probably so rapid that back flow is negligible.

5. Erosion of pre-existing lava flows between eruptions may disect the surface enough to interrupt the back flow surface.

6. In the lunar environment, lavas have the same inertia as terrestrial lavas, but have only 1/10 the viscosity and are subjected to only 1/6 the gravitation force. It is not presently clear what

effect this has on the mechanics of channel formation.

A few observations are left unexplained by this postulated mechanism for rille formation. The direct linear correlation between width and depth of the rille (ch. 6) is unexpected in a terrestrial fluid flow channel (Howard, Head, and Swann, 1972)[1]. There is no clear explanation for the apparent relationship between width and azimuth in several short sections of the rille (ch. 6).

Other lunar rilles. This study has concerned only Hadley Rille. The conclusion here should not be applied to other rilles without careful consideration. However, two points need to be made:

1. Rilles on the Aristarchus Plateau (very evident on photograph Lunar Orbiter V-188M) evidently downcut through pre-mare material. Back flow of lava from a large lava lake could superimpose a rille on highland material. As the lake level dropped, the channel would search for a gap in the terrain through which to flow. Unconsolidated material would probably be eroded, deepening the valley somewhat.

2. The inner rille in Schroeter's Valley (Lunar Orbiter $150H_3$ and $157H_3$) cross-cuts the outer rille. This is easily explained if the inner rille was formed by back flowing lava which originated in Oceanus Procellarum.

[1]Howard, K. A., Head, J. W. and Swann, G. A. (1972) Geology of Hadley Rille: Preliminary Report, U.S.G.S. Interagency Report No. 41.

A number of general questions have been raised by this study which deserve further attention.

1. It would be desirable to study the measurable geomorphic characteristics which define the direction of flow in fluid flow channels. A possible example is the asymmetric width-length curve discussed in chapter six. Knowledge of such relationships would be of considerable value in interpreting extra-terrestrial forms and would provide an independent check on photogrammetric determinations of equi-potential surfaces. A large amount of well planned high resolution data would be required to make such a study definitive.

2. An investigation of the relationship of channel form to fluid density should be made. This could be carried out with organic liquids and salt solutions using a stream table. The effect of different factors such as density and viscosity could be identified using analysis of variance if sufficient data were available.

3. Model experiments for extra-terrestrial phenomena appear to have limited value because so many parameters are varied at once. However, experiments using ponded liquid paraffin in a container with a drain might provide some insight into the mechanics of flow channel formation within a semi-liquid medium. A large scale terrestrial analogue to this type of flow is found in the meanders of the Gulf Stream (Leopold, Wolman and Miller, 1964)[1].

[1]Leopold, L. B., Wolman, M. G. and Miller, J. P. (1964) Fluvial Processes in Geomorphology, Freeman, San Francisco, p. 296.

APPENDIX 1

DERIVATION OF THE AZIMUTH EQUATION

This is a derivation of the equation used in chapter V to compute the azimuth from one point on a planetary surface to another. Figure A1-1 defines the vectors used in this proof, and the following notation has been adopted:

P_1 – point at which azimuth is desired

P_2 – point to which azimuth is desired

L_1, L_2 – Latitude angles to points P_1 and P_2 (negative if south)

G_1, G_2 – Longitude angles to points P_1 and P_2 (negative if west)

$\bar{i}$ – unit vector from sphere center to 0^o long. and lat.

$\bar{j}$ – unit vector from sphere center to 90^o long. and 0^o lat.

$\bar{k}$ – unit vector from sphere center to north pole.

$\bar{V}_1$ – Vector from sphere center to point P_1

$\bar{V}_2$ – Vector from sphere center to point P_2

x_1, y_1, z_1 – Magnitudes of components of $\bar{V}_1$ along $\bar{i}$, $\bar{j}$, $\bar{k}$

x_2, y_2, z_2 – Magnitudes of components of $\bar{V}_2$ along $\bar{i}$, $\bar{j}$, $\bar{k}$

$\bar{N}$ – North azimuth vector at point P_1

$\bar{A}$ – azimuth vector at P_1 tangent to sphere and to great circle through P_2

$\bar{E}_1$ – projection of $\bar{V}_1$ on equatorial plane.

$\bar{M}$ – (not shown on fig. A1-1) Intermediate vector perpendicular to plane defined by $\bar{M} = \bar{V}_2 \times \bar{V}_1$

$\bar{Q}$ – (not shown on fig. A1-1) Intermediate vector perpendicular to plane defined by $\bar{Q} = \bar{V}_2 \times \bar{V}_1$

r – planetary radius

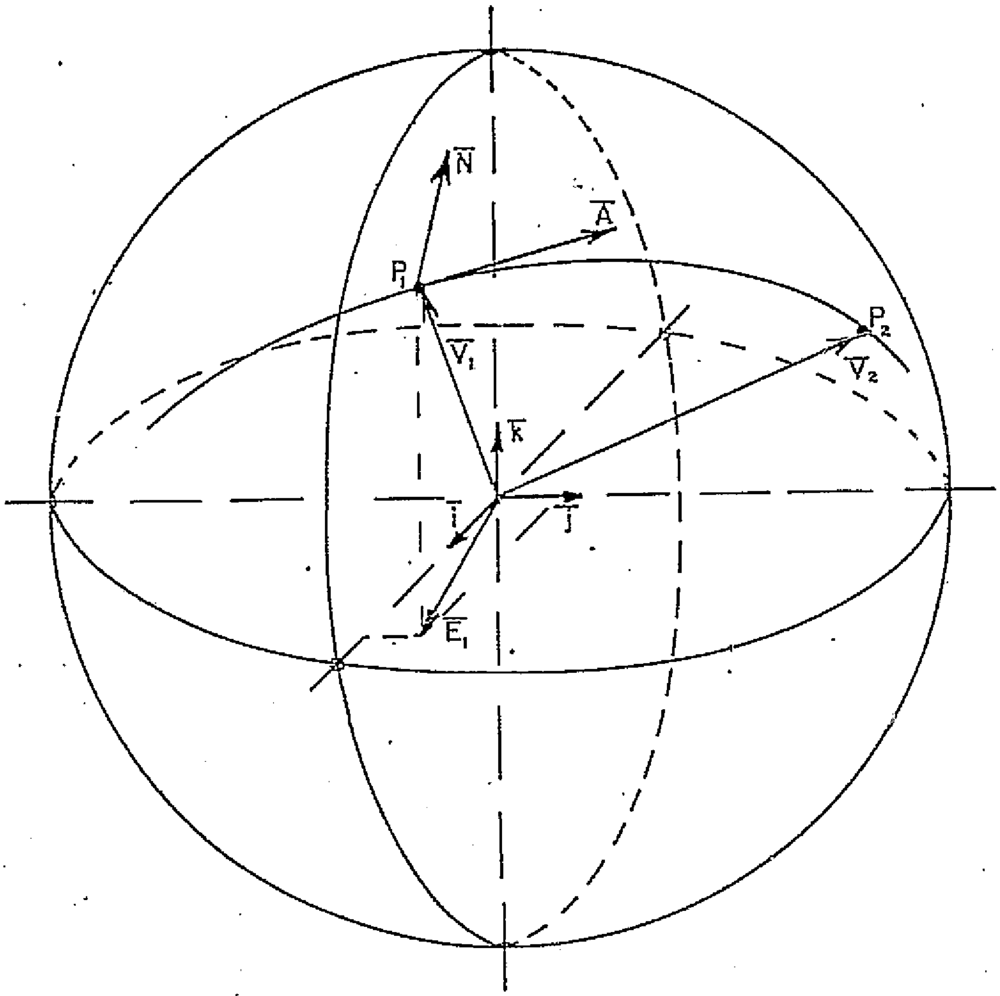

FIG. AI-1

VECTORS USED TO DERIVE AZIMUTH EQUATION

Given the latitudes and longitudes of two points on a spherical surface, determine the azimuth relative to north from one point (P_1) to the other (P_2).

A. Find x_1, y_1, and z_1; x_2, y_2, and z_2 in terms of the planetary radius (r) and the angles $L_{1,2}$ and $G_{1,2}$

By definition

$$\overline{V_1} = x_1\overline{i} + y_1\overline{j} + z_1\overline{k}$$

$\overline{E_1}$, the projection of $\overline{V_1}$ on the equatorial plane is found:

$$\overline{E_1} = x_1\overline{i} + y_1\overline{j}$$

also:

$$\left|\overline{V_1}\right| = \sqrt{x_1^2 + y_1^2 + z_1^2} = r$$

and:

$$\left|\overline{E_1}\right| = \sqrt{x_1^2 + y_1^2}$$

so:

$$x_1 = \overline{E_1} \cdot \overline{i} = \left|\overline{E_1}\right|\left|\overline{i}\right| \cos (G_1) = \sqrt{x_1^2 + y_1^2} \cos (G_1)$$

$$y_1 = \overline{E_1} \cdot \overline{j} = \left|\overline{E_1}\right|\left|\overline{j}\right| \cos (90 - G_1) = \left|\overline{E_1}\right|\left|\overline{j}\right| \sin (G_1)$$

$$= \sqrt{x_1^2 + y_1^2} \sin (G_1)$$

but:

$$\overline{E_1} \cdot \overline{V_1} = \left|\overline{E_1}\right|\left|\overline{V_1}\right| \cos (L_1) = \sqrt{x_1^2 + y_1^2}\, r \cos (L_1) = x_1^2 + y_1^2$$

so:

$$\sqrt{x_1^2 + y_1^2} = r \cos (L_1)$$

also:

$$\overline{V_1} \cdot \overline{k} = \left|\overline{V_1}\right|\left|\overline{k}\right| \cos (90 - L_1) = \left|\overline{V_1}\right|\left|\overline{k}\right| \sin (L_1)$$

$$= r \sin (L_1) = z_1$$

combining results:

$$x_1 = r \cos (G_1) \cos (L_1) \quad \text{(eq. 1)}$$

$$y_1 = r \sin (G_1) \cos (L_1) \quad \text{(eq. 2)}$$

$$z_1 = r \sin (L_1) \quad \text{(eq. 3)}$$

and similarly

$$x_2 = r \cos (G_2) \cos (L_2) \quad \text{(eq. 4)}$$

$$y_2 = r \sin (G_2) \cos (L_2) \quad \text{(eq. 5)}$$

$$z_2 = r \sin (L_2) \quad \text{(eq. 6)}$$

These are the familiar equations for transforming spherical to rectangular coordinates.

B. Find the north vector $\overline{N}$ tangent to the sphere at P_1, and its absolute value $|\overline{N}|$:

$$\overline{k} \times \overline{V}_1 = \overline{M} \quad (\overline{M} \text{ is an intermediate vector perpendicular to } \overline{k} \text{ and } \overline{V}_1)$$

$$\overline{V}_1 \times \overline{M} = \overline{N} = \overline{V}_1 \times \overline{k} \times \overline{V}_1$$

Then, by virtue of the vector identity:

$$\overline{A} \times \overline{B} \times \overline{C} = \overline{B}(\overline{A} \cdot \overline{C}) - \overline{C}(\overline{A} \cdot \overline{B}) \quad \text{(eq. 7)}$$

it is evident that

$$\overline{N} = \overline{k}(\overline{V}_1 \cdot \overline{V}_1) - \overline{V}_1(\overline{V}_1 \cdot \overline{k}) \quad \text{(eq. 8)}$$

The absolute value of $\overline{N}$, $|\overline{N}|$, is found by taking the dot product

$$|\overline{N}|^2 = \overline{N} \cdot \overline{N} = [\overline{k}(\overline{V}_1 \cdot \overline{V}_1) - \overline{V}_1(\overline{V}_1 \cdot \overline{k})] \cdot [\overline{k}(\overline{V}_1 \cdot \overline{V}_1) - \overline{V}_1(\overline{V}_1 \cdot \overline{k})]$$

or after expanding the expression and collecting terms

$$|\overline{N}|^2 = (\overline{k}.\overline{k})(\overline{V}_1.\overline{V}_1)(\overline{V}_1.\overline{V}_1) - (\overline{k}.\overline{V}_1)(\overline{V}_1.\overline{k})(\overline{V}_1.\overline{V}_1)$$

This can be simplified because $k.k = 1$ and:

$$(\overline{V}_1 \cdot \overline{V}_1) = r^2 \quad \text{(eq. 9)}$$

$$(\overline{V}_1 \cdot \overline{k}) = z_1 \quad \text{(eq. 10)}$$

to the form

$$|\overline{N}|^2 = r^4 - z_1^2 r^2$$

so that

$$|\overline{N}| = \sqrt{r^4 - z_1^2 r^2}$$

C. Find the vector A tangent to the sphere in the plane of the great circle defined by V_1 and V_2. This is the azimuth vector. Also, determine its magnitude.

$\overline{V_2} \times \overline{V_1} = \overline{Q}$ (Q is an intermediate vector perpendicular to V_1 and V_2)

$\overline{V_1} \times \overline{Q} = \overline{A}$

so that

$$\overline{A} = \overline{V_1} \times \overline{V_2} \times \overline{V_1}$$

which by the identity (eq. 7) is found to be

$$\overline{A} = \overline{V_2}\,(\overline{V_1}.\overline{V_1}) - \overline{V_1}\,(\overline{V_2}.\overline{V_1}) \qquad \text{(eq. 11)}$$

The magnitude is found as in part B by taking the dot product $\overline{A}.\overline{A}$ which gives:

$$|\overline{A}|^2 = (\overline{V_1}.\overline{V_2})(\overline{V_1}.\overline{V_1})(\overline{V_1}.\overline{V_1}) - (\overline{V_2}.\overline{V_1})(\overline{V_1}.\overline{V_1})(\overline{V_2}.\overline{V_1}).$$

Because of the relationships of equations 9 and 10 and because:

$$\overline{V_2} \cdot \overline{V_2} = r^2 \qquad \text{(eq. 12)}$$

the expression for $|\overline{A}|^2$ can be simplified to:

$$|\overline{A}|^2 = r^6 - r^2(\overline{V_2} \cdot \overline{V_1})^2$$

Furthermore, because:

$$\overline{V_2} \cdot \overline{V_1} = (x_1x_2 + y_1y_2 + z_1z_2)$$

it follows that

$$|\overline{A}| = \sqrt{r^6 - r^2(x_1x_2 + y_1y_2 + z_1z_2)^2}$$

D. Find the cosine of the azimuth angle, the angle between $\overline{A}$ and $\overline{N}$

$$\overline{A} \cdot \overline{N} = |\overline{A}||\overline{N}| \cos(\text{Azimuth}) \qquad \text{(eq. 13)}$$

by substituting equations 8 and 11:

$$\begin{aligned}\overline{A} \cdot \overline{N} &= [\overline{V}_2(\overline{V}_1 \cdot \overline{V}_1) - \overline{V}_1(\overline{V}_2 \cdot \overline{V}_1)] \cdot [\overline{k}(\overline{V}_1 \cdot \overline{V}_1) - \overline{V}_1(\overline{V}_1 \cdot \overline{k})] \\ &= (\overline{V}_2 \cdot \overline{k})(\overline{V}_1 \cdot \overline{V}_1)(\overline{V}_1 \cdot \overline{V}_1) - (\overline{V}_1 \cdot \overline{k})(\overline{V}_2 \cdot \overline{V}_1)(\overline{V}_1 \cdot \overline{V}_1) \\ &\quad - (\overline{V}_2 \cdot \overline{V}_1)(\overline{V}_1 \cdot \overline{V}_1)(\overline{V}_1 \cdot \overline{k}) + (\overline{V}_1 \cdot \overline{V}_1)(\overline{V}_2 \cdot \overline{V}_1)(\overline{V}_1 \cdot \overline{k})\end{aligned}$$

which after combining terms becomes:

$$\overline{A} \cdot \overline{N} = (\overline{V}_2 \cdot \overline{k})(\overline{V}_1 \cdot \overline{V}_1)^2 - (\overline{V}_1 \cdot \overline{k})(\overline{V}_2 \cdot \overline{V}_1)(\overline{V}_1 \cdot \overline{V}_1)$$

Using equations 9,10 and 12, and because $\overline{V}_2 \cdot \overline{k} = z_2$, it is found that:

$$\overline{A} \cdot \overline{N} = z_2 r^4 - (x_1x_2 + y_1y_2 + z_1z_2)\, z_1\, r^2$$

but by equation 13:

$$\cos(\text{Azimuth}) = \frac{\overline{A} \cdot \overline{N}}{|\overline{A}||\overline{N}|}$$

which gives:

$$\cos(\text{Azimuth}) = \frac{z_2 r^4 - (x_1x_2 + y_1y_2 + z_1z_2)\, z_1 r^2}{\sqrt{r^6 - r^2(x_1x_2 + y_1y_2 + z_1z_2)^2}\ \sqrt{r^4 - z_1^2 r^2}}$$

If the transformation values for x,y,z are substituted (equations 1 to 6)

it is found that:

$$\cos(\text{Azimuth}) = \frac{r^5[\sin(L_2)] - r^5\, S\, [\sin(L_1)]}{\sqrt{r^6 - r^6 S^2}\ \sqrt{r^4 - r^4 \sin^2(L_1)}}$$

where

$$\begin{aligned}S = {} & \cos(G_1)\cos(L_1)\cos(G_2)\cos(L_2) \\ & + \sin(G_1)\cos(L_1)\sin(G_2)\cos(L_2) \\ & + \sin(L_1)\sin(L_2)\end{aligned}$$

by combining terms it is found that:

$$S = [\cos (L_1) \cos (L_2)] [\cos (G_1 - G_2) + \sin (L_1) \sin (L_2)]$$

and that

$$\cos (\text{Azimuth}) = \frac{\sin (L_2) - S \sin (L_1)}{\sqrt{1 - S^2} \cos (L_1)}$$

This appears to be the simplest form of the expression.

APPENDIX 2

DATA AND RESULTS FROM CHAPTER V

Structure map. The following four pages contain a summary of the data which was assembled from the structure map, figure 5-2. The column headings have the following meanings:

Structure Number - the code number used on the map, figure 5-2

Structure Type - the following code applies:

1. Apparent grabens
2. Edges of mountain blocks
3. Undifferentiated lineaments
4. Crater chains
5. Apparent volcanic relief features
6. Small local systems of fractures
7. The general trend of sinuous rilles

Azimuth - measured azimuths

Length - measured length of structure on photograph

Relative Importance - The following code applies:

1. Obvious relief feature
2. Easily seen on metric photos
3. Can be found on monoscopic photo after search
4. Only evident in stereoscopic model

A discription of the second and third tables in this appendix is found preceding the tables.

—DATA CONCERNING STRUCTURES SURROUNDING HADLEY RILLE—

STRUCTURE NUMBER	STRUCTURE TYPE	AZIMUTH (Degrees from North)	LENGTH (mm. on photo)	RELATIVE IMPORTANCE
1	3	33	12	3
2	3	28	8	2
3	3	167	5	4
4	3	167	5	4
5	4	44	6	2
6	5	34	4	2
7	4	33	6	2
8	2	118	73	2
9	1	69	26	1
10	1	42	43	1
11	4	169	15	2
12	1	32	35	1
13	1	123	5	2
14	3	91	7	3
15	1	51	9	2
16	3	32	12	4
17	3	50	32	4
18	4	68	15	3
19	4	145	4	2
20	3	19	18	2
21	3	42	19	2
22	3	128	13	2
23	2	19	19	2
24	2	65	3	3
25	2	132	20	2
26	2	32	2	2
27	2	160	3	2
28	2	162	3	2
29	2	153	7	2
30	2	153	8	2
31	2	43	30	2
32	2	152	32	2
33	3	146	5	4
34	3	21	19	3
35	2	121	13	2
36	3	61	40	2
37	3	17	22	3
38	3	58	40	3
39	3	69	30	3
40	3	112	16	3
41	3	135	17	4
42	2	177	12	4
43	3	41	87	4
44	3	108	12	4
45	3	35	18	4
46	4	28	18	4
47	3	22	55	4
48	3	47	19	4
49	3	13	7	3
50	3	25	6	3
51	3	10	6	3
52	2	10	19	3
53	2	159	15	2
54	1	105	90	3
55	1	163	32	2
56	5	112	12	2

—DATA CONCERNING STRUCTURES SURROUNDING HADLEY RILLE (cont.)—

STRUCTURE NUMBER	STRUCTURE TYPE	AZIMUTH (Degrees from North)	LENGTH (mm. on photo)	RELATIVE IMPORTANCE
57	3	19	67	2
58	5	147	11	3
59	5	179	8	2
60	3	175	24	4
61	1	164	30	4
62	4	147	6	3
63	4	66	7	3
64	3	152	10	4
65	3	151	17	3
66	3	164	11	3
67	5	123	35	2
68	3	157	4	2
69	3	154	3	2
70	5	145	7	2
71	5	61	22	1
72	1	63	55	3
73	5	25	15	2
74	5	58	9	2
75	5	73	15	2
76	3	145	17	4
77	4	145	17	3
78	4	114	50	3
79	4	58	20	2
80	3	60	57	3
81	4	155	11	2
82	4	155	8	2
83	3	140	20	4
84	3	140	20	4
85	3	148	13	4
86	3	144	65	4
87	3	37	11	2
88	4	51	9	3
89	3	133	42	3
90	3	1	65	4
91	3	62	38	2
92	3	153	21	2
93	2	114	13	1
94	2	41	28	1
95	2	30	11	1
96	3	139	8	3
97	3	50	9	3
98	3	52	9	2
99	3	73	22	2
100	3	40	23	3
101	3	53	34	3
102	3	50	27	3
103	3	41	20	4
104	3	165	43	3
105	3	165	19	3
106	3	84	9	2
107	2	93	37	4
108	4	108	7	3
109	3	132	22	3
110	3	141	5	3
111	3	136	3	4
112	3	145	8	3
113	3	144	13	4

—DATA CONCERNING STRUCTURES SURROUNDING HADLEY RILLE (cont.)—

STRUCTURE NUMBER	STRUCTURE TYPE	AZIMUTH (Degrees from North)	LENGTH (mm. on photo)	RELATIVE IMPORTANCE
114	4	45	15	4
115	3	2	12	2
116	3	2	11	2
117	3	2	19	2
118	3	68	10	2
119	3	142	11	4
120	3	141	7	4
121	3	38	7	2
122	3	51	6	2
123	3	62	4	2
124	3	80	5	4
125	3	118	4	4
126	3	134	9	4
127	3	121	4	4
128	3	47	12	3
129	3	32	23	2
130	3	23	23	2
131	5	179	17	1
132	5	178	10	1
133	3	44	14	3
134	3	175	22	2
135	3	176	11	2
136	5	84	22	2
137	4	132	11	2
138	6	165	8	2
139	6	83	3	3
140	6	84	6	3
141	6	157	6	3
142	3	11	13	2
143	3	36	7	4
144	3	36	15	2
145	3	42	13	3
146	3	163	5	2
147	3	50	40	4
148	3	38	52	2
149	3	27	32	2
150	3	128	4	2
151	6	12	7	3
152	1	65	12	2
153	1	52	60	2
154	3	139	4	3
155	3	2	14	3
156	3	45	8	2
157	1	45	56	1
158	1	61	90	1
159	1	117	12	1
160	6	89	7	2
161	6	41	3	2
162	6	148	3	2
163	6	11	3	2
164	6	4	2	2
165	6	129	2	3
166	3	132	9	2
167	1	128	19	2
168	1	130	60	2
169	1	76	11	2
170	2	155	13	1

—DATA CONCERNING STRUCTURES SURROUNDING HADLEY RILLE (cont.)—

STRUCTURE NUMBER	STRUCTURE TYPE	AZIMUTH (Degrees from North)	LENGTH (mm. on photo)	RELATIVE IMPORTANCE
171	3	144	14	2
172	3	121	12	2
173	3	130	12	4
174	3	99	46	2
175	2	130	18	1
176	7	116	43	2
177	7	37	65	1
178	7	132	70	1
179	3	57	37	2
180	2	128	8	1
181	5	144	8	3

Results of structure classification program. The following two tables list the results of the program which classifies structures according to which basin related direction the structure azimuth most closely approximates.

The following two pages indicate the following directions from the center of each of the structures on fig. 5-2.

1. Direction radial to the Imbrium Basin
2. Direction circumferential to the Imbrium Basin
3. Direction radial to the Serenitatis Basin
4. Direction circumferential to the Serenitatis Basin.

The last two pages are a listing of the differences between these computed basin directions and the actual measured structure azimuths. This allows the determination of which basin-related direction each lineament most closely approximates. This direction is the one which has a minimum value for the diference. These values have been underlined in each case. The measured structure azimuths used to find this difference are found in the preceding tabulation.

DIRECTIONS RADIAL AND CIRCUMFERENTIAL TO BASINS FROM STRUCTURE LOCATIONS

STR.	IMBRIUM		SERENITATIS	
NO.	RADIAL	CIRCUM.	RADIAL	CIRCUM.
1	-64.8708	25.1291	88.7133	178.7133
2	-64.6734	25.3265	88.5418	178.5418
3	-64.9280	25.0719	88.8669	178.8669
4	-64.9311	25.0688	88.8754	178.8754
5	-64.1312	25.8687	87.8371	177.8371
6	-64.0639	25.9360	87.7857	177.7857
7	-64.0230	25.9769	87.7438	177.7438
8	-63.9546	26.0453	87.7901	177.7901
9	-63.8434	26.1565	87.6927	177.6927
10	-64.3202	25.6797	88.3317	178.3317
11	-64.5176	25.4823	88.6047	178.5047
12	-63.6504	26.3495	87.4536	177.4536
13	-64.1646	25.8353	88.1478	178.1478
14	-64.0655	25.9344	88.0102	178.0102
15	-64.1470	25.8529	88.1448	178.1448
16	-63.8532	26.1467	87.7584	177.7584
17	-63.2086	26.7913	86.8585	176.8585
18	-63.6240	26.3759	87.4253	177.4253
19	-63.5557	26.4442	87.3399	177.3399
20	-62.7085	27.2914	86.1744	176.1744
21	-62.8890	27.1109	86.4189	176.4199
22	-62.4798	27.5201	85.8602	175.8602
23	-62.5132	27.4867	85.8986	175.8986
24	-62.4268	27.5731	85.7995	175.7995
25	-62.2060	27.7939	85.4961	175.4961
26	-62.1270	27.8729	85.3830	175.3830
27	-62.0219	27.9780	85.2237	175.2237
28	-62.7036	27.2163	86.2782	176.2782
29	-63.1343	26.8656	86.7598	176.7598
30	-63.2342	26.7657	86.9008	176.9008
31	-63.3128	26.6871	87.0148	177.0148
32	-62.4017	27.5982	85.7027	175.7027
33	-62.5248	27.4751	85.8861	175.8861
34	-63.1532	26.8467	86.7847	176.7847
35	-63.5452	26.4547	87.3561	177.3561
36	-64.1138	25.8861	88.2177	178.2177
37	-62.7121	27.2878	86.1303	176.1303
38	-62.6986	27.3013	86.1144	176.1144
29	-62.3942	27.6057	85.6340	175.6340
40	-63.3516	26.6483	87.0766	177.0766
41	-63.1273	26.8726	86.7329	176.7329
42	-63.6735	26.3264	87.5616	177.5616
43	-62.3426	27.6573	85.5343	175.5343
44	-63.0307	26.9692	86.5862	176.5862
45	-61.5401	28.4598	84.3190	174.3190
46	-63.5486	26.4513	87.3750	177.3750
47	-60.9711	29.0288	83.4097	173.4097
48	-63.1334	26.8665	86.7218	176.7218
49	-64.9025	25.0974	89.5419	179.5419
50	-64.3568	25.6431	88.6830	178.6830
51	-64.6046	25.3953	89.1085	179.1085
52	-64.6212	25.3787	89.1497	179.1497
53	-64.7565	25.2434	89.3805	179.3805
54	-64.1116	25.8883	88.3095	178.3095
55	-63.9978	26.0021	88.1405	178.1405
56	-63.4272	26.5727	87.1074	177.1074
57	-62.1604	27.8395	84.8317	174.9317
58	-61.6526	28.3473	84.0096	174.0096
59	-60.6777	29.3222	82.0721	172.0721
60	-63.0191	26.9808	86.4995	176.4995
61	-61.7354	28.2645	84.3136	174.3136
62	-60.0559	29.9440	81.2617	171.2617
63	-60.0307	29.9692	81.2608	171.2608
64	-60.3828	29.6171	82.0272	172.0272
65	-60.1338	29.8661	81.6397	171.6397
66	-60.0957	29.9042	81.6352	171.6352
67	-60.1391	29.8608	81.8492	171.8492
68	-59.4732	30.5267	80.7166	170.7166
69	-59.4525	30.5474	80.7167	170.7167
70	-59.3593	30.6406	80.6415	170.6415
71	-59.4563	30.5436	79.9775	169.9775
72	-59.6328	30.3671	80.4699	170.4699
73	-59.0731	30.9268	79.2443	169.2443
74	-59.0022	30.9977	78.9816	168.9816
75	-58.7689	31.2310	78.5746	168.5746
76	-57.8013	32.1986	76.9659	166.9659
77	-58.3686	31.6313	78.2316	168.2316
78	-58.7107	31.2892	79.3280	169.3280
79	-58.2890	31.7109	78.6320	168.6320
80	-57.3162	32.6837	77.4779	167.4779
81	-57.0644	32.9355	76.3082	166.3082
82	-56.9587	33.0412	76.1570	166.1570
83	-57.1925	32.8074	76.9535	166.9535
84	-57.0679	32.9320	76.8129	166.8129
85	-58.3814	31.6185	79.4648	169.4648
86	-59.0931	30.9068	80.7780	170.7780
87	-58.5501	31.4498	79.6829	169.6829
88	-59.5650	30.4349	81.4916	171.4916
89	-60.4875	29.5124	82.7909	172.7909
90	-61.7094	28.2905	84.6918	174.6918
91	-61.1403	28.8596	83.9033	173.9033
92	-60.7910	29.2089	83.4138	173.4138
93	-61.6721	28.3278	84.6624	174.6624
94	-61.1120	28.8879	83.9238	173.9238
95	-60.1069	29.8931	82.5450	172.5450
96	-60.5139	29.4860	83.0521	173.0521
97	-60.4578	29.5421	82.9320	172.9320
98	-60.0109	29.9890	82.3568	172.3568
99	-59.8760	30.1239	82.0979	172.0979
100	-59.0395	30.9604	81.0351	171.0351
101	-58.6809	31.3190	80.4826	170.4826
102	-58.6151	31.3848	80.2747	170.2747
103	-58.5123	31.4876	80.0623	170.0623
104	-58.4026	31.5973	79.7727	169.7727
105	-57.7682	32.2317	78.6718	168.6718
106	-57.7883	32.2116	78.5836	168.5836
107	-58.1498	31.8501	79.6402	169.6402
108	-60.5641	29.4358	83.2944	173.2944
109	-59.2652	30.7347	81.1921	171.1921
110	-56.7565	33.2434	77.9087	167.9087
111	-57.1383	32.8616	78.5475	168.5475
112	-56.9942	33.0057	78.1798	168.1798
113	-56.7126	33.2873	77.6714	167.6714

DIRECTIONS RADIAL AND CIRCUMFERENTIAL TO BASINS FROM STRUCTURE LOCATIONS

STR.	IMBRIUM		SERENITATIS	
NO.	RADIAL	CIRCUM.	RADIAL	CIRCUM.
114	-56.3964	33.6035	77.6699	167.6699
115	-56.8765	33.1234	78.3596	168.3596
116	-56.8585	33.1414	78.3626	168.3626
117	-56.6167	33.3832	78.0974	168.0974
118	-56.9477	33.0522	78.5006	168.5006
119	-57.9462	32.0537	79.7201	169.7201
120	-57.7840	32.2159	79.5156	169.5156
121	-59.2905	30.7094	81.6113	171.6113
122	-59.2761	30.7238	81.6078	171.6078
123	-59.1352	30.8647	81.4644	171.4644
124	-57.7813	32.2186	79.7220	169.7220
125	-58.3962	31.6037	80.5250	170.5250
126	-58.1836	31.8163	80.2570	170.2570
127	-58.4662	31.5337	80.7144	170.7144
128	-58.5205	31.4794	80.7217	170.7217
129	-58.3865	31.6134	80.4620	170.4620
130	-58.4257	31.5742	80.4653	170.4653
131	-59.0846	30.9153	81.2840	171.2840
132	-59.0699	30.9300	81.2812	171.2812
133	-57.3161	32.6838	79.2579	169.2579
134	-57.4889	32.5110	79.5890	169.5890
135	-57.2123	32.7876	79.2618	169.2618
136	-56.9375	33.0624	78.8658	168.8658
137	-57.0592	32.9407	79.1329	169.1329
138	-56.8157	33.1842	78.8055	168.8055
139	-56.9494	33.0505	79.0029	169.0029
140	-57.0416	32.9583	79.1336	169.1336
141	-56.7978	33.2021	78.8069	168.8069
142	-56.0123	33.9876	78.0470	168.0470
143	-55.6275	34.3724	77.6731	167.6731
144	-56.0068	33.9931	78.1189	168.1189
145	-55.7566	34.2433	77.9400	167.9400
146	-57.0467	32.9532	79.2653	169.2653
147	-56.8383	33.1614	79.1389	169.1389
148	-60.5685	29.4314	83.3363	173.3363
149	-59.2849	30.7150	81.8675	171.8675
150	-58.7445	31.2554	81.1596	171.1596
151	-59.9554	30.0445	82.6670	172.6670
152	-57.9716	32.0283	80.4162	170.4162
153	-56.5040	33.4959	78.9528	168.9528
154	-57.5997	32.4002	80.0284	170.0284
155	-60.3474	29.6525	83.1010	173.1010
156	-60.6873	29.3126	83.5866	173.5866
157	-59.2345	30.7654	81.8512	171.8512
158	-57.1646	32.8353	79.7589	169.7589
159	-58.9963	31.0036	81.6333	171.6333
160	-60.2784	29.7215	83.1400	173.1400
161	-60.3600	29.6399	83.2208	173.2208
162	-60.3171	29.6828	83.1611	173.1611
163	-60.2248	29.7751	83.0376	173.0376
164	-60.2313	29.7686	83.0410	173.0410
165	-60.1950	29.8049	82.9838	172.9838
166	-59.3275	30.6724	82.0216	172.0216
167	-59.7417	30.2582	82.6079	172.6079
168	-60.5993	29.4006	83.7201	173.7201
169	-61.0505	28.9494	84.2267	174.2267
170	-58.6227	31.3772	81.2856	171.2856

STR.	IMBRIUM		SERENITATIS	
NO.	RADIAL	CIRCUM.	RADIAL	CIRCUM.
171	-58.9214	31.0785	81.7873	171.7873
172	-59.3525	30.6474	82.3149	172.3150
173	-58.8194	31.1805	81.7890	171.7890
174	-61.0524	28.9475	84.2897	174.2897
175	-60.4227	29.5772	83.6395	173.6395
176	-59.5910	30.4089	82.5351	172.5351
177	-60.8053	29.1946	83.5469	173.5469
178	-62.8654	27.1345	86.3889	176.3889
179	-58.9461	31.0538	81.3663	171.3663
180	-59.0971	30.9028	81.8940	171.8940
181	-57.8584	32.1415	80.1701	170.1701

DIFFERENCES BETWEEN STRUCTURE AZIMUTHS AND FOUR BASIN RELATED DIRECTIONS
(Minimum differences which therefore indicate closest relationship are underlined)

STR. NO.	IMBRIUM RADIAL	IMBRIUM CIRCUM.	SERENITATIS RADIAL	SERENITATIS CIRCUM.
1	82.1292	7.8711	55.7135	34.2868
2	87.3268	2.6735	60.5420	29.4582
3	51.9280	38.0723	78.1331	11.8672
4	51.9312	38.0691	78.1245	11.8758
5	71.8686	18.1309	43.8369	46.1626
6	81.9361	8.0642	53.7858	36.2145
7	82.9771	7.0232	54.7439	35.2564
8	1.9547	88.0456	30.2099	59.7904
9	47.1563	42.8432	18.6925	71.3071
10	73.6796	16.3199	46.3316	43.6679
11	53.5177	36.4826	80.3953	9.6050
12	84.3498	5.6505	55.4537	34.9466
13	7.1648	82.8355	34.8524	55.1479
14	24.9344	65.0651	2.9897	87.0106
15	64.8525	25.1470	37.1452	52.8551
16	84.1469	5.8534	55.7586	34.2417
17	66.7910	23.2085	36.8588	53.1415
18	48.3758	41.6237	19.4251	70.5744
19	28.5558	61.4445	57.6602	32.3401
20	81.7087	8.2916	67.1741	22.8254
21	75.1108	14.8887	44.4187	45.5808
22	10.4801	79.5202	42.1394	47.8601
23	81.5133	8.4870	66.8983	23.1012
24	52.5732	37.4271	20.7994	69.2001
25	14.2056	75.7939	46.5036	43.4959
26	85.8732	4.1271	53.3830	36.6173
27	42.0217	47.9778	74.7761	15.2234
28	44.7834	45.2161	75.7216	14.2779
29	36.1347	53.8656	66.2398	23.7597
30	36.2345	53.7657	66.0987	23.9008
31	73.6870	16.3125	44.0146	45.9849
32	34.4020	55.5983	66.2968	23.7027
33	28.5249	61.4754	60.1140	29.8863
34	84.1534	5.8469	65.7844	24.2151
35	4.5453	85.4550	33.6441	56.3562
36	54.8862	35.1141	27.2177	62.7825
37	79.7122	10.2881	69.1300	20.8695
38	59.3015	30.6988	28.1144	61.8859
29	48.6056	41.3939	16.6337	73.3658
40	4.6484	85.3519	24.9233	65.0762
41	18.1271	71.8724	48.2669	41.7326
42	60.6738	29.3265	89.4387	0.5616
43	76.6573	13.3422	44.5341	45.4654
44	8.9695	81.0308	21.4136	68.5859
45	83.4600	6.5403	49.3189	40.6806
46	88.4517	1.5486	59.3753	30.6250
47	82.9712	7.0290	61.4100	28.5903
48	69.8663	20.1333	39.7215	50.2780
49	77.9026	12.0977	76.5418	13.4577
50	89.3572	0.6431	63.6834	26.3169
51	74.6046	15.3949	79.1085	10.8918
52	74.6211	15.3784	79.1498	10.8505
53	43.7563	46.2432	69.6192	20.3803
54	10.8886	79.1117	16.6901	73.3094
55	46.9977	43.0018	74.8594	15.1401
56	4.5729	85.4274	24.8924	65.1071
57	81.1605	8.8398	65.9314	24.1681
58	28.6527	61.3476	62.9907	27.0096
59	59.6780	30.3223	83.0723	6.9280
60	58.0194	31.9809	88.5008	1.4995
61	45.7352	44.2643	79.6864	10.3139
62	27.0560	62.9443	65.7378	24.2617
63	53.9693	36.0310	15.2605	74.7390
64	32.3830	57.6173	69.9725	20.0270
65	31.1339	58.8664	69.3600	20.6395
66	44.0955	45.9040	82.3648	7.6355
67	3.1392	86.8611	41.1504	48.8491
68	36.4735	53.5268	76.2833	13.7162
69	33.4527	56.5476	73.2831	16.7164
70	24.3592	65.6403	64.3580	25.6415
71	59.5438	30.4565	18.9773	71.0222
72	57.3673	32.6330	17.4696	72.5299
73	84.0733	5.9270	54.2444	35.7559
74	62.9980	27.0023	20.9814	69.0181
75	48.2309	41.7686	5.5747	84.4256
76	22.8012	67.1983	68.0337	21.9658
77	23.3686	66.6309	66.7680	23.2315
78	7.2894	82.7109	34.6722	55.3261
79	63.7113	26.2890	20.6319	69.3676
80	62.6840	27.3163	17.4776	72.5219
81	32.0646	57.9357	78.6917	11.3086
82	31.9589	58.0414	78.8430	11.1573
83	17.1923	72.8072	63.0468	26.9535
84	17.0676	72.9319	63.1873	26.8130
85	26.3814	63.6189	68.5346	21.4647
86	23.0930	66.9065	63.2223	26.7780
87	84.4501	5.5502	42.6826	47.3169
88	69.4347	20.5648	30.4917	59.5086
89	13.4871	76.5124	50.2090	39.7905
90	62.7097	27.2906	83.6920	6.3083
91	56.8597	33.1406	21.9031	68.0964
92	33.7912	56.2091	69.5859	20.4136
93	4.3279	85.6724	29.3377	60.6626
94	77.8879	12.1124	42.9235	47.0760
95	89.8935	0.1068	52.5450	37.4553
96	19.5137	70.4858	55.9479	34.0524
97	69.5419	20.4576	32.9323	57.0680
98	67.9887	22.0108	30.3570	59.6433
99	47.1238	42.8757	9.0982	80.9021
100	80.9605	9.0398	41.0348	48.9647
101	68.3187	21.6808	27.4827	62.5176
102	71.3846	18.6149	30.2749	59.7254
103	80.4877	9.5126	39.0619	50.9376
104	43.4023	46.5972	85.2275	4.7728
105	42.7680	47.2315	86.3284	3.6719
106	38.2120	51.7883	5.4165	84.5838
107	28.8502	61.1501	13.3593	76.6402
108	11.4361	78.5642	24.7055	65.2940
109	11.2655	78.7348	50.8078	39.1917
110	17.7563	72.2432	63.0915	26.9088
111	13.1379	76.8616	57.4526	32.5477
112	21.9940	68.0055	66.8198	23.1797
113	20.7125	69.2870	66.3282	23.6713

DIFFERENCES BETWEEN STRUCTURE AZIMUTHS AND FOUR BASIN RELATED DIRECTIONS
(Minimum differences which therefore indicate closest relationship are underlined)

STR. NO.	IMBRIUM RADIAL	IMBRIUM CIRCUM.	SERENITATIS RADIAL	SERENITATIS CIRCUM.
114	78.6035	11.3968	32.6701	57.3302
115	58.8767	31.1236	76.3595	13.6400
116	58.8588	31.1415	76.3625	13.6370
117	58.6169	31.3834	76.0974	13.9021
118	55.0523	34.9480	10.5009	79.4994
119	19.9461	70.0535	62.2801	27.7202
120	18.7838	71.2157	61.4846	28.5157
121	82.7096	7.2907	43.6110	46.3885
122	69.7236	20.2759	30.6079	59.3924
123	58.8650	31.1353	19.4642	70.5353
124	42.2183	47.7812	0.2779	89.7223
125	3.6038	86.3965	37.4753	52.5250
126	12.1840	77.8163	53.7429	36.2574
127	0.5337	89.4665	40.2851	49.7144
128	74.4793	15.5202	33.7220	56.2783
129	89.6138	0.3865	48.4619	41.5376
130	81.4259	8.5744	57.4655	32.5348
131	58.0848	31.9155	82.2842	7.7161
132	57.0701	32.9302	82.2814	6.7189
133	78.6838	11.3165	35.2582	54.7421
134	52.4890	37.5113	84.5892	5.4111
135	53.2124	36.7879	83.2620	6.7383
136	39.0620	50.9375	5.1343	84.8660
137	9.0595	80.9408	52.8671	37.1332
138	41.8154	48.1841	86.1946	3.8056
139	40.0501	49.9494	3.9971	86.0031
140	38.9579	51.0416	4.8665	85.1338
141	33.7980	56.2023	78.1930	11.8073
142	67.0120	22.9875	67.0467	22.9528
143	88.3728	1.6275	41.6728	48.3267
144	87.9934	2.0069	42.1186	47.8809
145	82.2435	7.7568	35.9403	54.0600
146	40.0463	49.9532	83.7348	6.2655
147	73.1612	16.8383	29.1390	60.8613
148	81.4316	8.5687	45.3361	44.6634
149	86.2852	3.7151	54.8676	35.1327
150	6.7447	83.2556	46.8402	43.1593
151	71.9552	18.0443	70.6668	19.3327
152	57.0284	32.9718	15.4129	74.5836
153	71.4958	18.5038	26.9526	63.0475
154	16.5994	73.4001	58.9718	31.0285
155	62.3477	27.6526	81.1012	8.8991
156	74.3125	15.6870	38.5862	51.4133
157	75.7653	14.2342	36.8515	53.1488
158	61.8356	28.1647	18.7587	71.2408
159	4.0038	85.9965	35.3669	54.6334
160	30.7216	59.2787	5.8601	84.1402
161	78.6400	11.3603	42.2205	47.7790
162	28.3172	61.6831	64.8384	25.1611
163	71.2247	18.7749	72.0374	17.9621
164	64.2317	25.7686	79.0410	10.9593
165	9.1952	80.8050	46.0159	43.9836
166	11.3279	78.6724	49.9782	40.0213
167	7.7419	82.2584	45.3918	44.6077
168	10.5997	79.4006	46.2796	43.7199
169	42.9491	47.0504	8.2270	81.7733
170	33.6229	56.3774	73.7142	16.2853
171	22.9213	67.0782	62.2130	27.7873
172	0.3525	89.6478	38.6846	51.3149
173	8.8197	81.1806	48.2108	41.7887
174	19.9473	70.0522	14.7098	75.2897
175	10.4230	79.5773	46.3602	43.6393
176	4.4091	85.5912	33.4651	56.5352
177	82.1948	7.8055	46.5468	43.4527
178	14.8651	75.1344	45.6108	44.3887
179	64.0542	25.9461	24.3663	65.6332
180	7.0973	82.9030	46.1058	43.8937
181	21.8583	68.1412	63.8302	26.1701

APPENDIX 3

DATA AND RESULTS FROM CHAPTER VI

Mann comparator data reduction. The following three pages contain a listing of the basic rille parameters obtained from the Mann comparator data for each measurement location. The measurement locations are specified on figure 6-2.

The distance along the rille channel between any two measurement locations may be computed by subtracting the cumulative distance value for the southern-most location from the value for the northern-most location.

The azimuths reported here are the azimuths used for the structure-rille comparisons reported in chapter V. The azimuths have arbitrarily been placed in the two eastern quadrants.

Profile data. The second tabulation in this appendix is a listing of the data and calculated values obtain by direct measurement from profiles.

Fourier analysis. The third tabulation in this appendix is a listing of the Fourier analysis results for the northern and southern rille sections.

—DETERMINATION OF BASIC RILLE PARAMETERS FROM MANN COMPARATOR DATA—

MEASUREMENT LOCATION (fig. 6-2)	WIDTH	DISTANCE BETWEEN LOCATIONS	CUMULATIVE DISTANCE	AZIMUTH BETWEEN LOCATIONS
1	3.221	0.000	0.000	0.0
2	2.234	1.432	1.432	134.4
3	1.591	1.023	2.456	79.9
4	1.692	0.551	3.007	98.8
5	1.639	0.702	3.709	54.7
6	1.556	0.964	4.674	51.3
7	1.350	0.797	5.471	46.0
8	1.343	0.620	6.091	26.9
9	1.391	0.352	6.444	24.4
10	1.372	0.405	6.850	7.8
11	1.380	0.251	7.101	163.3
12	1.321	0.625	7.727	154.8
13	1.296	0.872	8.599	177.4
14	1.237	1.004	9.604	5.0
15	1.317	0.293	9.897	22.6
16	1.156	0.714	10.611	20.1
17	1.230	0.768	11.380	13.5
18	1.250	0.542	11.923	37.9
19	1.288	0.217	12.140	24.8
20	1.221	0.426	12.567	173.5
21	1.122	0.408	12.975	155.1
22	1.135	0.420	13.396	163.2
23	1.187	0.379	13.775	11.2
24	1.161	0.297	14.073	49.2
25	1.078	0.780	14.853	74.4
26	1.037	0.897	15.751	74.4
27	1.033	0.785	16.537	82.2
28	1.290	0.552	17.090	69.1
29	1.451	0.454	17.545	33.7
30	1.497	0.315	17.860	3.9
31	1.452	0.427	18.287	177.9
32	1.451	0.644	18.932	21.2
33	1.418	1.190	20.122	55.2
34	1.423	1.091	21.214	78.4
35	1.435	0.978	22.192	89.1
36	1.432	0.504	22.697	74.0
37	1.294	0.761	23.458	49.9
38	1.187	0.893	24.351	71.0
39	1.057	0.774	25.125	71.5
40	1.022	0.441	25.566	53.4
41	1.085	0.817	26.384	46.5
42	1.040	0.930	27.315	31.7
43	1.273	0.575	27.890	23.7
44	1.236	0.529	28.420	173.4
45	1.249	0.884	29.304	173.1
46	1.003	5.766	35.071	176.3
47	1.002	0.612	35.683	19.3
48	1.077	0.634	36.318	4.6
49	1.124	0.464	36.783	13.7
50	1.076	0.414	37.197	21.6
51	1.033	0.429	37.627	43.9
52	0.963	1.088	38.715	61.4
53	0.890	0.472	39.188	72.2
54	1.072	0.477	39.665	79.4
55	0.946	0.587	40.253	46.7
56	0.841	0.382	40.635	59.7

—DETERMINATION OF BASIC RILLE PARAMETERS FROM MANN COMPARATOR DATA (cont.)—

MEASUREMENT LOCATION (fig. 6-2)	WIDTH	DISTANCE BETWEEN LOCATIONS	CUMULATIVE DISTANCE	AZIMUTH BETWEEN LOCATIONS
57	0.902	0.462	41.097	80.7
58	0.900	0.378	41.476	83.1
59	0.982	0.548	42.025	119.3
60	0.972	0.561	42.586	110.6
61	1.389	0.897	43.484	72.2
62	1.136	0.381	43.865	169.1
63	1.056	0.498	44.364	156.6
64	1.106	0.681	45.046	9.5
65	1.239	0.788	45.834	12.7
66	1.298	0.750	46.585	19.4
67	1.366	0.677	47.263	13.0
68	1.286	0.826	48.089	159.2
69	1.184	1.188	49.277	22.4
70	1.092	1.046	50.324	33.3
71	0.969	1.216	51.541	66.6
72	1.172	0.961	52.502	97.0
73	0.945	0.999	53.502	93.1
74	0.865	0.743	54.246	95.0
75	0.833	0.824	55.070	93.8
76	1.054	0.774	55.844	114.9
77	1.259	1.520	57.365	51.7
78	1.060	0.684	58.050	179.9
79	1.044	0.365	58.415	3.0
80	1.050	1.146	59.562	54.6
81	1.102	1.148	60.710	87.6
82	1.005	0.782	61.493	80.3
83	1.344	0.463	61.957	76.8
84	1.336	0.617	62.574	24.2
85	1.234	0.404	62.978	169.3
86	1.252	0.701	63.680	148.2
87	1.322	0.751	64.432	145.2
88	1.341	0.762	65.194	150.0
89	1.183	0.963	66.158	167.4
90	0.943	0.828	66.986	147.9
91	1.016	1.035	68.021	148.4
92	1.205	1.011	69.032	155.7
93	1.172	0.726	69.759	122.0
94	1.117	0.949	70.709	130.4
95	0.912	0.667	71.376	134.8
96	1.029	0.550	71.927	127.9
97	0.825	1.128	73.056	126.4
98	0.860	0.772	73.828	125.5
99	1.014	0.626	74.455	113.2
100	0.989	0.571	75.026	89.4
101	0.928	0.268	75.295	74.8
102	0.686	0.731	76.027	62.0
103	0.417	0.651	76.678	58.7
104	0.216	0.872	77.551	70.8
105	1.097	1.157	78.709	84.0
106	0.863	0.861	79.570	49.2
107	1.165	1.029	80.600	55.4
108	1.002	0.868	81.468	83.5
109	0.880	0.435	81.904	98.5
110	0.[illegible]59	2.575	84.479	117.3
111	0.[illegible]55	0.730	85.209	142.0
112	1.007	0.895	86.105	130.8
113	0.823	0.795	86.900	120.5

—DETERMINATION OF BASIC RILLE PARAMETERS FROM MANN COMPARATOR DATA (cont.)—

MEASUREMENT LOCATION (fig. 6-2)	WIDTH	DISTANCE BETWEEN LOCATIONS	CUMULATIVE DISTANCE	AZIMUTH BETWEEN LOCATIONS
114	0.946	0.904	87.805	138.9
115	0.831	5.334	93.140	131.7
116	1.159	0.688	93.829	161.4
117	0.849	3.413	97.242	148.9
118	0.793	0.584	97.827	27.8
119	0.809	0.368	98.195	10.4
120	0.592	0.417	98.612	137.2
121	0.653	0.650	99.263	143.2
122	0.608	0.428	99.691	179.3
123	0.534	0.383	100.075	31.6
124	0.523	0.516	100.592	7.8
125	0.649	0.666	101.258	151.2
126	0.649	0.727	101.985	126.5
127	0.644	0.657	102.643	128.8
128	0.714	6.345	108.988	107.2
129	0.708	0.636	109.624	155.1
130	0.618	1.088	110.712	159.7
131	0.783	0.916	111.629	161.3
132	0.680	0.937	112.567	167.0
133	0.814	1.233	113.801	166.7
134	0.826	0.859	114.660	34.5
135	0.987	0.396	115.057	83.0
136	0.877	0.455	115.512	10.3
137	0.827	0.500	116.012	6.3
138	0.909	0.654	116.667	5.4
139	0.977	0.555	117.222	0.2
140	1.031	0.296	117.518	168.5
141	0.892	1.843	119.362	13.5
142	1.048	1.307	120.669	38.5
143	0.937	0.455	121.125	9.5
144	1.199	0.952	122.077	8.9
145	1.355	0.872	122.950	161.6
146	0.958	0.943	123.894	144.5
147	0.880	0.955	124.849	117.5
148	1.092	0.633	125.483	144.8
149	1.186	1.282	126.765	152.0
150	1.781	1.031	127.797	150.1
151	2.600	1.040	128.838	126.4
152	2.725	0.882	129.720	125.6

This table is a listing of the data which was measured directly from profiles. The profiles are found in chapter 4.

PROFILE NUMBER	DEPTH (meters)	W/D ratio	CROSS-SECTIONAL AREA (Planimeter measurement- 10^4 meters)
1	350	3.99	29.0
2	321	4.29	24.7
3	265	4.37	17.8
4	277	4.06	18.1
5	228	4.50	15.4
6	231	4.63	16.1
6a	226	4.69	15.5
7	228	5.20	12.5
8	242	5.74	20.2
9	Rille obscured by Hadley C		
10	241	4.30	16.2
11	280	3.79	17.7
12	228	4.07	14.3
13	267	4.06	16.8
14	245	3.73	14.0
15	287	3.73	13.7
16	217	4.56	13.5
17	259	4.87	23.9
18	304	3.86	21.9
19	303	4.16	20.6
20	274	4.19	18.9
21	265	4.18	16.3
22	305	3.87	21.2
23	264	3.73	15.2
24	217	4.34	19.8
25	238	4.53	12.4
26	116	6.26	not used in average
27	not a transverse profile		
28	" " " "		
29	" " " "		
30	120	6.17	5.72
30a	195	4.72	8.21

Results of Fourier Analysis: North 1/2 of Rille

This page lists the coefficients for the first 35 terms of the Fourier cosine series, the power spectrum and the root power spectrum for the south section of Hadley Rille. The units are arbitrary values.

THERE ARE 159 DATA POINTS IN THE DATA DECK
THE X SPACING IS 0.2500000
L =39.5000001 X ZERO = 0.0000000
A0 = 5.0991087

N	COS. COEF.	POWER SPECTRUM	ROOT POWER SPECTRUM
1	-0.8449922	0.7140117	0.8449921
2	-3.2269043	10.4129104	3.2269039
3	0.2050915	0.0420625	0.2050915
4	-0.9696233	0.9401692	0.9696232
5	1.4446780	2.0870943	1.4446778
6	0.2657320	0.0706135	0.2657319
7	0.2092852	0.0438003	0.2092852
8	0.6277210	0.3940336	0.6277209
9	-0.3822977	0.1461515	0.3822976
10	-0.2258743	0.0510192	0.2258743
11	-0.2034238	0.0413812	0.2034237
12	0.1210906	0.0146629	0.1210906
13	-0.0497057	0.0024706	0.0497057
14	0.2757021	0.0760116	0.2757020
15	0.1561999	0.0243984	0.1561999
16	-0.0360223	0.0012976	0.0360223
17	0.0303011	0.0009181	0.0303011
18	-0.1506940	0.0227086	0.1506940
19	-0.0812460	0.0066009	0.0812460
20	-0.0987620	0.0097539	0.0987619
21	0.0753786	0.0056819	0.0753786
22	0.0787523	0.0062019	0.0787523
23	0.0912511	0.0083267	0.0912511
24	-0.0245994	0.0006051	0.0245994
25	0.0296989	0.0008820	0.0296989
26	-0.0591724	0.0035013	0.0591724
27	-0.0298900	0.0008934	0.0298900
28	-0.0294490	0.0008672	0.0294490
29	-0.0222785	0.0004963	0.0222785
30	0.0579500	0.0033582	0.0579500
31	0.0067466	0.0000455	0.0067466
32	0.0433601	0.0018801	0.0433601
33	-0.0258160	0.0006664	0.0258160
34	0.0058615	0.0000343	0.0058615
35	-0.0351805	0.0012376	0.0351805

Results of Fourier Analysis: South 1/2 of Rille

This page lists the coefficient for the first 35 terms of the Fourier cosine series, the power spectrum and the root power spectrum for the south section of Hadley rille. The units are arbitrary values.

THERE ARE 153 DATA POINTS IN THE DATA DECK
THE X SPACING IS 0.2500000
L =38.0000001 X ZERO = 0.0000000
A0 = 1.0539224

N	COS. COEF.	POWER SPECTRUM	ROOT POWER SPECTRUM
1	-0.3565786	0.1271483	0.3565785
2	-0.6115021	0.3739348	0.6115020
3	0.7864060	0.6184343	0.7864059
4	-0.7050439	0.4970867	0.7050437
5	-0.7818020	0.6112142	0.7818019
6	-0.3242842	0.1051602	0.3242841
7	0.2291068	0.0524899	0.2291068
8	0.5789175	0.3351453	0.5789173
9	-0.5986967	0.3584376	0.5986965
10	0.3529534	0.1245761	0.3529534
11	0.1026809	0.0105433	0.1026808
12	0.0734645	0.0053970	0.0734645
13	0.1744639	0.0304376	0.1744639
14	0.1366625	0.0186766	0.1366625
15	-0.1311192	0.0171922	0.1311191
16	0.1482985	0.0219924	0.1482985
17	-0.1425915	0.0203323	0.1425915
18	0.2168260	0.0470135	0.2168259
19	-0.0951713	0.0090575	0.0951713
20	0.2786028	0.0776195	0.2786028
21	-0.1130992	0.0127914	0.1130992
22	0.1291523	0.0166803	0.1291523
23	-0.0982401	0.0096511	0.0982401
24	-0.0811495	0.0065852	0.0811495
25	-0.0620659	0.0038521	0.0620659
26	0.0267561	0.0007158	0.0267561
27	0.0196858	0.0003875	0.0196858
28	0.0343103	0.0011771	0.0343103
29	0.0621966	0.0038684	0.0621966
30	-0.0055480	0.0000307	0.0055480
31	0.0078379	0.0000614	0.0078379
32	0.0250842	0.0006292	0.0250842
33	-0.0484400	0.0023464	0.0484400
34	0.0386301	0.0014922	0.0386301
35	0.0459434	0.0021107	0.0459434

APPENDIX 4

COMPUTER PROGRAMS

This appendix is a listing of the important programs which have been developed for this study. The programs are described in chapter III. Their order in the appendix is:

1. FORIER
2. SELECT
3. SPENCR
4. RILLE
5. BASIN

—PROGRAM FORIER—

```
PAGE   1

// JOB T

LOG DRIVE   CART SPEC   CART AVAIL  PHY DRIVE
  0000        0051        0051        0000

V2 M10   ACTUAL  8K  CONFIG  8K

// FOR
*LIST SOURCE PROGRAM
*IOCS(CARD,1132 PRINTER)
*ONE WORD INTEGERS
      REAL  L, INCRE
      DIMENSION   DATA (400) , ACOEF (200)  ,  BCOEF ( 200)
C     THIS PROGRAM GENERATES A FOURIER SERIES FROM EQUALLY SPACED DATA.
C     THE INPUT SEGMENT TAKES DATA WHICH IS NOT DISTRIBUTED OVER PLUS
C     PLUS AND MINUS L AND CHANGES THE ORIGIN TO DO SO AFTER COMPUTING
C     L.  IT ALSO COUNTS THE DATA TO FIND K.  A CARD WITH DATUM GREATER
C     THAN 1,000,000. MUST BE PLACED AT THE END OF THE DECK TO TERMINATE
C     THE INPUT.  XZERO IS THE SMALLEST X VALUE, INCRE IS THE VALUE BY
C     WHICH X IS INCREMENTED
C     SIG1 INDICATES THAT A COSINE SERIES IS TO BE COMPUTED.
      READ (2,10)  INCRE,     XZERO      , PLACE    , SIG1
10    FORMAT ( 4F10.0)
C     THIS SEGMENT CHECKS TO SEE IF A MULTIPLICATION FACTOR HAS BEEN
C     ASSIGNED TO THE INPUT DATA, AND IF NOT, ASSIGNS A VALUE OF 1.
      IF (PLACE )   800, 801, 800
801   PLACE = 1.0
800   CONTINUE
C     CHECK P IS USED BELOW TO CHECK X DATA
      CHE KP   =  XZERO  -  INCRE
      K  =  0
      DO 19  IL = 1, 200
      READ  (2,  12)  XCO RD,    DATUM
12    FORMAT   (  F16.0,    F10.0  . )
C     THIS CHECKS FOR THE END OF THE DECK
      IF (DATUM - 1000000.    )  13,  20,  20
13    CONTINUE
C     K IS THE NUMBER OF DATA POINTS
      K = K + 1
C     CHECK TO ASSURE THAT EACH X VALUE AS READ IS ONE INCREMENT FROM THE
C     PRECEEDING X VALUE.  THIS CHECKS FOR ERRORS IN THE DIGITIZER OR CARDS IN
C     THE WRONG ORDER.
      CHECK = XCO RD - CHE KP
      IF   (ABS ( CHECK - INCRE )  - .00001 ) 16, 17, 17
17    CONTINUE
      CHE K1 = CHE KP + INCRE
      WRITE (3, 18)  K,  XCO RD,  CHE K1
18    FORMAT  (  ' XCOORDINATES LOUSED UP,  DATA CARD'  I4 ' READS  AN
     XX VALUE OF'     F 15.7 ' WHICH SHOULD BE' F15.7  )
      GO TO 52
16    CONTINUE
      CHE KP   =  XCO RD
C     THIS CHECKS TO SEE IF NEGATIVE VALUES OF Y ARE EQUAL TO 1,000,000
C     PLUS Y SINCE THE MSC COMPARATOR PRINTS CARDS THIS WAY.
C     IF SO, A CORRECTION IS MADE.
```

```
PAGE   2

      IF(DATUM -  100000.)  810, 811, 811
811   DATUM = DATUM - 1000000.
810   CONTINUE
      DATA (K) = DATUM * PLACE
19    CONTINUE
20    CONTINUE
      INCRE = INCRE * PLACE
C     JUMP AROUND THIS SEGMENT IF COSINE SERIES IS TO BE COMPUTED
      IF (SIG1  ) 905,905,30
905   CONTINUE
C     IS K EVEN OR ODD   IF EVEN, THE LAST DATA POINT IS HENCEFORTH IGNORED
C     BY SUBTRACTING 1 FROM K, AND A MESSAGE IS PRINTED
      N = K/2
C     IS K ODD
      HTWIC  = 2 * N
      IF (HTWIC  - K  )  30, 22, 22
22    CONTINUE
      WRITE ( 3, 25  )  K, INCRE
25    FORMAT ('  THERE ARE '  I4 ' DATA POINTS IN THE DATA DECK.'      /'
     XTHE LAST ONE HAS BEEN DELETED IN THE ANALYSIS SINCE AN ODD NUMBER
     XIS REQUIRED.'.  /   ' THE X SPACING IS'  F10.7  )
      K = K - 1
      N = K/2
      GO TO 34
30    CONTINUE
      WRITE (3,27)    K, INCRE
27    FORMAT ( ' THERE ARE'I4' DATA POINTS IN THE DATA DECK'/' THE X SPA
     XCING IS'  F10.7              )
34    CONTINUE
C     FIND 2L, THUS L, AND CHANGE XZERO TO MINUS L
      AKM1  =  K - 1
      TWOL = AKM1 * INCRE
      L = TWOL / 2.
      XZERO = - L
C     SKIP THIS SEGMENT IF A COSINE SERIES IS TO BE COMPUTED
      IF (SIG1)  907,907,906
906   L = TWOL
      XZERO = 0.
907   CONTINUE
      WRITE (3,31)  L    , XZERO
31    FORMAT  (' L =' F10.7    '   X ZERO =' F10.7                    )
C     COMPUTE THE FOURIER COEFFICIENTS.
      KMI = K - 1
      SUM = 0.
      DO 40  I = 2, KM1
      SUM = SUM + DATA (I)
40    CONTINUE
      ACO FO =(2./AKM1 ) *((DATA (1)  + DATA (K))  / 2.  +  SUM    )
      WRITE(3,41)   ACO FO
41    FORMAT  (' A0 = ' F10.7//9X  'AN' 18X 'BN' 12X 'POWER SPECTRUM'
     X  9X  'ROOT P.S.'                                          )
C     THIS FORMAT GIVES 4 COLUMNS 20 SPACES WIDE WITH CENTERED HEADINGS
C     THE SAME FORMAT IS USED BELOW.
      PI = 3.1415926
C     THIS SEGMENT GIVES AN APPROPRIATE VALUE TO N IF A COSINE SERIES IS TO
```

```
PAGE   3  -

C      BE COMPUTED.
       IF (SIG1)  925, 925, 926
926    N = K - 1
925    CONTINUE
       DO 43  IA = 1,  N
       COSUM  =  0.
       SINSU   =  0.
       REALN = IA
       DO 44  I =  2,  KM1
C.     GENERATE X VALUES-  THIS AVOIDS STORAGE
       BI = I-1
       XI = XZERO  +  BI  * INCRE
C      FIND COEFFICIENTS  AN, BN
       COSUM = COSUM  + DATA (I)  *  COS  (( PI * REALN * XI ) / L  )
C      SKIP THIS SEGMENT IF A COSINE SERIES IS TO BE COMPUTED
       IF (SIG1) 935, 935, 936
935    CONTINUE
       SINSU =SINSU   + DATA (I)  *  SIN  (( PI * REALN * XI ) / L  )
936    CONTINUE
44     CONTINUE
       ACOEF(IA) = (2./AKM1)*((DATA(1)+DATA(K))*COS(REALN*PI) /2. +COSUM)
       BCOEF (IA)  =  (2./AKM1)  * SINSU
       POWER  = ACOEF (IA) ** 2 +  BCOEF (IA) ** 2
       SQRTP  = SQRT (POWER  )
       WRITE(3, 49)   ACOEF (IA),  BCOEF (IA)  , POWER , SQRTP
49     FORMAT (4(F15.7, 8X   ))
43     CONTINUE
       WRITE (3,51)
51     FORMAT ( 7X ' XVALUE' 11X 'INPUT DATA' 13X'FOURIER APPROX.' 13X
      X  'RESIDUAL'                                          )
       DO 50  I = 1,K
       TOTAL = 0.
       REALI = I - 1
       XI = XZERO + REALI * INCRE
       DO 45  J = 1,N
       REALJ = J
       TOTAL = TOTAL + ACOEF (J) * COS (REALJ * PI * XI /L)
      X + BCOEF(J) * SIN (REALJ * PI * XI/L )
45     CONTINUE
       FX = ACO F0/2.0  +  TOTAL
       D = DATA(I) - FX
       WRITE (3, 60)  XI,  DATA (I),  FX,  D
60     FORMAT (4  ( F15.7, 8X))
50     CONTINUE
C      DATA FORMAT IS XCOORD, DATUM,     2F15.10
52     CONTINUE
       CALL EXIT
       END

FEATURES SUPPORTED
 IOCS

CORE REQUIREMENTS FOR
 COMMON      0  VARIABLES   1678  PROGRAM    948
```

—PROGRAM SELECT—

```
PAGE   1

// JOB T

LOG DRIVE   CART SPEC   CART AVAIL  PHY DRIVE
  0000        0051        0051        0000

V2 M10   ACTUAL  8K  CONFIG  8K

// FOR
*IOCS(CARD,1132 PRINTER)
*LIST SOURCE PROGRAM
      DIMENSION ISEL(20),  IDATA (20), ALENG (200) , AZ(200), FREQ(180)
C     THIS PROGRAM IS TO SELECT CARDS ACCORDING TO CRITERIA SUCH AS
C     LENGTH, AZMMTH, CURVATURE, POSITION ETC AND PUNCH A DECK OF THE
C     SELECTED DATA
      GO TO 47
46    CONTINUE
      PAUSE
47    CONTINUE
      N = 0
      DO 1000  IA = 1, 180
1000  FREQ (IA ) = 0.
      READ (2,10)  (ISEL(I), I = 1,20)
      READ (2,11)  LOWL
10    FORMAT(20I1  )
11    FORMAT (I3)
90    CONTINUE
      DO 95  II = 1,20
95    IDATA (II) = 0
      READ(2,30)   IREG, IMB, IPOS, LINE , IDISC, IMAG, ILENG, IAZ
30    FORMAT (3I1,1I3, 2I1, 2I3)
      IF (IAZ - 180)   60, 61, 61
61    IAZ = IAZ - 180
60    CONTINUE
      IF (ILENG)  900, 900, 901
901   CONTINUE
      IREG = IREG + 1
      IMB = IMB + 1
      IDATA (IREG) = 1
      IDATA (IMB + 4) = 1
      IDATA (IPOS + 6) = 1
      IDATA (IDISC + 9) = 1
      IDATA (IMAG + 16) = 1
      DO 100  J = 1,20
      IF ( ISEL(J) - IDATA(J))     105,106,106
105   GO TO 90
106   CONTINUE
100   CONTINUE
      IF (ILENG- LOWL)   115, 116, 116
115   GO TO 90
116   CONTINUE
      FREQ (       IAZ) = FREQ (IAZ) + 1.
      N = N + 1
      AZ(N) = IAZ
      ALENG (N) = ILENG
      GO TO 90
```

PAGE 2

```
900    CONTINUE
       WRITE (3,502)  N
502    FORMAT ( ' ', I3)
       WRITE (3,501)  (AZ(I), I = 1,N    )
       WRITE(3,501)  (ALENG(I), I = 1,N)
501    FORMAT (12F6.0/)
       WRITE(3, 1070)
1070   FORMAT  (  // 'FREQUENCY DISTRIBUTION'/     2X 'N', 2X 'FREQ' )
       DO 1050 IA = 1,180
       WRITE(3, 1055)  IA,    FREQ(IA)
1055   FORMAT ( 1X , I3 , 2X , F 4.0     )
1050   CONTINUE
       PAUSE 10
899    CONTINUE
       WRITE (2,500) N
500    FORMAT  (I3)
       PAUSE
       WRITE (2,503 )  (FREQ(IZ) , IZ = 1,180 )
       PAUSE
       WRITE (2,503)  (AZ(I), I = 1,N    )
       PAUSE
       WRITE(2,503)  (ALENG(I), I = 1,N)
503    FORMAT (12F6.0)
       GO TO 46
48     CONTINUE
       CALL EXIT
       END
```

—PROGRAM SPENCR—

```
PAGE   1

// JOB T

LOG DRIVE   CART SPEC   CART AVAIL  PHY DRIVE
  0000        0051        0051        0000

V2 M10   ACTUAL  8K  CONFIG  8K

// FOR
*IOCS(CARD,1132 PRINTER)
*LIST SOURCE PROGRAM
*ONE WORD INTEGERS
      INTEGER GRAPH(121), POINT, PLUS, MINUS, BLANK
      DIMENSION    X(220),  U(21)        ,DATA (200)
      DO 5  I = 1,220
5     X(I) = 0.
C     THIS PROGRAM COMPUTES A MOVING SUM OR A SMOOTHED CURVE
C     ACCORDING TO SPENCERS FORMULA
      READ (2,7)  SCALE, NDECK
7     FORMAT  (F8.0, I3 )
      READ (2,9). POINT,PLUS,MINUS, BLANK
9     FORMAT (4A1)
C     THIS STATEMENT ALLOWS THE PROGRAM TO READ IN A CUMULATIVE FREQUENCY
C     DIAGRAM DIRECTLY IF ONE IS AVAILABLE.  IN THIS CASE, SET N = 0
      NODEC = 0
      GO TO 4002
4001  PAUSE
4002  CONTINUE
      READ (2,10)  N, IWIDT, ISIGN
10    FORMAT (3I3)
      NODEC = NODEC + 1
      IF (N . EQ . 0  ) GO TO  20
      WRITE (3,  8)  N, IWIDT , ISIGN
8     FORMAT ( 3I4   )
C     N IS THE NUMBER OF DATA POINTS, IWIDTH IS THE WIDTH OF THE INTERVAL
C    FOR A MOVING SUM.  IWIDTH SHOULD BE AN EVEN NUMBER.
C     IF IWIDTH IS ZERO, THE PROGRAM COMPUTES SMOOTHED CURVE ORDINATES
C     IF ISIGN IS POSITIVE, THE PROGRAM WEIGHTS THE DATA
C     THIS FEATURE IS NOT INCLUDED YET
      IF (ISIGN)  30,30,31
31    CONTINUE
30    CONTINUE
C     THIS SEGMENT ACCUMULATES THE NUMBER OF DATA POINTS IN EACH ONE
C     DEGREE INTERVAL INTO AN ARRAY
      READ (2,35)  (DATA (I) , I = 1,N)
35    FORMAT (12F6.0)
      DO 20 I = 1,N
C     THIS MOVES ALL THE DATA INTO THE EAST TWO QUADRANTS
      IF (DATA(I)-180. )  1700, 1701, 1701
1701  DATB (I) = DATA (I) - 180.
1700  CONTINUE
      IDATA = DATA (I) + 20.
      X(IDATA) = X(IDATA) + 1.
20    CONTINUE
      IF (N . GT . 0  ) GO TO 1203
      READ (2, 1200 )  (X(I)    , I = 20, 199    )
```

PAGE 2

```
1200  FORMAT  (12F6.0  )
1203  CONTINUE
C     THIS FILLS IN THE EXTRA SLOTS AT EACH END OF THE ARRAY WHICH ARE
C     NEEDED FOR THE AVERAGING TECHNIQUES
      DO 38  I = 1,19
      X (I + 199) = X ( I + 19)
      KK = 20-I
      JJ = 200-I
      X ( KK) = X ( JJ )
38    CONTINUE
      WRITE (3,34)  (X(I),I = 1,220 )
34    FORMAT  (10F8.2)
C    CHECK IWIDTH TO SEE IF A SMOOTHED CURVE OR A MOVING SUM IS TO BE COMPUTED
      IF (IWIDT)  40,40,50
40    CONTINUE
      WRITE (3,46) SCALE
46    FORMAT ( '1SMOOTHED DATA ACCORDING TO SPENCERS FORMULA' //
     X' MID' 6X 'F(X)' 25X'GRAPH OF F(X) VS INTERVAL MID POINT'
     X ', SCALE FACTOR =' F6.1   /
     X ' POINT' 10X'0' 9X '10'8X'20' 8X'30' 8X'40' 8X '50' 8X '60' 8X
     X '70' 8X'80' 8X '90' 7X '100'                                   )
      DO48  I = 20,200
      DO 47 J = 1,21
      LL = I - J + 11
      U(J) = X(LL)
47    CONTINUE
C     THIS STATEMENT IS BROKEN INTO TWO PARTS TO LIMIT THE NUMBER OF
C     SUBSCRIPTED VARIABLES TO AN ACCEPTABLE NUMBER
      AVEA=            60. * U(11)
     X + 57. * (U(10) + U(12)) + 47. * (U(9) + U(13))
     X + 33. * (U(8) + U(14)) + 18. * (U(7) + U(15))
     X + 6.* (U(6) + U(16)) - 2. * (U(5) + U(17))
      AVEB =
     X - 5. * (U(4) + U(18)) - 5. * (U(3) + U(19))
     X - 3. * (U(2) + U(20)) -1.* (U(1) + U(21))
      AVE =(AVEA + AVEB) * (1./350.)
      JUMP = 1
3001  CONTINUE
      IDEG = I - 20
      DO 12 II = 1,121
12    GRAPH(II) = BLANK
      IF ((I/10) * (10) - I ) 1110, 1100, 1100
1100  CONTINUE
      DO 1115 JJ = 1, 121, 10
      GRAPH (JJ) = POINT
1115  CONTINUE
1110  CONTINUE
      IP = SCALE * AVE + 0.5
      SYMB = PLUS
      IF (IP) 1120, 1130, 1130
1120  SYMB = MINUS
      IP = ABS (IP) + 2
1130  GRAPH (IP + 1) = SYMB
      WRITE (3,49)  IDEG,  AVE,(GRAPH (IK) , IK = 1,101)
49    FORMAT(1X, I4,  3X ,  F7.3, 1X, 101A1   )
```

```
PAGE   3
       GO TO ( 48, 3000), JUMP
48     CONTINUE
       GO TO 200
50     CONTINUE
       IHWID = IWIDT/2
C      THIS SEGMENT COMPUTES A MOVING SUM OVER THE INTERVAL IWIDTH
       WRITE (3,99)  IHWID
99     FORMAT ( ' MOVING SUM OF DATA POINTS WITHIN PLUS OR MINUS' I3' DEG
      XREES OF INTERVAL CENTER' //                                      )
       WRITE (3, 3005)  SCALE
3005   FORMAT (' MID' 6X  'F(X)' 25X 'GRAPH OF SUM VS INTERVAL MID POINT'
      X ', SCALE FACTOR =' F6.1   /
      X ' POINT' 10X'0' 9X '10'8X'20' 8X'30' 8X'40' 8X '50' 8X '60' 8X
      X '70' 8X'80' 8X '90' 7X '100'                                   )
       JUMP = 2
       DO 59  I = 20, 200
       ISLOT = I - IHWID
       JSLOT = ISLOT + IWIDT
       SUM = 0.
       DO 52  J = ISLOT, JSLOT
       SUM = X(J) + SUM
52     CONTINUE
       AVE = SUM
3000   CONTINUE
       GO TO 3001
59     CONTINUE
200    CONTINUE
       IF  (NODEC . LT. NDECK) GO TO 4001
       CALL EXIT
       END
```

—PROGRAM RILLE—

```
PAGE   1

// JOB T

LOG DRIVE   CART SPEC   CART AVAIL  PHY DRIVE
  0000        0051        0051        0000

V2 M10   ACTUAL  8K  CONFIG  8K

// FOR
*LIST SOURCE PROGRAM
*IOCS(CARD,1132 PRINTER)
*ONE WORD INTEGERS
      INTEGER N
      DIMENSION XO (4) ,   X(4) , WI(152) , DGAZ (152)    , DD(152)
C     THIS PROGRAM PRODUCES (1) DISTANCE-WIDTH RELATIONSHIP DATA.  (2)
C     CENTER OF RILLE X-Y COORDINATES&  (3) WEIGHTED AVERAGE WIDTH DATA.
C     TO FIND THE WEIGHTED AVERAGE WIDTH ALONG ANY REACH IN THE RILLE,
C     FIND (WT CUMW (END) - WT CUMW (START)) / (DIFFERENCE IN CUMD)
      CUMD = 0.
      CUMW = 0.
      WTCUM = 0.
      WOLD = 0.
      UPD = 0.
      AD = 0.
      DOWND = 0.
      N = 0
      READ (2,40)  ALT,  FOCAL,  FACTR
40    FORMAT(3F 10.5                )
      FOCAL = FACTR * FOCAL
      SCALE = ALT / FOCAL
      READ (2,50)   (XO(I), I = 1,4)
50    FORMAT ( 10X , F6.0 , 4X       , F6.0
      DO 77  I = 1,4
      IF (XO(I) - 100000. ) 76, 76, 75
75    XO(I) = XO(I) - 1000000.
76    CONTINUE
      XO(I) = XO(I) * SCALE
77    CONTINUE
      X(1) = XO(1)
      X(2) = XO(2)
      X(3) = XO(3)
      X(4) = XO(4)
      WRITE   (3,149 )  FOCAL,   ALT,  SCALE
149   FORMAT ( ' SCALE OF PHOTOGRAPH TAKEN WITH AN' F8.2 ' MM LENSE AT
     XAN ALTITUDE OF ' F6.2 ' KILOMETERS IS ' F10.5//     )
      WRITE (3 , 150 )
150   FORMAT  ( ' WIDTH OF RILLE AS FUNCTION OF DISTANCE ALONG CENTER LI
     XNE' // '  N' 5X 'CUM DIST' 5X 'WIDTH' 5X 'CENT X' 6X 'CENT Y'
     X10X 'D' , 8X, 'AZMUTH ', 6X ,'CUMW' , 4X 'WT CUM W'6X'UPD'8X
     X  'DOWND'                                                  )
20    CONTINUE
      N = N + 1
      CENXO =  (XO(1) + XO(3) )     /  2.
      CENYO =  (XO(2) + XO(4) )     /  2.
      CENX = (X(1) + X(3) )    /2.
      CENY = (X(2) + X(4) )    /2.
```

PAGE 2

```
      D = SQRT (( CENXO - CENX) **2 + (CENYO - CENY)**2)
      CUMD = CUMD + D
      DD(N) =     D
      W = SQRT ((X(3) - X(1))**2 + (X(4) - X(2)) **2)
      WTW =  (W + WOLD) * D / 2.
      WTCUM = WTW + WTCUM
      IF (W-WOLD)  504, 501, 502
504   UPD = UPD + D
      GO TC 503
501   AD = AD + D
      GO TO 503
502   DOWND = DOWND        +  D
503   CONTINUE
      WOLD = W
      WI (N) = WTW
      WI (N) = W
      CUMW = CUMW + W
      AZ = ATAN (( CENXO - CENX ) / (CENYO - CENY ))
      DEGAZ = 360. * AZ /(2. * 3.14159  )
C     THIS STEP CHANGES THE AZIMUTH RELATIVE TO PHOTO LCORDINATES TO ONE
C     RELATIVE TO NORTH.  THE CONSTANT MUST BE REASSIGNED FOR EACH DECK
      DEGAZ = DEGAZ - 54.7
      IF (DEGAZ)      360, 370,370
360   DEGAZ = DEGAZ + 180.
370   CONTINUE
      DGAZ(N) = DEGAZ
      GO TO 2222
2223  CONTINUE
2222  CONTINUE
      IF (N . EQ . 1 ) DEGAZ = 0
      WRITE (3,500)N,CUMD,W, CENX, CENY, D, DEGAZ, CUMW, WTCUM  ,
     X UPD , DOWND
500   FORMAT (' ' I3, F12.3,  F10.3,  F12.4,  F12.4  ,F12.4, F12.2
     X, F12.4, F12.5 , F10.5,  F10.5                          )
      XO(1) = X(1)
      XO(2) = X(2)
      XO(3) = X(3)
      XO(4) = X(4)
      READ (2,50)  (X(I),  I = 1,4  )
      IF ( X(1))   200, 201, 201
201   CONTINUE
      DO 87  I = 1,4
      IF(X(I) - 100000.)  86, 86, 85
85    X(I) = X(I) - 1000000.
86    CONTINUE
      X(I) = X(I) * SCALE
87    CONTINUE
      GO TO 20
200   CONTINUE
      AN = N
      WAVE = CUMW/AN
      WTAVE = WTCUM/CUMD
      WRITE (3,293) WAVE, WTAVE      , UPD, DOWND , AD
293   FORMAT ( / ' AVERAGE WIDTH =' F8.4 '  WEIGHTED AVERAGE WIDTH = '
     XF8.4  /' WIDTH INCREASES FOR ' F8.4 'KM., DECREASES FOR ' F8.4'KM
```

PAGE 3

```
     X.'  F8.4' KM SHOW NO CHANGE.'                                        )
C      THESE STATEMENTS MOVE ALL THE DATA IN THE ARRAY UP ONE VALUE
C      SINCE THE FIRST VALUE IS ZERO OR MEANINGLESS IN THESE TWO ARRAYS
       DO 2002  KLM = 1,151
       KLMP1 = KLM + 1
       DD (KLM ) = DD (KLMP1          )
       DGAZ (KLM) = DGAZ (KLMP1   )
2002   CONTINUE
       NM1 = N - 1
       PAUSE
       WRITE (2,301 ) DGAZ
       PAUSE
       WRITE (2,301 ) DD
301    FORMAT (12F6.2)
       CALL EXIT
       END
```

—PROGRAM BASIN—

```
PAGE   1

// JOB T

LOG DRIVE   CART SPEC   CART AVAIL  PHY DRIVE
  0000        0051        0051        0000

V2 M10   ACTUAL  8K  CONFIG  8K

// FOR
*IOCS(CARD,1132 PRINTER)
*LIST SOURCE PROGRAM
*EXTENDED PRECISION
      REAL  LONGI, LONGS, LATI, LATS, LONG, LAT
      DIMENSION  RADIM(183), RADSE(183), CIRIM(183), CIRSE (183),
     X DEL(4), ID(183), DELAZ (183,4), KOUNT(4)
      EQUIVALENCE  (DELAZ(1,1),RADIM(1)),(DELAZ (1,2),RADSE(1)),
     X  (DELAZ (1,3), CIRIM(1)),  (DELAZ    (1,4), CIRSE(1))
      RAD (D) =  ( D * 2. * 3.1415927 / 360.      )
      DEG (R)  =         ( 360. * R / (2. * 3.1415927      )   )
      READ (2,10) LONGI, LONGS, LATI, LATS, N
10    FORMAT (4F10.0,I3 )
      LONGI=RAD(LONGI)
      LONGS=RAD(LONGS)
      LATI=RAD(LATI)
      LATS=RAD(LATS)
      DO 100 J = 1,N
      READ (2,12 ) ID(J), LONG, LAT
12    FORMAT  (I4, 1X, 2F11.0    )
      LONG=RAD(LONG)
      LAT=RAD(LAT)
      SI = COS(LAT) * COS(LATI) * ( COS (LONG-LONGI) + SIN(LAT ) * SIN
     X (LATI))
      SS = COS(LAT) * COS(LATS) * ( COS (LONG-LONGS) + SIN(LAT ) * SIN
     X(LATS) )
      RADIM(J) = (SIN(LATI)-SI*SIN(LAT))/(COS(LAT) * SQRT(1. -SI**2 ))
      RADSE(J) = (SIN(LATS)-SS*SIN(LAT))/(COS(LAT) * SQRT(1. - SS**2))
      IF  (J . GT. 10)  GO TO 1715
      WRITE (3,56) LONGI,LONGS, LATI,LATS,SI,SS,RADIM(J),RADSE(J)
56    FORMAT ( 8F10.4)
1715  CONTINUE
      RADIM(J)=DEG(ACOS(RADIM(J)))
      RADSE(J)=DEG(ACOS(RADSE(J)))
      IF  (J .GT. 10)  GO TO 1716
      WRITE (3,55)  RADIM(J), RADSE(J)
55    FORMAT (  2         F15.5 )
1716  CONTINUE
      IF (LONGI.LT. LONG )    RADIM(J) = -1.*RADIM(J)
      IF (LONGS.LT. LONG) RADSE(J) = -1.*RADSE(J)
      CIRIM(J) = RADIM(J) + 90.
      CIRSE (J) = RADSE (J) + 90.
100   CONTINUE
      WRITE (3,26)(ID(JK),RADIM(J K), CIRIM (JK) , RADSE(JK),
     X CIRSE (JK ) , JK = 1,N    )
26    FORMAT  (I5, 4F10.4      )
      DO 110 J = 1,N
      READ (2,14) IDD, AZI
```

PAGE 2

```
14     FORMAT (3X , I3 , 5X , F 3.0   )
       IF (IDD - ID(J))      50,51    , 51
50     PAUSE
51     CONTINUE
       DEL (1) =  AZI - RADIM (J)
       DEL (2) =  AZI - CIRIM (J)
       DEL (3) =  AZI - RADSE (J)
       DEL (4) =  AZI - CIRSE (J)
       DO 60 K = 1,4
       DEL(K)=RAD(DEL(K))
       DELAZ(J,K)=ASIN(SIN(DEL(K)))
       DELAZ(J,K)=ACOS(COS(DELAZ(J,K)))
       DELAZ(J,K)=DEG(DELAZ(J,K))
60     CONTINUE
       WRITE (3,102)  ID(J), (DELAZ (J,K),K = 1,4)
102    FORMAT (I5, 4F10.4)
  110  CONTINUE
       DO 112 KK = 1,4
112    KOUNT (KK) = 0
       DO 600  J = 1,N
       CHECK = DELAZ (J,1)
       KONT = 1
       DO 610 K = 2,4
       IF  (DELAZ (J,K) . GE. CHECK  )   GO TO 620
       CHECK = DELAZ (J,K)
       KONT = K
620    CONTINUE
  610  CONTINUE
       KOUNT (KO NT) = KOUNT ( KO NT) + 1
       DO 636 LM = 1,4
636    DEL (LM) = 0.
       DEL (KONT) = DELAZ (J,KONT )
       WRITE (3,2010)   J, (DEL( LLL ), LLL = 1,4  )
2010   FORMAT   (I4, 2X  ,  4 ( F 7.1 , 2X  ))
600    CONTINUE
       WRITE (3,3000)  (KOUNT(KK), KK = 1,4   )
3000   FORMAT (' NUMBER OF IMBRIUM RADIAL LINEAMENTS =' I4
      X / ' NUMBER OF IMBRIUM CIRCUMFRENTIAL LINEAMENTS =' I4
      X/' NUMBER OF SERENETATIS RADIAL LINEAMENTS =' I4
      X/  ' NUMBER OF SERENETATIS CIRCUMFRENTIAL LINEAMENTS ='  I4    )
       CALL EXIT
       END
```

BIBLIOGRAPHY

Adler, J. E. M. and Sallisbury, J. W. (1969) Behavior of water in a vacuum: implications for "lunar rivers": Science, Vol. 164, pp. 589-590

Advertising Displays, Inc. (1970) Instructions to accompany the Austin Photo Interpretometer: Covington, Kentucky, 35 pp.

Alter, D. (1967) Pictorial Guide to the Moon: Crowell, New York, 199 pp.

Anders, E. (1970) Water on the moon?: Science, Vol. 169, pp. 1309-1310.

Baldwin, R.B. (1971) Rima Goclenius II: J.G.R., Vol. 76, pp. 8459-8465.

Batson, R.M. (1971) Preliminary Catalog of Pictures Taken on the Lunar Surface During the Apollo-15 Mission: U.S.G.S. Interagency Report, No. 35, Washington, D.C. 61 pp.

Bendix Corp. (1968) Handbook for the AS11A-1 Automated Analytical Stereo Plotter: Vol. 1, Bendix Report No. 5073, 200 pp.

Blackman, R. B. and Tukey J. W. (1959) The Measurement of Power Spectra: Dover, New York, 188 pp.

Bowker, D. E. and Hughes, J. K. (1971) Lunar Orbiter Photographic Atlas of the Moon: NASA SP-206, NASA Scientific and Technical Information Office, Washington, D.C., 675 pp.

Bradley, J. V. (1968) Distribution-Free Statistical Tests: Prentice Hall, Englewood Clifs, New Jersey, 388 pp.

Burke, J. D., Brereton, R. G., and Muller, P. M. (1970) Desert stream channels resembling lunar sinuous rilles: Nature, Vol. 225, pp. 1234-1236.

Cameron, W. S. (1964) An interpretation of Schroeter's Valley and other lunar sinuous rilles: J.G.R., Vol. 69, pp. 2423-2430

Cameron, W. S. and Niksch, M. A. (1972) Apollo-15 Lunar Photography: National Space Craft Data Center Users' Note No. 72-07, NASA, Greenbelt, Maryland, 58 pp.

Carr, M. H. and El-Baz, F. (1971) Geologic map of the Apennine-Hadley region of the moon: U.S.G.S., Map No. I-723, Sheet 1, Washington, D.C.

Crow, E.L . et al. (1970) Statistics Manual, Dover, New York 288 pp.

Cruikshank, D. P. and Wood, L. A. (1972) Lunar rilles and Hawaiian volcanic features: possible analogues: Moon, Vol. 3, p. 412.

Dietrich, J. W. and Clanton, U. S. (1972) Photographic summary: in Apollo-15 Preliminary Science Report, NASA SP-289, Washington D.C., pp. 3-1 to 3-32.

Doyle, F. J. (1972) Photogrammetric analysis of Apollo-15 records: in Apollo-15 Preliminary Science Report, NASA SP-289, Washington D.C, pp. 25-27 to 25-36.

Duffield, W. A. (1972) Kilauea volcano provides a model for plate tectonics: Geotimes, Vol. 17, pp. 19-20.

El-Baz, Farouk (1968) Abstracts of the 1968 G.S.A. annual meeting, Geological Society of America, Boulder,Colorado.

Elger, T. G. (1895) The Moon, George Phillips & Son, London, 173 pp.

Elston, W. E., Laughlin, A. W. and Brower, J. A. (1971) Lunar near-side tectonic patterns from orbiter photographs: J.G.R., Vol.76, pp. 5670 - 5673

Esten, R. D. (1966) Automation of Stereo Compilation: in Manual of Photogrammetry, Vol. 2, American Society of Photogrammetry, Vol. 2, Falls Church, Virginia, pp. 759-802.

Fielder, G. (1960) A theory of the origin of lunar rilles: Sky and Telescope, Vol. 19, pp. 334-337

Fleischer, R. (1937) Story of the telescope: The Sky; reprinted in Page, T. & Page, W. L. (1966) Telescopes, Macmillan Co., New York, pp. 40-45.

Fuller, C.E. and Johnston, W.A. (1919) Applied Mechanics, Vol. 2, Wiley, New York, 556 pp.

Gaskell, R.E. (1958) Engineering Mathematics, Dryden, New York, 462 pp.

Gast, P. W. et al. (1972) Preliminary examination of lunar samples: in Apollo-15 Preliminary Science Report, NASA SP-289, Washington D.C., pp. 6-1 to 6-25

Gilvarry, J. J. (1969) Geometric and physical scaling of river dimensions on the earth and moon: Nature, Vol. 221. pp. 533-535.

Goodacre, W. (1931) The Moon with a Description of its Surface Configuration: Pardy & Son, Bournemouth, England, 464 pp.

Gold, T. (1961) Permafrost on the moon: J.G.R., Vol. 66. p. 2531.

______ (1966) The moon's surface: in The Nature of the Lunar Surface: Hess, W. N., Menzel, D. H. and O'Keefe, J. A., eds., Johns Hopkins, Baltimore, Md. pp. 107-127.

Greeley, R. (1971) Lava tubes and channels in the lunar Marius Hills: Moon, Vol. 3, pp. 289-314

______ (1971) Lunar Hadley Rille: considerations of its origin: Science, Vol. 17, pp. 722-725

Green, Jack (1969) Terrestrial analogs: water on the moon: Presentation at the North American Rockwell Science Center, Jan. 16, 1969.

Hackmann, R. J. (1960) Generalized photogeologic map of the moon: Army Map Service, C.E.

______ (1966) Geologic map of the Montes Apenninus region of the moon: U.S.G.S., Map No. I-463, Washington, D.C.

Hapke, B. and Greenspan, B. (1970) Crater densities in the vicinity of lunar sinuous rilles: EOS 51, p. 345.

Harbaugh, J.W. and Merriam, D.F. (1968) Computer Applications in Stratigraphic Analysis: Wiley, New York 282 pp.

Hartmann,W. K. and Kuiper, G. P. (1962) Concentric structures surrounding lunar basins; C.L.P.L. Vol. 1, pp. 1-66

Hartmann, W. K. (1963) Radial structures surrounding lunar basins, I: the Imbrium system: C.L.P.L., Vol.52. pp. 1-15

Hatheway, A.W. and Herring, A.K. (1970) Bandera lava tubes of New Mexico and lunar implications: C.L.P.L., Vol. 8, pp. 299-327.

Helmering, R.J. (1973) Selenodetic control derived from Apollo Metric photography: Moon, Vol. 8, pp. 450-460.

Holmes, A. (1965) Principles of Physical Geology: 2nd ed., Ronald, NewYork, 1288 pp.

Howard, K. A. (1971) Geologic map of part of the Apennine-Hadley region of the moon: U.S.G.S. Map No. I-723, Sheet 2, Washington D.C.

Howard, K. A. and Head, J. (1972) Regional Geology of Hadley Rille: in Apollo-15 Preliminary Science Report, NASA SP-289, Washington, D.C., pp 25-53 to 25-57.

Howard, K. A. and Larsen, B. R. (1972) Lineaments that are artifacts of lighting: in Apollo-15 Preliminary Science Report, NASA SP-289, Washington, D.C., pp. 25-58 to 25-62

Howard, K.A. et al. (1972) Geology of Hadley Rille: Preliminary Report: U.S.G.S. Interagency Report 41, Washington, D.C. 57 pp.

Husain, L. et al. (1972) The ages of lunar material from Fra Mauro, Hadley Rille, and Spur Crater: in Procedings of the Third Lunar Science Conference, Geochimica et Cosmocmimica Acta Supplement 3, Dieter Heyman, ed., Vol. 2, MIT Press, Cambridge, Mass. pp. 1557-1568.

Keil, K., et al. (1970) Mineral chemistry of lunar samples: Science, Vol. 167, pp. 597-599.

Koch, G.S. and Link, R.F. (1970) Statistical Analysis of Geological Data: Vol. 1, Wiley, New York, 375 pp.

Kopal, Z. (1969) The earliest maps of the moon: Moon, Vol. 1.

______ (1962) Physics and Astronomy of the Moon: Academic Press, New York, 303 pp.

Kosofsky, L. J. and El-Baz, F. (1970) The Moon as Viewed by Lunar Orbiter: NASA SP-200, Washington, D.C. 152 pp.

Langley, R. (1971) Practical Statistics: Dover, New York, 399 pp.

Leonardi, P (1972) Winding and meandering furrows on the lunar surface: Modern Geology, Vol. 31, pp. 151-156

Leopold, L. B., Wolman, M. G. and Miller, J. P. (1964) Fluvial processes in Geomorphology: Freeman, San Francisco, 522 pp.

Leopold, L. B. and Wolman, M. G. (1967) River Channel Patterns: Braided, Meander and Straight: U.S.G.S. Prof. Paper 282-B, pp. 31-84.

______ & ______ (1960) River meanders: G.S.A. Bull., Vol. 71, pp. 769-794.

Lockheed Electronics Co. Inc. (1972) Apollo-15 Index of Mapping Camera and Panoramic Camera Photographs, NASA, Houston, 217 pp.

Mason, B. and Melson, W.G. (1970) The Lunar Rocks: Wiley, New York, 179 pp.

McAdams, W. (1954) Heat Transmission: McGraw-Hill, New York, 532 pp.

McCall, G. J. H. (1970) Lunar rilles and a possible terrestrial analogue: Nature, Vol. 225, pp. 714-716.

Mills, A. A. (1969) Fluidization phenomena and possible implications for the origin of lunar craters: Nature, Vol. 224, pp. 863-866.

Morris, E. C. and Shoemaker, E. M. (1968) Fragmental debris., Geology, Television observations from surveyor: Part II of Surveyor Project Final Report, JPL Tech Rept. 32-1265, p. 69.

Murase, T. and McBirney, A. R. (1970) Thermal conductivity of lunar and terrestrial igneous rocks in their melting range: Science Vol. 170, pp. 165-167.

Murray, J. B. (1971) Sinuous rilles: in Geology and Physics of the Moon, G. Fielder, ed., Elsevier, Amsterdam, pp. 27-39.

Mutch, T. (1972) Geology of the Moon: Rev. Ed. Princeton University Press, Princeton, New Jersey, 391 pp.

Nasmyth, J. and Carpenter, J. (1874) The Moon Considered as a Planet, a World and a Satellite: 2nd ed., John Murray, London, 189 pp.

Neison, E. (1876) The Moon and the Condition and Configurations of its Surface: Longmans, Green & Co., London. 576 pp.

Oberbeck, V.R. and Quaide, W.L. (1967) Estimated thickness of a fragmental surface layer of Oceanus Procellarum: J.G.R., Vol. 72. pp. 4697-4704.

Oberbeck, V. R., Quaide, W. L. and Greeley, R. (1969) On the origin of lunar sinuous rilles: Modern Geology, Vol.1, pp 75-80.

Oberbeck, V. R. et al. (1972) Lunar Rilles-A Catalog and Method of Classification, NASA TEC. MEM. TM-X-62, 088, Wash. D.C., 82 pp.

O'Keefe, J. A. (1969) Water on the moon and a new non-dimensional number: Science, Vol. 163, pp. 669-670.

Ollier, C. (1969) Volcanoes: MIT Press: Cambridge, Mass. 177 pp.

Pickering, W.H. (1903) The Moon: Doubleday Page, New York, 103 pp.

Quaide, W. (1965) Rilles, ridges and domes-clues to maria history: Icarus, Vol. 4, pp. 374-379.

Roberson, F.I. and Kaula, W.M. (1972) Apollo-15 laser altimeter: in Apollo-15 Preliminary Science Report, NASA SP-289, Washington, D.C. pp. 25-48 to 25-49.

Scheidegger, A. E. (1970) Theoretical Geomorphology: Springer-Verlag, New York, 430 pp.

Schermerhorn, W. (1966) Plotting machines with mechanical or optical trains: in Manual of Photogrammetry, American Society of Photogrammetry, Vol. 2, Falls Church, Va. pp. 629-758.

Schubert, G., Lingenfelter, R. E. and Peale, S. J. (1970) The Morphology, distribution and origin of lunar sinuous rilles: Reviews of Geophysics and Space Physics, Vol. 8, pp. 199-224.

Schumm, S. A. (1969) Lunar rivers or coalesced chain craters?: Science, Vol. 165, p. 201.

Schumm, S. A. (1970) Experimental studies on the formation of lunar surface features by fluidization: G.S.A. Bull., Vol. 81, pp. 2539-2552.

Shaler, N. S. (1903) A Comparison of the Features of the Earth and Moon: Smithsonian contributions to knowledge, Vol. XXXIV, Smithsonian Institute, Washington, D.C., 130 pp.

Shoemaker, E. M. and Hackman, R. J. (1960) Stratigraphic basis for a lunar time scale: in Kopal, Zednek and Mikhailov, eds.: The Moon, Symposium 14, Internat. Astron. Union, Leningrad, London, Academic Press., pp. 289-300.

Skolnikoff, I. S. and Redheffer, R. M. (1958) Mathematics of Physics and Modern Engineering: McGraw-Hill, New York, 810 pp.

Smoluchowski, R. (1968) Mars: retention of ice: Science, Vol. 159, pp. 1348-1350.

Soderblom, L. A. and Lebofsky, L. A. (1972) Techniques for rapid determination of relative ages from orbital photography: J.G.R. Vol. 77, pp. 279-292.